

People's Democratic Republic of Algeria
Ministry of Higher Education and Scientific Research
University of Tissemsilt



THESIS

In Partial Fulfillment of the
requirements for the
LMD Doctorate Degree

Presented by : Mr. BOUADI Abdelkader Ilias

Title: Design and theoretical study of Heusler compounds based on transition metals for applications in spintronics and proper energy: Ab-initio approach with WIEN2k.

Faculty	: Sciences and Technology
Department	: Sciences of Matter
Domain	: Sciences of Matter
Field	: Physics
Formation title	: Computational Physics

In front of the jury composed of:

Members of the Jury	*Grade*	*Position*	*Affiliation*
BENALIA Salah eddine	Pr	Chairman	Tissemsilt university
DAHMANE Fethallah	Pr	Supervisor	Tissemsilt university
MOKHTARI Mohamed	Pr	Co-supervisor	Tissemsilt university
MERABET Mostefa	Pr	Examiner	Tissemsilt university
RACHED Habib	Pr	Examiner	Chlef university
RIGHI Haroun	Pr	Examiner	ESNEREDR Batna

Academic Year: 2025–2026

Acknowledgments

All praise is due to Allah, who, by His will and mercy, guided me to the path of light and knowledge.

These thanks go first and foremost to Professor **DAHMANE Fethallah**, Professor at the University of Tissemsilt, my thesis supervisor. He was always attentive and readily available throughout the completion of this thesis, and for the inspiration, help, and time he so generously dedicated to me. Without him, this thesis would never have been possible. I am delighted to have had the opportunity to work under his guidance. I learned a great deal from him and greatly benefited from all the very pleasant conversations we had.

I extend my sincere thanks to Professor **MOKHTARI Mohamed** of the University of Tissemsilt, my thesis co-supervisor for his interest in my work, and unwavering scientific support throughout. His involvement, inspiration, and encouragement all contributed to the completion of this high-quality work.

I warmly thank Pr.em. **NOUREDDINE ZEKRI**, President of the LEPM Laboratory at the University of Oran (USTO), for agreeing to serve as my supervisor and for reviewing my work. I also thank the entire LEPM Laboratory team for their invaluable support throughout my training.

I would also like to express my sincere gratitude to Professor **MOKHTARI Mohamed**, President of the LPMH Laboratory at Tissemsilt University, for welcoming us into his research team and for his valuable support.

My deepest gratitude also goes to Professor **BENALIA Salah eddine**, who honoured me by presiding over the thesis defence committee.

Also, we extend our sincere appreciation to the distinguished members of the jury for their invaluable contributions and insightful feedback throughout the evaluation process:

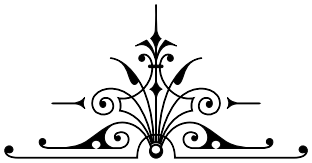
Pr. **MERABET Mostefa** (Examiner), Tissemsilt University,

Pr. **RACHED Habib** (Chlef University),

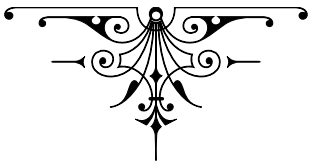
Pr. **RIGHI Haroun** (Examiner), ESNEREDR Batna,

and our Guest Dr. **AMARI Djilali** from Tamanrasset University.

We are deeply grateful for their expertise, time, and dedication to the advancement of knowledge in our field.



Dedications



This thesis is lovingly dedicated to the pillars of my life.

To my beloved parents, ***Pr. BOUADI Mohammed*** *and* ***DIFALLAH Fatima****, whose endless love, sacrifices, and prayers have been the light guiding my path. Your patience, wisdom, and unwavering belief in me have given me the strength to overcome every challenge. This achievement is a reflection of your dedication and devotion.*

To my dear brothers, ***Wajih****,* ***Chomous****,* ***Haroun****,* ***Wanis****, and my sister* ***Maria****, thank you for your constant encouragement, understanding, and for being my source of comfort and motivation during difficult times. Your presence in my life is a priceless blessing.*

To my cherished friends, ***Dr ABANE Mahdi****,* ***Hmitcha****,* ***Khalil****,* ***Jamal****, who stood by me through moments of doubt and celebration alike, your support, laughter, and sincere advice have made this journey lighter and more meaningful.*

I also extend my heartfelt gratitude to my colleagues at Lakri Ali middle school especially, for their cooperation, insightful discussions, and professional support that enriched both this research and my personal growth.

My supervisor, ***DAHMANE Fethallah*** *and Co-supervisor,* ***MOKHTARI Mohamed****, who supported me throughout this work, also other professors at Tissemsilt University:* ***Pr. BOUMIA Lakhder****,* ***Pr. CHAKER Yacine****,* ***Dr HADJZOUBIR Miloud****.*

This milestone is not mine alone; it belongs to everyone who believed in me, supported me, and walked beside me throughout this long and rewarding journey.

❖

Ilias

Abstract

In this thesis, we detailed the structural, elastic, thermodynamic, electronic, and magnetic properties of the following alloys: Pr_2RhZ, Pr_2CoZ, Ir_2ScZ, Rn_2MnZ, and the quaternary Heusler compound CrPrCoZ, where $Z =$ Al, Ga, In, Ge, Sb, Sn, or Te. The alloys were based on rare-earth and transition metals. The calculations were carried out within the framework of density functional theory (DFT) utilizing the full-potential linearized augmented plane wave method (FP-LAPW) as implemented in the WIEN2k package.

In order to optimize the structure, the GGA-PBE exchange-correlation functional was employed. This allowed precise calculation of the elastic constants, bulk moduli, equilibrium lattice parameters, and formation energies. Indicators of mechanical stability and ductility were assessed by calculating elastic moduli according to the Born–Huang criteria.

The presence of half-metallic or spin-gapless behavior, bandgap characteristics, and spin polarization were evaluated by analyzing spin-polarized electronic band structures together with total and projected densities of states (DOS/PDOS). Magnetic configurations were examined by comparing ferromagnetic, paramagnetic, and ferrimagnetic phases. For several compounds, the calculated total and atomic magnetic moments follow the Slater–Pauling rule, indicating strongly spin-polarized and well-defined integer magnetic moments.

Vibrational and thermodynamic properties were investigated using the quasi-harmonic Debye model to study heat capacities, entropies, thermal expansion coefficients, and Debye temperatures as functions of temperature and pressure. These results provide insights into lattice stability, anharmonic effects, and phonon-mediated thermal transport relevant to thermoelectric and magnetocaloric applications.

Overall, the computational results demonstrate that the investigated Heusler compounds are structurally stable, mechanically robust, and electronically promising. Their strong spin polarization, half-metallic character, and stable magnetic ordering make them attractive candidates for next-generation spintronic devices, magnetic sensors, and energy-efficient technologies.

Keywords: Full-Heusler alloys, DFT, half-metallic, ferromagnetism, spintronics.

الملخص

في هذه الرسالة أجرينا دراسة شاملة، اعتمادًا على حسابات المبادئ الأولية، للخصائص البنيوية والمرنة والديناميكية الحرارية والإلكترونية والمغناطيسية لسبائك هيوسلر الكاملة القائمة على العناصر الأرضية النادرة والمعادن الانتقالية، وهي: Pr_2RhZ و Ir_2ScZ و Pr_2CoZ و Ru_2MnZ إضافة إلى مركب هيوسلر الرباعي **CrPrCoZ** حيث أن **Z = Al** أو **Ga** أو **In** أو **Ge** أو **Sb** أو **Sn** أو **Te**.

أُجريت جميع الحسابات في إطار نظرية دالة الكثافة **(DFT)** باستخدام طريقة الموجة المستوية المعززة الخطية ذات الجهد الكامل **(FP-LAPW)** كما هي مطبقة في برنامج WIEN2k. وقد استُخدمت دالة التبادل والارتباط **GGA-PBE** لتحسين البنية البلورية مما سمح بحساب دقيق لثوابت الشبكة وثوابت المرونة عند التوازن ومعاملات الانضغاط وطاقات التكوين.

تم تقييم الاستقرار الميكانيكي وقابلية الليونة اعتمادًا على معايير بورن من خلال حساب معاملات المرونة. كما تم تحليل البنى الإلكترونية المستقطبة مغزليًا إضافة إلى كثافة الحالات الكلية والمُسقطة **(DOS/PDOS)** لدراسة استقطاب الدوران وخصائص فجوة الطاقة شبه المعدني ووجود السلوك أو السلوك المعدني شبه الخالي من قوة الدوران.

تمت دراسة الترتيبات المغناطيسية بمقارنة الأطوار المغناطيسية الحديدية والبارامغناطيسية والفيرومغناطيسية المضادة. وأظهرت النتائج أن العزوم المغناطيسية الكلية والذرية لعدد من المركبات تتبع قاعدة سلاتر-بولينغ مما يدل على وجود عزوم مغناطيسية صحيحة واستقطاب مغزلي قوي.

كما تمت دراسة الخصائص الاهتزازية والديناميكية الحرارية باستخدام نموذج ديباي شبه التوافقي لتحليل السعات الحرارية والإنتروبيا ومعاملات التمدد الحراري ودرجات حرارة ديباي بدلالة درجة الحرارة والضغط.

بشكل عام، تُظهر النتائج الحسابية أن مركبات هيوسلر المدروسة مستقرة بنيويًا ومتينة ميكانيكيًا وواعدة إلكترونيًا، كما أن استقطابها المغزلي القوي وطابعها شبه المعدني وترتيبها المغناطيسي المستقر يجعلها مرشحة مناسبة لتطبيقات السبينترونيك وأجهزة الاستشعار المغناطيسية والتقنيات الموفرة للطاقة.

الكلمات المفتاحية: سبائك هيوسلر الكاملة، نظرية دالة الكثافة، شبه معدني، مغناطيسية حديدية، سبينترونيك.

Résumé

Dans cette thèse, nous avons étudié les propriétés structurales, élastiques, thermodynamiques, électroniques et magnétiques des alliages suivants : Pr_2RhZ, Pr_2CoZ, Ir_2ScZ, Rn_2MnZ ainsi que du composé de Heusler quaternaire CrPrCoZ, où $Z =$ Al, Ga, In, Ge, Sb, Sn ou Te. Ces alliages sont constitués de terres rares et de métaux de transition.

Les calculs ont été réalisés dans le cadre de la théorie de la fonctionnelle de la densité (DFT) en utilisant la méthode des ondes planes augmentées linéarisées à potentiel complet (FP-LAPW) implémentée dans le code WIEN2k. L'optimisation structurale a été effectuée à l'aide de la fonctionnelle d'échange-corrélation GGA-PBE.

Cela a permis de déterminer avec précision les constantes élastiques, les modules de compressibilité, les paramètres de maille à l'équilibre et les énergies de formation. La stabilité mécanique et la ductilité ont été évaluées à partir des modules élastiques selon les critères de Born–Huang.

Les structures de bandes électroniques polarisées en spin ainsi que les densités d'états totales et projetées (DOS/PDOS) ont été analysées afin d'identifier le caractère semi-métallique, la présence d'un comportement spin-gapless et la polarisation de spin. Les configurations magnétiques ont été examinées en comparant les phases ferromagnétiques, paramagnétiques et ferrimagnétiques.

Les propriétés vibrationnelles et thermodynamiques ont été étudiées à l'aide du modèle de Debye quasi-harmonique afin d'analyser les capacités thermiques, les entropies, les coefficients de dilatation thermique et les températures de Debye en fonction de la température et de la pression.

Les résultats obtenus montrent que les composés de Heusler étudiés présentent une grande stabilité structurale, de bonnes propriétés mécaniques et des caractéristiques électroniques prometteuses, ce qui en fait des candidats potentiels pour les dispositifs spintroniques, les capteurs magnétiques et les technologies énergétiques avancées.

Mots-clés : Alliages Heusler, DFT, semi-métallique, ferromagnétisme, spintronique.

CONTENTS

Abstract **vi**

List of abbreviations and acronyms **xv**

General introduction **1**

I Heusler Compounds **6**

I.1 Introduction 6

I.2 Background on Transition Metals 7

I.2.1 Transition Metals 7

I.2.2 General Characteristics of Transition Elements 8

I.2.3 Electronic Configuration of the Transition Elements 9

I.2.4 Properties of Transition Metals 9

I.3 Rare Earth-Based Alloys 10

I.3.1 Definition of Rare Earth Compounds 10

I.3.2 I.3.2. Properties of rare earths 10

I.4 Different types of Heusler Alloys 11

I.4.1 History of Heusler Compounds 11

I.4.2 Different types of Heusler Alloys 12

I.5 Different magnetic forms 16

I.5.1 Diamagnetism 17

I.5.2 Paramagnetism 18

I.5.3 Ferrimagnetism . . . 19
I.5.4 Antiferromagnetism . . . 19
I.5.5 Ferromagnetism . . . 20
I.5.6 Principle of Slater–Pauling . . . 22
I.6 Electronic Properties . . . 24
I.6.1 Band Structure . . . 25
I.6.2 Density of electronic states . . . 26
I.7 Thermoelectric Effects . . . 27
I.7.1 Seebeck Effect . . . 27
I.7.2 Peltier Effect . . . 28
I.7.3 The Thomson effect . . . 29
I.8 Applications of Heusler compounds . . . 30
I.8.1 Spintronic materials . . . 31
I.8.2 Thermoelectric applications of Half-Heusler compounds . . . 33
I.9 Conclusion . . . 34

II Density Functional Theory (DFT) 40
II.1 Introduction . . . 40
II.2 Schrödinger Equation . . . 41
II.2.1 Born–Oppenheimer approximation . . . 43
II.2.2 Approximations based on the wave function . . . 44
II.2.3 Density Functional Theory (DFT) . . . 48
II.3 The linearized augmented plane wave (LAPW) method . . . 55
II.3.1 Linearized augmented plane waves method (LAPW) . . . 57
II.3.2 Development in local orbitals . . . 61
II.3.3 The concept of the FP-LAPW method . . . 63
II.4 The WIEN2k code . . . 64
II.5 Conclusion . . . 66

III Results and Discussion 73
III.1 Introduction . . . 73
III.2 Calculation Details . . . 74

III.3 Full-Heusler Alloys 75
III.3.1 Full-Heusler rare-earth-based alloys 75
III.3.2 Full Hesler transition metal-based alloys 110
III.4 Conclusion 132

General conclusion and future perspectives **139**

Appendix **141**

LIST OF FIGURES

I.1 The periodic table of transition metals 8

I.2 Full-Heusler alloy structures: (a) Cu_2MnAl and (b) Hg_2CuTi [18]. . . . 13

I.3 (a) the Rock salt structure, (b) the zinc blende structure and their relationships with the semi-Heusler structure (c) and with the Heusler structure (d) [21]. 15

I.4 Schematic illustration of the three possible non-equivalent structures of quaternary Heusler compounds (a) type 1, (b) type 2 and (c) type 3 [23]. 16

I.5 Variations in magnetization under the effect of the magnetic field (a), and thermal variation of magnetic susceptibility (b) for a diamagnetic substance. 17

I.6 Paramagnetism: (a) a spin network, (b) variation of magnetization under an applied field, (c) thermal variation of $1/\chi$. 18

I.7 Ferrimagnetism: (a) a spin lattice; (b) variation of the magnetization under an applied field; (c) thermal variation of $1/\chi$; (d) thermal variation of the spontaneous magnetization. 19

I.8 Antiferromagnetism: (a) a spin network; (b) variation in magnetization under an applied field; (c) thermal variation of $1/\chi$. 20

I.9 Ferromagnetism: (a) spin network; (b) variation under the effect of the magnetization field ($T_1 < T_C < T_2 < T_3$); (c) thermal variation of $1/\chi$; (d) thermal variation of spontaneous magnetization. 21

I.10 Magnetization curve of a non-magnetized material, known as the first magnetization curve (solid line). Hysteresis cycle (dashed lines). 22
I.11 Slater–Pauling curve [33]. 23
I.12 The total magnetic moment m calculated as a function of the number of valence electrons N_v for half-Heusler alloys (on the left), and full-Heusler alloys (on the right). The dashed lines represent the Slater–Pauling (SP) behavior [34]. 24
I.13 The total magnetic moment m calculated as a function of the number of valence electrons N_v for half-Heusler alloys (on the left), and full-Heusler alloys (on the right). The dashed lines represent the Slater–Pauling (SP) behavior [34]. 25
I.14 The total (TDOS) and partial (PDOS) densities of states for the compound Fe_2VGa. 26
I.15 First experimental setup described by Seebeck. 28
I.16 First experimental setup described by Peltier. 29
I.17 Represented Thomson and magneto-Thomson effects. 30
I.18 Representative diagram of energy bands of materials with polarized spins. 31
I.19 The two states, parallel and antiparallel, in a giant magnetic junction. . 32
I.20 The two states, parallel and antiparallel, in a magnetic tunnel junction. 33
I.21 A thermoelectric module. 33
I.22 Biolite Camp stove. 34

II.1 Self-consistent cycle of (DFT). 56
II.2 MT potential. 57
II.3 The WIEN code flowchart. 66

III.1 Crystallographic structure of full-Heuler alloy Pr_2RhZ (Z = Al, Ga and In) in which (a) Hg_2CuTi type and (b) Cu_2MnAl type (by VESTA [3]). 76
III.2 Total energy versus unit cell volume for Pr_2RhZ (Z = Al, Ga and In). . 78
III.3 Spin-polarized band structures of majority spin (Up) and minority spin (Down) of Pr_2RhZ (Z = Al, Ga, In) in ferromagnetic-Hg_2CuTi type structure. 82

III.4 Total and partial density of state with both majority and minority spin direction of Pr_2RhZ (Z = Al, Ga, In) alloys in ferromagnetic-Hg_2CuTi type structure. 83
III.5 Crystallographic structure of full-Heuler alloy Pr_2CoZ (Z = Al, Ga and In) in which (a) Hg_2CuTi type and (b) Cu_2MnAl type. 86
III.6 Total energy versus unit cell volume for Pr_2CoZ (Z = Al, Ga and In). . 89
III.7 3D representations of the influence of (a) Young's modulus (E, in GPa), (b) Bulk modulus (k,in GPa) and (c) Compressibility (β, in GPa^{-1}) on the crystal direction for Pr_2CoAl, Pr_2CoGa and Pr_2CoIn. 90
III.8 Spin-polarized band structures of majority spin (Up) and minority spin (Down) of Pr_2CoZ (Z = Al, Ga, In) in Hg_2CuTi type structure 93
III.9 Total density of state of Pr_2CoZ (Z = Al, Ga, In) alloys in Hg_2CuTi type structure. 94
III.10 Heat capacity as function of temperature in different pressure for Pr_2CoZ in witch (a) Pr_2CoAl, (b) Pr_2CoGa and (c) Pr_2CoIn. 97
III.11 Entropy as function of temperature in different pressures for Pr_2CoZ in which (a) Pr_2CoAl, (b) Pr_2CoGa and (c) Pr_2CoIn. 98
III.12 Debye temperature as function of temperature in different pressure for Pr_2CoZ witch (a) Pr_2CoAl, (b) Pr_2CoGa and (c) Pr_2CoIn 99
III.13 Crystallographic structure of Quaternary-Heuler alloy CrPrCoZ (Z=Al, Ga and In) (by VESTA [3]). 100
III.14 Total energy versus unit cell volume for CrPrCoZ (Z = Al, Ga and In). 102
III.15 Heat capacity as function of temperature in different pressure for CrPrCoZ (Z = Al, Ga and In). 103
III.16 Entropy as function of temperature in different pressures for CrPrCoZ (Z = Al, Ga and In). 104
III.17 Debye temperature as function of temperature in different pressure for CrPrCoZ (Z = Al, Ga and In). 105
III.18 Spin-polarized band structures of majority spin (Up) and minority spin (Down) of CrPrCoZ (Z = Al, Ga, In) in Hg_2CuTi type structure. . . . 108

III.19 Total and partial density of state for both spin direction (up and down) of CrPrCoZ (Z = Al, Ga, In) alloys in Hg_2CuTi type structure. 108
III.20 Total energy as a function of unit cell volume for: (a) Ir_2ScGa for both Hg_2CuTi and Cu_2MnAl type structures (b) Ir_2ScGe for both Hg_2CuTi and Cu_2MnAl type structures 111
III.21 Density of states (DOS) of Ir_2ScGa (a) with Hg_2CuTi type structures (b) with Cu_2MnAl type structures 115
III.22 Density of states (DOS) of Ir_2ScGe (a) with Hg_2CuTi type structures (b) with Cu_2MnAl type structures. 116
III.23 Ru_2MnSb and Ru_2MnSn total energy as a function of volume for Cu_2MnAl and Hg_2CuTi type structures. 121
III.24 Calculated spin-polarized density of states and band structure of Ru_2MnSb with both Hg_2CuTi and Cu_2MnAl types structures 124
III.25 Calculated spin-polarized density of Ru_2MnSn with both Hg_2CuTi and Cu_2MnAl types structures. 125
III.26 Calculated spin-polarized density of states and band structure of Ru_2MnTe with both Hg_2CuTi and Cu_2MnAl types structures. 126

LIST OF TABLES

I.1 Different types of occupations in the $C1_b$ type structure 14
I.2 The positions of the atoms for the three possible configurations for the quaternary Heusler alloys XX′YZ [23] 16

III.1 Optimized lattice constant a_0 (Å), Bulk modulus B (GPa), the pressure derivative B', the total energy $E_{\min}$ (Ry), and the Formation energy ΔH (Ry) for Full Heusler compounds Pr_2RhZ (Z = Al, Ga, In). 77
III.2 The calculated total magnetic moments (μ_{tot}), atomic and interstitial magnetic moments and the band gap energy (E_g) for the Pr_2RhZ (Z = Al, Ga, In). 81
III.3 Optimized lattice constant a_0 (Å), Bulk modulus B (GPa), the pressure derivative B', the total energy $E_{\min}$ (Ry), and the Formation energy ΔH (Ry) for Full Heusler compounds Pr_2CoZ (Z = Al, Ga, In). 87
III.4 Elastic constants (Cij), bulk modulus (K), Shear modulus (G) Young modulus (E), Poisson's coefficient (ν). The zener anisotropy (A) Pugh's Ratio (κ) 89
III.5 The calculated total magnetic moments (Mt) and atomic magnetic moments for the Pr_2CoZ (Z = Al, Ga, In) 92
III.6 Optimized lattice constant a_0 (Å), Bulk modulus B (GPa), the pressure derivative B', the total energy $E_{\min}$ (eV), and the Formation energy ΔH (Ryd) for Quaternary Heusler compounds CrPrCoZ (Z = Al, Ga, In). . 101

III.7 Elastic constants (C_{ij}), bulk modulus (B), Shear modulus (G) Young modulus (E), Poisson's coefficient (ν). The zener anisotropy (A). . . . 103
III.8 The calculated total magnetic moments (Mt) and atomic magnetic moments for the CrPrCoZ (Z = Al, Ga, In). 107
III.9 The variation of the lattice constant (a_0), bulk modulus (B_0), the bulk modulus' derivative, and the ground state energies of the seven quaternary Heusler alloys at both ferromagnetic and paramagnetic states . . . 111
III.10 Elastic properties. 113
III.11 The variation of the total and partial magnetic moment calculated by GGA approximations. 116
III.12 The sites occupied by atoms: A, B, C and D for both structure Hg_2CuTi and Cu_2MnAl. 120
III.13 Calculated structural parameters of Ru_2Mn(Sb,Sn,Te) alloys for both Hg_2CuTi and Cu_2MnAl type structures; a(Å) lattice parameters, B (GPa) bulk modulus, B' pressure derivative of bulk the modulus, E minimum energy (Ry), and formation energies ΔH_f (Ry). 122
III.14 Calculated elastic constants and moduli (in GPa) for Ru_2MnZ (Z = Sb, Sn, Te) in the Hg_2CuTi and Cu_2MnAl structures. 128
III.15 The calculated total spin magnetic moment M_{tot} (μ_B/f.u.) and atomic magnetic moments (μ_B/atom) of Ru_2Mn(Sb,Sn,Te). 131

LIST OF ABBREVIATIONS AND ACRONYMS

DFT Density Functional Theory.

FH Full-Heusler.

FCC Face-Centred Cubic.

XRD X-ray diffraction.

HFM Half-Metallic Ferromagnets.

BZ Brillouin Zone.

GMR Giant Magneto-Resistance.

MRAM Magnetic Random Access Memory.

DRAM Dynamic Random Access Memory.

SpinLED Spin Light Emitting Diode.

SpinFET Spin Field Effect Transistor.

MOSFETs Metal–Oxide–Semiconductor Field-Effect Transistor.

FP-LAPW Full Potential Linearized Augmented Plane Wave.

LDA Local Density Approximation.

LSDA Local Spin Density Approximation.

GGA-PBE Generalized Gradient Approximation (Perdew–Burke–Ernzerhof).

KS Kohn–Sham.

LCOA Linear Combination Of Atomic Orbitals.

OPW Orthogonalizing Plane Waves.

APW Augmented Plane Waves.

KKR Korringa, Kohn and Rostoker.

LMTO Linearized "Muffin-Tin" Orbitals.

LAPW Linearized Augmented Plane Waves.

BI Band Inversion.

RMT Muffin-Tin Radii.

DOS Density Of States.

PDOS Projected Density Of States.

VB Valence Band.

CB Conduction Band.

BCS Bardeen–Cooper–Schrieffer.

AFM Antiferromagnetic.

GENERAL INTRODUCTION

In the last few decades, intermetallic compounds made from transition metals and rare-earth elements have been of great interest in condensed-matter physics and materials science. This is because they have a wide range of structural, electronic, magnetic, and thermoelectric properties. Heusler alloys have become especially flexible systems within this wide group. Since de Groot *et al.* [1] discovered half-metallic ferromagnetism in Heusler-type compounds and then explained their Slater–Pauling behavior [2, 3], these materials have been seen as the best choices for spintronic devices, magnetocaloric refrigeration, and thermoelectric energy conversion [4, 5]. Their capacity to integrate elevated Curie temperatures, robust spin polarization, and adjustable band structures within chemically adaptable frameworks necessitates a comprehensive theoretical and experimental investigation.

The physical properties of Heusler alloys are closely linked to the presence of partially filled d and f shells in transition metals and rare-earth elements. Transition metals offer a fertile environment for itinerant magnetism, alloy formation, and intricate bonding due to the delocalized nature of their d electrons [6, 7]. Rare-earth elements, on the other hand, have localized $4f$ electrons that cause sharp spectroscopic features and large magnetic moments that stay strong even when the elements are in condensed phases [8]. When these two families of elements are put together in ordered intermetallic structures, small $3d$–$4f$ exchange interactions and hybridization effects can create a wide range of ground states, from simple ferromagnets to more complex ferrimagnetic or antiferromagnetic configurations, often with strong magnetocrystalline anisotropy.

There are now for main types of Heusler compounds: full-Heusler (X_2YZ), half-Heusler (XYZ), and a double Heusler end quaternary Heusler (XX′YZ) alloys [9, 10].

The crystal structures of these materials are made up of interpenetrating face-centered cubic sublattices, with atoms in very specific Wyckoff positions in very symmetric cubic space groups [11]. Small changes in the chemical makeup, site order, or atomic disorder can have a big effect on their electronic structure, making them stable in metallic, semiconducting, half-metallic, or even topologically non-trivial states [12]. This structural and chemical adaptability elucidates the current investigation of Heusler alloys for applications in giant and tunnel magnetoresistance, spin-filtering junctions, rare-earth permanent magnets, and thermoelectric modules [13].

Even though a lot of research has been done on Heusler systems, there are still some questions that need to be answered. The combined effects of rare-earth $4f$ magnetism, transition-metal $3d$ states, and main-group elements on the stability, electronic structure, and magnetism of full-Heusler alloys remain inadequately elucidated across systematic families. Furthermore, the relationships among structural parameters (lattice constants, phase preference between Cu_2MnAl-type and Hg_2CuTi-type structures), mechanical properties (elastic constants, anisotropy, ductility), and finite-temperature thermodynamic behavior (heat capacity, entropy, Debye temperature) necessitate thorough, internally consistent studies for chemically related series. First-principles calculations grounded in density-functional theory (DFT) offer a suitable framework to tackle these inquiries and to direct experimental initiatives [14, 15].

We divided this work into three main chapters. The first chapter gives a broad overview of Heusler compounds and ideas that are related to them. It covers the basics of the physics of transition metals and rare-earth elements, the crystallographic structures of full, half, and quaternary Heusler alloys, the main types of magnetic order and the Slater–Pauling rule, and the main ideas of electronic structure, thermoelectric effects, and the main uses of Heusler materials in technology.

The second chapter is all about the theoretical and computational framework. It goes over the main ideas of quantum many-body theory that led to DFT, lists different ways to approximate the exchange–correlation functional (LDA, GGA), and explains the FP-LAPW method and how to use it in the WIEN2k code in detail.

The original results of the thesis are in the third chapter. This chapter presents a comprehensive first-principles investigation of the structural, electronic, magnetic, elastic, and thermodynamic properties of various families of full-Heusler alloys comprising rare-earth and transition-metal atoms. The primary emphasis is on Pr-based full-Heusler compounds of the type Pr_2YZ, where Y = Rh, Co, and Z = Al, Ga, In, as well as Cr-doped quaternary systems represented by CrPrCoZ (Z = Al, Ga, In). To enhance the comparison and isolate the function of $4f$ electrons, the analysis is expanded to include transition-metal-based full-Heusler alloys Ir_2ScZ (Z = Ga, Ge).

We used DFT grounded in the Kohn–Sham formulation [16]. We use generalized-gradient approximations of the PBE type to handle exchange–correlation effects. These

are a good balance between accuracy and computational cost for metallic and intermetallic systems. We use a full-potential linearized augmented plane-wave (FP-LAPW) scheme to get the electronic structure [17]. This is one of the most accurate methods for getting the electronic structure of crystalline solids that is currently available. This method gives an exact description of both core and valence states, including the localized $4f$ electrons of rare-earth elements, without having to guess the shape of the potential.

To find the ground-state phase among competing Cu_2MnAl- and Hg_2CuTi-type structures, structural optimizations and formation-energy calculations are used. To find the magnetic ground state, total-energy differences between magnetic configurations (non-magnetic, ferromagnetic, antiferromagnetic) are evaluated. Small, uniform deformations of the optimized cells are used to obtain the elastic constants. The thermodynamic quantities are then calculated using the elastic data within a quasi-harmonic Debye model.

References

[1] R. A. De Groot, F. M. Mueller, P. G. van Engen, and K. H. J. Buschow. New class of materials: Half-metallic ferromagnets. *Phys. Rev. Lett.*, 50(25):2024–2027, 1983.

[2] I. Galanakis. Slater–Pauling behavior in half-metallic Heusler compounds. *Nanomaterials*, 13(13), 2023.

[3] I. Galanakis, P. Mavropoulos, and P. H. Dederichs. Electronic structure and Slater–Pauling behaviour in half-metallic Heusler alloys calculated from first principles. *J. Appl. Phys.*, 39(5):765–775, 2006.

[4] A. J. Minnich, M. S. Dresselhaus, Z. F. Ren, and G. Chen. Bulk nanostructured thermoelectric materials: current research and future prospects. *Energy Environ. Sci.*, 2(5):466, 2009.

[5] J. E. Fischer et al. Magnetic properties and Curie temperatures of disordered Heusler compounds. *Phys. Rev. B*, 94(2):024418, 2016.

[6] U. Krämer, I. N. Talken, and M. Hanke. Transition metal transport. *FEBS Lett.*, 581(12):2263–2272, 2007.

[7] M. Albrecht. Cyclometalation using d-block transition metals: Fundamental aspects and recent trends. *Chem. Rev.*, 110(2):576–623, 2010.

[8] S. V. Eliseeva and J.-C. G. Bünzli. Rare earths: jewels for functional materials of the future. *New J. Chem.*, 35(6):1165, 2011.

[9] L. Bainsla and K. G. Suresh. Equiatomic quaternary Heusler alloys: A material perspective for spintronic applications. *Appl. Phys. Rev.*, 3(3):031101, 2016.

[10] D. Amari, M. Mokhtari, F. Dahmane, and G. Benabdallah. Structural, elastic, electronic, magnetic, and half-metallic properties of a novel rare-earth-based quaternary Heusler alloys. *Emergent Mater.*, 6(1):299–306, 2023.

[11] A. Candan. Magnetic, electronic, mechanical, anisotropic elastic and vibrational properties of antiferromagnetic Ru_2TGa (T = Cr, Mn, Co) Heusler alloys. *J. Electron. Mater.*, 48(12):7608–7622, 2019.

[12] M. Khalfa et al. Mechanical, electronic and thermodynamic properties of full Heusler compounds Fe_2VX (X = Al, Ga). *Int. J. Mod. Phys. B*, 29(31):1550229, 2015.

[13] C. Felser, G. H. Fecher, and B. Balke. Spintronics: A challenge for materials science and solid-state chemistry. *Angew. Chem. Int. Ed.*, 46(5):668–699, 2007.

[14] N. Asli et al. Structural, electronic, magnetic and mechanical properties of the full-Heusler compounds Ni_2Mn(Ge,Sn) and Mn_2NiGe. *Z. Naturforsch. A*, 76(8):693–702, 2021.

[15] M. Lazizi et al. Structural properties, electronic band structure, magnetic and mechanical characteristic of XFeGe (X = Co, Cr, Ni) half-Heusler compounds. *Inorg. Chem. Commun.*, 142:109675, 2022.

[16] P. Senet. Kohn–Sham orbital formulation of the chemical electronic responses, including the hardness. *J. Chem. Phys.*, 107(7):2516–2524, 1997.

[17] E. Wimmer, H. Krakauer, M. Weinert, and A. J. Freeman. Full-potential self-consistent linearized-augmented-plane-wave method for calculating the electronic structure of molecules and surfaces. *Phys. Rev. B*, 24:864–875, 1981.

CHAPTER I

HEUSLER COMPOUNDS

I.1 Introduction

Intermetallic compounds based on transition metals and rare-earth elements have become a major focus in materials research and condensed matter physics throughout the last few decades. Heusler alloys hold a special place among these systems because of the extraordinary variety of their structural, electrical, magnetic, and thermoelectric characteristics. Heusler compounds were first identified in the early 20th century by the unexpected finding that non-ferromagnetic elements could form ferromagnetic alloys. Since then, they have developed into model systems for investigating the connections between crystal structure, chemical composition, and physical behavior.. Their ability to exhibit half- metallicity, high Curie temperatures and tunable band structures makes them especially attractive for spintronics and energy-conversion technologies.

Since Heusler discovered in 1903 that ferromagnetic alloys could be created from non- ferromagnetic components, Heusler alloys named for the German mining engineer and chemist Friedrich Heusler have garnered significant attention [1].

The examination of these materials is inextricably linked to the broader context of transition metals and rare earths, whose incompletely filled d and f orbitals dictate various phenomena, including magnetism, superconductivity, alloy formation, and pronounced electron correlation effects. Transition metals are the backbone of many technological uses, from special steels to functional intermetallics. This is because they are good conductors of electricity and heat and tend to form alloys easily. Rare earths, on the other hand, have unique magnetic and optical properties because their 4f electrons are localized and their spectroscopic signatures are sharp. These families of elements work together to make the chemical building blocks that make up the different types of Heusler compounds.

Heusler alloys can be classified into for primary categories from a crystallographic perspective: full-Heusler (X_2YZ), half-Heusler (XYZ), a double Heusler ($X_2YY'Z$), and quaternary Heusler ($XX'YZ$) compounds. Each family is distinct due to a particular arrangement of atoms on well defined Wyckoff positions within highly symmetric cubic structures.. The arrangement of transition and main-group elements on these sites, as

well as any possible order–disorder phenomena, has a big effect on their stability and the appearance of certain electronic and magnetic states. A comprehensive comprehension of these structural elements is essential for the rational customization of Heusler alloy properties for specific applications.

Magnetism and electrical structure constitute the second major theme of this chapter. Explicit correlations between the number of valence electrons, the spin polarization, and the total magnetic moment of Heusler compounds can be identified by going over the main types of magnetic behavior, including diamagnetism, paramagnetism, ferromagnetism, antiferromagnetism, and ferrimagnetism, and by introducing the Slater–Pauling rule [2].

Concurrently, a critical comprehension of the semi-metallic or half-metallic character displayed by many alloys can be obtained by analyzing their band structures and densities of states. This type of explanation is crucial for understanding why certain Heusler systems can function as nearly ideal spin filters or as effective thermoelectric materials throughout a broad temperature range [3].

Lastly, this chapter talks about the thermoelectric effects (Seebeck, Peltier, and Thomson) and looks at the main uses of Heusler compounds in spintronic devices, magnetoresistive junctions, and thermoelectric modules. It brings together the chemical, structural, magnetic, and electronic foundations. This sets the stage for the more in-depth studies that will be done in the next chapters, where specific Heusler alloys will be looked at with the goal of both deepening our understanding of their properties and figuring out how they could be used in real-world technology.

I.2 Background on Transition Metals

I.2.1 Transition Metals

Transition metals play a crucial role in current technology, being widely used in the production of superconductors, alloy formation, etc.

The high conductivity of these materials predisposes them to use in electrochemical applications. They are employed in the production of fuel cells and sensors.

Chemical elements with atomic numbers between 21 and 30, between 39 and 48, between 72 and 80, and between 104 and 112 are generally referred to as transition metals [4]. This term is derived from their position in the periodic table, which reflects the progressive increase in the number of electrons in the d orbital of atoms as one moves from one element to another across the period. Figure I.1 illustrates the periodic table, highlighting the transition elements in purple.

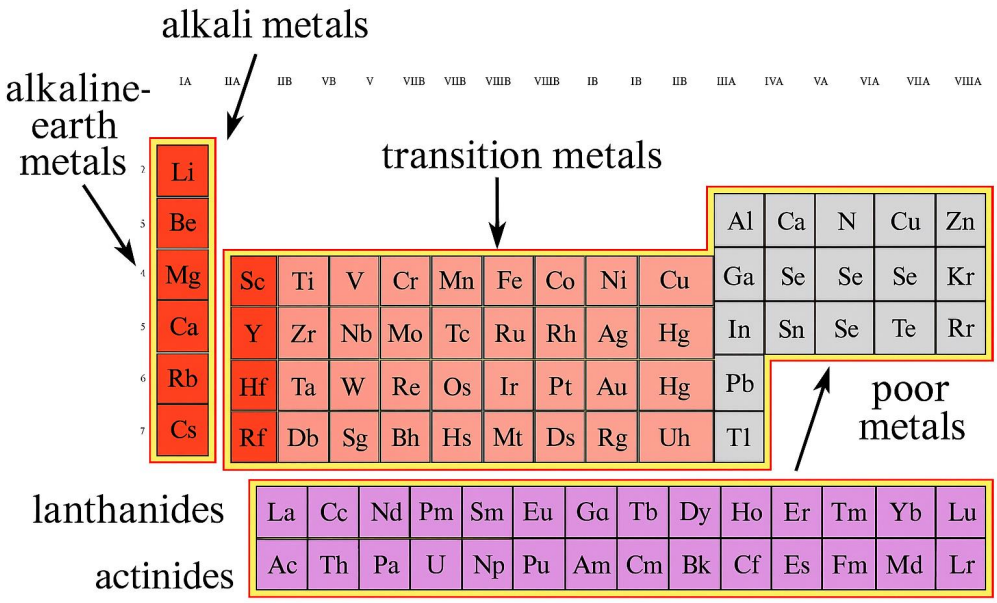


Figure I.1: The periodic table of transition metals

I.2.2 General Characteristics of Transition Elements

In general, transition metals have characteristics that interest business. They usually have high melting and vaporization temperatures as well as high densities. These properties result from the shell electrons' capacity to diffuse throughout the metal structure. The quantity of electrons shared by the nuclei in metallic materials directly correlates with the metal's strength. This property leads to a high density and melting point [5].

Occasionally, these materials display unusual physical characteristics like superconductivity or ferromagnetism. They are important players in industries like advanced metallurgy (special steels), nuclear physics (reactors), and aviation (titanium alloys)

due to their remarkable capacity to create alloys or solid solutions with other elements, such as hydrogen [6], carbon, nitrogen, or oxygen.

I.2.3 Electronic Configuration of the Transition Elements

From scandium to zinc, the d-block elements progressively occupy their d orbitals within the series. With the exception of copper and chromium, all d-block elements have two electrons in their outer s orbitals, including those with incomplete d orbitals.

This is atypical, as lower-energy orbitals are usually filled before the outer ones. However, in this example, the $(n+1)s$ orbitals of the elements have a lower energy level than the nd orbitals. Since atoms remain in their most stable energy state, the $(n+1)s$ orbitals are filled first [7].

Copper and chromium have a single electron in their outer s orbital due to electronic repulsion. The distribution of one electron between the s and d orbitals is energetically more stable than the presence of two electrons in the outer orbital.

I.2.4 Properties of Transition Metals

Transition metals generally exhibit high density, melting, and vaporization temperatures, with the exception of group 12 metals, which have a relatively low melting point: mercury remains liquid above $-38.8\,^{\circ}\mathrm{C}$, and copernicium could potentially be gaseous at room temperature. These characteristics result from the ability of d-subshell electrons to delocalize within the metal lattice. In metallic substances, an increase in the number of electrons shared between nuclei results in increased cohesion of the metal [8].

They exhibit remarkable characteristics for industry, construction, and everyday life:

- They exhibit greater rigidity than group 1 and 2 metals.
- They possess good thermal and electrical conductivity.
- They are capable of forming alloys with each other.
- They exhibit multiple oxidation states.

I.3 Rare Earth-Based Alloys

I.3.1 Definition of Rare Earth Compounds

In 1789, Johan Gadolin, a Finnish chemist, discovered a new oxide (or "earth") in a sample of ytterbite, which would later be renamed *gadolinite* in his honor. This new rock was discovered two years earlier by Lieutenant Carl Axel Arrhenius near the village of Ytterby in Sweden. In 1797, Anders Gustaf Ekeberg confirmed this research by naming the new oxide *yttria* [9].

Nearly fifty years later, Swedish scientist Carl Gustav Mosander successfully separated several rare-earth elements (cerium, lanthanum, and didymium) using innovative fractional crystallization techniques. Convinced that the *yttria* from *gadolinite* was also a compound, he began searching for some of these new compounds. In the autumn of 1842, he succeeded in separating two oxides, one white (which produced colorless salts) which he identified as authentic yttrium, and the other yellow (which produced pink salts) which he named "odinium" in reference to the god Odin of Norse mythology. Before publishing the results of his research in 1843, Mosander completed an additional step of fractionating the oxalate oxides of these compounds, which allowed him to discover a third oxide. He opted to retain the term "yttria" to designate the colorless fraction (pure yttrium oxide) and designated the yellow fraction as "erbine" and the pink fraction as "terbine", in constant reference to the village of Ytterby [10].

I.3.2 I.3.2. Properties of rare earths

Their main characteristic lies in the presence of "f" electrons which, due to the parameters linked to their radial function ($n = 4$), are tightly embedded within the core of the atom. Even in a condensed form like a liquid or solid, the $4f$ electrons, which are located close to the atomic nucleus, show little regard for the type of chemical bond. As a result, in the condensed form, atoms maintain their characteristics from the free state. When exposed to an electric arc, an atom in a free state of excitation within a plasma will actually produce a variety of light lines.

This is demonstrated in the context of our focus by the observation of narrow

spectral lines for the lanthanides in emission or absorption, whether in a solid or liquid medium, which can be precisely measured. It is worth noting that these elements are the only ones in Mendeleev's periodic table to exhibit these properties [11].

This is where the importance of "Rare Earths" lies, as it is impossible to obtain monochromatic transitions with such narrow lines. A crucial aspect to consider is that each "Rare Earth" is associated with a specific base level that influences the magnetic properties of the atom. From this point on, it is possible to produce alloys that exhibit unique magnetic characteristics. This will make it possible to develop high-value permanent magnets, in particular.

I.4 Different types of Heusler Alloys

I.4.1 History of Heusler Compounds

Heusler compounds were first identified in the early 1900s when Friedrich Heusler, a German chemist, discovered an unexpected phenomenon: an alloy made of copper (Cu), manganese (Mn), and aluminum (Al) displayed ferromagnetic behavior despite the fact that none of its constituent elements were inherently ferromagnetic. This observation, published in 1903 [12], marked the beginning of increasing interest in metallic alloys with emergent properties.

The finding was revolutionary, as it showed that collective magnetism could arise from electronic and crystallographic organization rather than from the intrinsic nature of individual elements. It paved the way for the modern understanding of exchange interactions and electron-induced magnetism.

I.4.1.1 Early Developments

The first Heusler compounds were primarily investigated for their unusual magnetic properties, attracting significant attention in solid-state physics. The Cu_2MnAl alloy became the prototype of the Full-Heusler family, characterized by a cubic $L2_1$-type crystal structure. This ordered and highly symmetric structure promotes indirect exchange interactions between Mn atoms via Cu conduction electrons, leading to ferromagnetic

alignment.

In subsequent decades, research extended to other ternary and quaternary combinations [13], revealing a wide diversity of electronic and magnetic behaviors, such as half-metallicity, magnetostructural transitions, and giant magnetoresistance. From the 1970s onwards, advances in experimental methods and *ab initio* calculations enabled direct correlations between magnetic/electronic properties and atomic crystal structures, confirming the importance of disorder and chemical substitution effects.

I.4.1.2 Classification and Evolution

The Heusler compounds are now classified into three major families:

- Full-Heusler (X_2YZ): two X-type atoms (usually transition metals), one Y (transition metal), and one Z (main-group element).
- Half-Heusler (XYZ): derived from the $C1_b$ structure, with a vacant sublattice site, resulting in semiconducting or thermoelectric behavior.
- Quaternary Heusler ($XX'YZ$): an extension to four elements for precise tuning of electronic, magnetic, and mechanical properties.

Advances in synthesis techniques (arc melting, sputtering, controlled-atmosphere annealing) and characterization methods [14] (XRD, SEM, magnetic measurements, DFT) have allowed exploration of hundreds of combinations, some exhibiting semiconducting, topological, thermoelectric, or exceptional elastic properties.

I.4.2 Different types of Heusler Alloys

These many types of alloys are represented by a variety of Heusler alloys found in the literature.

I.4.2.1 Full-Heusler Alloys

The chemical formula for full-Heusler alloys is X_2YZ, where Z is an element from groups III, IV, or V of the periodic chart and X and Y stand for transition metals. However, under some circumstances, an alkaline earth metal or a rare earth element

can take the role of Y. As demonstrated by the examples Co_2YAl (Y = Fe, Ti) [15], $Ni_2Mn(Ge, Sn)$, and Mn_2NiGe [16], and the typical cubic crystal structure of their ordered phase, the metal which is present in duplicate is typically positioned at the head of the formula, while the main group element is placed at the end. The compound Cu_2MnAl crystallizing in the space group $Fm\bar{3}m$ (No. 225) is an illustration of this regular structure [17].

I.4.2.2 Crystal structure of Full-Heusler alloys

Heusler alloys in full typically crystallize into two cubic structures.

Type-Cu_2MnAl, another name for the regular cubic Heusler structure, has the space group $Fm\bar{3}m$ (No. 225). The two atoms of element X occupy tetrahedral sites at positions (0, 0, 0) and (1/2, 1/2, 1/2), whereas the atoms of elements Y and Z are located on octahedral sites at coordinates (1/4, 1/4, 1/4) for element Y and (3/4, 3/4, 3/4) for element Z when the atomic number of element X is greater than that of element Y ($Z(X) > Z(Y)$), as shown in Figure I.2(a).

The inverse cubic Heusler structure of type Hg_2CuTi crystallizes in the space group $F\bar{4}3m$ (No. 216) [13]. In this case, the X atoms are positioned at 4a (0, 0, 0) and 3d (3/4, 3/4, 3/4) sites when $Z(Y) > Z(X)$, whereas the Y and Z atoms occupy the 4b (1/2, 1/2, 1/2) and 4c (1/4, 1/4, 1/4) positions, respectively, as illustrated in Figure I.2(b).

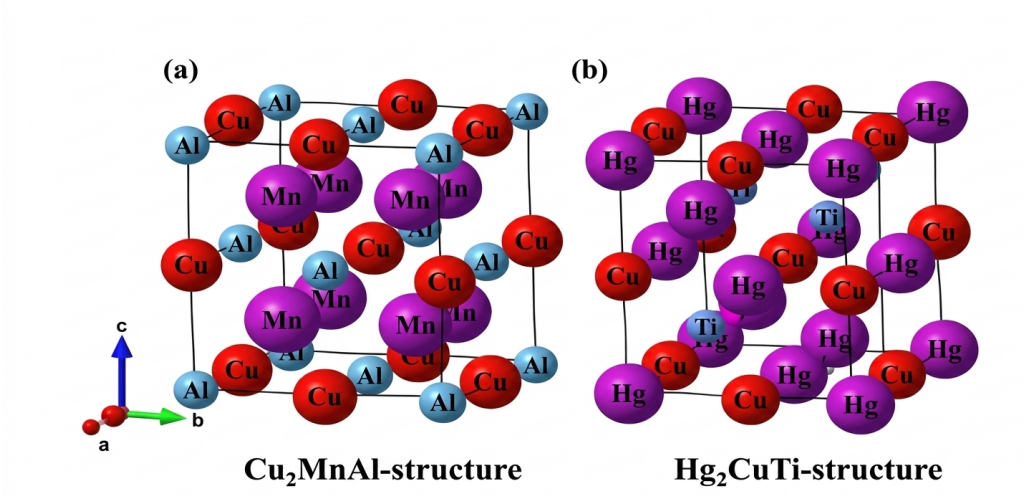


Figure I.2: Full-Heusler alloy structures: (a) Cu_2MnAl and (b) Hg_2CuTi [18].

I.4.2.3 Half-Heusler Alloys

The general formula for ternary intermetallic alloys in the second family consists of compounds with two components, one covalent and one ionic, which can be thought of as XYZ. The element Z can be considered as the anionic counterpart, whereas atoms X and Y exhibit a clear cationic character.

The element with the highest electropositivity is often positioned at the beginning of the formula. It may be a rare-earth element, a transition metal, or an element from the main group. However, a main-group element from the second half of the periodic table is usually placed at the end of the formula, acting as the most electronegative element, such as in XVSb (X = Fe, Co, Ni) and XFeGe (X = Co, Cr, Ni) [19, 20].

I.4.2.4 Crystal structure of Half-Heusler alloys

These alloys crystallize in a non-centrosymmetric cubic structure with space group $F\bar{4}3m$ (No. 216), commonly referred to as the $C1_b$ structure. This ternary system is closely related to the CaF_2 structure and can be derived from the ZnS-type tetrahedral structure by filling the octahedral lattice sites, as illustrated in Figure I.3.

The crystal structure consists of three interpenetrating face-centered cubic (fcc) sublattices, each occupied by atoms X, Y, and Z, respectively. The atomic positions are: 4a (0, 0, 0), 4b (1/2, 1/2, 1/2), and 4c (1/4, 1/4, 1/4). Three non-equivalent atomic configurations are theoretically possible within this structure, as summarized in Table I.1.

Table I.1: Different types of occupations in the $C1_b$ type structure

	4a (0,0,0)	4b (1/2,1/2,1/2)	4c (1/4,1/4,1/4)
Type I	X	Y	Z
Type II	Z	X	Y
Type III	Y	Z	X

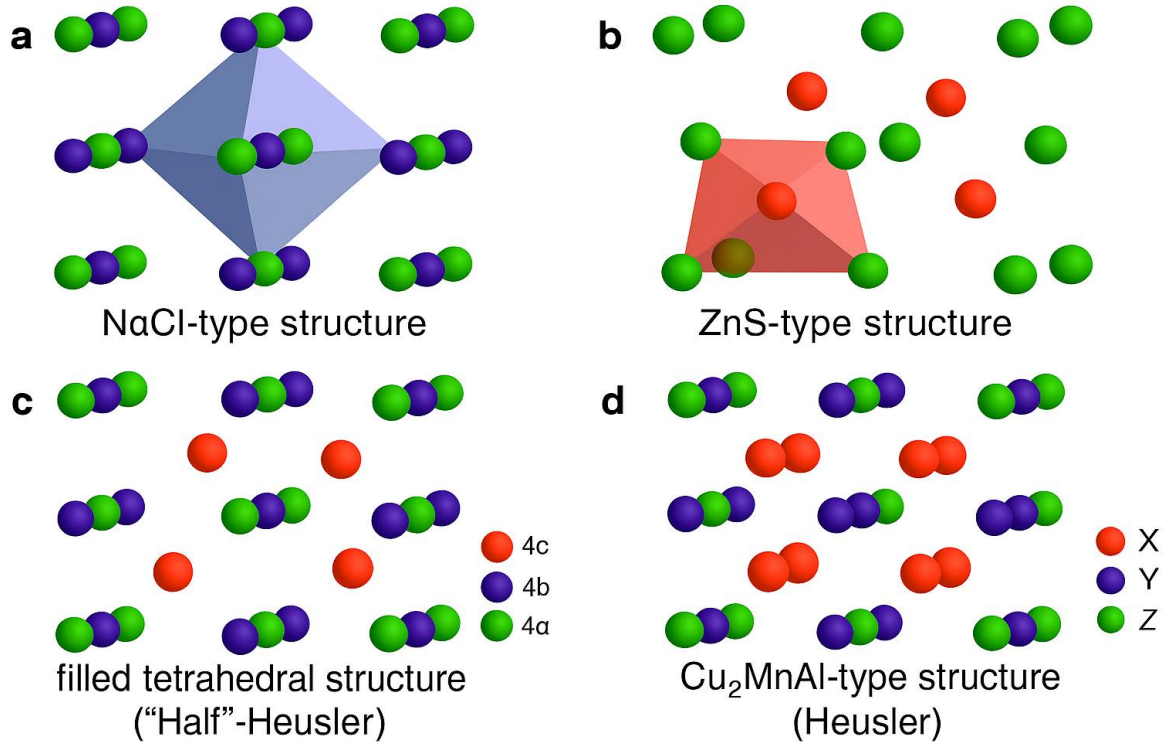


Figure I.3: (a) the Rock salt structure, (b) the zinc blende structure and their relationships with the semi-Heusler structure (c) and with the Heusler structure (d) [21].

I.4.2.5 Quaternary Heusler alloys

Another kind of Heusler alloys, termed quaternary Heusler compounds, such as LaX-TiSi (where X = Co, Rh, Ir) [22], comprises four distinct chemical elements, including two variations, X and X′. These are situated in the 4a and 4d positions, respectively. Element Y occupies the 4b places, while element Z occupies the 4c positions, crystallising in the F$\bar{4}$3m space group (space group 216).

I.4.2.6 Crystal structure of quaternary Heusler compounds

The class of quaternary Heusler alloys is garnering considerable attention owing to its prospective applications in spintronic devices. Replacing one of the X atoms in X_2YZ compounds, classified as complete Heusler compounds, with another transition metal designated X′ can provide a quaternary compound of the form XX′YZ. This compound is classified as a quaternary Heusler, with the designations X, X′, and Y denoting transition metals, and Z indicating a main group element. The XX′YZ compound

crystallises in a ZnCdRhMn-type structure Figure I.4.

Three unique atomic configurations are feasible for ZnCdRhMn-type quaternary Heusler compounds, as illustrated Table I.2. Theoretical and experimental investigations have established the accountability of this profession concerning Heusler quaternary alloys.

Table I.2: The positions of the atoms for the three possible configurations for the quaternary Heusler alloys XX′YZ [23]

STRUCTURE	X	X′	Y	Z
Type I	4a (0,0,0)	4c (1/2,1/2,1/2)	4b (1/4,1/4,1/4)	4d (3/4,3/4,3/4)
Type II	4b (1/4,1/4,1/4)	4c (1/2,1/2,1/2)	4a (0,0,0)	4d (3/4,3/4,3/4)
Type III	4a (0,0,0)	4b (1/4,1/4,1/4)	4c (1/2,1/2,1/2)	4d (3/4,3/4,3/4)

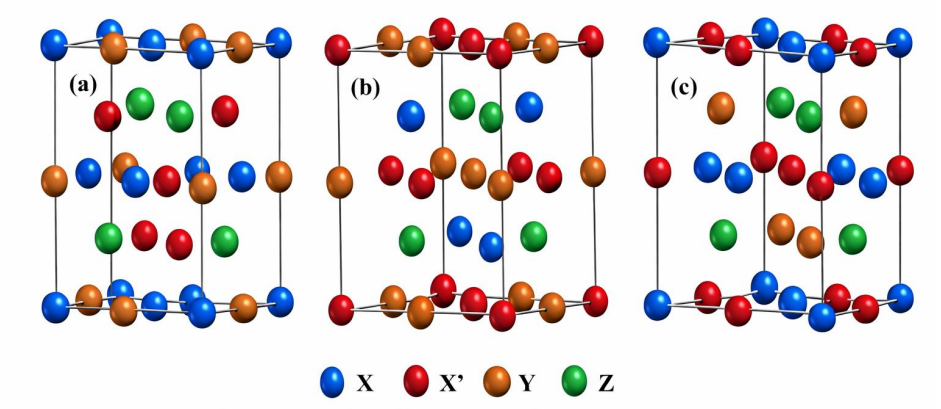


Figure I.4: Schematic illustration of the three possible non-equivalent structures of quaternary Heusler compounds (a) type 1, (b) type 2 and (c) type 3 [23].

I.5 Different magnetic forms

Magnetism has preoccupied humans since the dawn of time. There is, in fact, a legend of magnetic materials, the discovery of which by the Chinese dates back to 2500 BC. At that time, rudimentary compasses were made, which guided travelers across deserts, from lodestone (magnetite: Fe_3O_4).

According to historical evidence, the first effects of magnetism date back to the 6th century BC, when Thales of Miletus discovered that certain iron ores from Magnesia (Asia Minor) attracted iron [24].

Theories of magnetism became abundant. Lucretius (1st century BC) had predicted in his *Rerum Natura* that it would take some time to understand the phenomena observed on the lodestone, a prediction that proved to be of great pertinence. In 1269, the French engineer Pierre de Maricourt wrote the first detailed treatise on magnetism, describing in particular the laws of magnetic attraction and repulsion. In 1895, Pierre Curie spoke of a modern theory of magnetism, distinguishing different types of materials according to their power sources.

I.5.1 Diamagnetism

Diamagnetism typically characterises objects composed solely of non-magnetic atoms, when all electrons are coupled in doublets, with two electrons of opposite spin occupying the same energy level. Their resultant overall magnetic moment is null, whereas these media remain unmagnetized in the absence of an external magnetic field. The alteration in the orbital motion of electrons due to an applied magnetic field is the source of this phenomenon, wherein the electrons' rotation around the nucleus induces a magnetic intensity in each localised region (resulting in weak magnetisation) that is proportional to the external field but orientated in the opposite direction [25].

This form of magnetism is defined by a negative magnetic susceptibility and an exceedingly low absolute amplitude, remaining largely unaffected by temperature and the strength of the applied magnetic field. Bismuth, mercury, and silver exemplify diamagnetic materials.

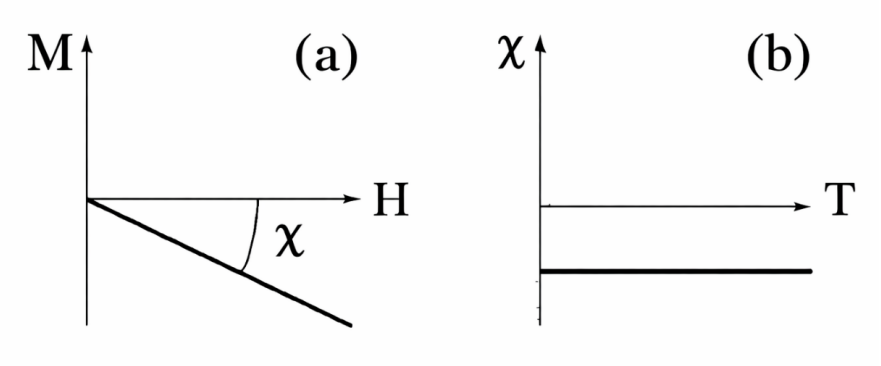


Figure I.5: Variations in magnetization under the effect of the magnetic field (a), and thermal variation of magnetic susceptibility (b) for a diamagnetic substance.

In reality, everybody exhibits a diamagnetic response, however, this is often negligible compared to other forms of magnetism because its effect is very weak.

I.5.2 Paramagnetism

In paramagnetism, we see substances with atoms that have permanent magnetic moments which do not interact, allowing them to orient freely in any direction. In this paramagnetism, the electrons are not entirely coupled. In the presence of an external magnetic field, the elementary moments align with the field's direction, resulting in an increase in the material's magnetisation, referred to as "induced magnetisation". The magnetisation ceases instantaneously with the removal of the excitation field [26].

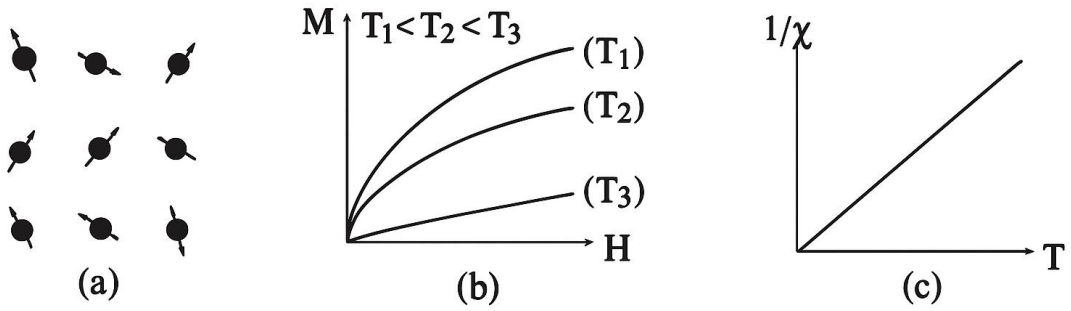


Figure I.6: Paramagnetism: (a) a spin network, (b) variation of magnetization under an applied field, (c) thermal variation of $1/\chi$.

These magnetic materials demonstrate a moderately positive and low-amplitude magnetic susceptibility ranging from 10^{-3} to 10^{-5} due to thermal agitation continuously reorienting the moments. The inverse of susceptibility is a diminishing function of absolute temperature, assessed in accordance with Curie's law. Oxygen, aluminium, manganese, and tungsten are all examples of paramagnetic substances. Ordered magnetic materials demonstrate cooperative magnetism, with some displaying a spontaneous magnetic configuration even without an external field.

Atomic magnetic moments are arranged in a regular manner due to the existence of an electrostatic interaction of quantum nature: this is the exchange interaction. This arrangement can be parallel (ferromagnetism), antiparallel with moment compensation

(antiferromagnetism), or antiparallel without moment compensation (ferrimagnetism). This arrangement may not be collinear.

I.5.3 Ferrimagnetism

Unlike the antiferromagnetic type, there is an imbalance in the substance of these materials due to the two distinct sublattices. This imbalance arises from a lack of precise compensation of the magnetizations. These materials exhibit spontaneous polarization, even in the absence of an applied external field, which varies with temperature. A specific temperature, called the Curie temperature [27].

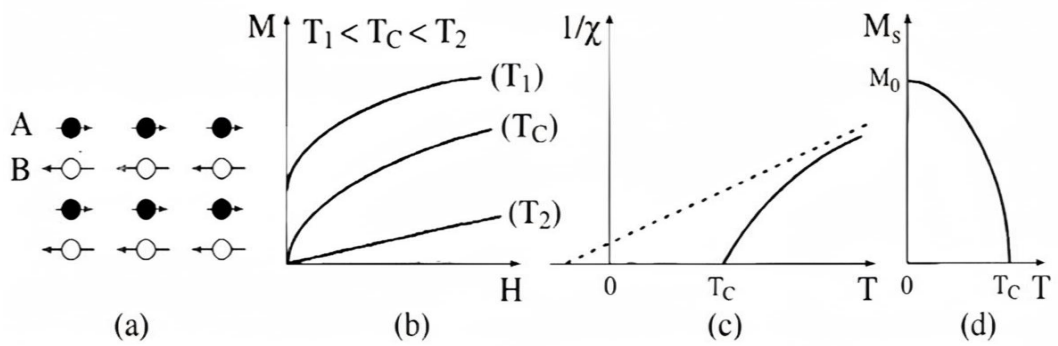


Figure I.7: Ferrimagnetism: (a) a spin lattice; (b) variation of the magnetization under an applied field; (c) thermal variation of $1/\chi$; (d) thermal variation of the spontaneous magnetization.

Compared to the Curie temperature, at all temperatures below this temperature, we observe ferromagnetic behavior; however, at all temperatures above it, the magnetic moments are randomly redistributed, which reduces the magnetization. In this case, we observe paramagnetic behavior.

I.5.4 Antiferromagnetism

The atoms in this material exhibit uniform atomic magnetic moments and are organised in an antiparallel configuration. This configuration results in the division of the substance into two identical magnetisation sublattices, each orientated in different directions. In the absence of an external field, the magnetisation is entirely null. The antiparallel configuration of the individual moments arises from antiferromagnetic cou-

pling, which opposes the influence of the applied field that seeks to align the moments parallelly [28].

Antiferromagnetism is defined by a minimal and positive variation in magnetic susceptibility as a function of temperature, with the configurations deteriorating as temperature rises.

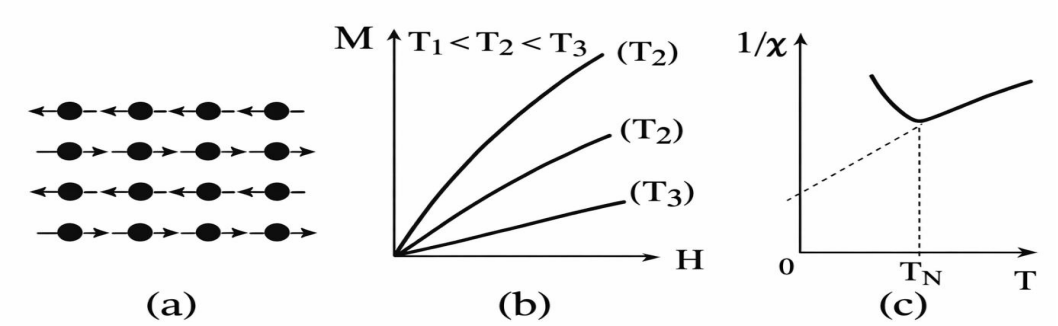


Figure I.8: Antiferromagnetism: (a) a spin network; (b) variation in magnetization under an applied field; (c) thermal variation of $1/\chi$.

The diminished influence of the alignment force enhances sensitivity to an external field, reaching a temperature known as the Néel temperature [29], at which antiferromagnetic coupling is interrupted.

I.5.5 Ferromagnetism

Ferromagnetism is a model of magnetism arising from the parallel alignment of permanent magnetic moments. The alignment of the latter can be regarded as a result of the restoring force arising from the mutual interactions between neighbouring atoms. The energy related to this occurrence is the exchange energy [30].

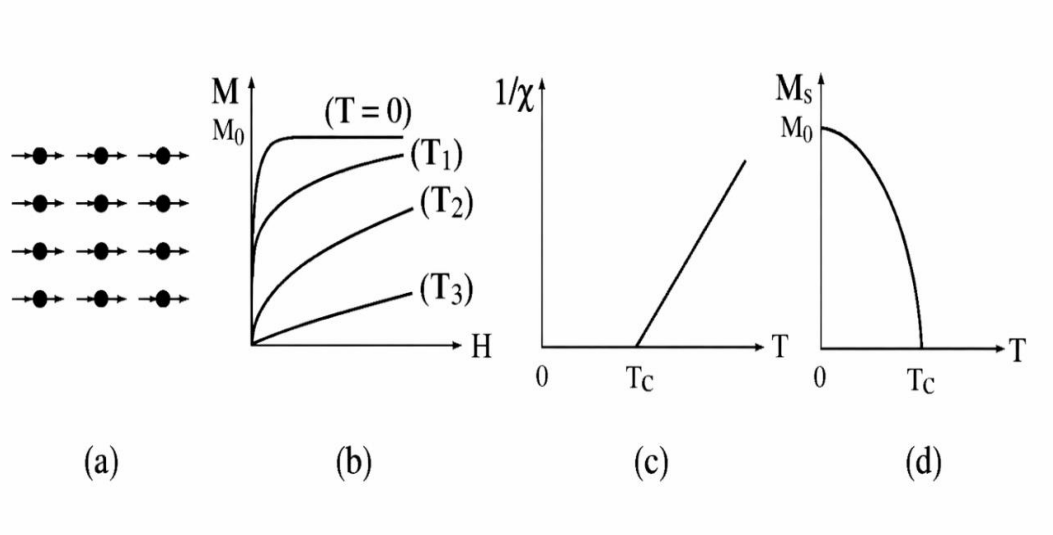


Figure I.9: Ferromagnetism: (a) spin network; (b) variation under the effect of the magnetization field ($T_1 < T_C < T_2 < T_3$); (c) thermal variation of $1/\chi$; (d) thermal variation of spontaneous magnetization.

This polarization generally occurs under the action of an external field, a subdivision of a macroscopically sized sample into several small volumes of different orientations and energetically more favorable because it allows the magnetic field to be maintained inside the material, known as the Weiss domain separated by walls (Bloch). The magnetisation of a ferromagnetic material alters the alignment of all magnetic moments in the same direction, leading to a change in magnetisation referred to as the first magnetisation curve [31]. This occurs when the magnetisation approaches saturation, corresponding to a high energy state.

In the absence of a magnetic field, the magnetic moments spontaneously orient in various directions, resulting in a net magnetic moment of zero for the sample. Consequently, a ferromagnetic material is not invariably spontaneously magnetised; its magnetic moment may be null, resulting in the substance being demagnetised. The alteration in magnetisation becomes irreversible when the field variation is applied between the extreme values H_0, resulting in a hysteresis loop, which underpins numerous technological applications.

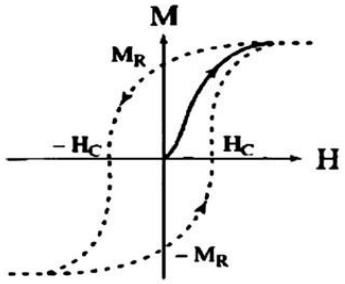


Figure I.10: Magnetization curve of a non-magnetized material, known as the first magnetization curve (solid line). Hysteresis cycle (dashed lines).

Thermal agitation affects ferromagnetic materials, while elevating the temperature may disturb the alignment, concurrently diminishing the magnetisation. Above the Curie temperature, the exchange interaction fails to maintain the alignment of magnetic moments, resulting in the material exhibiting paramagnetic behaviour.

This category, crucial for electronics, has strong, positive, and variable susceptibility in response to magnetic excitation. Certain alloys, composed of elements that are not inherently ferromagnetic, can exhibit ferromagnetism, such as Cu – Mn, Cu – Mn – Sn, and Cu – Mn – Al alloys, referred to as Heusler alloys.

I.5.6 Principle of Slater–Pauling

Magnetism in Heusler alloys is closely related to their electronic structure and the distribution of valence electrons. A useful approach for understanding and predicting the magnetic behavior of these materials is provided by the Slater–Pauling (SP) rule, which establishes a relationship between the total magnetic moment and the total number of valence electrons in the unit cell.

Slater and Pauling demonstrated that the average number of valence electrons (NV) per atom can be utilised to forecast the magnetic moment m of $3d$ elements and their binary alloys [32]. Materials are categorised into two zones based on the magnetic moment m (NV).

The initial segment of the Slater–Pauling curve pertains to the domain characterised by localised magnetism and diminished valence electron concentrations (NV $\leq$ 8). Structures pertaining to bcc are predominantly located here. The second domain is

characterised by elevated concentrations of valence electrons (NV $\geq$ 8) and itinerant magnetism. This zone contains systems with closed structures, specifically FCC and HCP. The demarcation between itinerant and localised magnetism is the locus of iron presence.

The Slater–Pauling curve is illustrated for certain alloys and transition metals (Figure I.10). The localised segment of this curve encompasses Heusler compounds. Therefore, this segment of the curve is our principal focus. The multiplication of the magnetic moment by the Bohr magneton μ_B yields the following relation:

$$m = N_v - 2n_\downarrow \tag{I.1}$$

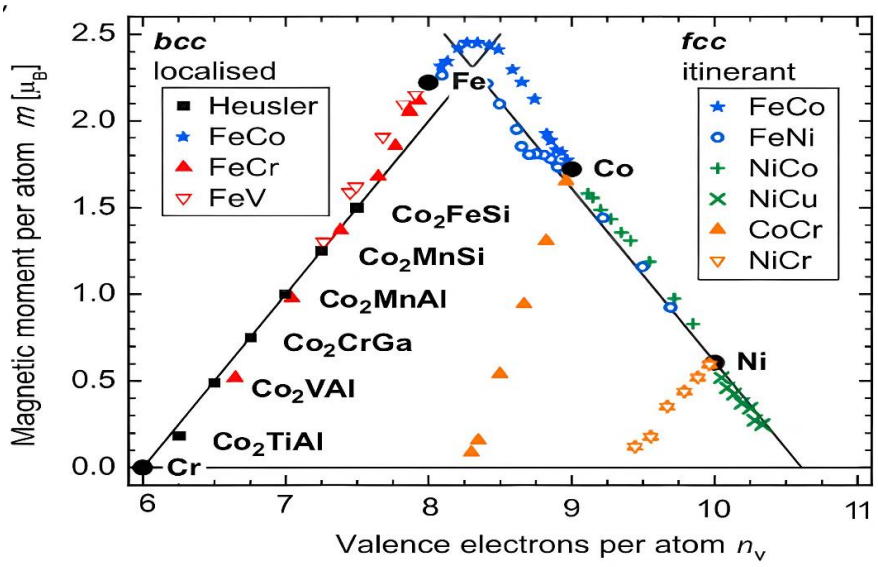


Figure I.11: Slater–Pauling curve [33].

Where $2n_\downarrow$ denotes the number of electrons in the minority states. The minimal density of the minority state requires that the electron count in the minority d band is around three. Excluding the s and p electrons yields the calculation of the magnetic moment using the following formula:

$$m = N_v - 6 \tag{I.2}$$

This rule may provide non-integer values if the average concentration of valence elec-

trons is not an integer. Thus, it is often more pragmatic to employ the number of valence electrons per formula unit. In half-Heusler alloys with the chemical formula XYZ, the filled states of the minority spins contain nine electrons, resulting in a total magnetic moment per primitive cell that conforms to the following rule:

$$m_{\mathrm{XYZ}} = N_v - 18\ (\mu_B) \tag{I.3}$$

Furthermore, for full-Heusler alloys characterised by the chemical formula X_2YZ, there are 12 electrons in the filled states of minority spins, so the total magnetic moment per primitive cell adheres to the following principle:

$$m_{\mathrm{X_2YZ}} = N_v - 24\ (\mu_B) \tag{I.4}$$

The magnetic moment as a function of the valence electron count per unit is depicted in Figure I.12.

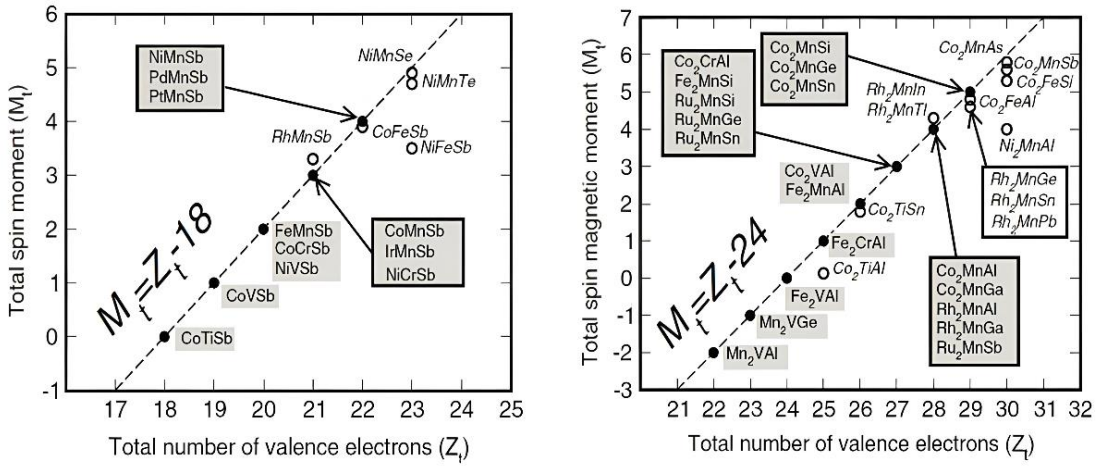


Figure I.12: The total magnetic moment m calculated as a function of the number of valence electrons N_v for half-Heusler alloys (on the left), and full-Heusler alloys (on the right). The dashed lines represent the Slater–Pauling (SP) behavior [34].

I.6 Electronic Properties

Analysing the properties of a material allows us to evaluate and understand the interactions of its various components, occurring in the most stable magnetic phase. We

provide two complementary tools to delineate the electronic structure of a solid: the electronic density of states (DOS) and projected density of states (PDOS), as well as the band structure (BS).

I.6.1 Band Structure

Band theory, which delineates the energy levels accessible to electrons inside a solid, elucidates the insulating or conductive properties of a material. Electrons may only possess energy values inside designated periods, which are divided by restricted energy bands. This modeling prompts a debate on energy bands or band structure.

Energy bands denote the many energy levels accessible to electrons based on their wave vector. Consequently, they are shown in reciprocal space and the higher symmetries of the first Brillouin zone. Figure I.13 presents the spin-polarized band structure of the compounds Fe_2VGa for spin-up and spin-down channels [35]. We observe that the maximum of the valence band is located at the Γ point, whereas the minimum of the conduction band is located at the X point, which clearly identifies the semi-metallic character.

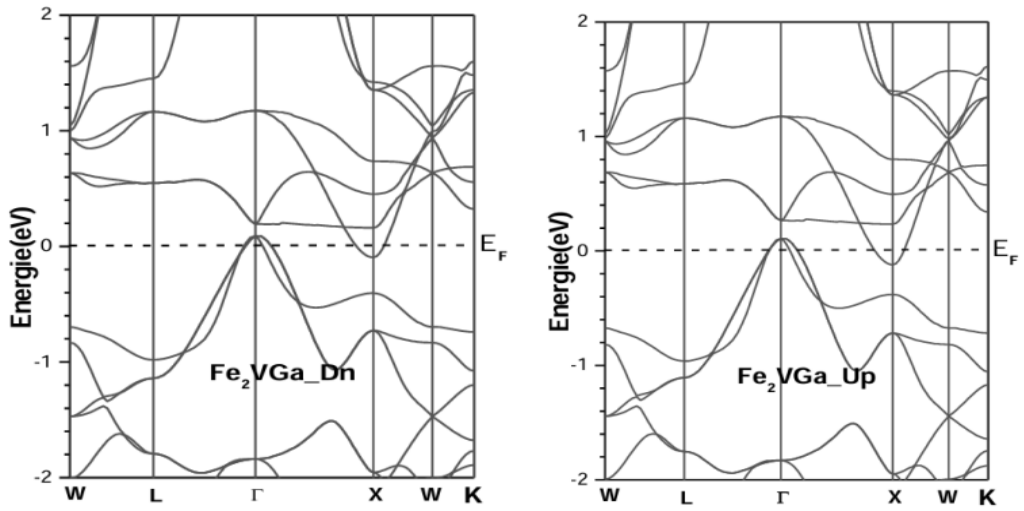


Figure I.13: The total magnetic moment m calculated as a function of the number of valence electrons N_v for half-Heusler alloys (on the left), and full-Heusler alloys (on the right). The dashed lines represent the Slater–Pauling (SP) behavior [34].

I.6.2 Density of electronic states

The total density of states (TDOS) reveals the electrical conduction characteristics of a material. Additionally, for each atom, a sphere of influence is established, inside which the electron density is represented using spherical harmonics of the s, p, d, or f types. This produces the partial densities of states (PDOS), facilitating the assessment of the chemical bonding configuration among the atoms within a crystal or molecule.

The projections of the total density of states are contingent upon the radii of the spheres onto which the partial densities of states are projected, thereby yielding only qualitative information. Figure I.14 depicts the total (TDOS) and partial (PDOS) densities of states for the compound Fe_2VGa [36].

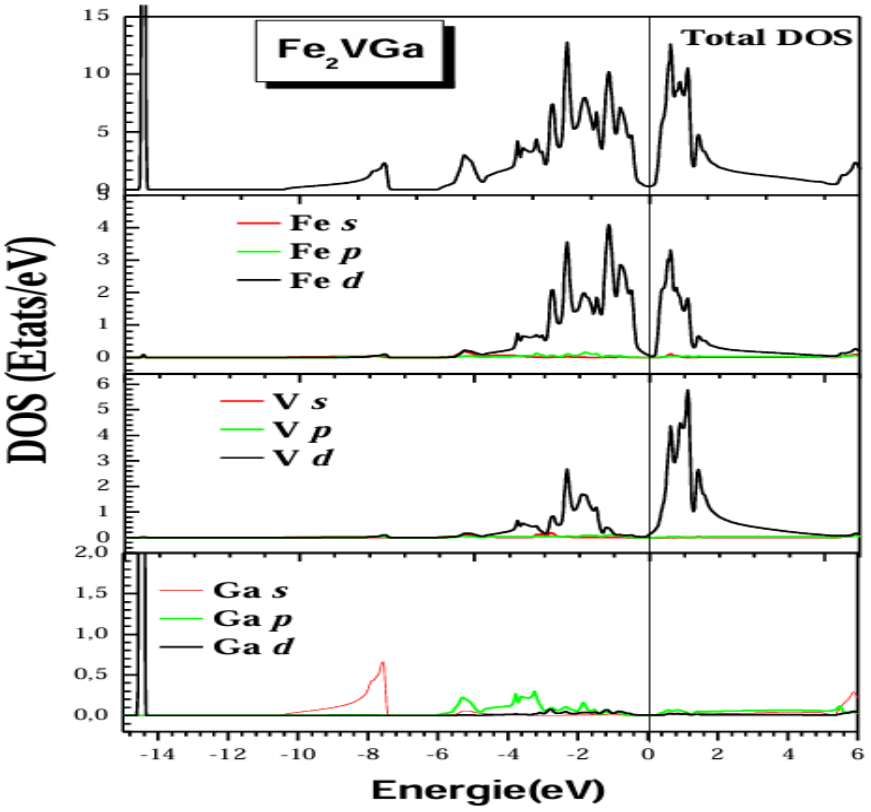


Figure I.14: The total (TDOS) and partial (PDOS) densities of states for the compound Fe_2VGa.

I.7 Thermoelectric Effects

Thermoelectric effects elucidate the interplay between thermal energy and electrical conductivity in solid materials. Consequently, thermoelectric devices have been designed and employed for energy generation or cooling. The thermoelectric phenomena present in a thermoelectric module (TEM) encompass the Seebeck effect, the Peltier effect, and the Thomson effect. The three effects are interconnected through Kelvin relations. They embody the principles of thermoelectricity [37].

I.7.1 Seebeck Effect

The Seebeck effect was identified in 1821 by Thomas Seebeck, who, by forming a circuit between two dissimilar materials and holding their junctions at different temperatures, observed the deflection of a compass needle. Over the next 130 years, various efforts were made to exploit thermoelectric materials as generators, but success was limited by low efficiency. During the 1950s to 1970s, the rise of space applications led to the development of thermoelectric generators through the refinement of tellurium-based technology [38].

Thermoelectric equipment is used in applications such as the Apollo missions and the Voyager I and II space probes. The materials treatment comes to a room. Essential in recent thermogenerative improvements, they have enabled improvements which continue to this day [39]. The thermoelectric appliances are numerous. Many devices utilize modern applications, including spatula engines, those that use the rover Curiosity and New Horizons probes, vibration-free refrigerators, portable coolers, and even camping stoves that charge electronic devices. As shown in Figure I.15, when a material is held at a certain temperature, the electronic charge carriers (ΔT) on the heated side exhibit a higher velocity than those on the cold side. This leads to a comparatively greater density of charge carriers on the cold side of the material [40]. The resultant voltage differential is characterised as a function of the Seebeck coefficient and the temperature gradient:

$$\Delta V = -S\,\Delta T \tag{I.5}$$

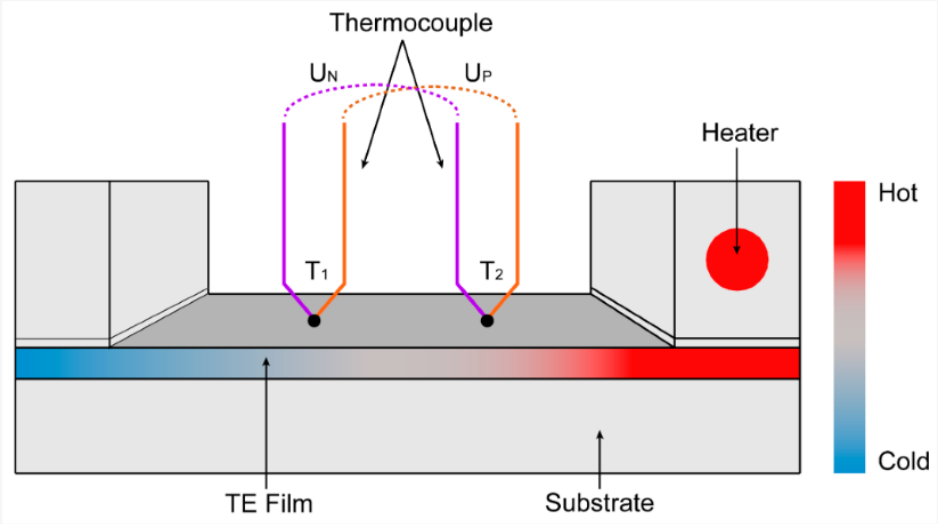


Figure I.15: First experimental setup described by Seebeck.

The Seebeck coefficient, or thermoelectric power, is then defined by:

$$S_{AB} = \frac{\Delta V}{\Delta T} \tag{I.6}$$

ΔV: Potential difference

ΔT: Temperature difference.

I.7.2 Peltier Effect

The second thermoelectric phenomenon was found in 1834 by the French physicist Jean Peltier. When an electric current is applied to the interfaces of two materials with different properties, a temperature gradient is observed. So, as demonstrated, a thermoelectric material can be used to produce heat or cold by use of an electric current. Figure I.16 [41].

$$\Pi_{AB} = \frac{Q}{I} \tag{I.7}$$

I: electric current

Q: heat released

If an imposed current in the direction $A \rightarrow B$ causes heat to be released at B and heat to be absorbed at A, then Π_{AB} is positive.

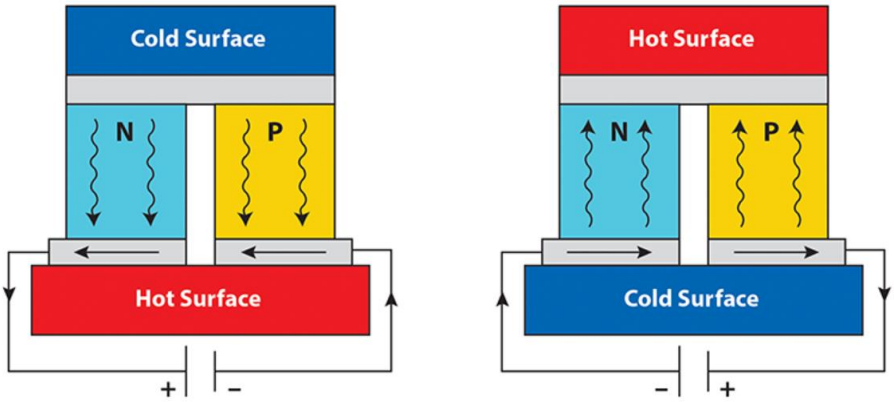


Figure I.16: First experimental setup described by Peltier.

I.7.3 The Thomson effect

Lord Kelvin, whose real name is William Thomson, found the Thomson effect in 1851 [42]. It explains how a conductor can be heated or cooled by a current and a temperature differential acting on it at the same time. The density of the heat flux (q) under the assumption of one-dimensional transit is:

$$\frac{dQ}{dT} = \tau I \frac{dT}{dx} \tag{I.8}$$

Where x is the spatial coordinate and τ is the Thomson factor, given by the relation

$$\tau_A - \tau_B = T \frac{dS_{AB}}{dT} \tag{I.9}$$

The three absolute coefficients S, Π and τ are related by the relations

$$\Pi_{AB} = \tau S T \tag{I.10}$$

$$\tau = T \frac{dS}{dT} \tag{I.11}$$

Applications of thermoelectric effects require the presence of two different materials, A and B, which will form the junction. The thermoelectric coefficients are therefore

related to the pair of materials taken separately according to:

$$S_{AB} = S_A - S_B \tag{I.12}$$

The Figure I.17 represented Thomson and magneto-Thomson effects. (a) Schematic of the conventional Thomson effect. When a charge current J_c and a temperature gradient ∇T are applied to a conductor, the Thomson effect induces heat absorption or release depending on the scalar product of J_c and ∇T. (b) Schematic of the magneto-Thomson effect. The heat production rate due to the Thomson effect can be modulated by applying a magnetic field H to a conductor [43].

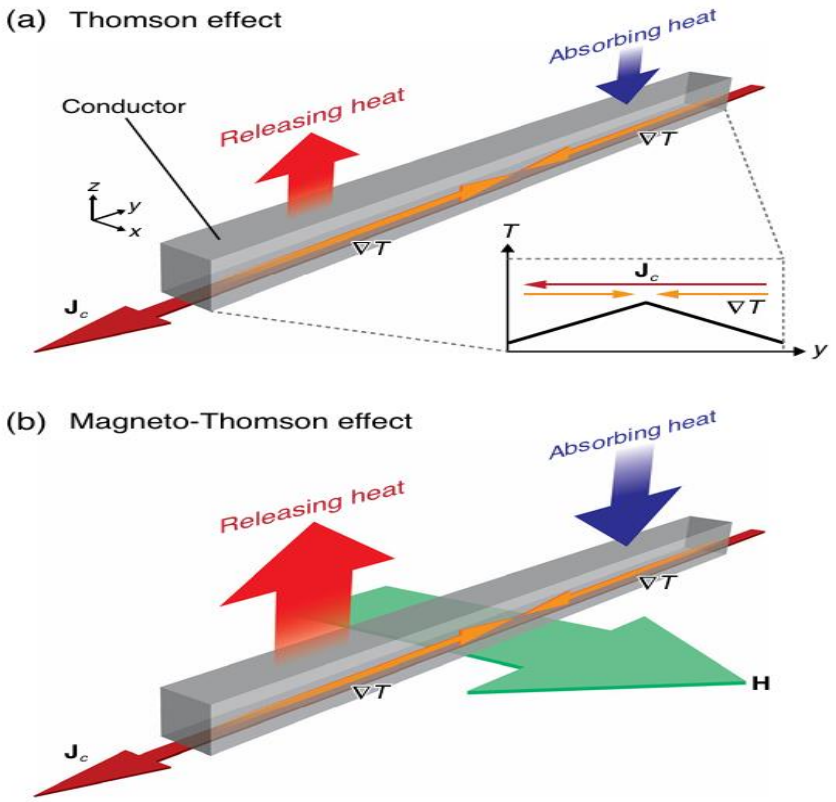


Figure I.17: Represented Thomson and magneto-Thomson effects.

I.8 Applications of Heusler compounds

The flexible tuning of Heusler compounds' structural and physical properties is a key benefit. Because of this, they find value in many fields, including thermoelectricity and spintronics.

I.8.1 Spintronic materials

A relatively new field of study, spintronics (also known as spin electronics) brings together phonons, electronic charges, and electronic spins as primary data carriers. The three main areas of information and communication technology symbolised by these carriers are data transportation, data storage via spin assembly, and data processing via electron transport. With its non-volatility data storage and vastly improved data processing speed, spintronics which depends on the motion of spin-polarized electrons is expected to meet the needs of future technologies while consuming very little energy [44].

New magnetic materials, magnetic semiconductors, and half-metallic ferromagnets (HFM) are necessary to realise spintronics' potential. As far as spintronics is concerned, ferromagnetic half-metals seem to be an appropriate class of materials. Their extraordinary electrical structure is the main cause; when the majority of electrons are in them, they act like metals, but when the minority are in them, they act like semiconductors. Figure I.18 At room temperature, Heusler compounds have the best chance of becoming half-metallicity. Band structure models predict that Heusler alloys based on iron and cobalt will exhibit half-metallicity. Because of their high Curie temperature and low lattice mismatch with main substrates, ferromagnetic half-metals made of Co and Fe are ideal candidates.

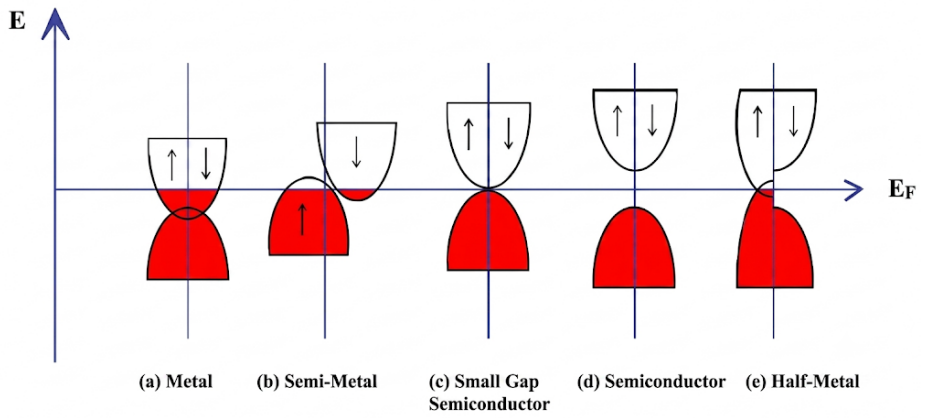


Figure I.18: Representative diagram of energy bands of materials with polarized spins.

I.8.1.1 Giant Magnetoresistance (GMR)

Giant magnetoresistance (GMR) manifests itself in structures composed of multilayered ferromagnetic materials interleaved with non-magnetic materials (spacer layers).

This structure's electrical resistance varies according to the relative orientation of the electron spins in the ferromagnetic layers, which is the basis of the GMR effect. There is little resistance when the electron spins are parallel and a great deal of resistance when they are antiparallel. One common application of GMR is in hard drive read heads, which can detect magnetic oscillations stored on the disc, as demonstrated in Figure I.19 [45].

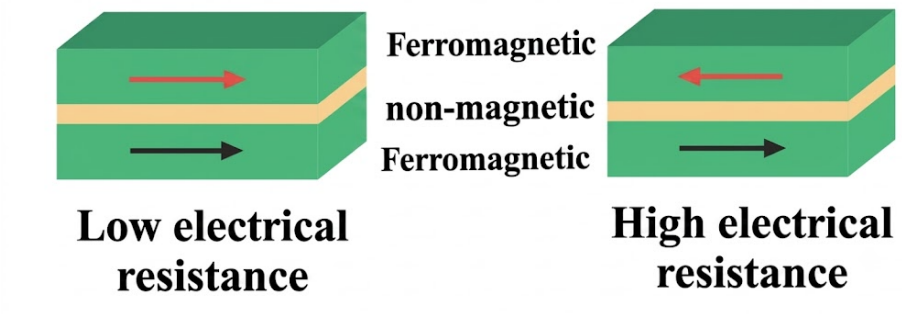


Figure I.19: The two states, parallel and antiparallel, in a giant magnetic junction.

I.8.1.2 Tunnel Magnetoresistance (TMR)

TMR is another magnetoresistance effect that relies on the phenomenon of electron transmission through a very thin insulating barrier, generally called a "tunnel barrier." In a TMR structure, two ferromagnetic layers are separated by a very thin insulating layer [46], which creates a tunnel barrier. It is based on the fact that the electrical resistance changes significantly depending on the relative orientation of the electron spins between the ferromagnetic layers as shown in Figure I.20. When the spins are parallel, transmission through the tunnel barrier is favored, reducing the resistance. When the spins are antiparallel, transmission is reduced, increasing the resistance.

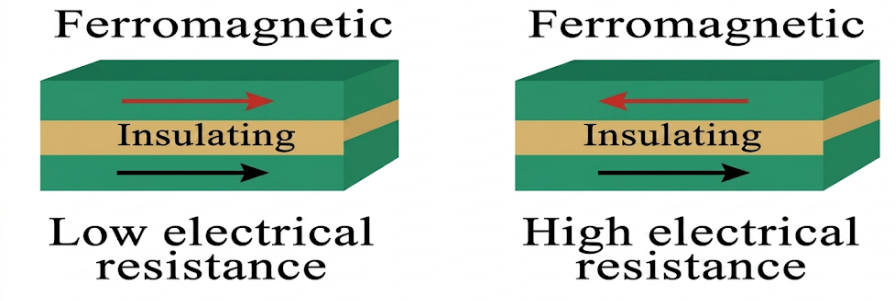


Figure I.20: The two states, parallel and antiparallel, in a magnetic tunnel junction.

I.8.2 Thermoelectric applications of Half-Heusler compounds

Thermoelectricity was extensively researched for uses in refrigeration and electricity generation during and after the two world wars.

I.8.2.1 Application in thermoelectric generation and cooling mode

Two types of semiconductor materials one p-type and one n-type form the thermocouple that is part of the thermoelectric module. Voltage and current can be increased in tandem thanks to these galvanic couplings, which are thermally arranged in parallel and electrically linked in series. Figure I.21 [47].

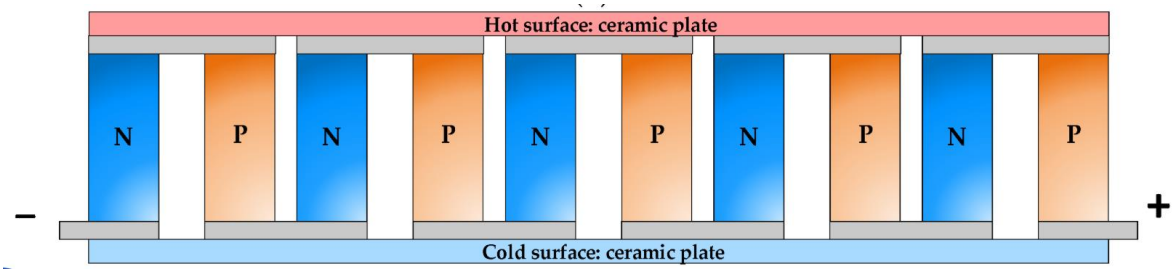


Figure I.21: A thermoelectric module.

Refrigerators and thermoelectric generators are two categories of thermoelectric devices. The Seebeck effect enables generators to transform waste heat into electricity, whereas the Peltier effect allows refrigerators to utilise electrical energy for cooling purposes. The two categories of thermoelectric devices are characterised by the orientation of energy conversion, facilitated by thermoelectric modules.

I.8.2.2 Power Generator

The space industry depends on thermoelectricity (TE) for critical applications because of its extended longevity. A notable breakthrough is the capability to dispatch space probes to traverse the cosmos, exemplified by the Voyager probes launched in 1977, which remain functioning. In 2011, Biolite introduced a thermoelectric-based product: a wood-burning stove equipped with a USB connector for charging electrical devices Figure I.22 [48].



Figure I.22: Biolite Camp stove.

I.9 Conclusion

In summary, this chapter has given a full picture of Heusler compounds, which sets the scientific and technological stage for the current thesis. We have emphasized the fundamental electronic, structural, and magnetic principles that dictate the behavior of Heusler alloys by initially analyzing the basic properties of transition metals and rare-earth elements.

We have talked about the full-Heusler, half-Heusler, and quaternary Heusler compounds. We focused on their crystal structures, site occupations, and order–disorder phenomena. This structural flexibility is a big part of why their physical properties can be changed so easily, from normal metallic behavior to half-metallicity, complex magnetic ordering, and promising thermoelectric performance.

The chapter has also gone over the main ideas behind magnetism (diamagnetism, paramagnetism, ferromagnetism, antiferromagnetism, and ferrimagnetism) and the Slater–Pauling rule to make the link between the electronic structure and the magnetic response of these materials clearer. In this context, Heusler alloys represent a notably complex model system wherein localized and itinerant magnetism, exchange interactions, and band-structure effects converge to generate highly spin-polarized states that are advantageous for spintronic applications.

Additionally, the analysis of the band structure and electronic density of states has revealed that Heusler compounds can simultaneously display metallic, semiconducting, or semi-metallic properties, placing them at the convergence of several essential categories of functional materials. The Seebeck, Peltier, and Thomson effects demonstrate their utility in energy conversion, either by transforming waste heat into electricity or by utilising solid-state technology for cooling purposes.

Finally, the different uses of Heusler alloys that were looked at in this chapter, such as giant and tunnel magnetoresistance devices, thermoelectric modules, and spintronic components, show that they are a flexible platform for the creation of new electronic and energy technologies. Nonetheless, despite the extensive array of experimental and theoretical investigations focused on these materials, numerous microscopic mechanisms remain only partially elucidated.

References

[1] R. A. De Groot, F. M. Mueller, P. G. van Engen, and K. H. J. Buschow. New class of materials: Half-metallic ferromagnets. *Phys. Rev. Lett.*, 50(25):2024–2027, 1983.

[2] I. Galanakis. Slater–Pauling behavior in half-metallic Heusler compounds. *Nanomaterials*, 13(13), 2010.

[3] J. E. Fischer et al. Magnetic properties and Curie temperatures of disordered Heusler compounds $Co_{1+x}Fe_{2-x}Si$. *Phys. Rev. B*, 94(2):024418, 2016.

[4] U. Krämer, I. N. Talke, and M. Hanikenne. Transition metal transport. *FEBS Lett.*, 581(12):2263–2272, 2007.

[5] P. P. Power. Main-group elements as transition metals. *Nature*, 463(7278):171–177, 2010.

[6] F. X. Hu, J. Wang, L. Chen, J. L. Zhao, J. R. Sun, and B. G. Shen. Effect of the introduction of H atoms on magnetic properties and magnetic entropy change in metamagnetic Heusler alloys Ni–Mn–In. *Appl. Phys. Lett.*, 95(11):112503, 2009.

[7] M. Albrecht. Cyclometalation using d-block transition metals: Fundamental aspects and recent trends. *Chem. Rev.*, 110(2):576–623, 2010.

[8] I. B. Bersuker. *Electronic Structure and Properties of Transition Metal Compounds: Introduction to the Theory*. Wiley, Hoboken, NJ, 2013.

[9] S. V. Eliseeva and J.-C. G. Bünzli. Rare earths: jewels for functional materials of the future. *New J. Chem.*, 35(6):1165, 2011.

[10] P. Enghag. *Encyclopedia of the Elements: Technical Data, History, Processing, Applications*. Wiley-VCH, Weinheim, 2005.

[11] G. Liu and B. Jacquier. *Spectroscopic Properties of Rare Earths in Optical Materials*. Springer, Berlin and Tsinghua University Press, 2005.

[12] F. Heusler. Über magnetische Manganlegierungen, 1903.

[13] L. Bainsla and K. G. Suresh. Equiatomic quaternary Heusler alloys: A material perspective for spintronic applications. *Appl. Phys. Rev.*, 3(3):031101, 2016.

[14] P. Punia et al. Recent advances in synthesis, characterization, and applications of nanoparticles for contaminated water treatment – a review. *Ceram. Int.*, 47(2):1526–1550, 2021.

[15] B. Fadila et al. Structural, magnetic, electronic and mechanical properties of full-Heusler alloys Co_2YZ (Y = Fe, Ti): First-principles calculations with different exchange-correlation potentials. *J. Magn. Magn. Mater.*, 448:208–220, 2018.

[16] N. Asli et al. Structural, electronic, magnetic and mechanical properties of the full-Heusler compounds $Ni_2Mn(Ge,Sn)$ and Mn_2NiGe. *Z. Für Naturforschung A*, 76(8):693–702, 2021.

[17] B. Govind, M. Srivastava, J. J. Pulikkotil, and D. K. Misra. Electronic structure and magnetic properties of a full-Heusler Mn_2NiSb: Cu_2MnAl type structure. *J. Magn. Magn. Mater.*, 517:167375, 2021.

[18] A. Candan. Magnetic, electronic, mechanical, anisotropic elastic and vibrational properties of antiferromagnetic Ru_2TGa (T = Cr, Mn, Co) Heusler alloys. *J. Electron. Mater.*, 48(12):7608–7622, 2019.

[19] M. Lazizi et al. Structural properties, electronic band structure, magnetic and mechanical characteristic of XFeGe (X = Co, Cr, Ni) half-Heusler compounds. *Inorg. Chem. Commun.*, 142:109675, 2022.

[20] M. Mokhtari, F. Dahmane, G. Benabdellah, L. Zekri, S. Benalia, and N. Zekri. Theoretical study of the structural stability, electronic and magnetic properties of XVSb (X = Fe, Ni, and Co) half-Heusler compounds, 2018.

[21] T. Graf, C. Felser, and S. S. P. Parkin. Simple rules for the understanding of Heusler compounds. *Prog. Solid State Chem.*, 39(1):1–50, 2011.

[22] D. Amari, M. Mokhtari, F. Dahmane, and G. Benabdellah. Structural, elastic, electronic, magnetic, and half-metallic properties of a novel rare earth-based quaternary Heusler alloy LaTiSi. *Emergent Mater.*, 6(1):299–306, 2023.

[23] H. Moujri, M. Berber, M. Mebrek, A. Boudali, and T. Ouahrani. Structural, elastic, electronic, and magnetic properties of new quaternary Heusler alloy PdCoMnGa and PdCoMnAl. *Indian J. Phys.*, 96(4):1025–1035, 2022.

[24] J. M. D. Coey and T. R. Ni Mhíocháin. History of magnetism. In *Reference Module in Materials Science and Materials Engineering*. Elsevier, 2016.

[25] R. Jackson. John Tyndall and the early history of diamagnetism. *Ann. Sci.*, 72(4):435–489, 2015.

[26] N. H. Duc, T. D. Hien, D. Givord, J. J. M. Franse, and F. R. de Boer. Exchange interactions in rare earth–transition metal compounds. *J. Magn. Magn. Mater.*, 124(3):305–311, 1993.

[27] Z. W. Li and A. H. Morrish. Negative exchange interactions and Curie temperatures for Sm_2Fe_{17} and $Sm_2Fe_{17}Y$. *Phys. Rev. B*, 55(6):3670–3676, 1997.

[28] Antiferromagnetism. *Proc. R. Soc. Lond. Ser. A*, 232(1188):48–68, 1955.

[29] M. Tadić, D. Nikolić, M. Panjan, and G. R. Blake. Magnetic properties of NiO nanoparticles: Blocking temperature and Néel temperature. *J. Alloys Compd.*, 647:1061–1068, 2015.

[30] R. Peierls. On Ising's model of ferromagnetism. *Math. Proc. Camb. Philos. Soc.*, 32(3):477–481, 1936.

[31] C. S. Edmund. Ferromagnetism: magnetization curves. *Rep. Prog. Phys.*, 13(1):83–183, 1950.

[32] I. Galanakis, P. Mavropoulos, and P. H. Dederichs. Electronic structure and Slater–Pauling behaviour in half-metallic Heusler alloys calculated from first principles. *J. Phys. Appl. Phys.*, 39(5):765–775, 2006.

[33] M. Robert. Oxygen affinity of haemoglobin. *Bull. Physiopathol. Respir.*, 11(1):79–170, 1975.

[34] C. Felser, G. H. Fecher, and B. Balke. Spintronics: A challenge for materials science and solid-state chemistry. *Angew. Chem. Int. Ed.*, 46(5):668–699, 2007.

[35] A. Šlebarski and J. Goraus. Electronic structure and thermodynamic properties of Fe_2VGa. *Phys. Rev. B*, 80(23):235121, 2009.

[36] M. Khalfa et al. Mechanical, electronic and thermodynamic properties of full Heusler compounds Fe_2VX (X = Al, Ga). *Int. J. Mod. Phys. B*, 29(31):1550229, 2015.

[37] C. M. Bhandari and D. M. Rowe. Electronic contribution to the thermal conductivity of narrow band gap semiconductors. *J. Phys. Appl. Phys.*, 18(5):873–883, 1985.

[38] J. P. Heremans, M. S. Dresselhaus, L. E. Bell, and D. T. Morelli. When thermoelectrics reached the nanoscale. *Nat. Nanotechnol.*, 8(7):471–473, 2013.

[39] A. J. Minnich, M. S. Dresselhaus, Z. F. Ren, and G. Chen. Bulk nanostructured thermoelectric materials: current research and future prospects. *Energy Environ. Sci.*, 2(5):466, 2009.

[40] K. Uchida et al. Observation of the spin Seebeck effect. *Nature*, 455(7214):778–781, 2008.

[41] D. C. Spanner. The Peltier effect and its use in the measurement of suction pressure. *J. Exp. Bot.*, 2(2):145–168, 1951.

[42] C. Watson. William Thomson, Lord Kelvin (1824–1907). In *Some Nineteenth Century British Scientists*, pages 96–153. Elsevier, 1969.

[43] K. Uchida, M. Murata, A. Miura, and R. Iguchi. Observation of the magneto-Thomson effect. *Phys. Rev. Lett.*, 125(10):106601, 2020.

[44] A. Fert and I. A. Campbell. Two-current conduction in nickel. *Phys. Rev. Lett.*, 21(16):1190–1192, 1968.

[45] C. Felser, G. H. Fecher, and B. Balke. Spintronics: eine Herausforderung für Materialwissenschaften und Festkörperchemie. *Angew. Chem.*, 119(5):680–713, 2007.

[46] Z. Zhou, K. Zhang, and Q. Leng. Tunneling magnetoresistance materials and devices for magnetic sensors. In *Spintronics*, pages 51–92. Wiley, 2022.

[47] Y. Liu, J.-R. Riba, M. Moreno-Eguilaz, and J. Sanllehí. Application of thermoelectric generators for low-temperature-gradient energy harvesting. *Appl. Sci.*, 13(4):2603, 2023.

[48] F. Tohidi, S. Ghazanfari Holagh, and A. Chitsaz. Thermoelectric generators: A comprehensive review of characteristics and applications. *Applied Thermal Engineering*, 201:117793, 2022.

CHAPTER II

DENSITY FUNCTIONAL THEORY (DFT)

II.1 Introduction

Density functional theory (DFT) is a widely employed quantum method in solid-state physics and quantum chemistry for calculating the physical and quantum properties of systems, particularly those with numerous electrons, including electronic structure and ionisation energy. It is referred to as a first-principles method. It is fundamentally grounded in quantum mechanics and requires only a restricted amount of input data. It enables the resolution of the Schrödinger equation for a multi-body system without the use of empirically altered parameters. DFT has become an important method for understanding and engineering new functional materials, like half-metallic ferromagnets, which have distinctive spin-dependent electronic structures that are very useful for spintronic applications [1].

DFT is a first-principles (ab initio) method since it is based on quantum physics and only needs a few input parameters, such as the atomic numbers and locations of the elements that make up the material. It is important because it does not use empirically fitted or experimentally changed parameters, which makes it possible to describe material properties in an unbiased and predictable way. This property has proved very important for the theoretical study of many other materials, such as thermoelectric systems [2], where a precise description of the electronic structure is necessary to understand how charge and heat move about [3, 4].

This chapter aims to elucidate the theoretical foundation of the WIEN2K code employed in this thesis. Initially, we will elucidate the fundamental concepts of first-principles calculations, followed by an introduction to the employed approximation methods: the spin- polarized local density approximation (LSDA) and the generalised gradient approximation (GGA). Subsequently, we introduce the linearised augmented plane wave approach along with its many enhancements. Ultimately, we will provide a concise overview of the WIEN2K code.

II.2 Schrödinger Equation



Erwin Schrödinger 1887–1961

Isaac Newton established the principles of classical mechanics in the 17th century; these principles control the motion of large objects. Physicists found around the turn of the twentieth century that extremely tiny particles like electrons, atomic nuclei, and molecules do not behave according to the rules of classical mechanics. Specifically, the "Schrödinger's equation," a fundamental equation in quantum mechanics, governs their behaviour. In 1926, Schrödinger put out this equation [5] to describe minuscule objects (atoms) made up of a single particle (like the electron in a hydrogen atom). The building blocks of matter, known as ions and electrons, form solids. Determining the precise structure of these particles and how their properties are derived is the primary theoretical challenge in solid-state physics. The system's wave function Ψ, which is represented by the time-independent Schrödinger equation and depends on the nuclei's and electrons' coordinates, contains all the information that can be derived about a system with N ions and n electrons:

$$\hat{H}\Psi = E\Psi \tag{II.1}$$

which:

- E : Total energy
- H : Total Hamiltonian

and:

- Ψ : Wave function

The presence of electrostatic interaction forces repulsion or attraction depending on the charge of the particles allows us to express the equations of motion of all crystal particles using the accurate Hamiltonian of crystal (non-relativistic). The crystal's Hamiltonian can be expressed as:

$$\hat{H}_T = \hat{T}_n + \hat{T}_e + \hat{V}_{n-n} + \hat{V}_{n-e} + \hat{V}_{e-e} \tag{II.2}$$

In which: $\hat{T}_n = -\sum_i \frac{\hbar^2}{2M_i}\nabla^2_{R_i}$: kinetic energy of nuclei.
$\hat{T}_e = -\sum_i \frac{\hbar^2}{2m_e}\nabla^2_{r_i}$: kinetic energy of electrons.
$\hat{V}_{n-n} = \frac{1}{4\pi\varepsilon_0}\sum_{i<j}\frac{Z_i Z_j e^2}{|\vec{R}_i - \vec{R}_j|}$: Coulomb repulsion energy between nuclei.
$\hat{V}_{n-e} = -\frac{1}{4\pi\varepsilon_0}\sum_{i,j}\frac{Z_i e^2}{|\vec{R}_i - \vec{r}_j|}$: Coulomb attraction energy between nuclei and electrons.
$\hat{V}_{e-e} = \frac{1}{4\pi\varepsilon_0}\sum_{i<j}\frac{e^2}{|\vec{r}_i - \vec{r}_j|}$: Coulomb repulsion energy between electrons.
Solving even the most basic situations of the equation (Eq II.1), which is by Erwin Schrödinger (1926), becomes exceedingly complex when dealing with N. Computing becomes exponentially more complex as the number of atoms grows. Their wave functions are thus dependent on the three-dimensional coordinates of the "N"th electron when we think about a specific number of electrons. Consequently, "$3N$" variables are crucial to the global function.

Methods for computing the electronic band structure of solid-state materials have evolved over the past few decades, with each approach relying on a different set of approximations distributed across three tiers:

1. Born–Oppenheimer approximation.
2. Hartree–Fock approximation where the formalism of density functional theory (DFT).

3. Approximations inherent in solving equations.

II.2.1 Born–Oppenheimer approximation



Max Born 1882–1970



Robert Oppenheimer 1904–1967

We disregard the nuclei's motion in comparison to the electrons' because, as Born–Oppenheimer [6] argues, nuclei are heavier and hence slower. Therefore, we solely consider the electron kinetic energy and ignore the nuclei kinetic energy, denoted as "T_n", in which case we can change the source of the energies to be the potential energy between nuclei, and the equation (Eq. II.2) becomes:

$$\hat{H}_T = \hat{T}_e + \hat{V}_{n-e} + \hat{V}_{e-e} \tag{II.3}$$

By decoupling the electronic issue from the vibrations of the mesh, the Born–Oppenheimer approximation achieves adiabatic behaviour. Thus, the following form can be used to express the system's wave function, which is the adiabatic approximation solution to the Schrödinger equation:

$$\Psi(R, r) = \Psi_n(R)\,\Psi_e(r) \tag{II.4}$$

Where:

- $\Psi_n(R)$: is nuclear wave function

- $\Psi_e(r)$: is electronic wave function

Multiple approaches exist to solve the equation (Eq. II.4), the initial ones being those of Hartree [7] and Hartree–Fock [8], which are predicated on the free electron theory.

These approaches are predominantly employed in quantum chemistry for the treatment of atoms and molecules; however, their precision diminishes when applied to solids. Nonetheless, there exists a contemporary and undoubtedly more potent approach known as Density Functional Theory (DFT).

II.2.2 Approximations based on the wave function

II.2.2.1 Hartree Methods



Douglas Hartree (1897–1958)

It is possible to rewrite the Hamiltonian as a sum of mono-electronic terms when the electron–electron interaction term is not present. One method proposed by Hartree [9] is to use an effective potential V to describe the Coulomb interaction. By applying Hartree's law to each electron and translating its average effect, the following is defined:

$$V_{\text{Hartree}} = \frac{1}{2}\sum_j \int d\vec{r}\,' \frac{\Psi_j(\vec{r})\Psi_j^*(\vec{r}\,')}{|\vec{r}\,' - \vec{r}|} \tag{II.5}$$

Also, to express the wave function as a product of wave functions for mono-electronic components.

$$\Psi(\vec{r}) = \prod_{i=0}^{N_{\text{ele}}} \Psi_i(\vec{r}) \tag{II.6}$$

Each mono-electronic wave function is then a solution of

$$H_{\text{eff}}\,\Psi_i(\vec{r}) = \left(-\frac{1}{2}\nabla + V_{\text{Hartree}} + V_{\text{Ext}}\right)\Psi_i(\vec{r}) = \varepsilon_i\,\Psi_i(\vec{r}) \tag{II.7}$$

The Hartree potential depending on the orbital i, the resolution of equation (Eq. II.7) must be done in a self-consistent manner. The ground state is obtained by filling the first n electronic levels. This approach still serves as the basis for solving the problem of interacting electrons today, particularly through the Kohn–Sham formalism discussed in the following section. However, it suffers from various problems: the starting Hamiltonian is only a mean-field approximation and the electrons are not treated as fermions.

II.2.2.2 The Hartree–Fock approach



Vladimir Fock 1898–1974

This method, initially implemented for atoms in 1930 [10], does not include any approximation of the Hamiltonian. Conversely, it is posited that the wave function can be expressed as a Slater determinant formed from n mono-electronic wave functions ψ_i

to accommodate the Pauli exclusion principle.

$$\Psi_{\text{ele}}(\vec{r}) = \frac{1}{\sqrt{n!}} \begin{vmatrix} \Psi_1(\vec{r}_1) & \cdots & \Psi_n(\vec{r}_1) \\ \vdots & \ddots & \vdots \\ \Psi_1(\vec{r}_n) & \cdots & \Psi_n(\vec{r}_n) \end{vmatrix} \tag{II.8}$$

The wave function being normalized, it can be shown that the energy is written as:

$$E_{HF} = \sum_i H_i + \frac{1}{2} \sum_{i,j} (J_{ij} - K_{ij}) \tag{II.9}$$

With:

$$H_i = \int dr\, \Psi_i(r)^* \left[-\frac{1}{2}\nabla^2 + V_{\text{el-nu}}(r) + V_{\text{ext}}(r) \right] \Psi_i(r) \tag{II.10}$$

And

$$J_{ij} = \frac{1}{2} \iint dr\, dr'\, \Psi_i(r)\Psi_i^*(r) \frac{1}{|r' - r|} \Psi_j^*(r')\Psi_j(r) \tag{II.11}$$

Next

$$K_{ij} = \frac{1}{2} \iint dr\, dr'\, \Psi_i^*(r)\Psi_j(r) \frac{1}{|r' - r|} \Psi_i(r)\Psi_j^*(r')\delta(\sigma_i - \sigma_j) \tag{II.12}$$

The term J_{ij} is the Coulomb integral, already present in the Hartree approach, while K_{ij} is the exchange integral or Fock term, which arises from the necessity to antisymmetrize the wave function $\Psi_i(r)$. To determine the functions, we use the Rayleigh–Ritz [11] minimization principle for the energy $E_{HF}(r)$, with the constraint of the normalization of the wave functions.

$$\delta \left(E_{EF}(r) - \sum_{i,j} \lambda_{i,j} \left(\langle \Psi_i(\vec{r}) \mid \Psi_j(\vec{r}) \rangle - \delta_{i,j} \right) \right) = 0 \tag{II.13}$$

By a unitary transformation, we can diagonalize the matrix of Lagrange multipliers $\lambda_{i,j}$, which leads to the mono-electronic Fock equations:

$$\left(\hat{T}_{\text{el}} + \hat{V}_{\text{el-nuc}} + \hat{V}_{\text{Hartree}} + \hat{V}_{\text{Ext}} + \hat{V}_{\text{Fock}}(\Psi(\vec{r})) \right) \Psi_i(\vec{r}) = \varepsilon_i \Psi_i(\vec{r}) \tag{II.14}$$

With:

$$V_{\text{Hartree}} = \sum_i \int dr'\, \Psi_j(r)\Psi_j(r')^* \frac{1}{|r' - r|} \tag{II.15}$$

$$V_{\text{Fock}} = \left[\sum_j \int dr' \, \Psi_j(r) \Psi_j(r')^* \frac{1}{|r' - r|} \right] \frac{\Psi_j(r)}{\Psi_i(r)} \delta(\sigma_i - \sigma_j) \tag{II.16}$$

Where we identify the Lagrange parameter with a one-electron energy ε_i. This set of equations is self-consistent (via the Hartree term and the non-local Fock term).

II.2.2.3 The Hartree–Fock–Slater approximation



John Clarke Slater 1900–1976

In contrast to the AHF, Slater [12] uses the assumption that the exchange term is local in nature to estimate it. The following is the format of this exchange potential:

$$V_x(\vec{r}) = -6\alpha \left(\frac{3\rho(\vec{r})}{4\pi} \right)^{1/3} \tag{II.17}$$

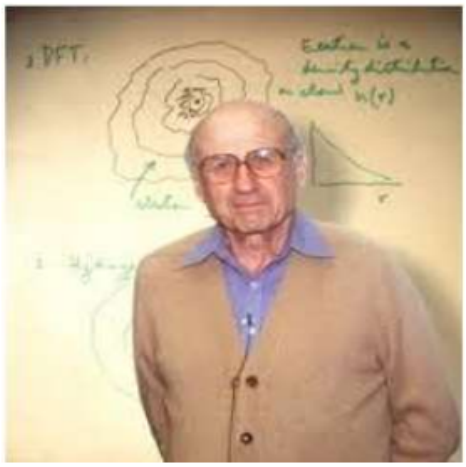
The charge density is denoted by $\rho(\vec{r})$ the charge density. In his calculations, Slater sets $\alpha = 1$, which corresponds to a homogeneous gas without interaction.

We describe below the local approximation of density functional theory (DFT), which is one of the most significant approximations in the context of the single-electron scheme nowadays.

II.2.3 Density Functional Theory (DFT)

The basic idea behind density-functional theory (DFT) is that the energy of an electrical system may be described by its density. Thomas [13] and Fermi [14] primarily developed this concept in 1951, therefore it's not new. It is worth mentioning that the precise fundamental theorems of Hohenberg and Kohn, which uniquely connect the energy and density of the ground state, were published in 1964 [15], thus establishing DFT.

II.2.3.1 Hohenberg and Kohn's theorems



Walter Kohn 1923-2016



Pierre C. Hohenberg 1934-2017

In density functional theory (DFT), the formalism relies on the theorems of Hohenberg and Kohn [15].

To begin with, Hohenberg and Kohn demonstrated that the electronic density $\rho(r)$ and the external potential are directly proportional, enabling the former to be denoted as a function of the latter's ground state. "The total energy of the system in the ground state is also a unique universal functional of the electron density", thus:

$$E = E[\rho(r)] \tag{II.18}$$

Density functional theory (DFT) differs from the Hartree–Fock technique, where the system's total energy is functional to the wave function; this theorem is the foundation

of DFT and hence its name (DFT).

The fact that the system's Hamiltonian operator is uniquely determined by the electron density is an immediate result of this theorem. Consequently, one may determine the material's various properties by knowing the electron density and then using this information to find the Hamiltonian operator.

Additionally, it was demonstrated by Hohenberg and Kohn that, given a potential $\langle V_{\text{ext}} \rangle$ and a specific number of electrons N, the system's total energy is at its lowest when the density $\rho(r)$ matches the precise density of the ground state $\rho_0(r)$:

$$E(\rho_0) = \min E(\rho) \tag{II.19}$$

The functional of the total energy of the ground state is written as follows:

$$E[\rho(\vec{r})] = F[\rho(\vec{r})] + \int V_{\text{ext}}(\vec{r})\, \rho(\vec{r})\, d^3\vec{r} \tag{II.20}$$

Where: $V_{ext}(r)$ denotes the external potential exerted on the particles, whereas $F[\rho(\vec{r})]$ signifies the universal functional as established by Hohenberg and Kohn, with:

$$F[\rho(\vec{r})] = \langle \Psi | \hat{T} + \hat{V} | \Psi \rangle \tag{II.21}$$

Understanding this functional enables the calculation of the total energy and charge density of the ground state for a specified external potential, employing the variational principle. Regrettably, Hohenberg and Kohn's theorem provides little insight into the nature of $F[\rho(\vec{r})]$.

II.2.3.2 The Kohn and Sham equations

Substituting a fictional, non-interactive system for the actual, interactive one is a new improvement proposed by Kohn and Sham (KS) [16]. With this method, the electron densities, ground state energy of a system of non-interacting fermions in an effective potential and the real system with multiple interacting electrons subjected to a real potential are exactly matched. This fictional system thus maintains the genuine system's electron density and energy.



Lu Jeu Sham 1938

The hypothetical system was also subject to the Hohenberg and Kohn theorems. The following expression can be used to express the density functional $F[\rho(\vec{r})]$ for the interactive system:

$$F[\rho(\vec{r})] = T_0[\rho(\vec{r})] + E_H[\rho(\vec{r})] + E_{xc}[\rho(\vec{r})] + V_{ext}[\rho(\vec{r})]. \tag{II.22}$$

The kinetic energy of the non-interacting electron gas is denoted by $T_0[\rho(\vec{r})]$, the Hartree term is $E_H[\rho(\vec{r})]$, the exchange-correlation energy is $E_{xc}[\rho(\vec{r})]$, and $V_{ext}[\rho(\vec{r})]$ describes the inter-electronic interaction, including the Coulomb interactions between electrons and nuclei as well as between nuclei themselves.

Free electron states are best described by the Hartree term and the kinetic energy term. Regarding the study of electron interaction, several concepts are crucial. The exchange and correlation energy $E_{xc}[\rho(\vec{r})]$, is calculated by comparing the actual kinetic energy with that of non-interacting electrons and the actual interaction energy with that of Hartree.

The form of the Schrödinger equation that needs to be solved using the Kohn and Sham framework is:
method takes the following shape:

$$\left[-\frac{\hbar^2}{2m_e}\nabla^2 + V_{\text{eff}}(\mathbf{r})\right]\varphi_i(\mathbf{r}) = \varepsilon_i\varphi_i(\mathbf{r}), \qquad i = 1, \ldots, N. \tag{II.23}$$

If the form of the effective potential is:

$$\hat{V}_{eff} = \hat{V}_{ext} + \int \frac{\rho(\vec{r}')}{|\vec{r} - \vec{r}'|} d\vec{r}' + \hat{V}_{xc} \tag{II.24}$$

In terms of possibilities for exchange and correlation, the derivative functional provides:

$$\hat{V}_{xc}(\vec{r}) = \frac{\delta E_{xc}[\rho(\vec{r})]}{\delta \rho(\vec{r})} \tag{II.25}$$

In addition, the density is expressed as a summation over all occupied orbitals:

$$\rho(\vec{r}) = \sum_{i=1}^{N} |\varphi_i(\vec{r})|^2 \tag{II.26}$$

Equations (Eq. II.23) are equivalent to the Kohn and Sham equations and need to be solved in a fashion that is consistent with itself. This means that we need to start with a specific initial density, $V_{eff}(\vec{r})$, and then solve equation (Eq. II.22) to find the new electron density. One can get a fresh effective potential from this revised density.

Convergence is achieved when the new electron density is equal to or extremely near to the previous one, which is determined by the fixed convergence criterion. This procedure is continued in a self-consistent way until then.

II.2.3.3 The exchange-correlation functional

The development of the Kohn and Sham equations made it possible to highlight the fact that the only density functional which remains unknown in this formalism is the exchange correlation functional $E_{xc}[\rho(\vec{r})]$. Thus, to solve Kohn and Sham equations, various exchange-correlation functional were considered.
The effects result from interaction between electrons are of three categories: The exchange, the dynamic correlation and the non-dynamic correlation.

The exchange effect arises from the anti-symmetry of the total wave function about the interchange of electronic coordinates, corresponding to Pauli's principle [17], which dictates that two electrons with identical spin cannot occupy the same position. This effect is independent of the electron's charge and is considered in Hartree–Fock theory due to the antisymmetry of the Slater determinant that represents the wave function.

The correlation effect pertains to the relationship between electronic movements induced by Coulombic inter-electronic repulsion in $\frac{1}{|r-r'|}$. It fundamentally pertains to correlation effects for core electrons. This effect, unlike the exchange effect, is attributable to the electron's charge and is independent of spin. This effect is overlooked by Hartree–Fock theory.

The third effect originates from the formulation of electronic wave functions in terms of independent particles. This is the self-interaction adjustment, which is essential for accurately calculating the number of electron pairs.

The kinetic energy differential between the real system and the hypothetical non-interacting system must also be considered by the exchange-correlation functional, in addition to the previously mentioned factors. Consequently, a set of approximations form the basis of the energy and exchange-correlation potential calculations.

Local density approximation (LDA)

In the local density approximation, it is posited that electronic density can be locally regarded as a uniform electron gas. This results in the formulation of the subsequent two hypotheses:

- The exchange-correlation effects are dominated by the density located at point r.
- The density $\rho(r)$ is a function varying slowly with respect to r.

The idea behind this approximation is to treat the non-uniform gas as though it were locally uniform and sum up the contributions of each part to the total system energy, denoted as $E_{xc}[\rho(r)]$.

What follows is one possible representation of the exchange-correlation energy (LDA):

$$E_{xc}^{LDA}[\rho(\vec{r})] = \int \rho(\vec{r})\, \varepsilon_{xc}^{LDA}[\rho(\vec{r})]\, d^3\vec{r} \tag{II.27}$$

Where $\varepsilon_{xc}^{LDA}[\rho(\vec{r})]$ denotes the exchange-correlation energy for each electron in an electron gas.

From $\varepsilon_{xc}^{LDA}[\rho(\vec{r})]$, the $V_{xc}^{LDA}[\rho(\vec{r})]$ may be derived variationally in accordance with the equation:

$$V_{xc}^{LDA}(\vec{r}) = \frac{\delta\left(\rho(\vec{r})\,\varepsilon_{xc}^{LDA}[\rho(\vec{r})]\right)}{\delta\rho(\vec{r})} \tag{II.28}$$

In magnetic systems, electron spin adds a new axis of rotation, necessitating an extension of the Local Density Approximation (LDA) to the Local Spin Density Approximation (LSDA), where the correlation and exchange energies are related to the two up and down spin densities:

$$E_{xc}^{LSDA}[\rho_\uparrow, \rho_\downarrow] = \int \rho(\vec{r})\,\varepsilon_{xc}[\rho_\uparrow(\vec{r}), \rho_\downarrow(\vec{r})]\,d^3\vec{r} \tag{II.29}$$

The LDA put that the functional $\varepsilon_{xc}^{LDA}[\rho(\vec{r})]$ is local, and divided this energy into two terms:

$$\varepsilon_{xc}[\rho(\vec{r})] = \varepsilon_x[\rho(\vec{r})] + \varepsilon_c[\rho(\vec{r})] \tag{II.30}$$

Where: $\varepsilon_x^{LDA}[\rho(\vec{r})]$ is exchange energy.

$\varepsilon_c[\rho(\vec{r})]$ is correlation energy.

That give

$$\varepsilon_x^{LDA}[\rho(\vec{r})] = -0.4581/r_s \tag{II.31}$$

With:

$$\rho = \left(\frac{4\pi r_s^3}{3}\right)^{-1}$$

the correlation term:

$$\varepsilon_c^{LDA}[\rho(\vec{r})] = -\frac{0.44}{r_s + 7.8} \tag{II.32}$$

Also, according to Perdew and Zunger [18], the correlation energy of a gas of free electrons was calculated using the model developed by Ceperly and Alder [19]:

$$\varepsilon_c[\rho(\vec{r})] = -\frac{0.1423}{1 + 1.0529\sqrt{r_s} + 0.3334 r_s}, \qquad r_s > 1 \tag{II.33}$$

$$\varepsilon_c^{LDA}[\rho(\vec{r})] = -0.048 + 0.0311 \ln r_s - 0.0116 r_s + 0.002 r_s \ln r_s, \qquad r_s < 1 \tag{II.34}$$

Kohn and Sham, Hedin and Lundqvist, and Perdew and Wang are among the alternative parameterizations available for the correlation energy of a homogeneous electron gas [20, 21].

Generalized Gradient Approximation (GGA)

It enhances LDA by making the exchange-correlation energy dependent on both electron density and its gradient $|\nabla\rho(\vec{r})|$. Consequently, the functional $E_{xc}[\rho(\vec{r})]$ addresses the non-uniform nature of the electron flow.

The effect of $E_{xc}[\rho(\vec{r})]$ to the system's total energy can be cumulatively added from each segment of the non-uniform gas, treating each segment as locally non-uniform. It is articulated in the format:

$$E_{xc}^{GGA}[\rho(\vec{r})] = \int \rho(\vec{r})\, \varepsilon_{xc}[\rho(\vec{r}), |\nabla\rho(\vec{r})|]\, d^3\vec{r} \tag{II.35}$$

Where: $\varepsilon_{xc}[\rho(\vec{r}), |\nabla\rho(\vec{r})|]$, the exchange-correlation energy per electron of non-uniform density.

When compared to the LDA description, the usage of GGA type functional allows for far more accurate calculations, especially for molecule binding energies.

Because of this, DFT saw enormous use among chemists in the '90s.

Various parameterizations of the GGA have been proposed, such as Perdew et al. (1991) [22] and Perdew et al. (1996) [23], with the most popular versions being Perdew and Wang and Perdew as stated in [24].

II.2.3.4 Solving the Kohn–Sham equations

Resolving the Kohn and Sham equations (Eq. II.22) necessitates the selection of a basis for the wave functions, which may be represented as a linear combination of orbitals known as Kohn–Sham orbitals (KS) expressed in the following form:

$$\psi_i(\vec{r}) = \sum_j C_{ij}\, \phi_j(\vec{r}) \tag{II.36}$$

In which: $\phi_j(\vec{r})$ represents the fundamental functions and C_{ij} indicates the expansion coefficients.

Resolving the Kohn and Sham equations involves identifying the coefficients C_{ij} for the occupied orbitals that minimise the total energy. Resolving the KS equations at the symmetry sites within the first Brillouin zone streamlines the computations.

This resolution is executed iteratively through a self-consistent cycle of iterations, as depicted in the flowchart in Figure II.1. We commence by introducing the initial charge density ρ_{in} to diagonalise the time-honoured equation:

$$(H - \varepsilon_i S)C_i = 0 \tag{II.37}$$

In which: H the Hamiltonian matrix and S the covering.

The novel density of charges ρ_{out} is formulated using the eigenvectors of this long-standing equation, derived from the total charge density obtained through a summing of all occupied orbitals (Eq II.26).

In the event of discrepancies in the calculations, we combine the two densities ρ_{in} and ρ_{out}:

$$\rho_{in}^{i+1} = (1 - \alpha)\rho_{in}^{i} + \alpha\rho_{out}^{i} \tag{II.38}$$

i signifies the ith iteration, whereas α indicates a mixing parameter. The iterative process may be sustained until convergence is attained Figure II.1.

II.3 The linearized augmented plane wave (LAPW) method

Depending on whether they rely on experimental results or fundamental data, the three primary approaches to calculating band structures are as follows:

- Calculations based on empirical methodologies necessitate experimental data.
- A semi-empirical approach is one that uses both experimental data and basic facts in its computations.
- Among the many first-principle approaches that have been developed in recent years by researchers, three distinct sets of approaches based on density functional theory (DFT) have been developed for solving the Schrödinger equation:

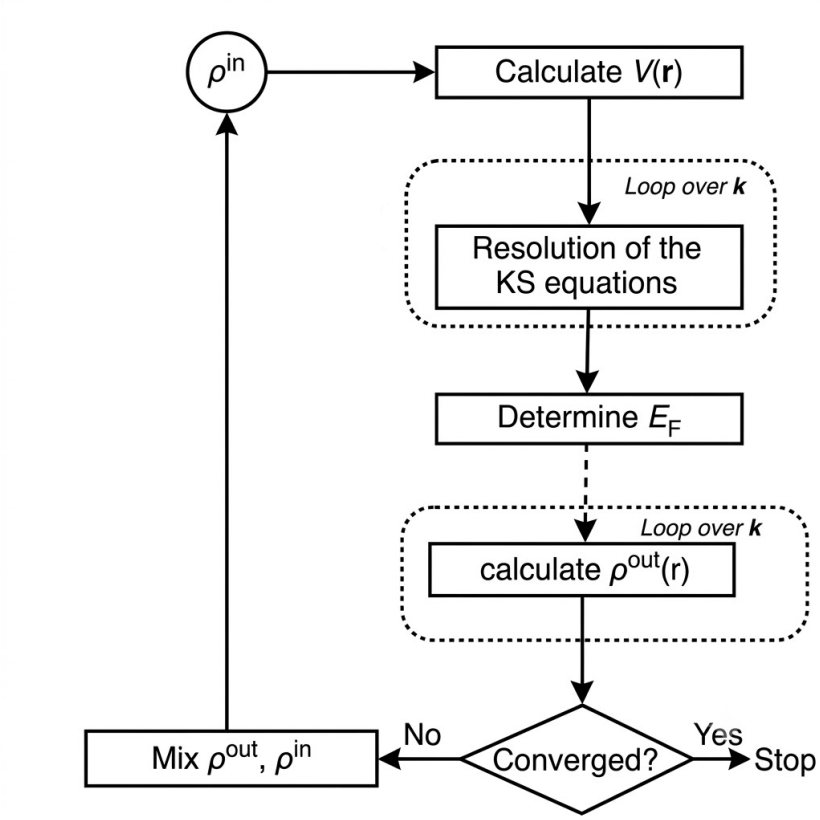


Figure II.1: Self-consistent cycle of (DFT).

- The "d" bands of transition metals can be analysed using methods based on a linear combination of atomic orbitals (LCAO) [25, 26].
- The "s-p" character conduction band of simple metals is better handled by methods acquired from orthogonalising plane waves (OPW) [27, 28].
- The green function method of Korringa, Kohn, and Rostoker (KKR) [30, 31] and augmented plane waves (APW) [29] are cellular approaches that can be used to a broader range of materials.

Linearised augmented plane waves (LAPW) and linearised "Muffin-Tin" orbitals (LMTO), two linearised methods created by Anderson [32], allow for time savings in computations that are several orders of magnitude greater.

II.3.1 Linearized augmented plane waves method (LAPW)

First, we need to recall the foundations of the APW method, since the LAPW method is an improvement of the APW method (Augmented plane waves), as described by Slater [29, 33, 34, 35].

II.3.1.1 APW method

In 1937, Slater presented augmented plane waves (APW) as fundamental functions to solve one electron equations, which relate to the Kohn-Sham equations today. His article exposes the APW approach [36].

There are two kinds of primitive cell areas shown in the APW diagram:

- Concentric Muffin-Tin spheres with radii surrounding each atomic location R_α
- A remaining interstitial region.

The potential and wave functions in the vicinity of the atomic nucleus have a "Muffin-Tin" shape, which exhibits symmetry within the MT sphere of radius R_α. Because the potential and wave functions between atoms are smooth, the crystal's wave functions develop in different ways depending on the area under consideration: radial solutions of the Schrödinger equation inside the MT sphere, and plane waves in the interstitial region (Figure II.2).

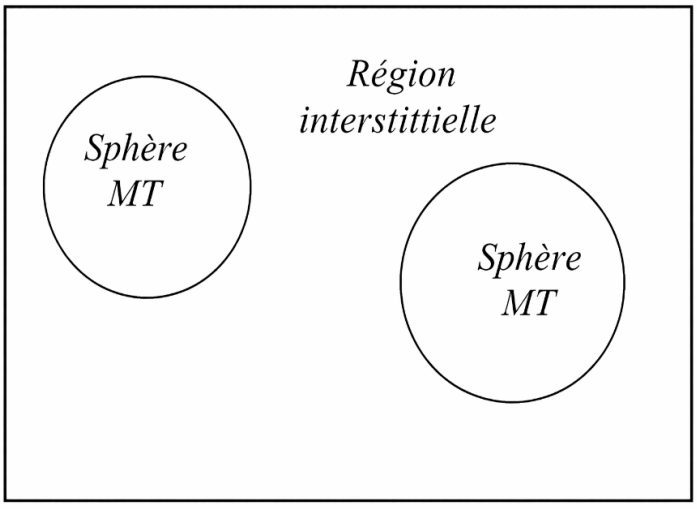


Figure II.2: MT potential.

Therefore, the form of the wave function is:

$$\phi(\mathbf{r}) = \begin{cases} \frac{1}{\Omega^{1/2}} \sum_G C_G e^{i(\mathbf{G}+\mathbf{K})\cdot\mathbf{r}}, & r > R_\alpha \\ \sum_{lm} A_{lm} U_l(r) Y_{lm}(\hat{r}), & r < R_\alpha \end{cases} \tag{II.39}$$

In which:

R_α is radius of MT sphere.

Ω the cell volume.

C_G and A_{lm} the coefficients of the development in spherical harmonics Y_{lm}.

The function $U_l(r)$ constitutes a regular solution to the radial component of the Schrödinger equation, expressed as follows:

$$\left[-\frac{d^2}{dr^2} + \frac{l(l+1)}{r^2} + V(r) - E_l \right] r U_l(r) = 0 \tag{II.40}$$

$V(r)$ denotes the Muffin-Tin potential as well as E_l signifies the linearisation energy. The radial functions $rU_l(r)$ are orthogonal to any legitimate state of the core. This orthogonality vanishes at the boundary of the sphere, as demonstrated by the subsequent Schrödinger equation:

$$(E_2 - E_1) r U_1 U_2 = U_2 \frac{d^2 r U_1}{dr^2} - U_1 \frac{d^2 r U_2}{dr^2} \tag{II.41}$$

U_1 and U_2 are radial solutions for energies E_1 and E_2. The overlap is being produced using equation Eq II.40 and integrating by parts. Slater elucidates his specific selection of functions by observing that plane waves constitute solutions to the Schrödinger equation under conditions of constant potential. Radial functions serve as solutions for a spherical potential when "E_l" is an eigenvalue. This approximation is highly effective for materials exhibiting a face-centered cubic structure, becoming progressively less suitable as material symmetry diminishes.

To maintain the continuity of the function $\varphi(r)$ on the surface of the sphere MT, the coefficients A_{lm} derived from the coefficients C_G of the plane waves present in the interstitial areas. Consequently, these coefficients are articulated by the subsequent

expression:

$$A_{lm} = \frac{4\pi i^l}{\Omega^{1/2} U_l(R_\alpha)} \sum_G C_G j_l(|\mathbf{K}+\mathbf{G}|R_\alpha) Y_{lm}^*(\mathbf{K}+\mathbf{G}) \tag{II.42}$$

The origin is established at the sphere's centre, and the coefficients A_{lm} are derived from the coefficients of the plane waves C_G. The energy parameters E_l are referred to as the variational coefficients of the APW approach. The functions designated as G thus align with the radial functions within the spheres, resulting in the acquisition of augmented plane waves (APW).

The APW functions are solutions to the Schrödinger equation within spherical domains, specifically for the energy E_l. Consequently, the energy E_l must correspond to that of the band indexed by G. This indicates that the energy bands (for a specific **k**-point) cannot be derived through straightforward diagonalisation, necessitating the treatment of the secular determinant as a function of energy.

The developed APW method encounters challenges associated with the function $U_l(R_\alpha)$ that exists in the denominator of equation Eq II.46. Indeed, contingent upon the parameter E_l, the value of $U_l(R_\alpha)$ may attain a value of zero at the MT sphere's surface, resulting in a divergence of the radial functions from the plane wave functions.

To address this issue, numerous improvements to the APW approach have been implemented, particularly those suggested by Korringa [37] and Andersen [38]. The modification entails expressing the wave function $\varphi(r)$ within the spheres as a linear combination of the radial functions $U_l(r)$ and their energy derivatives $\dot{U}_l(r)$, so resulting in the FP-LAPW approach.

II.3.1.2 Principle of the LAPW method

In the LAPW approach, the basis functions within the MT spheres are linear combinations of the radial functions $U_l(r)Y_{lm}(r)$ and their energy derivatives $\dot{U}_l(r)Y_{lm}(r)$. The U_l functions are delineated as per the APW approach, Equation II.41, and the function $U_l(r)Y_{lm}(r)$ must adhere to the subsequent condition:

$$\left[-\frac{d^2}{dr^2} + \frac{l(l+1)}{r^2} + V(r) - E_l\right] r\dot{U}_l(r) \tag{II.43}$$

In the non-relativistic scenario, the radial functions $U_l(r)$ and $\dot{U}_l(r)$ guarantee continuity with the external plane waves on the MT sphere's surface. The FP-LAPW approach's basis functions (LAPW) are the enhanced wave functions:

$$\varphi(r) = \begin{cases} \frac{1}{\Omega^{1/2}} \sum_G C_G e^{i(\mathbf{G}+\mathbf{K})\cdot\mathbf{r}}, & r > R_\alpha \\ \sum_{lm} \left[A_{lm} U_l(r) + B_{lm} \dot{U}_l(r)\right] Y_{lm}(r), & r < R_\alpha \end{cases} \tag{II.44}$$

Hence, the derivative $\dot{U}_l(r)$ and the energy E_l can be used to build the function U_l:

$$U_l(E, r) = U_l(E_l, r) + (E - E_l)\dot{U}_l(E_l, r) + O\Big((E - E_l)^2\Big) \tag{II.45}$$

Where: $((E - E_l)^2)$ represents the energy squared error.

All the valence bands in a vast energy range can be obtained with a single E_l thanks to the LAPW functions, which form a solid basis despite this order of error. In cases when this is not feasible, a much simpler alternative to the APW method is to split the energy window in half.

In most cases, the derivative $\dot{U}_l(r)$ will not be zero if U_l is zero on the sphere's surface. Consequently, the LAPW approach will not encounter the issue of continuity at the MT sphere's surface.

Applying N radial functions and their $(N-1)$ derivatives, Takeda and Kubler [39] presented a variant of the LAPW approach. A unique parameter E_{li} is used for each radial function to prevent linearization-related errors. For $N = 2$ and E_{l1} close to E_{l2}, the usual LAPW approach is discovered; however, for $N > 2$, it is not.

Mistakes can be lessened. Regrettably, the computing time required to guarantee convergence using high-order derivatives is significantly more than that of the typical FP-LAPW method. To make it work with less energy required for plane waves, Singh [40] adjusted the method by including local orbitals in the basis.

II.3.1.3 The roles of linearization energies E_l

Both U_l and $\dot{U}_l$ are perpendicular to any core state that is firmly contained within the MT sphere. Unfortunately, this requirement is met only when no other core states have

the same l, which means that semi-core states can be mistaken for valence states. The APW approach does not handle this issue, while the FP-LAPW method necessitates a careful selection of E_l due to the non-orthogonality of certain core states. We need to change E_l in order to do the calculation in this scenario.

In these situations, a local orbital expansion is the best option. Nevertheless, not all applications provide this option; in such a situation, we need to select the maximum conceivable sphere radius.

Lastly, it needs to be mentioned that each E_l needs to be described separately. There are distinct orbitals for the energy bands. It is recommended to choose E_l as near to the band energy as possible for an accurate electronic structure computation, provided that the band has a similar l.

II.3.2 Development in local orbitals

Accurate band energies close to the linearisation energies E_l are sought after by the LAPW approach [41]. Selecting these energies close to the band centres is adequate for the majority of materials. For the vast majority of materials, picking these energies close to the band centres becomes plenty. For some materials, such as those with $4f$ orbitals [42, 43] or transition metals [44], it is not feasible to determine all of the energy bands using only one value of E_l. This is the major issue with the semi-core state, which lies between the core and valence states. Either using several energy windows or a development in local orbitals allows us to fix the problem.

II.3.2.1 The LAPW+LO method

The advancement of the LAPW approach in local orbitals involves altering the basis orbitals to eliminate the necessity for multiple windows, by incorporating a third category of basis functions. The principle is to address all bands within a singular energy window. Singh [45] presented these orbitals, referred to as "LO," as a linear combination of two radial functions associated with distinct energies, along with the

derivative of one of these functions concerning energy:

$$\phi(r) = \begin{cases} 0, & r > R_\alpha \\ \left[A_{lm}U_l(r, E_l) + B_{lm}\dot{U}_l(r, E_l) + C_{lm}U_l(r, E_l)\right] Y_{lm}(r), & r < R_\alpha \end{cases} \tag{II.46}$$

which the coefficients C_{lm} possess the same characteristics as the previously stated coefficients A_{lm} and B_{lm}.

An atomic orbital is specified for particular values of l and m, as well as for a specific atom within the unit cell, encompassing all atoms rather than solely the inequivalent ones.

Local orbitals can moreover be employed outside the analysis of semi-core states to enhance the basis for conduction bands.

The enhancement of the LAPW approach underpins the efficacy of the linearisation technique derived from it, since it facilitates the use of this foundational method to a far broader range of chemicals.

II.3.2.2 The APW+lo method

The issue faced with the APW technique was the energy dependence of the basis function set. The LAPW+LO method can reduce this dependence, but at the expense of an increased basis size, resulting in a notable drawback for both the APW and LAPW+LO methods.

Sjöstedt, Nordström, and Singh [46] have enhanced the approach by developing a framework that integrates the benefits of the APW method with those of the LAPW+LO method. This technique, termed "APW+lo," utilises an energy-independent base, akin to the LAPW+LO approach, and necessitates a plane wave cutoff energy somewhat exceeding that of the APW method. It involves employing a standard APW basis while incorporating $U_l(r)$ for a specified energy E_l to maintain the benefits afforded by the linearisation of the eigenvalue problem. Nevertheless, a fixed energy basis fails to adequately characterise the eigenfunctions; thus, local orbitals are used to provide variational flexibility concerning the radial basis functions.

An "APW+lo" denotes the association of two distinct types of wave functions that

constitute a basis:

- APW plane waves with a fixed energies E_l:

$$\phi(r) = \begin{cases} \frac{1}{\Omega^{1/2}} \sum_G C_G e^{i(G+K)r}, & r > R_\alpha \\ \sum_{lm} A_{lm} U_l(r) Y_{lm}(r), & r < R_\alpha \end{cases} \tag{II.47}$$

- Local orbitals different from those of the LAPW+LO method defined by:

$$\phi(r) = \begin{cases} 0, & r > R_\alpha \\ \left[A_{lm} U_l(r, E_l) + B_{lm} \dot{U}_l(r, E_l) \right] Y_{lm}(r), & r < R_\alpha \end{cases} \tag{II.48}$$

A hybrid LAPW and APW+lo basis can be employed for several atoms and distinct values of the quantum number l in a calculation. Typically, orbitals that converge more gradually with the plane wave number, such as the $3d$ states of transition metals, or atoms with a diminutive sphere size, are characterised using the APW+lo basis, while all others utilise the LAPW basis.

II.3.3 The concept of the FP-LAPW method

The (FP-LAPW) approach [47, 48] does not employ any approximations regarding the configuration of the potential or the charge density. Rather, they are extended into lattice harmonics within each atomic sphere and into Fourier series in the interstitial areas. This is the etymology of the term "Full-Potential".

This procedure thus guarantees the continuation of the potential on the surface of the MT sphere and extends it into the subsequent form:

$$V(r) = \begin{cases} \sum_K V_K e^{iKr} & r > R_\alpha \\ \sum_{lm} V_{lm}(r) Y_{lm}(r) & r < R_\alpha \end{cases} \tag{II.49}$$

Likewise, the charge density is expressed as follows:

$$\rho(r) = \begin{cases} \sum_{K} \rho_K e^{iKr} & r > R_\alpha \\ \sum_{lm} \rho_{lm}(r) Y_{lm}(r) & r < R_\alpha \end{cases} \tag{II.50}$$

II.4 The WIEN2k code



Peter Blaha 5 July 1955

Former members of the Institute of Materials Chemistry at Austria's Technical University of Vienna, Peter Blaha and Karlheinz Schwartz, were responsible for developing Wien2k. The initial distribution of this code occurred in 1990. Wien97, WIEN2K, and WIEN93 were the subsequent versions. Blaha, Schwarz, and colleagues constructed the WIEN code, which includes the FP-LAPW algorithm [49, 50]. The electric field gradient, minerals, transition metal surfaces, high-temperature superconducting systems, non-ferromagnetic oxides, and molecules have all been effectively addressed by this code.

The WIEN code has been upgraded to produce WIEN2k [51, 52] from earlier versions, such as WIEN97 [53] (Figure II.3). The C-SHELL SCRIPT links the different independent programs that comprise the WIEN code. They can be executed using

either a sequential or a parallel architecture. The calculation procedure goes through three steps.

1. **Initialization:**

   It involves the construction of the spatial configuration (geometry), symmetry operations, initial densities, and the requisite number of special points for integration within the irreducible Brillouin zone, among other factors. All these actions are executed utilising a sequence of auxiliary programs that produce:

   ***NN*:** the distances between nearest neighbours and equivalent positions as well as the calculated atomic radius of the sphere.

   ***LSTART*:** It is used to generate atomic densities and used to determine how the different atomic orbitals are treated.

   ***SYMMETRY*:** Generate the symmetry operations of the space group also to determine the point group of the individual atomic sites.

   KGEN : the number of points k in the Brillouin zone.

   ***DSART*:** It generates a starting density for the self-consistent cycle (the SCF cycle) by superimposing the atomic densities generated in *LSTART*.

2. **Self-consistent calculation:**

   In this phase, the energies and electron density of the ground state are computed based on a convergence criterion (energy, charge density, force). The employed subroutines are:

   ***LAPW0*:** it generates the Poisson potential for the density calculation.

   ***LAPW1*:** it allows calculating valence bands, eigenvalues and eigenvectors.

   ***LAPW2*:** It calculates the valence densities for the eigenvectors.

   ***LCORE*:** It calculates core states and densities.

   ***MIXER*:** it performs the mixing of the input and output densities (start, valence and core).

3. **Determination of properties:**

   once the self-consistent calculation is completed, the properties of the ground state (charge density, band structure, optical properties, etc.) are then determined.

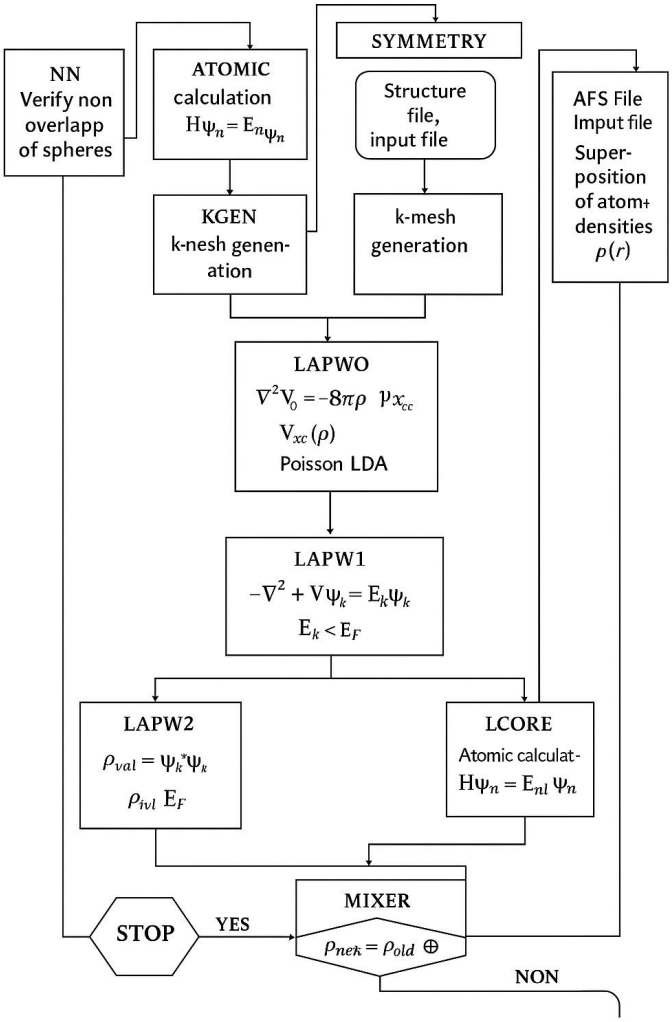


Figure II.3: The WIEN code flowchart.

II.5 Conclusion

In this chapter, we discussed ab-initio methods, which are recognized as the most accurate and straightforward, although they require considerable time to implement. These methods are increasingly used in materials science thanks to the constant improvement in computing power and approximate theoretical developments. In particular, density

functional theory is a powerful theory that allows the study of new materials and the prediction of new properties.

The FP-LAPW method is commonly used as a prediction tool for electronic, optical, and magnetic properties, and serves as a benchmark for many approximate methods. However, it is essential to emphasize the approximations and limitations inherent in the use of these methods.

References

[1] R. A. De Groot, F. M. Mueller, P. G. van Engen, and K. H. J. Buschow, "New class of materials: Half-metallic ferromagnets," *Phys. Rev. Lett.*, vol. 50, no. 25, pp. 2024–2027, 1983. doi: 10.1103/PhysRevLett.50.2024.

[2] M. Lv, C. Jiang, and G. Zhang, "A simple setup for thermoelectric power factor of thermoelectric coatings," *Coatings*, vol. 15, no. 6, p. 679, 2025. doi: 10.3390/coatings15060679.

[3] T. M. Tritt, "Thermoelectric materials: Principles, structure, properties, and applications," in *Encyclopedia of Materials: Science and Technology*, Elsevier, 2002, pp. 1–11. doi: 10.1016/B0-08-043152-6/01822-2.

[4] K. Uchida, M. Murata, A. Miura, and R. Iguchi, "Observation of the magneto-Thomson effect," *Phys. Rev. Lett.*, vol. 125, no. 10, p. 106601, 2020. doi: 10.1103/PhysRevLett.125.106601.

[5] E. Schrödinger, "Der Energieimpulssatz der Materiewellen," *Ann. Phys.*, vol. 387, no. 2, pp. 265–272, 1927. doi: 10.1002/andp.19273870211.

[6] M. Born and W. Heisenberg, "Zur Quantentheorie der Molekeln," in *Original Scientific Papers*, Springer, 1985, pp. 216–246. doi: 10.1007/978-3-642-61659-4_16.

[7] D. R. Hartree, "The wave mechanics of an atom with a non-Coulomb central field," *Math. Proc. Camb. Philos. Soc.*, vol. 24, no. 1, pp. 89–110, 1928. doi: 10.1017/S0305004100011919.

[8] V. Fock, "Self-consistent field with exchange for sodium," *Z. Phys.*, vol. 62, no. 11–12, pp. 795–805, 1930. doi: 10.1007/BF01330439.

[9] P. Lykos and G. W. Pratt, "Discussion on the Hartree-Fock approximation," *Rev. Mod. Phys.*, vol. 35, no. 3, pp. 496–501, 1963. doi: 10.1103/RevModPhys.35.496.

[10] V. Fock, "Näherungsmethode zur Lösung des quantenmechanischen Mehrkörperproblems," *Z. Phys.*, vol. 61, no. 1–2, pp. 126–148, 1930. doi: 10.1007/BF01340294.

[11] A. W. Leissa, "The historical bases of the Rayleigh and Ritz methods," *J. Sound Vib.*, vol. 287, no. 4–5, pp. 961–978, 2005. doi: 10.1016/j.jsv.2004.12.021.

[12] J. C. Slater, "A simplification of the Hartree-Fock method," *Phys. Rev.*, vol. 81, no. 3, pp. 385–390, 1951. doi: 10.1103/PhysRev.81.385.

[13] L. H. Thomas, "The calculation of atomic fields," *Math. Proc. Camb. Philos. Soc.*, vol. 23, no. 5, pp. 542–548, 1927. doi: 10.1017/S0305004100011683.

[14] E. Fermi, "Angular distribution of the pions produced in high energy nuclear collisions," *Phys. Rev.*, vol. 81, no. 5, pp. 683–687, 1951. doi: 10.1103/PhysRev.81.683.

[15] P. Hohenberg and W. Kohn, "Inhomogeneous electron gas," *Phys. Rev.*, vol. 136, no. 3B, pp. B864–B871, 1964. doi: 10.1103/PhysRev.136.B864.

[16] W. Kohn and L. J. Sham, "Self-consistent equations including exchange and correlation effects," *Phys. Rev.*, vol. 140, no. 4A, pp. A1133–A1138, 1965. doi: 10.1103/PhysRev.140.A1133.

[17] S. Saito, "Interaction between clusters and Pauli principle," *Prog. Theor. Phys.*, vol. 41, no. 3, pp. 705–722, 1969. doi: 10.1143/PTP.41.705.

[18] D. M. Ceperley and B. J. Alder, "Ground state of solid hydrogen at high pressures," *Phys. Rev. B*, vol. 36, no. 4, pp. 2092–2106, 1987. doi: 10.1103/PhysRevB.36.2092.

[19] J. P. Perdew and A. Zunger, "Self-interaction correction to density-functional approximations," *Phys. Rev. B*, vol. 23, no. 10, pp. 5048–5079, 1981. doi: 10.1103/PhysRevB.23.5048.

[20] L. Hedin and B. I. Lundqvist, "Explicit local exchange-correlation potentials," *J. Phys. C*, vol. 4, no. 14, pp. 2064–2083, 1971. doi: 10.1088/0022-3719/4/14/022.

[21] J. P. Perdew and Y. Wang, "Accurate and simple analytic representation of the electron-gas correlation energy," *Phys. Rev. B*, vol. 45, no. 23, pp. 13244–13249, 1992. doi: 10.1103/PhysRevB.45.13244.

[22] J. P. Perdew *et al.*, "Atoms, molecules, solids, and surfaces: Applications of the generalized gradient approximation for exchange and correlation," *Phys. Rev. B*, vol. 46, no. 11, pp. 6671–6687, 1992. doi: 10.1103/PhysRevB.46.6671.

[23] J. P. Perdew, K. Burke, and M. Ernzerhof, "Generalized gradient approximation made simple," *Phys. Rev. Lett.*, vol. 77, no. 18, pp. 3865–3868, 1996. doi: 10.1103/PhysRevLett.77.3865.

[24] J. P. Perdew and W. Yue, "Accurate and simple density functional for the electronic exchange energy: Generalized gradient approximation," *Phys. Rev. B*, vol. 33, no. 12, pp. 8800–8802, 1986. doi: 10.1103/PhysRevB.33.8800.

[25] S. Froyen and W. A. Harrison, "Elementary prediction of linear combination of atomic orbitals matrix elements," *Phys. Rev. B*, vol. 20, no. 6, pp. 2420–2422, 1979. doi: 10.1103/PhysRevB.20.2420.

[26] W. A. Harrison and S. Froyen, "Universal linear-combination-of-atomic-orbitals parameters for d-state solids," *Phys. Rev. B*, vol. 21, no. 8, pp. 3214–3221, 1980. doi: 10.1103/PhysRevB.21.3214.

[27] T. O. Woodruff, "The orthogonalized plane-wave method," in *Solid State Physics*, vol. 4, Elsevier, 1957, pp. 367–411. doi: 10.1016/S0081-1947(08)60156-3.

[28] C. Herring, "A new method for calculating wave functions in crystals," *Phys. Rev.*, vol. 57, no. 12, pp. 1169–1177, 1940. doi: 10.1103/PhysRev.57.1169.

[29] J. C. Slater, "Wave functions in a periodic potential," *Phys. Rev.*, vol. 51, no. 10, pp. 846–851, 1937. doi: 10.1103/PhysRev.51.846.

[30] J. Korringa, "On the calculation of the energy of a Bloch wave in a metal," *Physica*, vol. 13, no. 6–7, pp. 392–400, 1947. doi: 10.1016/0031-8914(47)90013-X.

[31] W. Kohn and N. Rostoker, "Solution of the Schrödinger equation in periodic lattices with an application to metallic lithium," *Phys. Rev.*, vol. 94, no. 5, pp. 1111–1120, 1954. doi: 10.1103/PhysRev.94.1111.

[32] O. K. Andersen, "Linear methods in band theory," *Phys. Rev. B*, vol. 12, no. 8, pp. 3060–3083, 1975. doi: 10.1103/PhysRevB.12.3060.

[33] J. Korringa, "On the calculation of the energy of a Bloch wave in a metal," *Physica*, vol. 13, no. 6–7, pp. 392–400, 1947. doi: 10.1016/0031-8914(47)90013-X.

[34] F. S. Ham and B. Segall, "Energy bands in periodic lattices—Green's function method," *Phys. Rev.*, vol. 124, no. 6, pp. 1786–1796, 1961. doi: 10.1103/PhysRev.124.1786.

[35] J. C. Slater, "Energy band calculations by the augmented plane wave method," in *Advances in Quantum Chemistry*, vol. 1, Elsevier, 1964, pp. 35–58. doi: 10.1016/S0065-3276(08)60374-3.

[36] J. C. Slater, "Wave functions in a periodic potential," *Phys. Rev.*, vol. 51, no. 10, pp. 846–851, 1937. doi: 10.1103/PhysRev.51.846.

[37] D. D. Koelling and G. O. Arbman, "Use of energy derivative of the radial solution in an augmented plane wave method: Application to copper," *J. Phys. F: Met. Phys.*, vol. 5, no. 11, pp. 2041–2054, 1975. doi: 10.1088/0305-4608/5/11/016.

[38] O. K. Andersen, "Linear methods in band theory," *Phys. Rev. B*, vol. 12, no. 8, pp. 3060–3083, 1975. doi: 10.1103/PhysRevB.12.3060.

[39] T. Takeda and J. Kübler, "Linear augmented plane wave method for self-consistent calculations," *J. Phys. F: Met. Phys.*, vol. 9, no. 4, pp. 661–672, 1979. doi: 10.1088/0305-4608/9/4/013.

[40] D. Singh, "Ground-state properties of lanthanum: Treatment of extended-core states," *Phys. Rev. B*, vol. 43, no. 8, pp. 6388–6392, 1991. doi: 10.1103/PhysRevB.43.6388.

[41] O. K. Andersen, "Linear methods in band theory," *Phys. Rev. B*, vol. 12, no. 8, pp. 3060–3083, 1975. doi: 10.1103/PhysRevB.12.3060.

[42] D. J. Singh, "Adequacy of the local-spin-density approximation for Gd," *Phys. Rev. B*, vol. 44, no. 14, pp. 7451–7454, 1991. doi: 10.1103/PhysRevB.44.7451.

[43] S. Goedecker and K. Maschke, "Alternative approach to separable first-principles pseudopotentials," *Phys. Rev. B*, vol. 42, no. 14, pp. 8858–8863, 1990. doi: 10.1103/PhysRevB.42.8858.

[44] D. J. Singh, K. Schwarz, and P. Blaha, "Electric-field gradients in $YBa_2Cu_3O_7$: Discrepancy between experimental and local-density-approximation charge distributions," *Phys. Rev. B*, vol. 46, no. 9, pp. 5849–5852, 1992. doi: 10.1103/PhysRevB.46.5849.

[45] D. Singh, "Ground-state properties of lanthanum: Treatment of extended-core states," *Phys. Rev. B*, vol. 43, no. 8, pp. 6388–6392, 1991. doi: 10.1103/PhysRevB.43.6388.

[46] E. Sjöstedt, L. Nordström, and D. J. Singh, "An alternative way of linearizing the augmented plane-wave method," *Solid State Commun.*, vol. 114, no. 1, pp. 15–20, 2000. doi: 10.1016/S0038-1098(99)00577-3.

[47] G. K. H. Madsen, P. Blaha, K. Schwarz, E. Sjöstedt, and L. Nordström, "Efficient linearization of the augmented plane-wave method," *Phys. Rev. B*, vol. 64, no. 19, p. 195134, 2001. doi: 10.1103/PhysRevB.64.195134.

[48] P. Blaha, K. Schwarz, P. Dufek, G. Vielsack, and W. Weber, "The breathing mode of $BaBiO_3$: Electric field gradient and total energy calculations," *Z. Naturforsch. A*, vol. 49, no. 1–2, pp. 129–132, 1994. doi: 10.1515/zna-1994-1-220.

[49] K. Schwarz, C. Ambrosch-Draxl, and P. Blaha, "Charge distribution and electric-field gradients in $YBa_2Cu_3O_{7-x}$," *Phys. Rev. B*, vol. 42, no. 4, pp. 2051–2061, 1990. doi: 10.1103/PhysRevB.42.2051.

[50] B. Winkler, P. Blaha, and K. Schwarz, "Ab initio calculation of electric-field-gradient tensors of forsterite," *Am. Mineral.*, vol. 81, no. 5–6, pp. 545–549, 1996. doi: 10.2138/am-1996-5-602.

[51] X.-G. Wang *et al.*, "The hematite (α-Fe_2O_3) (0001) surface: Evidence for domains of distinct chemistry," *Phys. Rev. Lett.*, vol. 81, no. 5, pp. 1038–1041, 1998. doi: 10.1103/PhysRevLett.81.1038.

[52] P. Blaha, K. Schwarz, P. Dufek, and J. Luitz, *WIEN97*, Vienna University of Technology, 1997.

[53] P. Blaha, K. Schwarz, G. K. Madsen, D. Kvasnicka, and J. Luitz, "WIEN2k: An augmented plane wave + local orbitals program for calculating crystal properties," Vienna University of Technology, 2001.

CHAPTER III

RESULTS AND DISCUSSION

III.1 Introduction

This chapter is devoted to a comprehensive investigation of the structural, electronic, magnetic, elastic, and thermodynamic properties of several families of full-Heusler alloys based on rare-earth and transition-metal elements. The present study focuses primarily on the Pr_2YZ systems, where Y = Rh or Co and Z = Al, Ga, or In. In addition, the effect of chromium substitution on the quaternary compounds CrPrCoZ (Z = Al, Ga, In) is systematically examined. Furthermore, the scope of this work is extended to transition-metal-based full-Heusler alloys Ir_2ScZ (Z = Ga, Ge) in order to compare their physical behavior with that of Pr-based systems.

All calculations are carried out within the framework of density functional theory (DFT) using the generalized gradient approximation (GGA) in the Perdew–Burke–Ernzerhof (PBE) formalism. The full-potential linearized augmented plane wave (FP-LAPW) method, as implemented in the WIEN2K package, is employed for all first-principles calculations.

The equilibrium structural parameters are obtained by minimizing the total energy as a function of the unit-cell volume. Both crystallographic prototypes, namely the conventional Cu_2MnAl-type ($L2_1$) and the inverse Hg_2CuTi-type structures, are considered. The most stable crystallographic phase and the ground-state magnetic configuration (non-magnetic, ferromagnetic, or antiferromagnetic) are determined on the basis of total-energy and formation-energy calculations.

The elastic properties are investigated by calculating the single-crystal elastic constants C_{ij} using the IRELAST package[1]. The mechanical stability of the cubic systems is verified, and the ductile or brittle nature of the investigated compounds is analyzed using Pugh's ratio B/G and Poisson's ratio ν. The macroscopic elastic moduli, including the bulk modulus B, shear modulus G, and Young's modulus E, are obtained using the Voigt–Reuss–Hill (VRH) averaging scheme. The elastic anisotropy is discussed through the anisotropy factor A.

The electronic and magnetic properties are analyzed by means of spin-polarized band structure calculations and total as well as partial densities of states (DOS). Particular attention is paid to the half-metallic character, the minority-spin band gap, and the

spin polarization at the Fermi level E_F. The Slater–Pauling rule, which relates the total magnetic moment M_{tot} to the total number of valence electrons Z_{tot}, is also examined . Moreover, the influence of chemical substitution at the X site (Pr $\longrightarrow$ Cr) on the electronic structure and magnetic moments is discussed for the Pr_2CoZ and CrPrCoZ series.

The thermodynamic properties are investigated within the quasi-harmonic Debye model as implemented in the GIBBS2 code [2]. The temperature and pressure dependences of thermodynamic quantities such as the heat capacity C_V, entropy S, and Debye temperature Θ_D are analyzed. These results provide insight into the lattice dynamics and thermal stability of the studied compounds.

III.2 Calculation Details

In this chapter, a systematic study of the physical properties of rare-earth-based full-Heusler alloys Pr_2YZ (Y = Rh, Co and Z = Al, Ga, In) is presented. Subsequently, the effect of Cr doping on the structural, elastic, thermodynamic, electronic, and magnetic properties of Pr_2CoZ (Z = Al, Ga, In) is discussed in detail.

We also investigated several physical properties of other transition-metal-based full-Heusler alloys Ir_2ScZ (Z = Ga, Ge), with the primary objective of examining their semi-metallic behavior and magnetic moments. The calculations were performed using the full-potential linearized augmented plane wave (FP-LAPW) method within the framework of density functional theory (DFT), as implemented in the WIEN2K code [3]. The exchange–correlation effects were treated using the generalized gradient approximation in the Perdew–Burke–Ernzerhof (GGA-PBE) scheme [4] for all investigated properties.

Within the FP-LAPW formalism, the unit cell is divided into non-overlapping muffin-tin (MT) spheres and an interstitial region. In all calculations, the muffin-tin radii (R_{MT}) were chosen to be as large as possible while ensuring that the MT spheres do not overlap. For all studied alloys, the R_{MT} values were set automatically by the WIEN2K code with a reduction of 5% [3].

To ensure the convergence of the total energy per unit cell, a Monkhorst–Pack grid of

$10 \times 10 \times 10$ **k**-points was used for Brillouin-zone integration. The radial expansion of the potential and charge density was performed up to $l_{\max} = 8$. Furthermore, the basis functions were expanded up to $R_{\mathrm{MT}} \times K_{\max} = 7$, where $K_{\max}$ represents the maximum modulus of the reciprocal lattice vector. The maximum value of $K_{\max}$ used for the expansion of the potential and charge density in the Brillouin zone was set to 12 (u.a.$^{-1}$). The self-consistent field (SCF) cycle was considered converged when the total energy difference between successive iterations was less than 10^{-6} eV.

III.3 Full-Heusler Alloys

III.3.1 Full-Heusler rare-earth-based alloys

III.3.1.1 Full-Heusler Pr_2RhZ (Z = Al, Ga, In)

a. Structural properties

The investigated compounds are rare-earth-based full-Heusler alloys containing three different atomic species per primitive cell: one transition metal (Rh), one post-transition metal (Al, Ga, or In), and two rare-earth atoms (Pr). These compounds follow the general stoichiometric formula X_2YZ. The studied alloys crystallize in two possible cubic structures: the conventional Cu_2MnAl-type ($L2_1$) structure and the inverse Hg_2CuTi-type structure, both based on face-centered cubic (fcc) lattices (see Fig. III.1).
Both structures consist of four interpenetrating fcc sublattices with four inequivalent Wyckoff positions: $4a$ $(0, 0, 0)$, $4b$ $(0.25, 0.25, 0.25)$, $4c$ $(0.5, 0.5, 0.5)$, and $4d$ $(0.75, 0.75, 0.75)$.

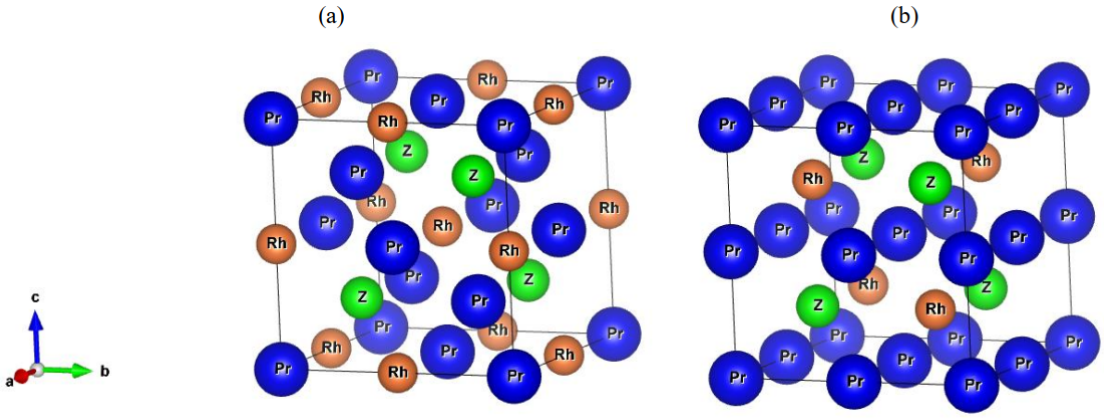


Figure III.1: Crystallographic structure of full-Heuler alloy Pr_2RhZ (Z = Al, Ga and In) in which (a) Hg_2CuTi type and (b) Cu_2MnAl type (by VESTA [3]).

In the Cu_2MnAl type structure, referred to as $L2_1$, the atomic arrangement inside the four sites of the unit cell adheres to the sequence X–Y–X–Z. Conversely, in the Hg_2CuTi type structure, designated as the XA structure, the sequence of atoms occupying the four sites of the unit cell is X–X–Y–Z [6].

In Figure III.2, we show the total energy versus the volume graphs of our alloys for both Hg_2CuTi-type and Cu_2MnAl-type in both non-magnetic and ferromagnetic phases, using the Birch-Murnaghan equation as represented in [7]:

$$E(V) = E_0 + \frac{B}{B'(B'-1)}\left[V\left(\frac{V_0}{V}\right)^{B'} - V_0\right] + \frac{B}{B'}(V - V_0) \qquad \text{(III.1)}$$

This equation incorporates the variables E for energy, V for volume, B for the equilibrium bulk modulus, V_0 for the volume of the experimental unit cell, and B' for the pressure derivative of the bulk modulus at the equilibrium volume.

The obtained results resumed in the Table III.1.

Table III.1: Optimized lattice constant a_0 (Å), Bulk modulus B (GPa), the pressure derivative B', the total energy $E_{\min}$ (Ry), and the Formation energy ΔH (Ry) for Full Heusler compounds Pr_2RhZ (Z = Al, Ga, In).

Alloy	Phases	a_0 (Å)	B (GPa)	B'	$E_{\min}$ (Ry)	ΔH (Ry)
Pr_2RhAl	Cu_2MnAl (NM)	7.0545	65.9072	4.6375	-47027.28187	-1.236609
	Cu_2MnAl (FM)	7.1736	65.5744	4.3500	-47027.35622	-1.310959
	Hg_2CuTi (NM)	6.7733	87.5915	5.1169	-47027.36992	-1.324659
	Hg_2CuTi (FM)	6.8460	82.1681	5.9021	-47027.42028	-1.375019
Pr_2RhGa	Cu_2MnAl (NM)	7.0201	75.3812	4.7326	-50429.91749	-1.200406
	Cu_2MnAl (FM)	7.1492	68.5380	4.5062	-50429.99060	-1.273516
	Hg_2CuTi (NM)	6.7517	97.7184	6.0264	-50429.93873	-1.221646
	Hg_2CuTi (FM)	6.8264	89.5538	4.0515	-50430.01555	-1.298466
Pr_2RhIn	Cu_2MnAl (NM)	7.2497	65.0587	4.2979	-58308.20951	-1.093645
	Cu_2MnAl (FM)	7.3721	63.3522	3.9451	-58308.29583	-1.179965
	Hg_2CuTi (NM)	6.9663	86.7731	4.4292	-58308.24569	-1.129825
	Hg_2CuTi (FM)	7.0375	75.5786	4.7752	-58308.33122	-1.215355

As shown in Figure III.2, the Hg_2CuTi configuration in the ferromagnetic state exhibits lowest energy stability compared to the alternative states of the Cu_2MnAl structure. These results are in good agreement with previous investigations, which have indicated that the Hg_2CuTi structure is more likely to develop when the Y element has a higher electronegativity than the X element [8].

We computed the formation energy to establish the viability of this chemical and its potential for experimental synthesis, using the following relation [9]:

$$\Delta H = E_f^{Pr_2RhZ} = E_{tot}^{Pr_2RhZ} - E_{Rh}^{bulk} - E_{Z}^{bulk} - 2E_{Pr}^{bulk} \quad \text{(III.2)}$$

Where $E_f^{Pr_2CoZ}$ is the equilibrium energy of these compounds, in which $E_{tot}^{Pr_2CoZ}$ is the total energy of compounds and E_{Pr}^{bulk}, E_{Rh}^{bulk} and E_{Z}^{bulk} are the chemical potential of atoms in their stable bulk for Pr, Rh, and Z (Al, Ga, In).

The estimated formation energies of the compounds Pr_2RhZ (Z = Al, Ga, In) for the Hg_2CuTi-type structure are -1.375019, -1.298466 and -1.215355 Ry, respectively,

indicating the thermodynamic stability of these alloys [10].

Conversely, we can remark that the Hg_2CuTi-type structure is the most stable phase by comparing the formation energy values of the Hg_2CuTi-type and Cu_2MnAl-type structures (III.2).

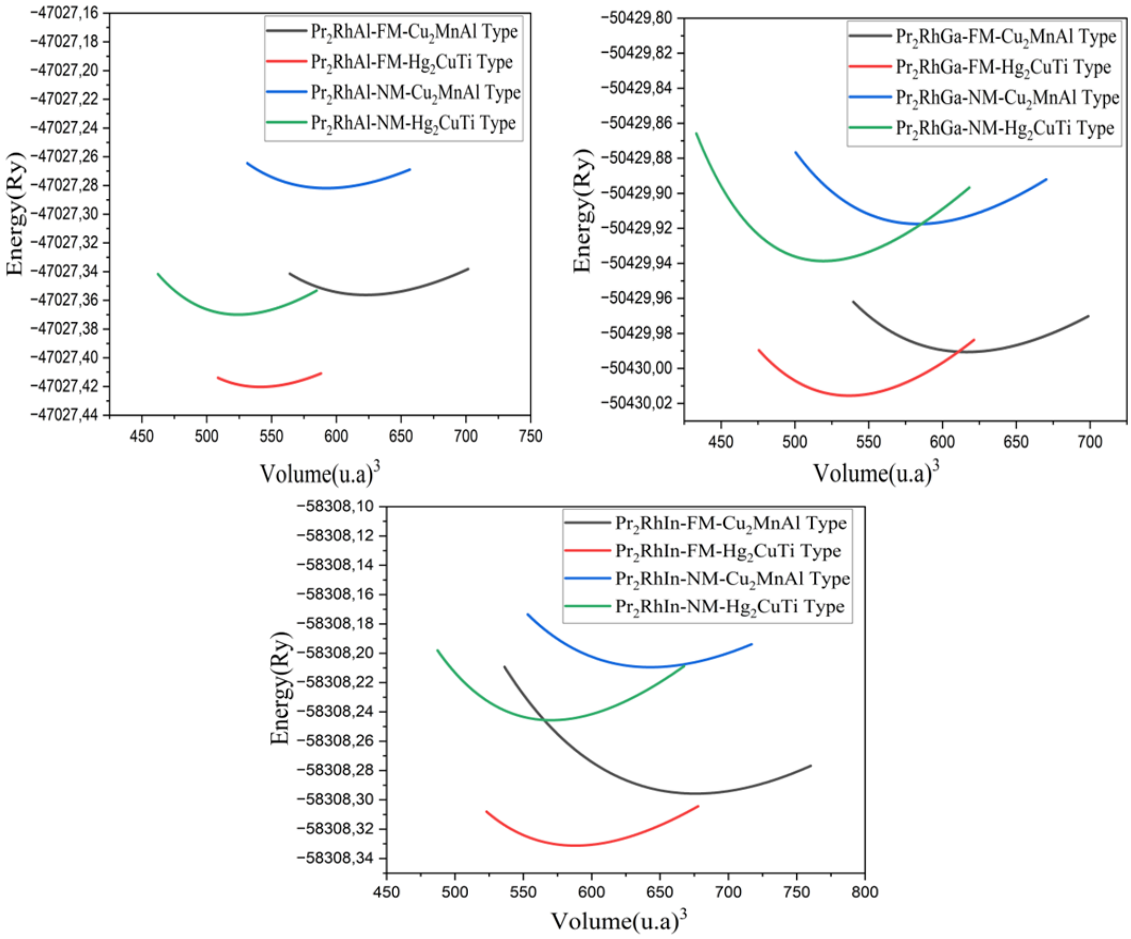


Figure III.2: Total energy versus unit cell volume for Pr_2RhZ (Z = Al, Ga and In).

b. Electronic Properties

The distribution of electrons in the valence and conduction bands, as well as the magnitude of the gap, fundamentally determines the solid's electronic characteristics, including its band structure, density of states, and Fermi surface. As mentioned above, we plotted the band structures and the total density of states of Pr_2RhZ (Z = Al, Ga, In) compounds for both spin directions (down and up). This investigation aims to elucidate the electronic structure of these compounds within the stable Hg_2CuTi struc-

ture in a ferromagnetic configuration at the equilibrium lattice parameter, employing the GGA-PBE approximation. The band structure and DOS are illustrated in Figure III.4 and Figure III.5, respectively, with the corresponding band gap values detailed in Table III.2.

From Figure III.4 (a, c and e), in which we plotted the majority spin direction (up) of our compounds Pr_2RhZ (Z = Al, Ga and In) respectively, we remark an overlap between conduction and valence band indicating the metallic behaviour of our alloys in this direction.

Furthermore, the minority spin direction of our alloys is plotted in Figure III.4 (b, d, and f), where we observe an indirect band gap; an energy gap emerges between the higher valence band at the Γ and X points and the lower conduction band at the L point. Consequently, these compounds display the traits of indirect band gap semiconductors, possessing energy band gaps of 0.235, 0.345, and 0.34 eV for Pr_2RhAl, Pr_2RhGa, and Pr_2RhIn, respectively. Consequently, we conclude that all compounds exhibit half-metallic behaviour.

The formation of the half-metallic gap in these compounds originates from the strong hybridization between the d states of Rh and the f/d states of Pr within the $L2_1$ crystal symmetry. This hybridization splits the electronic states into bonding and anti-bonding bands. Owing to the exchange interaction, the spin-up and spin-down bands experience different energy shifts: the majority-spin channel remains metallic, whereas the minority-spin channel exhibits a gap at the Fermi level. The size and position of this gap are controlled by the degree of d–d hybridization and the crystal-field splitting of the Rh atoms, which together determine the spin polarisation at the Fermi level. Such a mechanism of gap formation has been reported for several half-metallic Heusler systems [11], and our results confirm that the same physical picture applies to Pr_2RhAl, Pr_2RhGa, and Pr_2RhIn.

Faleev et al. [12] have provided persuasive evidence for the probable hybridization of d-orbitals in transition metals, specifically in the context of the X_2YZ inverse Heusler compounds. They assert that the mutual symmetry of X (1) and Y atoms induces the hybridization of their d-orbitals, resulting in five bonding d states (2eg and 3t2g) and five non-bonding d states (2eu and 3tu). The five X(1)-Y bonding d states subsequently

experience hybridization with the d-orbital of X(2) atoms, leading to the creation of novel bonding and anti-bonding states [13].

It is worth noting that the electronic structure of Pr_2RhZ (Z = Al, Ga, In) alloys involves localized 4f electrons from Pr and partially filled 4d states from Rh. In the present work, the exchange-correlation potential was treated within the framework of the generalized gradient approximation (GGA). Although this approach provides accurate structural and magnetic trends for Heusler compounds, it does not explicitly include the on-site Coulomb repulsion (U) associated with localized electrons. Incorporating the GGA+U correction could further improve the description of the 4f and 4d states and slightly modify the position of the Fermi level or the width of the half-metallic gap. Nevertheless, the overall features of the electronic and magnetic behaviour reported here are consistent with previous GGA-based studies of rare-earth–transition-metal Heusler alloys.

The electronic structure and cohesive energy results can help us understand how the chemical bonds work in the Heusler alloys Pr_2RhZ (Z = Al, Ga, In). The intense mixing of the Rh d and Pr f/d states near the Fermi level shows that the material has a mixed metallic-covalent character. These enable efficient spin exchange interactions and promote ferromagnetic ordering. The relatively high cohesive energy values indicate that these compounds have strong bonds and are structurally stable. In Heusler systems, the arrangement of valence electrons determines both bonding and magnetic behaviour. Delocalized conduction electrons contribute to metallic bonding and electrical conductivity, while localized states enhance magnetic exchange interactions. An Electron Localisation Function (ELF) analysis—though not conducted here—would generally reveal intermediate ELF values (≈ 0.4–0.6) in the Rh–Pr regions, indicative of metallic–covalent bonding, and low ELF values (< 0.2) in interstitial regions, signifying delocalized electrons. Similar correlations among ELF profiles, cohesive energy, and magnetic properties have been documented in related research [14].

Table III.2: The calculated total magnetic moments (μ_{tot}), atomic and interstitial magnetic moments and the band gap energy (E_g) for the Pr_2RhZ (Z = Al, Ga, In).

Alloys	a (Å)	μ_{tot} (μ_B)	μ_{Pr1} (μ_B)	μ_{Pr2} (μ_B)	μ_{Rh} (μ_B)	μ_{Z} (μ_B)	E_g (eV)
Pr_2RhAl	6.8460	4.05	2.04395	1.90365	-0.18607	-0.05934	0.235
Pr_2RhGa	6.8264	4.02	2.04779	1.92582	-0.20469	-0.06759	0.345
Pr_2RhIn	7.0375	4.06	2.08040	1.95148	-0.21877	-0.04845	0.340

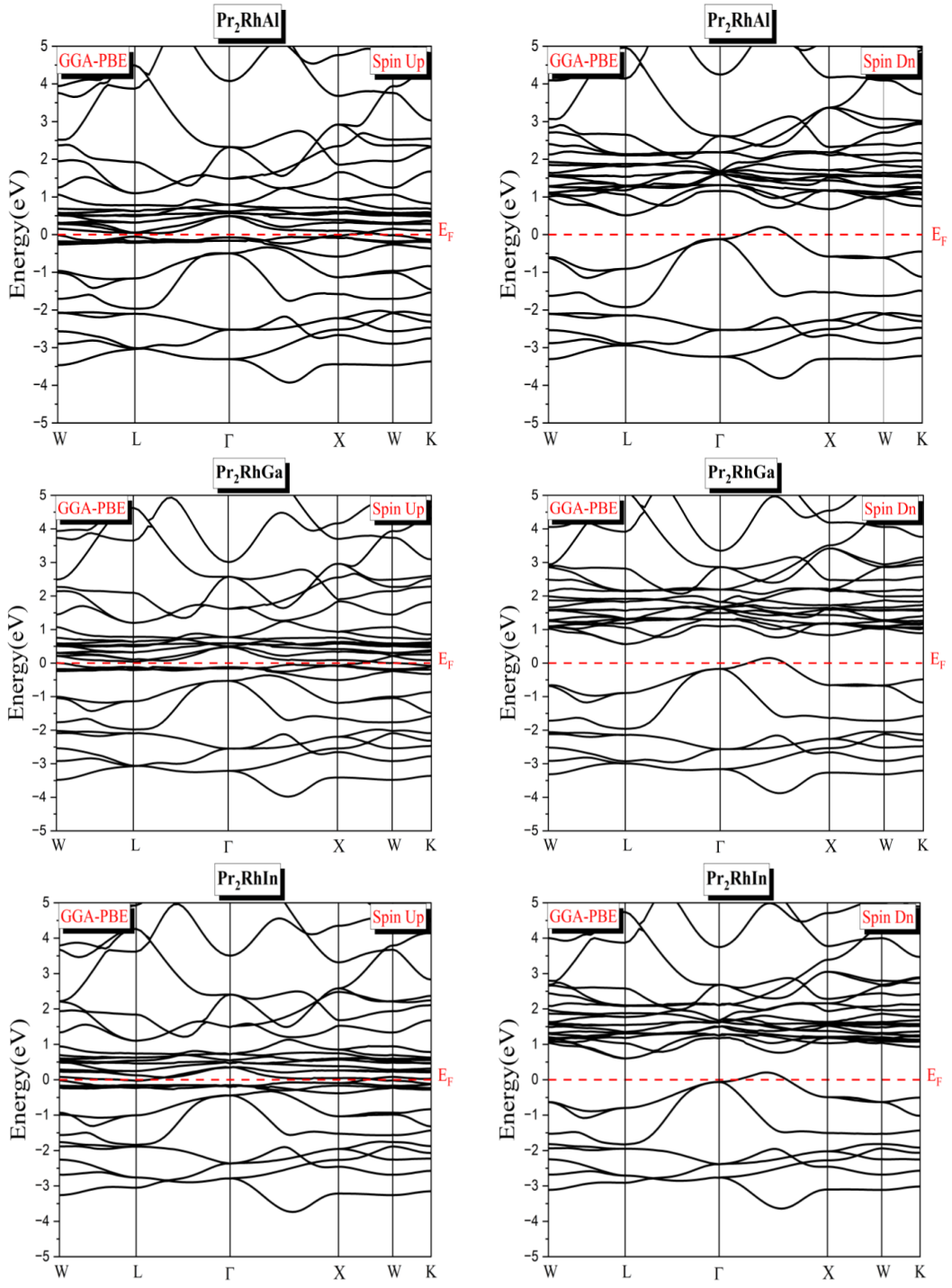


Figure III.3: Spin-polarized band structures of majority spin (Up) and minority spin (Down) of Pr_2RhZ (Z = Al, Ga, In) in ferromagnetic-Hg_2CuTi type structure.

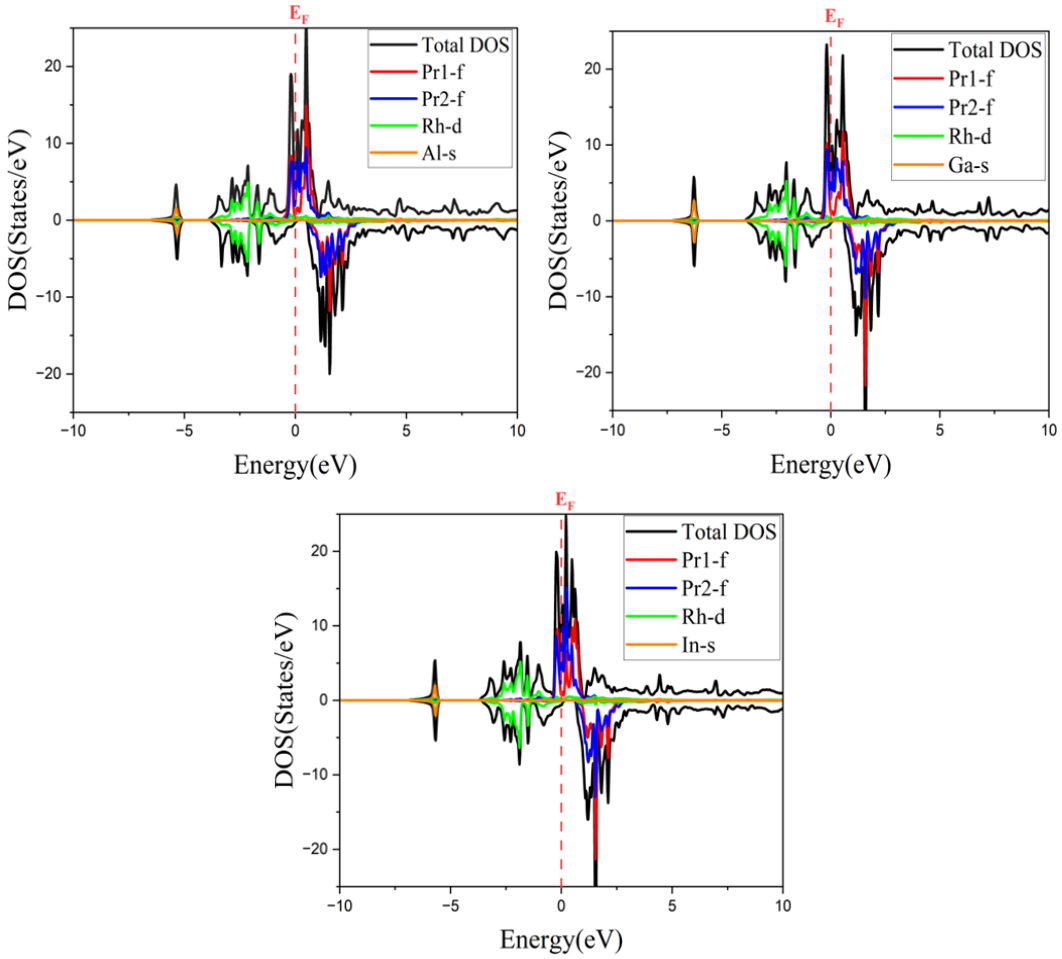


Figure III.4: Total and partial density of state with both majority and minority spin direction of Pr_2RhZ (Z = Al, Ga, In) alloys in ferromagnetic-Hg_2CuTi type structure.

The computed spin polarisation total density of states (DOS) and partial DOS of Pr_2RhZ (Z = Al, Ga, In) compounds at their equilibrium lattice parameters are presented in Figure III.4.

Energy levels below -5 eV, predominantly derived from the s states of post-transition metal (Al, Ga or In) atoms, are committed from Figure III.4 owing to their near-symmetry in both majority and minority spin orientations. These states are much removed from the Fermi level and, as a result, do not influence the magnetic characteristics. The Rh-d orbitals dominated our valence band, and the f states of Pr1 and Pr2 constitute the predominant portion of the total density of states (DOS) at the Fermi level. The f electrons of Pr2 atoms and the d orbitals of Rh atoms determine the band gap around the Fermi level in all alloys. The density of states above the Fermi level is affected mainly by the Pr-f and Rh-d orbitals. We have computed the spin polari-

sation ratio (P) for these three compounds. The computation of spin polarisation can be accomplished using:

$$P = \frac{N^{\uparrow}(\varepsilon_F) - N^{\downarrow}(\varepsilon_F)}{N^{\uparrow}(\varepsilon_F) + N^{\downarrow}(\varepsilon_F)} \tag{III.3}$$

were $N^{\uparrow}(\varepsilon_F)$ and $N^{\downarrow}(\varepsilon_F)$ indicate the density of states (DOS) for majority-spin and minority-spin states at the Fermi level, respectively. The three analysed compounds have a complete (90%) spin polarisation ratio at the Fermi level.

c. Magnetic Properties

Slater and Pauling established in two seminal publications that, for binary magnetic compounds, the addition of one valence electron causes the compound to inhabit spin-down states, resulting in a reduction of the total spin magnetic moment by $1\,\mu_B$ [15]. Notably, half-metallic Heusler alloys demonstrate analogous behaviour. The total spin magnetic moment in the unit cell is proportional to the total number of valence electrons [16].

Error! Reference source not found. displays the computed magnetic moment for the entire Heusler alloys Pr_2RhAl, Pr_2RhGa, and Pr_2RhIn at their optimized lattice parameters. All studied alloys exhibit integer magnetic moments of $4\,\mu_B$. Half-metallic materials are distinguished by an integer total magnetic moment. Consequently, Pr_2RhAl, Pr_2RhGa, and Pr_2CoIn are classified as half-metallic ferromagnets (HMF) under the category of complete Heusler alloys.

The emergence of these integer magnetic moments in bulk Heusler alloys originates from specific microphysical mechanisms related to the electronic structure. The strong hybridisation between the Rh–Rh and Rh–Pr d orbitals give rise to bonding and antibonding states. Due to exchange splitting, the minority-spin channel develops a semiconducting gap, whereas the majority-spin channel remains metallic. These result in complete spin polarisation at the Fermi level and give rise to an integer total magnetic moment per formula unit. Furthermore, the localised 4f electrons of Pr contribute indirectly through Ruderman–Kittel–Kasuya–Yosida (RKKY)-type exchange interactions with the Rh d states, thereby reinforcing the ferromagnetic alignment and stabilising the half-metallic state. Similar microscopic mechanisms explaining the origin of integer magnetic moments in Heusler-type compounds have been reported in the literature [17], [18], [19].

Based on the magnetic moment values for each atom in the compounds presented in Table III.2, we deduce that the predominant contribution to the total magnetic moment arises from the Pr atoms. In contrast, the Al, Ga, and In atoms contribute minimally to the total magnetic moment.

The electronic configurations of the atoms in our compounds are Pr: $[Xe]4f^3 6s^2$, Rh: $[Kr]4d^8 5s^1$, Al: $[Ne]3s^2 3p^1$, Ga: $[Ar]3d^{10} 4s^2 4p^1$, In: $[Kr]4d^{10} 5s^2 5p^1$.

Furthermore, the compounds Pr_2RhAl, Pr_2RhGa, and Pr_2RhIn possess the same quantity of valence electrons, totalling 22. Our findings demonstrate a linear correlation between the total spin magnetic moment and the number of valence electrons, consistent with the established Slater–Pauling connection [**?**], expressed by the following equation:

$$\mu_{\text{tot}} = Z_{\text{tot}} - 18 \tag{III.4}$$

where Z_{tot} is the total number of valence electrons per unit cell and μ_{tot} is the total spin magnetic moment [21].

It is worth noting that the Gilbert damping constant (α), which characterises the energy dissipation and magnetisation relaxation processes, is a crucial quantity for evaluating the spintronic potential of half-metallic ferromagnets. However, its precise determination requires spin–orbit coupling and dynamic simulations, which are beyond the present static DFT framework. Future work will focus on estimating α to further clarify the spin dynamics of Pr_2RhZ alloys [22], [23].

III.3.1.2 Full Heusler Pr_2CoZ (Z = Al, Ga and In):

a. Structural properties

Heusler alloys consist of transition metal elements X and Y, along with main group element Z [24]. Their composition adheres to stoichiometry, characterised by the formula X_2YZ. These alloys exhibit two distinct crystal structures: face-centered cubic (fcc) lattices, specifically the Cu_2MnAl and Hg_2CuTi structures (Figure III.5). The two structures consist of four interpenetrating face-centered cubic (fcc) sublattices with four unique crystal sites: A(0, 0, 0), B(0.25, 0.25, 0.25), C(0.5, 0.5, 0.5), and D(0.75,

0.75, 0.75).

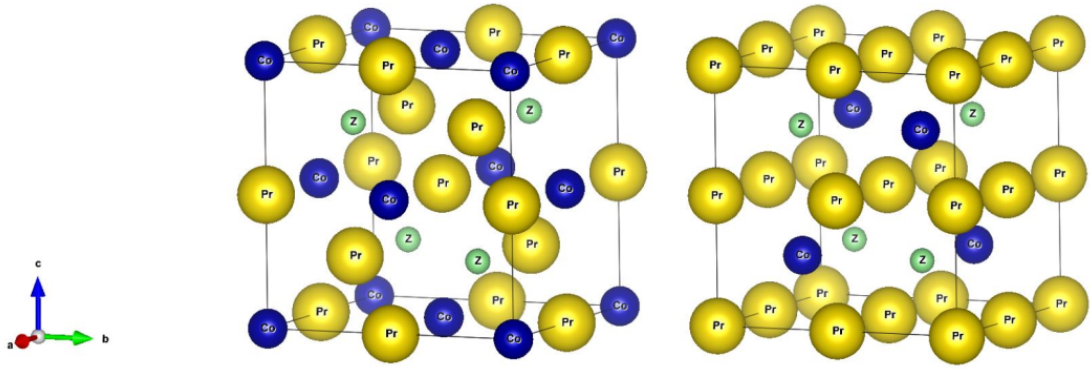


Figure III.5: Crystallographic structure of full-Heuler alloy Pr_2CoZ (Z = Al, Ga and In) in which (a) Hg_2CuTi type and (b) Cu_2MnAl type.

In the Cu_2MnAl type structure, referred to as $L2_1$, the atomic arrangement inside the four sites of the unit cell adheres to the sequence X–Y–X–Z. Conversely, in the Hg_2CuTi type structure, designated as the XA structure, the sequence of atoms occupying the four sites of the unit cell is X–X–Y–Z [25].

The empirical Birch–Murnaghan equation of states delineates the relationship between total energies and volumes per formula unit for both Hg_2CuTi-type and Cu_2MnAl-type, as represented in [5]:

$$E(V) = E_0 + \frac{B}{B'(B'-1)}\left[V\left(\frac{V_0}{V}\right)^{B'} - V_0\right] + \frac{B}{B'}(V - V_0) \qquad \text{(III.5)}$$

Table III.3: Optimized lattice constant a_0 (Å), Bulk modulus B (GPa), the pressure derivative B', the total energy $E_{\min}$ (Ry), and the Formation energy ΔH (Ry) for Full Heusler compounds Pr_2CoZ (Z = Al, Ga, In).

Alloy	Phases	a_0 (Å)	B (GPa)	B'	$E_{\min}$ (Ry)	ΔH (Ry)
Pr_2CoAl	Cu_2MnAl (NM)	6.9426	68.4729	3.6102	-40243.64009	-1.232703
	Cu_2MnAl (FM)	7.1111	52.5918	4.2491	-40243.70746	-1.286372
	Cu_2MnAl (AFM)	7.1294	49.6159	5.2811	-40243.69635	-1.269491
	Hg_2CuTi (NM)	6.6416	88.1645	4.1350	-40243.69562	-1.270491
	Hg_2CuTi (FM)	6.7422	74.4919	4.6438	-40243.76273	-1.322845
	Hg_2CuTi (AFM)	6.7930	69.2096	4.8924	-40243.72873	-1.304328
Pr_2CoGa	Cu_2MnAl (NM)	6.9207	69.2837	3.9519	-43646.28321	-1.173918
	Cu_2MnAl (FM)	7.0910	44.8762	5.4881	-43646.33556	-1.246940
	Cu_2MnAl (AFM)	7.0829	61.7320	4.8798	-43646.33234	-1.240953
	Hg_2CuTi (NM)	6.6223	84.5964	5.7954	-43646.28764	-1.203819
	Hg_2CuTi (FM)	6.7184	81.2231	4.1335	-43646.36170	-1.273954
	Hg_2CuTi (AFM)	6.7640	73.6881	4.9131	-43646.32450	-1.239753
Pr_2CoIn	Cu_2MnAl (NM)	7.1719	52.3517	5.7862	-51524.54414	-1.052953
	Cu_2MnAl (FM)	7.3445	51.6078	4.1110	-51524.63701	-1.148534
	Cu_2MnAl (AFM)	7.3515	40.5122	5.6966	-51524.62934	-1.133629
	Hg_2CuTi (NM)	6.8599	82.4667	4.5535	-51524.57210	-1.082489
	Hg_2CuTi (FM)	6.9696	69.0836	4.4314	-51524.65776	-1.171425
	Hg_2CuTi (AFM)	7.0233	59.1493	5.5422	-51524.62849	-1.130629

Table III.1 shows the optimised lattice constants and bulk modulus, obtained from the minimum of the energy-volume curves seen in Figure III.1. 6, including all ferromagnetic and non-magnetic phases for both Hg_2CuTi and Cu_2MnAl-type structures.

The equation employed in this study incorporates the variables E for energy, V for volume, B for the equilibrium bulk modulus, V_0 for the volume of the experimental unit cell, and B' for the pressure derivative of the bulk modulus at the equilibrium volume.

The findings demonstrate that the Hg_2CuTi configuration in the ferromagnetic state

has greater energy stability compared to the alternative states of the Cu_2MnAl structure. Previous investigations have indicated that the Hg_2CuTi structure is more likely to develop when the Y element possesses more electronegativity than the X element [8]. Consequently, our further computations will be predicated on the ferromagnetic (FM) condition of the Hg_2CuTi-type structure.

We examine the formation energy to establish the viability of this chemical and its potential for experimental synthesis; the formation energy is expressed by the following relation [9]:

$$\Delta H = E_f^{\mathrm{Pr_2CoZ}} = E_{\mathrm{tot}}^{\mathrm{Pr_2CoZ}} - E_{\mathrm{Co}}^{\mathrm{bulk}} - E_{\mathrm{Z}}^{\mathrm{bulk}} - 2E_{\mathrm{Pr}}^{\mathrm{bulk}} \tag{III.6}$$

Where $E_f^{\mathrm{Pr_2CoZ}}$ is the equilibrium energy of these compounds, in which $E_{\mathrm{tot}}^{\mathrm{Pr_2CoZ}}$ is the total energy of compounds and $E_{\mathrm{Pr}}^{\mathrm{bulk}}$, $E_{\mathrm{Co}}^{\mathrm{bulk}}$ and $E_{\mathrm{Z}}^{\mathrm{bulk}}$ are the chemical potential of atoms in their stable bulk for Pr, Co, and Z (Al, Ga, In).

The estimated formation energies of the compounds Pr_2CoZ (Z = Al, Ga, In) for the Hg_2CuTi-type structure are -1.322845, -1.273954, and -1.171425 Ry, respectively, indicating the stability of these alloys [8].

Conversely, we can as certain that the Hg_2CuTi-type structure is the most stable phase by comparing the formation energy values of the Hg_2CuTi-type and Cu_2MnAl-type structures (Table III.3).

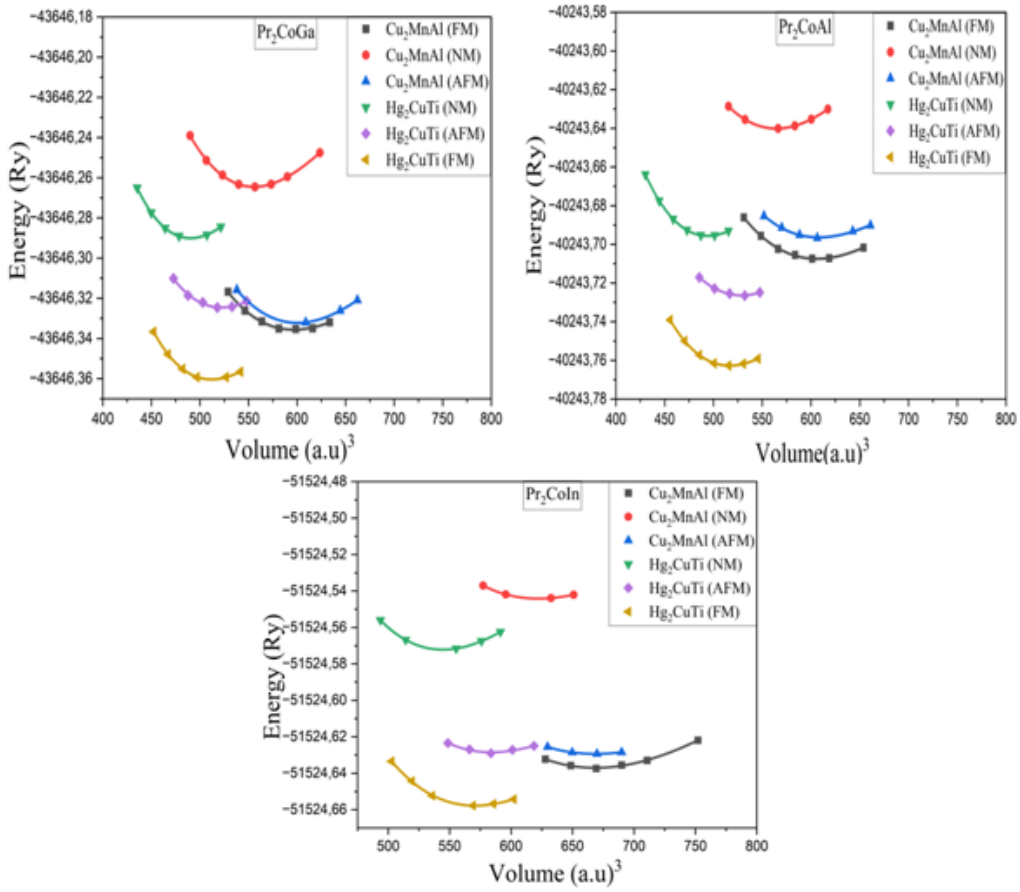


Figure III.6: Total energy versus unit cell volume for Pr_2CoZ (Z = Al, Ga and In).

b. Elastic properties

Table III.4: Elastic constants (Cij), bulk modulus (K), Shear modulus (G) Young modulus (E), Poisson's coefficient (ν). The zener anisotropy (A) Pugh's Ratio (κ)

	C_{11}	C_{12}	C_{44}	K	G	E	ν	A	κ
Pr_2CoAl	105.986	57.924	53.975	73.944	41.997	105.935	0.261	2.25	0.56
Pr_2CoGa	111.118	61.348	49.820	77.938	39.846	102.133	0.282	2.00	0.51
Pr_2CoIn	97.897	49.189	38.249	65.425	32.69	84.070	0.286	1.57	0.50

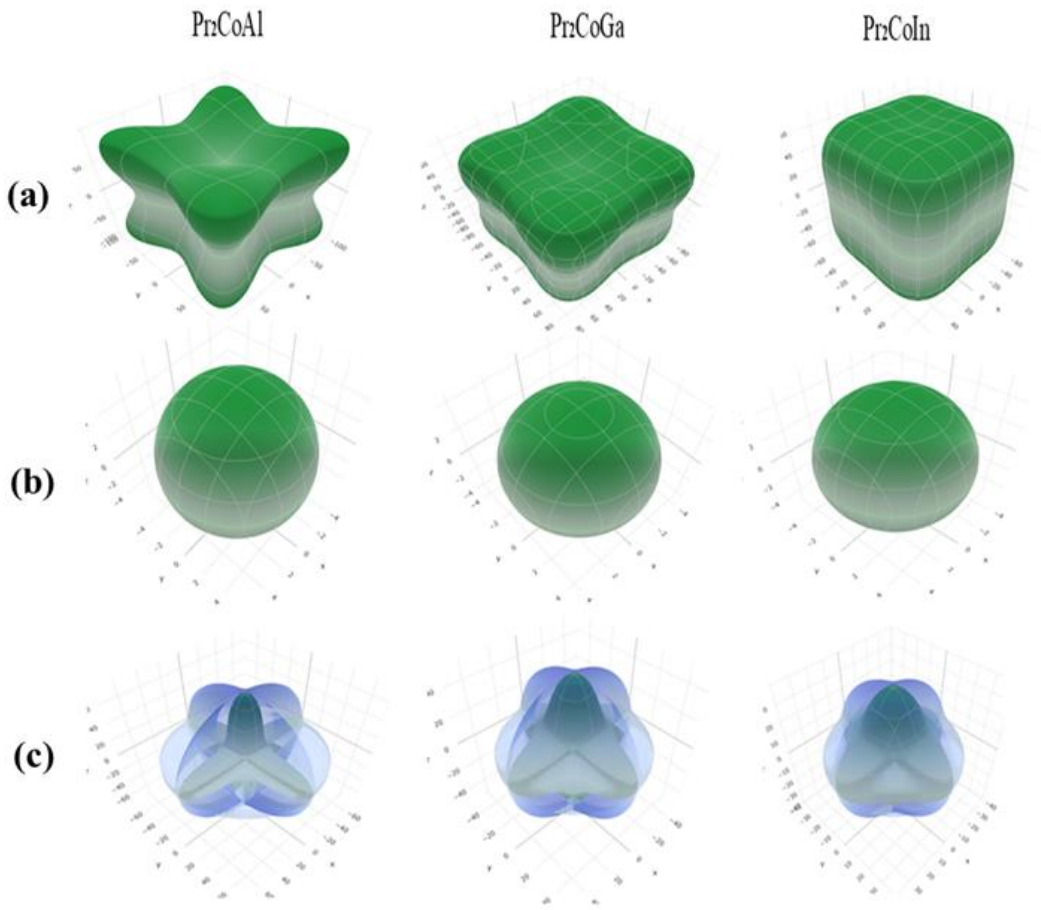


Figure III.7: 3D representations of the influence of (a) Young's modulus (E, in GPa), (b) Bulk modulus (k,in GPa) and (c) Compressibility (β, in GPa^{-1}) on the crystal direction for Pr_2CoAl, Pr_2CoGa and Pr_2CoIn.

We calculated the elastic properties of our Heusler ferromagnetic (Pr_2Co (Z=Al, Ga and In)) in Hg_2CuTi-Type structure by the IRelast package [26]. Table III.4 represents our results using the Voigt–Reuss–Hill approximations [27]. As one can observe, C_{11}, C_{12}, and C_{44} values satisfy the condition C_{11} - $C_{12} > 0$, $C_{11} + 2C_{12} > 0$, $C_{11} > 0$, and $C_{44} > 0$ [28]. Thus, the structure of Hg_2CuTi is mechanically stable. The values of anisotropy in Pr_2CoAl, Pr_2CoGa, and Pr_2CoIn are 2.25, 2.00, and 1.57, respectively; Pugh's ratios are 0.56, 0.51, and 0.50 (see Table III. 4). Thus, indicating a high elastic anisotropy and confirming that full-Heusler compounds are ductile and not elastically isotropic.

Then we drew the influence of Young's modulus (E), Linear compressibility (β) and Bulk modulus (K) in Figure III.7. The analyses of 3D representations show a marked deviation from the spherical shape characteristic of homogeneous materials in both the Young's modulus (E) and shear modulus (G) plots. The minimum values of Young's modulus appear along the crystal axes (100), (010), and (001), while the maximum values are identified along the (111) direction for all compounds. Conversely, the shear modulus (G) reaches its highest values along the axes (100), (010), and (001), but decreases to its lowest values along the (111) direction. These directional variations highlight the irregular nature of the crystalline materials, with stiffness and resistance to bond angle deformation increasing significantly along the (111) direction. Meanwhile, the linear compressibility (β) plots show significant compressive strength in all directions, for all full Heusler compounds Pr_2CoAl, Pr_2CoGa, and Pr_2CoIn.

c. Electronic Properties

We analyse the band structures and the total density of states of Pr_2CoZ (Z = Al, Ga, In) compounds for both spins' direction (down and up). This investigation aims to elucidate the electronic structure of these compounds within the stable Hg_2CuTi structure in a ferromagnetic configuration at the equilibrium lattice parameter, employing the GGA approximation. The findings are illustrated in Figure III.8, with the corresponding band gap values detailed in Table III.5.

Band structures act as a depiction of the allowable electronic energy levels in solid materials, and they are utilised to deepen our comprehension of their electronic properties. The band structure facilitates a swift evaluation of whether a material exhibits metallic, semi-metallic, or insulating characteristics. For materials possessing a band gap, it also elucidates whether the gaps are direct or indirect, in addition to their magnitude.

Furthermore, the curvature of the bands serves as an indicator of the mobility of the carriers residing within those bands. Upon examination of the band structure for all compounds analysed, as illustrated in Figure III.8, it is evident that in the spin-polarized state (specifically spin down), an energy gap emerges between the higher of the valence band at the Γ point and the lower of the conduction band at the X

point. Consequently, these compounds display the traits of indirect band gap semiconductors, possessing energy band gaps of 0.359, 0.483, and 0.492 eV for Pr_2CoAl, Pr_2CoGa, and Pr_2CoIn, respectively. Moreover, it is clear that in the spin-up direction, the bands demonstrate overlap, signifying the metallic character of these compounds. Consequently, we arrive at the conclusion that all compounds exhibit half-metallic behaviour. Three distinct origins of band gaps are typically identified: the charge transfer band gap, the *d–d* band gap, and the covalent band gap. The covalent band gap has been found to be present in the Half Heusler compounds. The *d–d* band gap is responsible for the half-metallicity observed in Full Heusler compounds [29], [30].

Table III.5: The calculated total magnetic moments (Mt) and atomic magnetic moments for the Pr_2CoZ (Z = Al, Ga, In)

Alloys	a (Å)	μ_{tot}	μ_{Pr1}	μ_{Pr2}	μ_{Co}	μ_{Z}	$\mu_{\text{interstitial}}$	E_g (eV)
Pr_2CoAl	6.7422	4.00	2.14972	2.06037	-0.77074	-0.02783	0.58868	0.359
Pr_2CoGa	6.7184	4.00	2.15491	2.09430	-0.78300	-0.03955	0.57506	0.483
Pr_2CoIn	6.9696	4.00	2.21622	2.15584	-1.01045	-0.03128	0.66852	0.492

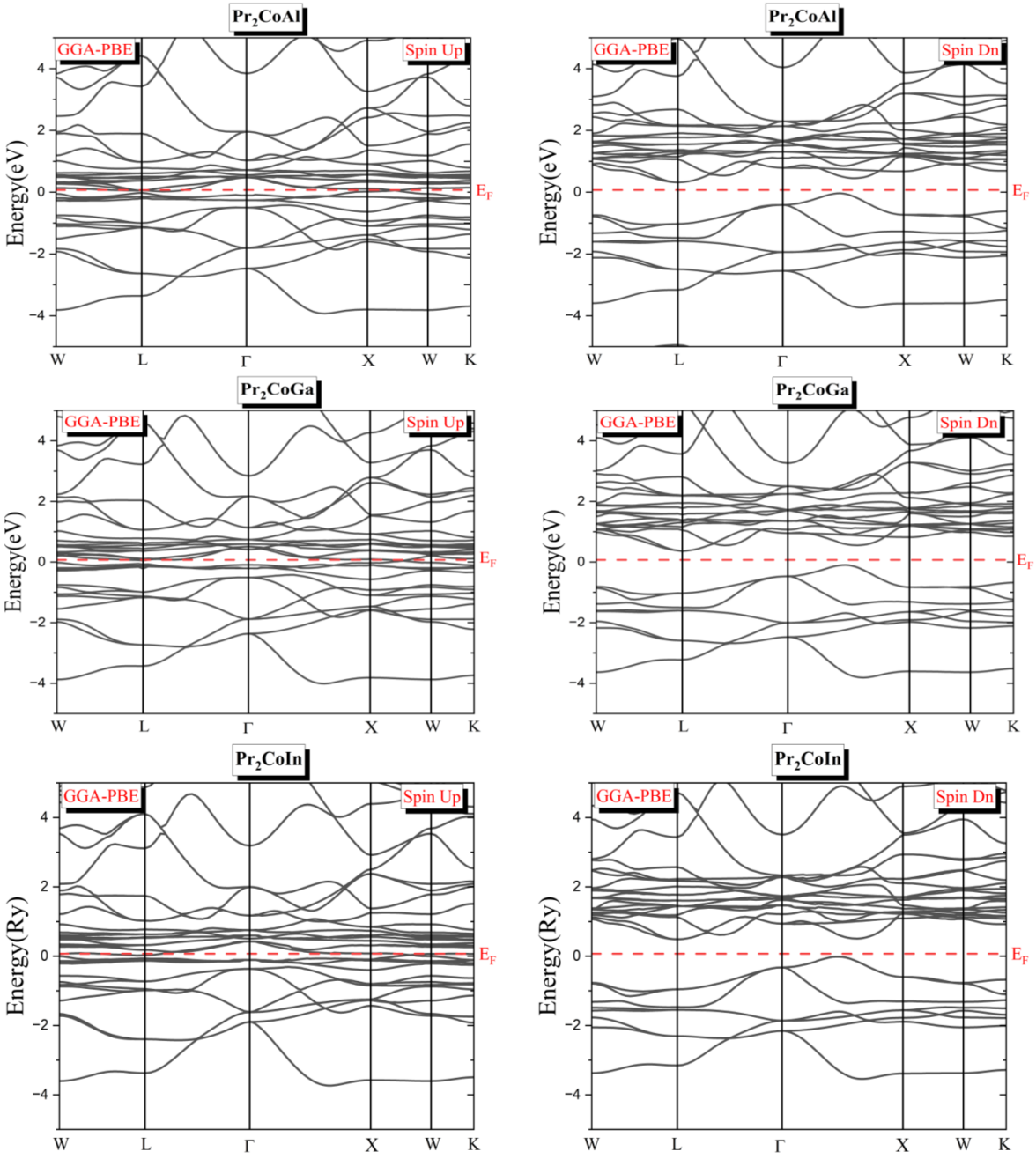


Figure III.8: Spin-polarized band structures of majority spin (Up) and minority spin (Down) of Pr_2CoZ (Z = Al, Ga, In) in Hg_2CuTi type structure

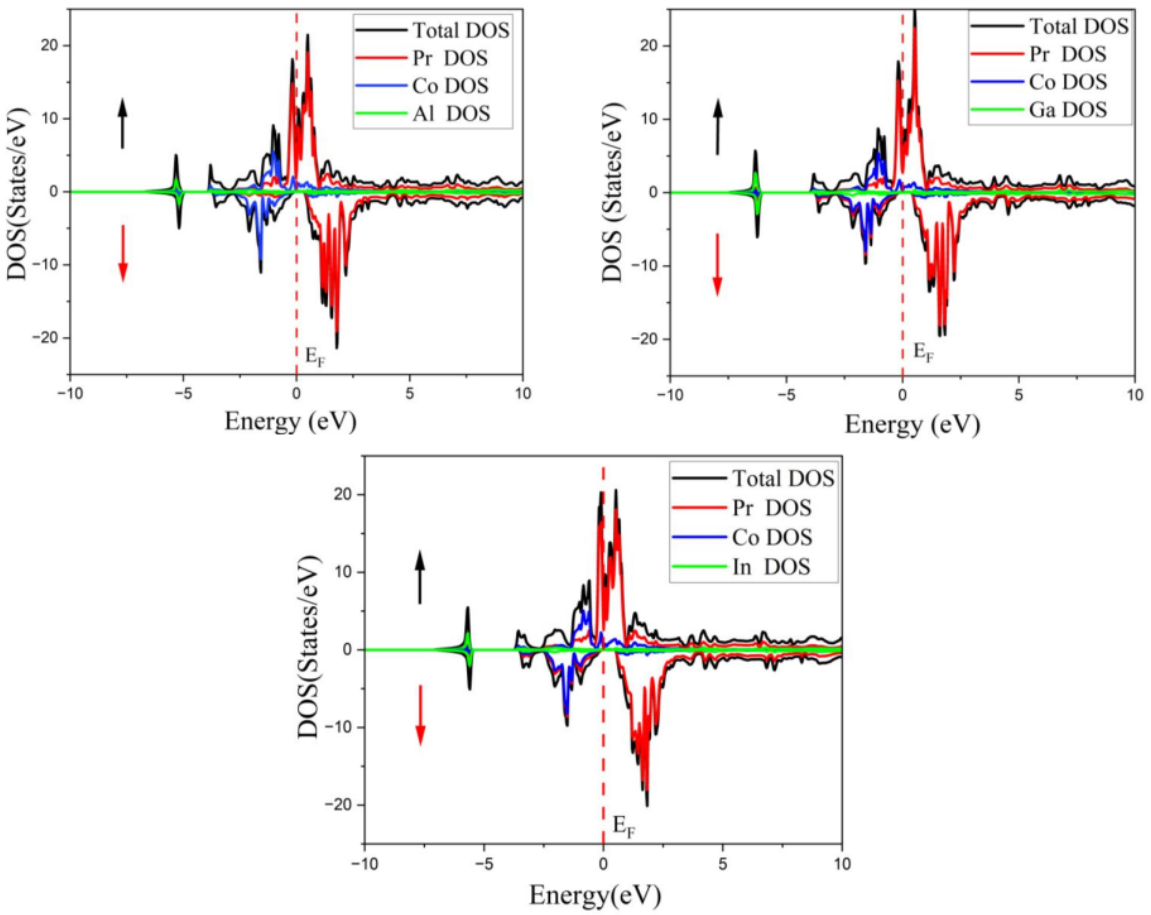


Figure III.9: Total density of state of Pr_2CoZ (Z = Al, Ga, In) alloys in Hg_2CuTi type structure.

Faleev et al. [31] have provided persuasive evidence for the probable hybridisation of *d*-orbitals in transition metals concerning the X_2YZ inverse Heusler compounds.

They assert that the mutual symmetry of X(1) and Y atoms induces the hybridisation of their *d*-orbitals, resulting in five bonding *d* states ($2e_g$ and $3t_{2g}$) and five non-bonding *d* states ($2e_u$ and $3t_{1u}$). The five X(1)-Y bonding *d* states subsequently experience hybridisation with the *d*-orbital of X(2) atoms leads to the creation of novel bonding and anti-bonding states [13].

The computed spin polarisation total density of states (DOS) and partial DOS of Pr_2CoZ (Z = Al, Ga, In) compounds at their equilibrium lattice parameters are presented in Figure III.9.

Energy levels below −5 eV, predominantly derived from the *s* states of transition metal (TM = Co, Pr) atoms, are committed from Figure III.9 owing to their near-

symmetry in both majority and minority spin orientations. These states are much removed from the Fermi level and, as a result, do not influence the magnetic characteristics. The d states of Pr constitute the predominant portion of the total density of states (DOS) at the Fermi level. The d electrons of Pr atoms determine the band gap around the Fermi level in all alloys. The density of states above the Fermi level is mostly affected by the Pr and Co atoms, and we have computed the spin polarisation ratio (P) for these three compounds. The computation of spin polarisation can be accomplished using by

$$P = \frac{N\uparrow(\varepsilon_F) - N\downarrow(\varepsilon_F)}{N\uparrow(\varepsilon_F) + N\downarrow(\varepsilon_F)} \tag{III.7}$$

Were $N\uparrow(\varepsilon_F)$ and $N\downarrow(\varepsilon_F)$ indicate the density of states (DOS) for majority-spin and minority-spin states at the Fermi level, respectively. The three analysed compounds have a complete (100%) spin polarisation ratio at the Fermi level.

d. Magnetic Properties

Slater and Pauling established in two seminal publications that, for binary magnetic compounds, the addition of one valence electron causes the compound to inhabit spin-down states, resulting in a reduction of the total spin magnetic moment by 1 μ_B [13]. Notably, half-metallic Heusler alloys demonstrate analogous behaviour. The total spin magnetic moment in the unit cell is proportional to the total number of valence electrons [14].

Table III.5 displays the computed magnetic moment for the entire Heusler alloys Pr_2CoAl, Pr_2CoGa, and Pr_2CoIn at their optimised lattice parameters. All studied alloys exhibit integer magnetic moments of 4 μ_B. Half-metallic materials are distinguished by an integer total magnetic moment. Consequently, Pr_2CoAl, Pr_2CoGa, and Pr_2CoIn are classified as half-metallic ferromagnets (HMF) under the category of complete Heusler alloys.

Based on the magnetic moment values for each atom in the compounds presented in Table III.5, we deduce that the predominant contribution to the total magnetic moment arises from the Pr atoms. In contrast, the Al, Ga, and In atoms contribute

minimally to the total magnetic moment.

The electronic configurations of the atoms in our compounds are Pr: [Xe]$4f^3 6s^2$, Co: [Ar]$4s^2 3d^7$, Al: [Ne]$3s^2 3p^1$, Ga: [Ar]$3d^{10} 4s^2 4p^1$, In: [Kr]$4d^{10} 5s^2 5p^1$.

Furthermore, the compounds Pr_2CoAl, Pr_2CoGa, and Pr_2CoIn possess the same quantity of valence electrons, totalling 22. Our findings demonstrate a linear correlation between the total spin magnetic moment and the number of valence electrons, consistent with the established Slater–Pauling connection [18], expressed by the following equation:

$$\mu_{\text{tot}} = Z_{\text{tot}} - 18 \tag{III.8}$$

where Z_{tot} the total number of valence electrons per unit cell and μ_{tot} is the total spin magnetic moment [21].

III.3.1.3 e. Thermodynamic properties

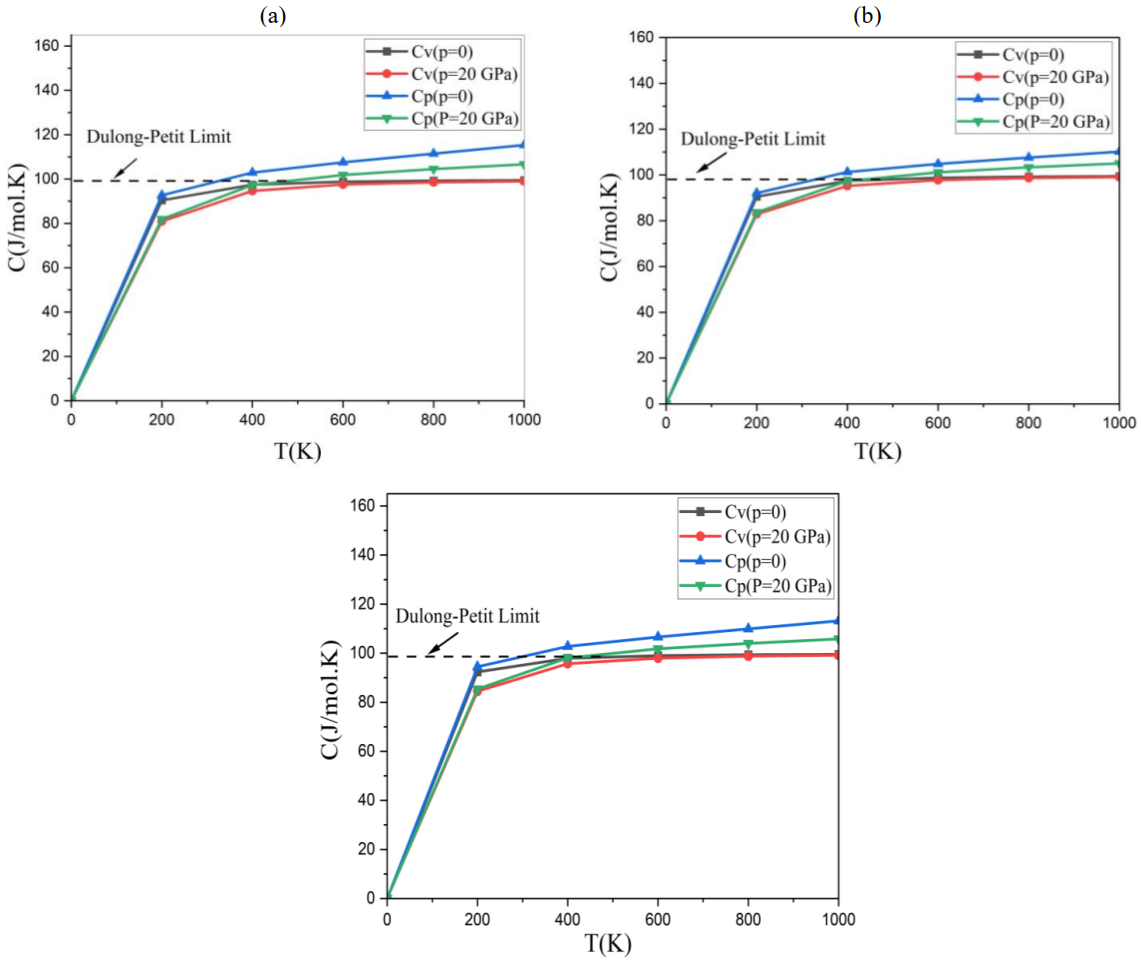


Figure III.10: Heat capacity as function of temperature in different pressure for Pr_2CoZ in witch (a) Pr_2CoAl, (b) Pr_2CoGa and (c) Pr_2CoIn.

The thermodynamic properties of our Heusler ferromagnetic alloys (Pr_2Co (Z = Al, Ga and In)) in Hg_2CuTi-Type structure were calculated using the Gibbs 2 package, a new version of the quasiharmonic model for solid-state thermodynamics [32]. The temperature range was chosen between 0 and 1000 K. In addition, the pressure value varies from 0 to 20 GPa to evaluate the energy or the number of phonons needed to raise the temperature of the materials. Figure III.10 shows the calculated connections between heat capacities (C_V and C_P) and temperatures at various pressures for all materials: (a) Pr_2CoAl, (b) Pr_2CoGa, and (c) Pr_2CoIn.

Within the range of 0 to 300 K, C_V increase rapidly until it's reached the Dulong–Petit Limit (100 J/mol·K) then increase linearly in the rest of the range and C_P increase

rapidly then increase slowly. We have also seen that for C_V and C_P, their values at ambient pressure are higher than under pressure (up to 20 GPa). This behavior indicates that atomic interactions are dominant at low temperatures in these compounds.

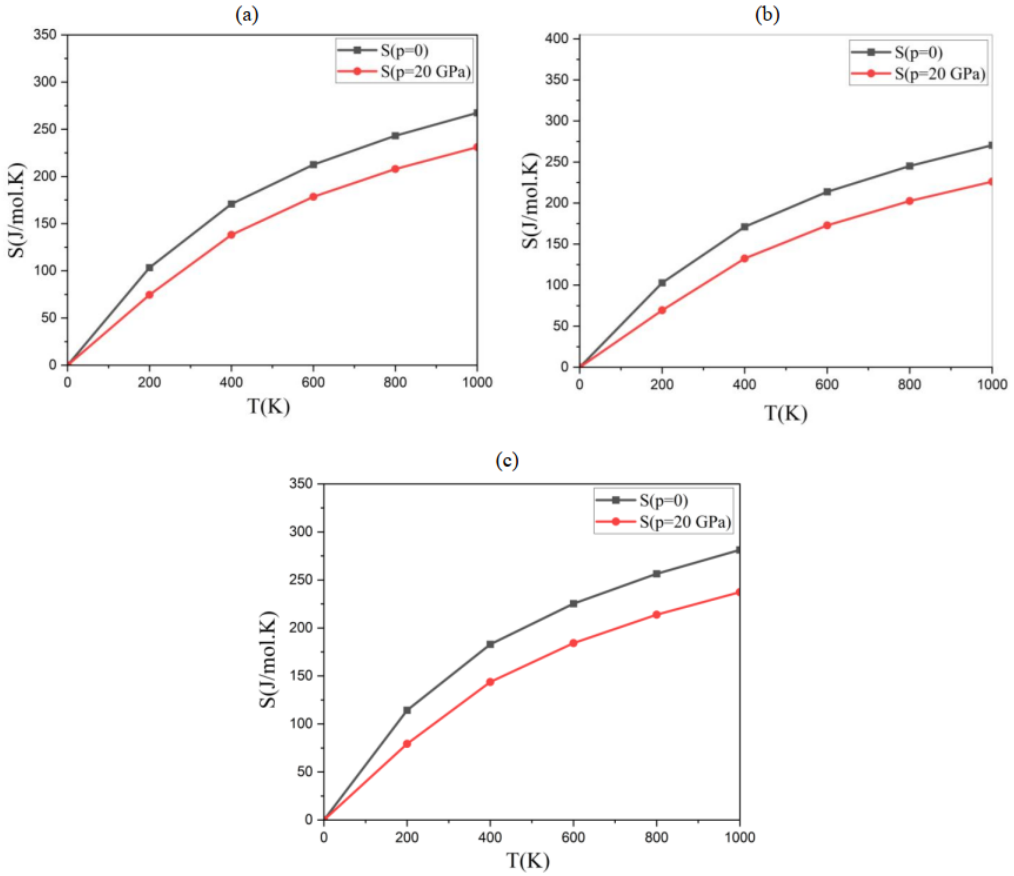


Figure III.11: Entropy as function of temperature in different pressures for Pr_2CoZ in which (a) Pr_2CoAl, (b) Pr_2CoGa and (c) Pr_2CoIn.

The Figure III.11 shows the entropy (S) as a function of temperature (T) under two different pressures (0 GPa and 20 GPa) for three Heusler ferromagnetic alloys (Pr_2Co (Z=Al, Ga and In)) in Hg_2CuTi-Type structure. We observe that the entropy increases monotonically with temperature due to increased thermal disorder. This is consistent with the basic thermodynamic relationship[33]. However, at constant temperatures, the entropy decreases with increasing pressure. This is due to the decrease in atomic disorder under pressure. This indicates that higher pressure reduces entropy, likely due to the inhibition of vibrational motion in the crystal lattice.

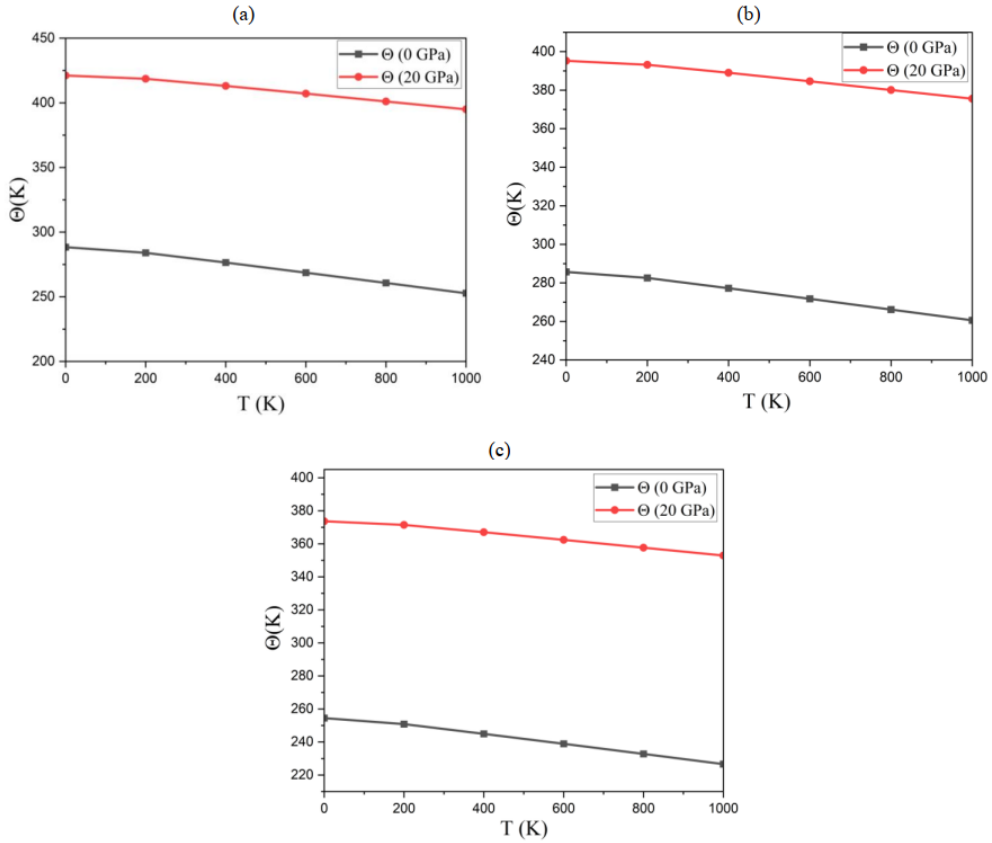


Figure III.12: Debye temperature as function of temperature in different pressure for Pr_2CoZ witch (a) Pr_2CoAl, (b) Pr_2CoGa and (c) Pr_2CoIn

The Figure III.12 illustrates how the Debye temperature Θ (K) changes with temperature (T) at two pressure values (0 GPa, 20 GPa). This basic parameter provides important information on the specific heat and melting temperature . We note that the Debye temperature decreases with increasing temperature in all Heusler ferromagnetic (Pr_2CoZ (Z=Al, Ga and In)) in Hg_2CuTi-Type structure, whether at 0 or 20 GPa. As the temperature increases in these materials, the intensity of atomic vibrations increases, causing the atoms to vibrate around their positions at relatively regular frequencies [34]. This leads to a weakening of the dynamic rigidity of the material, meaning that the atoms move more freely, thus decreasing the Debye temperature. Meanwhile, the Debye temperature increases with increasing pressure at a constant temperature.

When we apply high pressure to a solid, the atoms in the crystal lattice become closer together. This closeness leads to increased interatomic forces because the atoms are now at shorter distances. As a result, the rigidity of the crystal lattice increases, and

it becomes more difficult to make the atoms vibrate, which increases the vibrational frequencies of the phonons, thus increasing the Debye temperature.

III.3.1.4 Cr- doping effect on Pr_2CoZ (Z=Al, Ga and In):

We have done a Cr-doping on the full Heusler alloys Pr_2CoZ (Z=Al, Ga and In) in which we substituted the second atom of Pr atom with Cr atom, where we obtained a quaternary alloys PrCrCoZ (Z=Al, Ga and In).

a. Structural properties

Heusler alloys consist of transition metal elements X and Y, along with main group element Z [24]. Their composition adheres to stoichiometry, characterised by the formula X_2YZ. These alloys exhibit two distinct crystal structures: face-centered cubic (fcc) lattices, specifically the Cu_2MnAl and Hg_2CuTi structures (Figure III.13). The two structures consist of four interpenetrating face-centered cubic (fcc) sublattices with four unique crystal sites: A(0, 0, 0), B(0.25, 0.25, 0.25), C(0.5, 0.5, 0.5), and D(0.75, 0.75, 0.75).

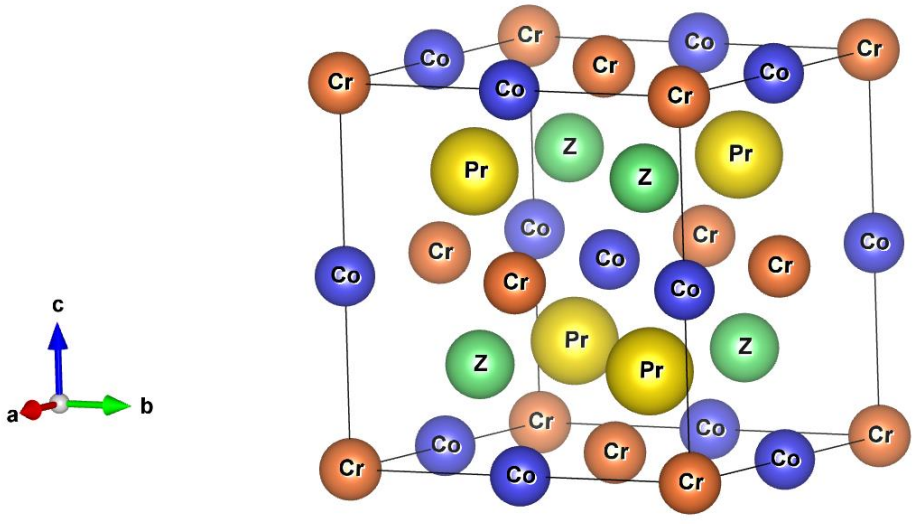


Figure III.13: Crystallographic structure of Quaternary-Heuler alloy CrPrCoZ (Z=Al, Ga and In) (by VESTA [3]).

In the Cu_2MnAl type structure, referred to as $L2_1$, the atomic arrangement inside the four sites of the unit cell adheres to the sequence X–Y–X–Z. Conversely, in the

Hg_2CuTi type structure, designated as the XA structure, the sequence of atoms occupying the four sites of the unit cell is X–X–Y–Z [6], in our work, we used the more stable structures of full Heusler alloys Pr_2CoZ (Z=Al, Ga and In) [35] with substituting the X atom (Pr) with Cr one.

In Figure III.14, we show the total energy versus the volume graphs of our alloys CrPrCoZ (Z=Al, Ga and In) for Hg_2CuTi-type in ferromagnetic phases used the Birch–Murnaghan equation as represented in [7]:

$$E(V) = E_0 + \frac{B}{B'(B'-1)}\left[V\left(\frac{V_0}{V}\right)^{B'} - V_0\right] + \frac{B}{B'}(V - V_0) \tag{III.9}$$

This equation employed in this study incorporates the variables E for energy, V for volume, B for the equilibrium bulk modulus, V_0 for the volume of the experimental unit cell, and B′ for the pressure derivative of the bulk modulus at the equilibrium volume.

The obtained results resumed in the Table III.6.

Table III.6: Optimized lattice constant a_0 (Å), Bulk modulus B (GPa), the pressure derivative B', the total energy $E_{\min}$ (eV), and the Formation energy ΔH (Ryd) for Quaternary Heusler compounds CrPrCoZ (Z = Al, Ga, In).

Alloy	Phases	a_0 (Å)	B (GPa)	B'	$E_{\min}$ (eV)	ΔH (Ryd)
CrPrCoAl	Hg_2CuTi (FM)	6.419	100.491	5.46	-23859.91958	-1.613
CrPrCoGa	Hg_2CuTi (FM)	6.4033	100.189	5.68	-27262.51354	-1.535
CrPrCoIn	Hg_2CuTi (FM)	6.6426	79.6275	4.49	-35140.81884	-1.442

We computed the formation energy to establish the viability of this chemical and its potential for experimental synthesis; using the following relation [9]:

$$\Delta H = E_f^{\mathrm{CrPrCoZ}} = E_{\mathrm{tot}}^{\mathrm{CrPrCoZ}} - E_{\mathrm{Pr}}^{\mathrm{bulk}} - E_{\mathrm{Cr}}^{\mathrm{bulk}} - E_{\mathrm{Co}}^{\mathrm{bulk}} - E_{\mathrm{Z}}^{\mathrm{bulk}} \tag{III.10}$$

Where E_f^{CrPrCoZ} is the equilibrium energy of these compounds, in which $E_{\mathrm{tot}}^{\mathrm{CrPrCoZ}}$ is the total energy of compounds and $E_{\mathrm{Cr}}^{\mathrm{bulk}}$, $E_{\mathrm{Pr}}^{\mathrm{bulk}}$, $E_{\mathrm{Co}}^{\mathrm{bulk}}$ and $E_{\mathrm{Z}}^{\mathrm{bulk}}$ are the chemical potential of atoms in their stable bulk for Cr, Pr, Co, and Z (Al, Ga, In), respectively.

The estimated formation energies of the compounds CrPrCoZ (Z = Al, Ga, In)

for the ferromagnetic Hg_2CuTi-type structure are −1.613, −1.535, and −1.442 Ry, respectively, indicating the stability of these alloys [10].

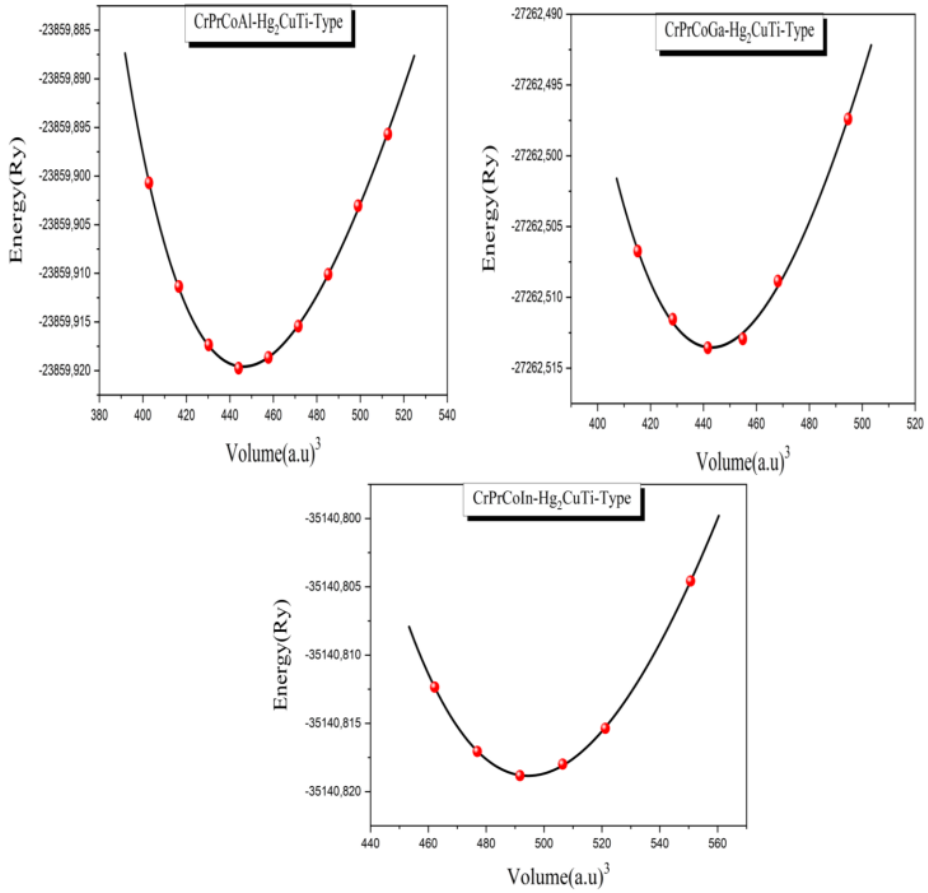


Figure III.14: Total energy versus unit cell volume for CrPrCoZ (Z = Al, Ga and In).

b. Elastic properties

For investigating the mechanical stability of ours alloys CrPrCoZ (Z = Al, Ga and In), we calculated the elastic properties of them in Hg_2CuTi-Type structure by the IRelast package [26]. *Error! Reference source not found.* represents our results using the Voigt–Reuss–Hill approximations [25]. We observe that C_{11}, C_{12}, and C_{44} values satisfy the condition $(C_{11} - C_{12}) > 0$, $(C_{11} + 2C_{12}) > 0$, $C_{11} > 0$, and $C_{44} > 0$ [26]. Thus, the structure of ferromagnetic Hg_2CuTi is mechanically stable. The values of Zener anisotropy in CrPrCoAl, CrPrCoGa, and CrPrCoIn are 5.45, 8.45, and 4.96, respectively; and the Poisson ratio are 0,379, 0.383 and 0.45 for CrPrCoAl, CrPrCoGa and CrPrCoIn, respectively. Thus, indicating a high elastic anisotropy and confirming

that our quaternary compounds are ductile and not elastically isotropic.

Table III.7: Elastic constants (C_{ij}), bulk modulus (B), Shear modulus (G) Young modulus (E), Poisson's coefficient (ν). The zener anisotropy (A).

Alloy	C_{11}	C_{12}	C_{44}	B	G	E	ν	A
CrPrCoAl	124.632	104.012	56.258	110.884	29.047	80.142	0.379	5.45
CrPrCoGa	109.663	96.240	56.745	100.714	25.490	70.520	0.383	8.45
CrPrCoIn	111.389	94.118	42.838	69.874	28.664	25.355	0.450	4.96

c. Thermodynamic properties

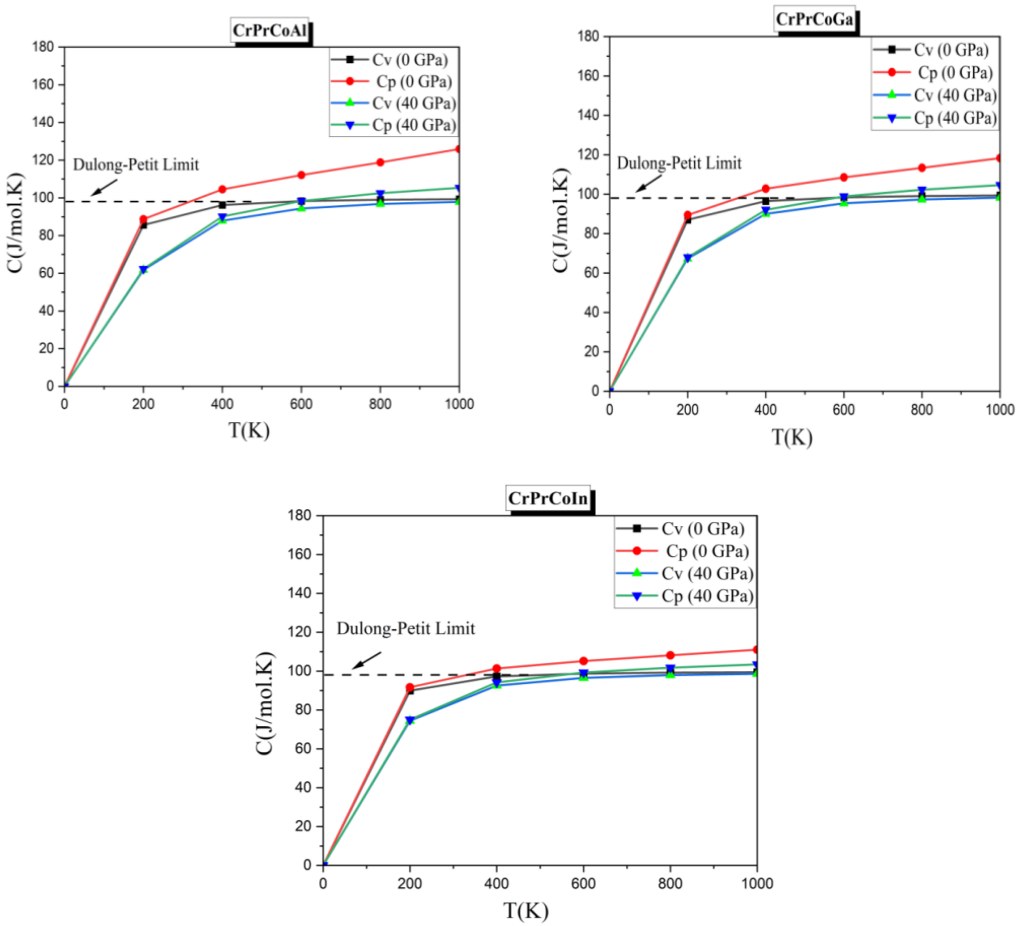


Figure III.15: Heat capacity as function of temperature in different pressure for CrPrCoZ (Z = Al, Ga and In).

The thermodynamic properties of our quaternary Heusler alloys CrPrCoZ (Z=Al, Ga and In), in ferromagnetic Hg_2CuTi-Type structure were calculated using the Gibbs2

package , a new version of the quasiharmonic model for solid-state thermodynamics [32, 36, 37]. The temperature range was chosen between 0 and 1000 K. In addition, the pressure value varies from 0 to 40 GPa to evaluate the energy or the number of phonons needed to raise the temperature of the materials. The Figure III.15 shows the calculated connections between heat capacities (C_v and C_p) and temperatures at various pressures for all materials.

Within the range of 0 to 300 K, C_V increase rapidly until it's reached the Dulong–Petit Limit (100 J/mol·K) then increase linearly in the rest of the range and C_P increase rapidly then increase slowl. We have also seen that for C_v and C_p, their values at ambient pressure are higher than under pressure (up to 40 GPa). This behavior indicates that atomic interactions are dominant at low temperatures in these compounds.

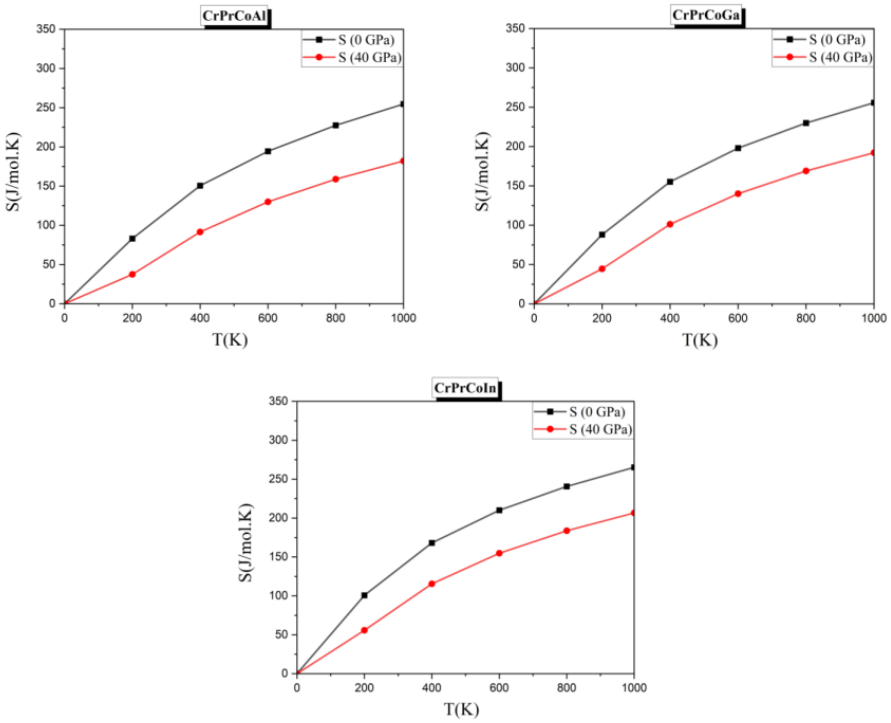


Figure III.16: Entropy as function of temperature in different pressures for CrPrCoZ (Z = Al, Ga and In).

The Figure III.16 shows the entropy (S) as a function of temperature (T) under two different pressures (0 GPa and 40 GPa) for three Heusler ferromagnetic alloys CrPrCoZ (Z=Al, Ga and In), in ferromagnetic Hg_2CuTi-Type structure. We observe that the entropy increases monotonically with temperature due to increased thermal

disorder. This is consistent with the basic thermodynamic relationship [31]. However, at constant temperatures, the entropy decreases with increasing pressure. This is due to the decrease in atomic disorder under pressure. This indicates that higher pressure reduces entropy, likely due to the inhibition of vibrational motion in the crystal lattice.

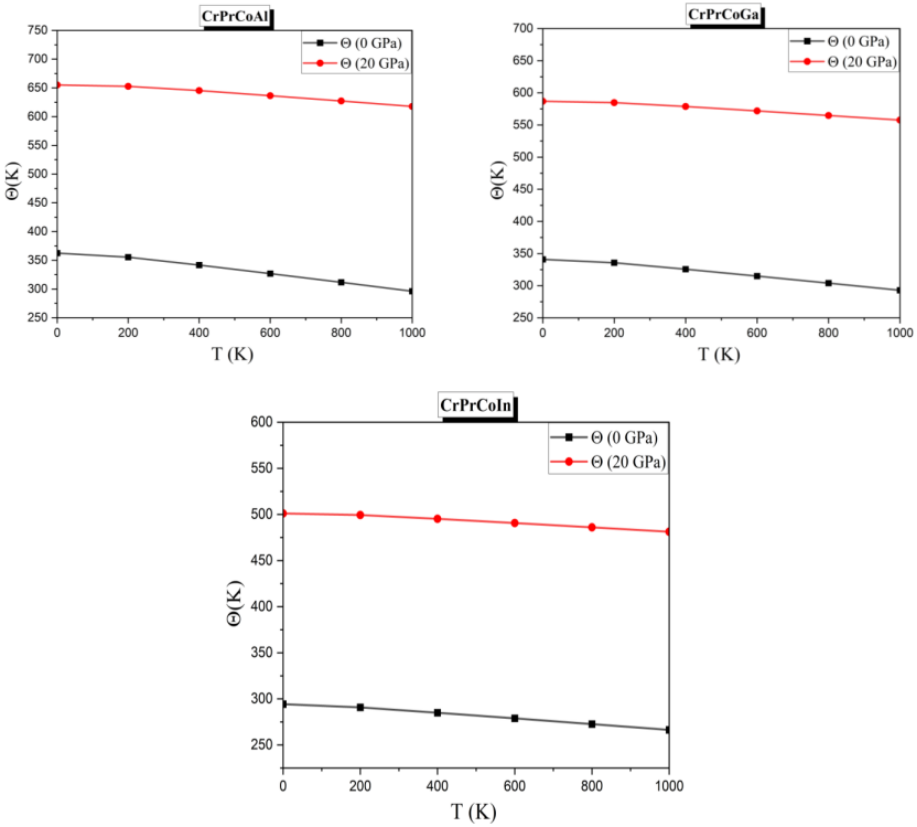


Figure III.17: Debye temperature as function of temperature in different pressure for CrPrCoZ (Z = Al, Ga and In).

The Figure III.17 illustrates how the Debye temperature Θ (K) changes with temperature (T) at two pressure values (0 GPa, 40 GPa). This basic parameter provides important information on the specific heat and melting temperature. We note that the Debye temperature decreases with increasing temperature in all quaternary Heusler CrPrCoZ (Z=Al, Ga and In), in ferromagnetic Hg_2CuTi-Type structure, whether at 0 or 40 GPa. As the temperature increases in these materials, the intensity of atomic vibrations increases, causing the atoms to vibrate around their positions at relatively regular frequencies [34]. This leads to a weakening of the dynamic rigidity of the material, meaning that the atoms move more freely, thus decreasing the Debye temperature. Meanwhile, the Debye temperature increases with increasing pressure at a

constant temperature.

When we apply high pressure to a solid, the atoms in the crystal lattice become closer together. This closeness leads to increased interatomic forces because the atoms are now at shorter distances. As a result, the rigidity of the crystal lattice increases, and it becomes more difficult to make the atoms vibrate, which increases the vibrational frequencies of the phonons, thus increasing the Debye temperature.

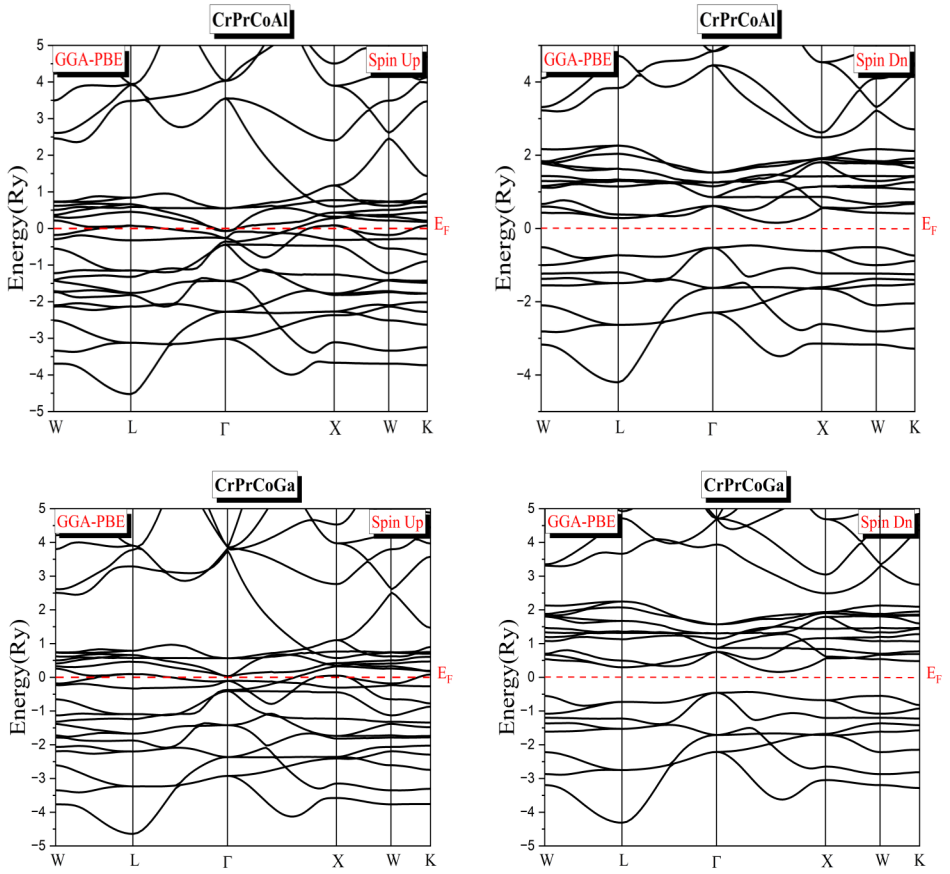
d. Electronic Properties

The distribution of electrons in the valence and conduction bands, as well as the gap value, fundamentally determine the solid's electronic properties, including its band structure, density of states. As mentioned above, we plotted the band structures and the total density of states of CrPrCoZ (Z = Al, Ga, In) compounds for both spins' direction (down and up). This investigation aims to elucidate the electronic structure of these compounds within the stable Hg_2CuTi structure in a ferromagnetic configuration at the equilibrium lattice parameter, employing the GGA-PBE approximation [4]. The band structure and DOS illustrated in Figure III.19, respectively with the corresponding band gap values detailed in Table III. 8.

From Figure III.18 (a, c and e) in which we plotted the majority spin direction (up) our compounds CrPrCoZ (Z=Al, Ga and In) respectively, we remark an overlap between conduction and valence band indicating the metallic behaviour of our alloys in this direction. Furthermore, the minority spin direction of our alloys plotted in Figure III. 18 (b, d and f), where we observe an indirect band gap, an energy gap emerges between the higher of the valence band between the Γ and X points and the lower of the conduction band between Γ and X points with gap energy of 0.526 eV and 0.495 eV for CrPrCoAl and CrPrCoGa, respectively, in which they increase comparing with Pr_2CoAl and Pr_2CoGa of gap energy of 0.36 and 0.474 eV [35], respectively, however it emerges between the higher of the valence band at Γ point and the lower of the conduction band between Γ and X points with gap energy of 0.337 eV for CrPrCoIn in which decease in value comparing with Pr_2CoIn of energy gap of 0.49 eV [35]. Consequently, we arrive at the conclusion that all compounds exhibit half-metallic behaviour.

Table III.8: The calculated total magnetic moments (Mt) and atomic magnetic moments for the CrPrCoZ (Z = Al, Ga, In).

Alloys	a (Å)	μ_{tot}	μ_{Cr}	μ_{Pr}	μ_{Co}	μ_{Z}	$\mu_{\text{interstitial}}$	E_g (eV)
CrPrCoAl	6.420	5.00	2.9533	1.6886	0.1885	-0.0547	0.2249	0.526
CrPrCoGa	6.403	5.00	3.0176	1.7230	0.0586	-0.0606	0.2565	0.495
CrPrCoIn	6.642	5.00	3.2997	1.8608	-0.4205	-0.0438	0.3139	0.337



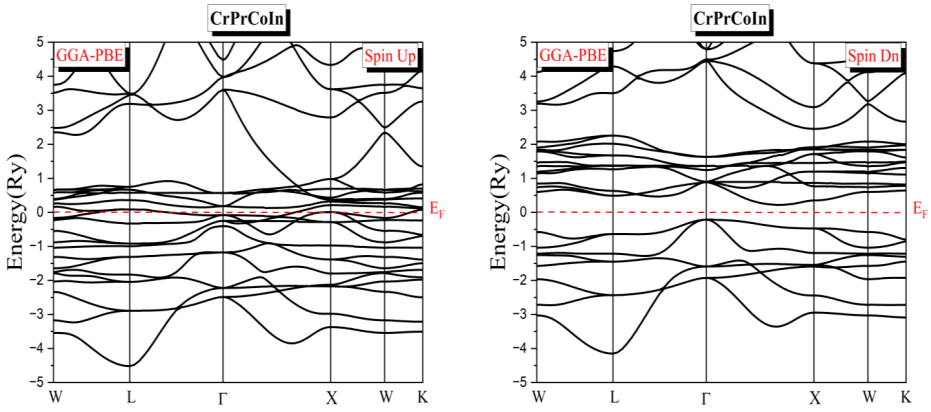


Figure III.18: Spin-polarized band structures of majority spin (Up) and minority spin (Down) of CrPrCoZ (Z = Al, Ga, In) in Hg_2CuTi type structure.

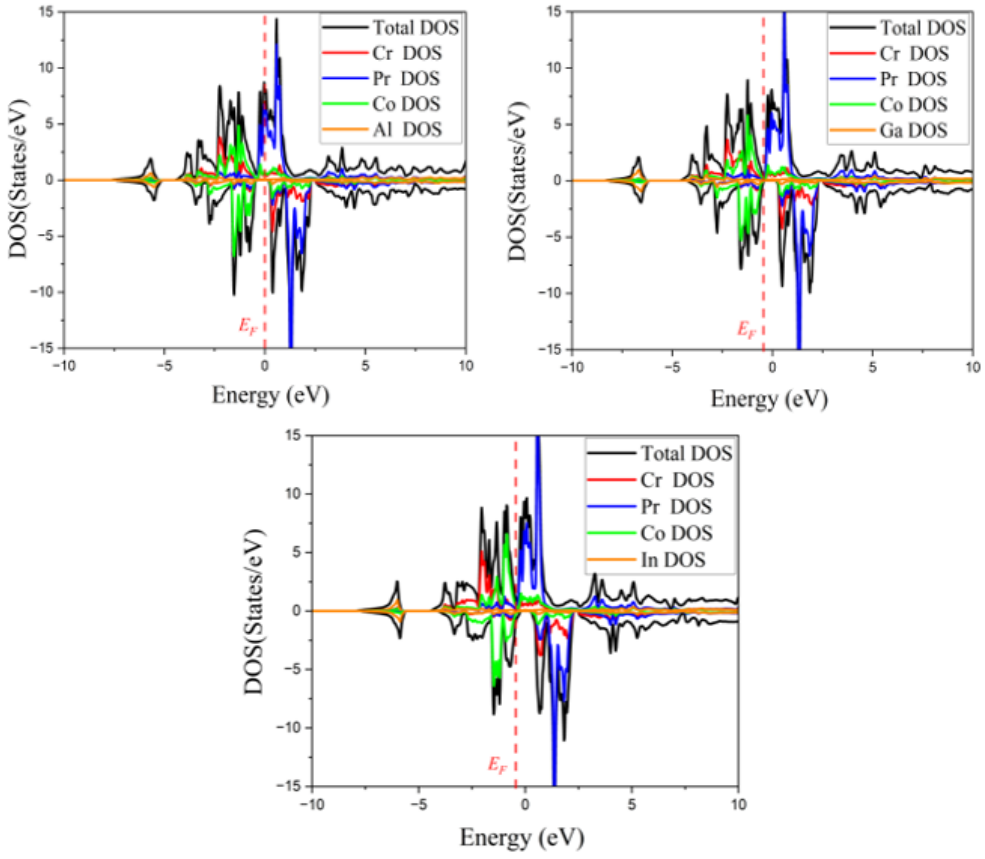


Figure III.19: Total and partial density of state for both spin direction (up and down) of CrPrCoZ (Z = Al, Ga, In) alloys in Hg_2CuTi type structure.

The computed spin polarisation total density of states (DOS) and partial DOS of CrPrCoZ (Z = Al, Ga, In) compounds at their equilibrium lattice parameters are presented in Figure III.19.

Energy levels below −5 eV, predominantly derived from the s states of post-transition metal (Al, Ga or In) atoms, are committed from Figure III. 19 owing to their near-symmetry in both majority and minority spin orientations. These states are much removed from the Fermi level and, as a result, do not influence the magnetic characteristics. The f states of Pr constitute the predominant portion of the total density of states (DOS) at the Fermi level. The d electrons of Co atoms determine the band gap around the Fermi level in all alloys. The d-orbitals of Cr atoms dominated below the Fermi level for majority spins and above the fermi level for minority spin and the d-orbitals of Co atoms dominated the majority of valence band for both spin direction. The density of states above the Fermi level is mostly affected by the Pr and Co atoms, and we have computed the spin polarisation ratio (P) for these three compounds. The computation of spin polarisation can be accomplished using by

$$P = \frac{N^{\uparrow}(\varepsilon_F) - N^{\downarrow}(\varepsilon_F)}{N^{\uparrow}(\varepsilon_F) + N^{\downarrow}(\varepsilon_F)} \tag{III.11}$$

Were $N^{\uparrow}(\varepsilon_F)$ and $N^{\downarrow}(\varepsilon_F)$ indicate the density of states (DOS) for majority-spin and minority-spin states at the Fermi level, respectively. The three analysed compounds have a complete (100%) spin polarisation ratio at the Fermi level.

e. Magnetic Properties

In two pivotal articles, Slater and Pauling demonstrated that the introduction of a single valence electron in binary magnetic compounds leads to occupancy of spin-down states, hence diminishing the overall spin magnetic moment by 1 μ_B [15]. Significantly, half- metallic Heusler alloys exhibit similar characteristics. The total spin magnetic moment within the unit cell is directly proportional to the total count of valence electrons [16].

Table III.8 presents the calculated magnetic moment for the complete Heusler alloys CrPrCoAl, CrPrCoGa, and CrPrCoIn at their optimum lattice parameters. All examined alloys display integer magnetic moments of 5 μ_B. Half-metallic materials are characterised by an integer total magnetic moment. Thus, CrPrCoAl, CrPrCoGa, and CrPrCoIn are categorised as half-metallic ferromagnets (HMF) within the classification

of full Heusler alloys.

Analysis of the magnetic moment values for each atom in the compounds listed in Table III. 8 indicates that the primary contribution to the total magnetic moment originates from the Pr atoms. Conversely, the contributions of Al, Ga, and In atoms to the overall magnetic moment are negligible.

The electronic configurations of the atoms within our molecules are Cr:$[Ar]_3d^5\,4\,s^1$, Pr:$[Xe]_4f^3\,6\,s^2$, Co:$[Ar]_4s^2\,3\,d^7$, Al:$[Ne]_3s^2\,3\,p^1$, Ga:$[Ar]_3d^{10}\,4\,s^2\,4\,p^1$, In:$[Kr]_4d^{10}\,5\,s^2\,5\,p^1$.

Furthermore, the compounds CrPrCoAl, CrPrCoGa, and CrPrCoIn possess the same quantity of valence electrons, totalling 23. Our findings demonstrate a linear correlation between the total spin magnetic moment and the number of valence electrons, consistent with the established Slater–Pauling connection [**?**], expressed by the following equation:

$$\mu_{\text{tot}} = Z_{\text{tot}} - 18 \tag{III.12}$$

where Z_{tot} the total number of valence electrons per unit cell and μ_{tot} is the total spin magnetic moment [21].

III.3.2 Full Hesler transition metal-based alloys

III.3.2.1 Full Heusler Ir_2ScZ (Z = Ga, Ge)

a. Structural stability

The Heusler compounds have a stoichiometry composition of X_2YZ where X and Y are transition metals and Z is a main group element. The full-Heusler compounds crystallizing in the cubic structure have two types: the $AlCu_2Mn$ and $CuHg_2Ti$. The two structures consist of four interpenetrating fcc sub-lattices and four crystal sites: A (0,0,0), B (1/4,1/4,1/4), C (1/2,1/2,1/2) and D (3/4,3/4,3/4). In the Cu_2MnAl-type, X atoms occupy the (A, C) site, while in the Hg_2CuTi-type structure the (A, B) sites are occupied by X atoms.

Table III.9 summarizes the optimal lattice constants and bulk moduli obtained for the $L2_1$ crystal structure of Ir_2ScGa and Ir_2ScGe alloys in both Cu_2MnAl and Hg_2CuTi type structure in ferromagnetic (FM) states. These values were determined

by analyzing the "volume–energy curves" for each sample (Figure III.20).

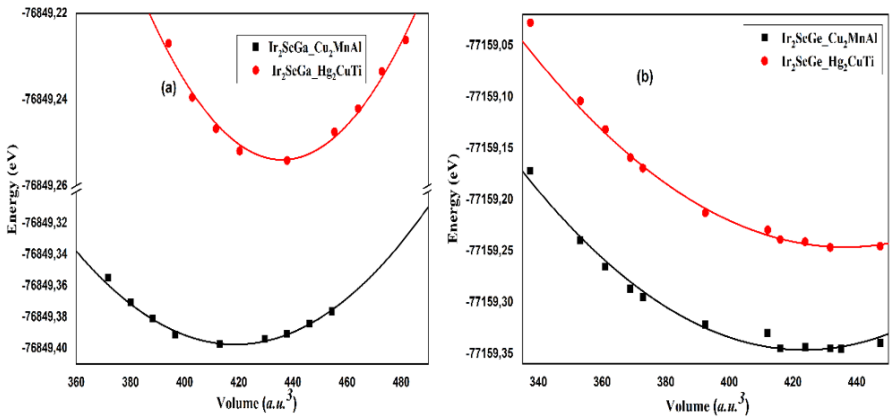


Figure III.20: Total energy as a function of unit cell volume for: (a) Ir_2ScGa for both Hg_2CuTi and Cu_2MnAl type structures (b) Ir_2ScGe for both Hg_2CuTi and Cu_2MnAl type structures

Our results reveal that the Cu_2MnAl type structure has lower energy compared to the Hg_2CuTi type structure for all alloys, indicating their inherent stability in the ferromagnetic configuration. The lattice parameter steadily increases from 6.27 Å for Ir_2ScGa Heusler compound to 6.37 Å for Ir_2ScGe Heusler compound as the atomic size of the Z atom increases from Ga to Ge. This expansion is accompanied by a corresponding decrease in the bulk modulus, which measures the material's stiffness.

Table III.9: The variation of the lattice constant (a_0), bulk modulus (B_0), the bulk modulus' derivative, and the ground state energies of the seven quaternary Heusler alloys at both ferromagnetic and paramagnetic states

Alloys	a (Å)	B (GPa)	B'	$E_{\min}$ (eV)	Magnetic phase
Ir_2ScGe–Hg_2CuTi type	6.4053	133.3756	6.1399	-77159.2461	FM
Ir_2ScGe–Cu_2MnAl type	6.3711	81.7118	6.5216	-77159.3430	FM
Ir_2ScGa–Hg_2CuTi type	6.3528	191.3582	5.5967	-76849.2544	FM
Ir_2ScGa–Cu_2MnAl type	6.2715	210.6013	5.0614	-76849.3976	FM

In this section, we explore the stability of the Ir_2ScGa and Ir_2ScGe alloys in both Cu_2MnAl and Hg_2CuTi type structure; we use the GGA-PBE method to calculate its cohesion and formation energies. This calculation can indicate the feasibility of synthesizing these compounds within a laboratory environment. Cohesion energy (E_c) reflects

the binding strength between atoms in a solid state, and it's linked to the material's ground-state structural stability. To calculate the cohesion energy per formula unit of Ir_2ScGa and Ir_2ScGe alloys, we compare the total energies of individual Ir, Sc, Ga and Ge atoms with the total energy of the entire Ir_2ScGa and Ir_2ScGe alloys compounds in its equilibrium state. That is:

$$E_c = 2E_{Ir}^{iso} + E_{Ge}^{iso} + E_{Sc}^{iso} - E_{Ir_2ScGe}^{iso} \tag{III.13}$$

Where $E_{Ir_2ScGe}^{iso}$ is the calculated equilibrium total energy of the Ir_2ScGe compound per formula unit, and E_{Ir}^{iso}, E_{Ge}^{iso}, E_{Sc}^{iso} are the calculated total energies of isolated Ir, Ge, Sc atoms respectively.

Our calculations reveal a high cohesion energy of 11, 34 eV and 11, 62 eV for Ir_2ScGe and Ir_2ScGa alloys, signifying strong chemical bonding between its atoms. This indicates to a high degree of stability for the compound.

Formation energy provides another measure of stability, in this case, the resistance of Ir_2ScGe to decompose into its constituent elements. Formation energy is calculated by difference between the total energy of Ir_2ScGe Heusler in its equilibrium state and the combined total energies of the individual atoms.

Mathematically, this can be expressed as

$$E_F = E_{Ir_2ScGe}^{bulk} - (2E_{Ir}^{bulk} + E_{Ge}^{bulk} + E_{Sc}^{bulk}) \tag{III.14}$$

Where E_F represents the formation energy, and E_{Ir}^{bulk}, E_{Ge}^{bulk}, E_{Ga}^{bulk} and E_{Sc}^{bulk} represent the total energies per atom for bulk Ir, Ge, Ga and Sc respectively.

The calculated formation energy for Ir_2ScGe and Ir_2ScGa are -0,83 Ry and -0,85 Ry respectively, indicating its thermodynamic stability in the regular cubic Heusler structure.

b. Elastic proprieties

The study of elastic constants provides a valuable tool for predicting the mechanical behaviour of materials due to the inherent connection between a material's mechanical and dynamical properties, ultimately determined by the internal forces. In this

work, we utilized the IRelast package within the WIEN2k software to calculate the elastic constants for Ir_2ScGe and Ir_2ScGa Heusler alloys [38, 39]. In a cubic structure, the determination of elastic constants can be simplified, as only three independent parameters are needed (C_{11}, C_{12}, C_{44}). The first two components (C_{11} and C_{12} can be derived from the bulk modulus, while the second component is established through volume-conserving tetragonal strain calculations based on the total energy of both strained and unstrained structures. The third independent component is determined using a volume-conserving rhombohedral strain approach, again relying on total energy considerations [39, 40].

After calculating the elastic constants C_{ij}, various important physical properties can be derived, such as the bulk modulus, shear modulus, Young's modulus, and Poisson's ratio, using the Hill-Voigt-Reuss approximations [38, 41, 42]. Table III.10 provides the resulting values for C_{11}, C_{12}, C_{44}, B, G, E, ϑ, Anisotropy A and the B/G ratio. It is noteworthy that for Ir_2ScGa Heusler alloys in the Cu_2MnAl structure, the computed elastic constants satisfy the Born mechanical stability criteria [38], confirming their mechanical stability. However, Ir_2ScGa Heusler alloys in the Hg_2CuTi structure, as well as Ir_2ScGe Heusler alloys in both the Hg_2CuTi and Cu_2MnAl structures, are mechanically unstable.

Table III.10: Elastic properties.

Material	C_{11}	C_{12}	C_{44}	Bulk modulus (B)	Shear modulus (G)
$Ir_2ScGa\_Hg_2CuTi$	124.901	210.672	73.0815	182.081	26.694
$Ir_2ScGa\_Cu_2MnAl$	335.946	181.523	122.601	232.998	104.445
$Ir_2ScGe\_Hg_2CuTi$	72.6486	194.984	26.4425	154.205	8.602
$Ir_2ScGe\_Cu_2MnAl$	22.6220	240.165	68.2386	167.650	2.565

Material	Poisson's ratio (ν)	Anisotropy factor (A)	B/G ratio
$Ir_2ScGa\_Hg_2CuTi$	.430	1.704	6.82
$Ir_2ScGa\_Cu_2MnAl$	.305	1.5879	2.23
$Ir_2ScGe\_Hg_2CuTi$	.528	0.432	17.93
$Ir_2ScGe\_Cu_2MnAl$	.507	0.627	65.35

Several mechanical parameters, including the bulk modulus (B), shear modulus (G), Young's modulus (Y), and Poisson's ratio (ν), offer insights into a material's stiffness and resistance to uniaxial stress. The calculated Young's modulus for Ir_2ScGe

is higher than that of Ir_2ScGa, signifying greater elastic stiffness in Ir_2ScGe. This difference likely arises from variations in cohesive forces between the two materials. Poisson's ratio (ν) serves as an indicator of solid stability, with a range of -1.0 to 0.5 for stable materials [43]. The Poisson's ratio values for Ir_2ScGa Heusler alloys in the Cu_2MnAl structure are 0.305, fall within this range, suggesting their stability under shear stress. Furthermore, according to Frantsevich et al. [44], materials with a Poisson's ratio exceeding 1/3 are typically ductile, while those below this value are brittle. Both Ir_2ScGe in both Hg_2CuTi and Cu_2MnAl structure and Ir_2ScGa in the Hg_2CuTi structure possess a Poisson's ratio greater than 1/3, indicating their ductility.

Finally, the anisotropy factor (A) serves as another indicator of mechanical stability. A negative value of (A) suggests structural instability. The positive anisotropy factors obtained Ir_2ScGa Heusler alloys in the Cu_2MnAl structure confirms their mechanical stability.

The analysis of elastic constants demonstrates the mechanical stability of Ir_2ScGa Heusler alloys in Cu_2MnAl structure. Their positive C_{ij} values satisfy the Born-Huang criteria, and their Poisson's ratio values indicate stability under shear stress. Additionally, the higher Young's modulus of Ir_2ScGe suggests greater elastic stiffness compared to Ir_2ScGa. The positive anisotropy factor (A) further supports the mechanical stability of Ir_2ScGa Heusler alloys in Cu_2MnAl structure.

c. Electronic and magnetic properties

The Density of states of Ir_2ScGa and Ir_2ScGe alloys, considering both spin-up and spin-down electrons, were calculated for the Cu_2MnAl and Hg_2CuTi crystal structures. In the Hg_2CuTi-type structure, neither Ir_2ScGe nor Ir_2ScGa exhibits any spin polarization around the Fermi level (EF), indicating their non-magnetic character. This is because both majority and minority spin bands intersect the Fermi level, making both spin channels conducting (metallic). The presence of these intersecting bands across both spin channels signifies that Ir_2ScGe and Ir_2ScGa in the Hg_2CuTi structure are metals with a fully-compensated total magnetic moment.

The Ir_2ScGe alloy in the Cu_2MnAl-type structure does not exhibit half-metallic behavior. Instead, it shows no significant spin polarization near the Fermi level, indi-

cating a non-magnetic or weakly magnetic state. III.22 illustrates the Density of states (DOS) of Ir_2ScGe in this configuration, where both the majority and minority-spin channels are metallic, without any energy gap around the Fermi level. This characteristic classifies Ir_2ScGe (Cu_2MnAl-type) as a conventional metallic material rather than a half-metallic ferromagnet.

On the other hand, Ir_2ScGa in the Cu_2MnAl-type structure presents a fully compensated magnetic behaviour, with the total magnetic moment close to zero. This suggests that Ir_2ScGa is a fully compensated material in this structure, where the spin moments of the different atoms cancel each other out, maintaining a non-magnetic state.

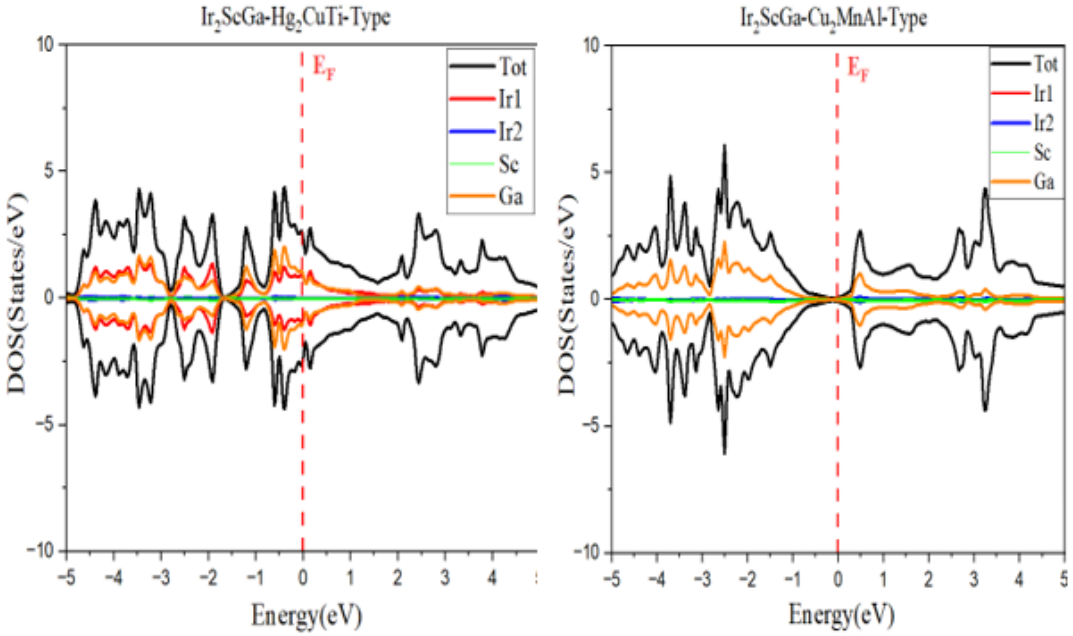


Figure III. 21. Density of states (DOS) of Ir₂ScGa (a) with Hg₂CuTi type structures (b) with Cu₂MnAl type structures

Figure III.21: Density of states (DOS) of Ir_2ScGa (a) with Hg_2CuTi type structures (b) with Cu_2MnAl type structures

Figure III.21 and Figure III.22 show the total DOS for Ir_2ScGa and Ir_2ScGe, respectively. For Ir_2ScGa III.21, both Cu_2MnAl (a) and Hg_2CuTi (b) structures exhibit metallic behavior with finite DOS at E_F from both spin channels, leading to no spin polarization and fully compensated magnetism in Cu_2MnAl (logical from symmetric up/down DOS). Similarly, Ir_2ScGe (Figure III.22) shows metallic crossing at E_F in

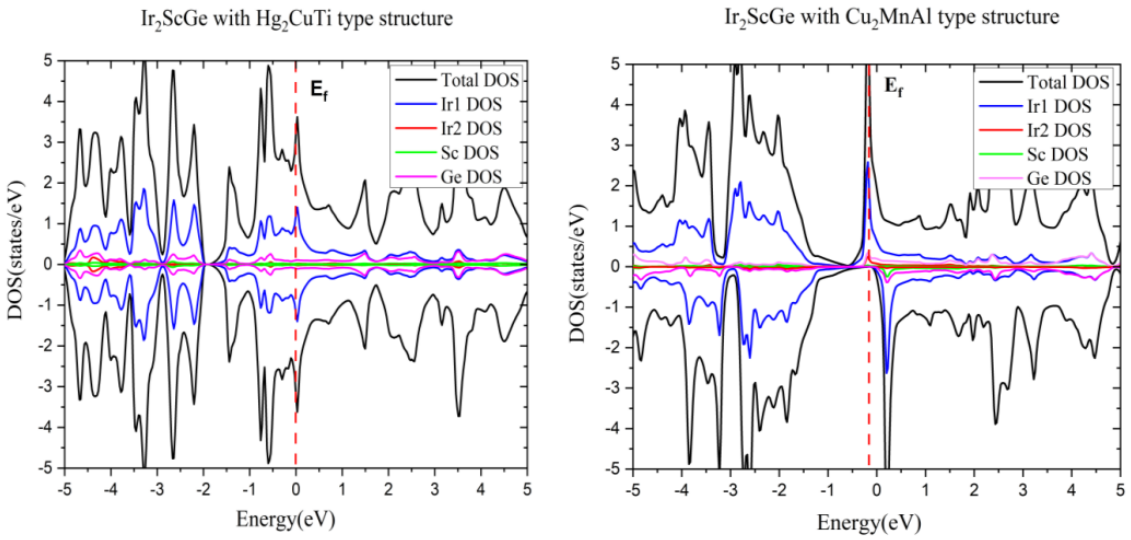


Figure III.22: Density of states (DOS) of Ir_2ScGe (a) with Hg_2CuTi type structures (b) with Cu_2MnAl type structures.

both structures, with weak asymmetry in Cu_2MnAl suggesting minor magnetism (total moment $\sim 0.98\mu_B$ from Table III.11.), contrasting compensated cases. This DOS profile implies conduction via both spins, unsuitable for half-metallicity but viable for metallic optoelectronics.

In contrast to 2D materials like Sc-implanted B_5N_{10} nanocarriers, which exhibit ferromagnetic semiconductor behavior with enhanced NO sensing via DFT-calculated Density of states as reported by [45], our bulk Ir_2ScZ alloys show metallic DOS without gaps, and fully compensated magnetism in Ir_2ScGa–Cu_2MnAl. This highlights the structural dimensionality's role in tuning magnetism: 2D systems often favor ferromagnetism for sensing, while our 3D Heusler suit non-magnetic applications.

Table III.11: The variation of the total and partial magnetic moment calculated by GGA approximations.

Alloys	μ_{Tot}	μ_{Ir}	μ_{Ir}	μ_{Sc}	μ_Z	Interstitial
Ir_2ScGe–Hg_2CuTi	0.00002	0.00001	0.00001	0.00000	0.00000	0.00000
Ir_2ScGa–Hg_2CuTi	0.00045	0.00000	0.00051	0.00009	0.00003	0.00000
Ir_2ScGe–Cu_2MnAl	0.98312	0.45354	0.45353	0.00038	0.03968	0.03598
Ir_2ScGa–Cu_2MnAl	0.00000	0.00001	0.00001	-0.00001	0.00000	0.00001

Strain engineering, where controlled deformation is applied to a material, is a recognized approach for tailoring its fundamental properties. In this context, we investigated the impact of uniform strain on the band structures of Ir_2ScGa and Ir_2ScGe in both

the regular and inverted cubic Heusler phases. Our initial focus was on how uniform strain affects the total and atomic magnetic moments of the two Ir atoms (Ir(A) and Ir(B)). As shown in Table III.11, the total magnetic moment of both Ir_2ScGa and Ir_2ScGe in the Cu_2MnAl-type structure remains constant at 0.0 μ_B indicates preserved fully-compensated magnetism under strain. However, the individual spin moments of the two Ir atoms exhibit sensitivity to changes in the lattice constant. The magnitudes of the atomic magnetic moments for Ir at distinct crystallographic sites consistently decrease as the lattice is compressed. The magnetic moments of Sc(C) and (Ge, Ga) atoms are negligible and not shown. Notably, the characteristic of fully-compensated ferrimagnetism arises from the antiparallel alignment of the two Ir moments.

III.3.2.2 Full Heusler Ru_2MnZ (Z = Sb, Sn, Te):

a. structural properties

Heusler compounds are generally expressed as X_2YZ (full Heusler compound), XX′YZ (quaternary Heusler compound), or XYZ (half Heusler compound); these compounds exhibit a high degree of order. Four FCC sublattices, which move 1/4 of the way along the body's diagonal line, make up the crystal structure of a complete Heusler compound [**?**]. There are two potential crystal structures for the full Heusler X_2YZ compounds, and they are mentioned in Table III.12. The first crystal structure is called Cu_2MnAl and has the space group number 216 $Fm\bar{3}m$. The second crystal structure is called Hg_2CuTi and has the space group number 225 $F\bar{4}3m$.

The structure displays four equidistant sites, with Wyckoff locations of A(0,0,0), B(0.25,0.25,0.25), C(0.5,0.5,0.5), and D(0.75,0.75,0.75). The full Heusler alloys with the general formula X_2YZ typically crystallize in two different ways: the inverse Heusler with the XA structure and the prototype being Hg_2CuTi, and the full Heusler with the $L2_1$ structure with Cu_2MnAl as the prototype (Table III.12).

Their symmetry and atomic ordering are the main distinctions between these structures. Compared to the less symmetric Hg_2CuTi structure (F-43m), the Cu_2MnAl structure's higher symmetry (Fm-3m) frequently results in increased stability and unique magnetic characteristics. The differences in the physical characteristics examined in the following tables are framed by this structural distinction.

The number of valance electrons in transition metal elements has a considerable influence on the type of structure. A prototype of an inverse Heusler alloy with Hg_2CuTi as the element Y is observed if Y is more electronegative than X [47]. The distinction between the two groups, which are both made up of four interpenetrating fcc sub lattices, is that one of the four sublattices—the C1b structure may remain empty [47]. The equilibrium ground state of characteristics will be emphasized in this section. This is an essential first step towards comprehending the properties of Ru_2Mn(Sb,Sn,Te) HAs compounds from a microscopic perspective, of Cu_2MnAl, and Hg_2CuTi phases. Plots of the estimated total energy for $L2_1$ and XA-type structures as a function of volume are shown in Figure III.20.

In the ferromagnetic state, the equilibrium lattice parameters of the Hg_2CuTi and Cu_2MnAl type structure for the Ru_2Mn(Sb,Sn,Te) Heusler alloy were examined. By fitting the total energy and volume of the alloy under consideration, the minimal lattice parameters were determined using the second order Birch Murnaghan equation of state [43, 7].

$$E(V) = E_0 + \frac{B}{B'(B'-1)}\left[V\left(\frac{V_0}{V}\right)^{B'} - V_0\right] + \frac{B}{B'}(V - V_0) \tag{III.15}$$

Where B, V, B', E_0, and V_0 denote the bulk modulus, volume, first derivative of the bulk modulus, minimum energy at $T = 0$ K, and the equilibrium volume, respectively.

Table III.13 provides calculated structural parameters, including lattice constants (a), bulk modulus (B), its pressure derivative (B'), ground-state energy (E), and formation energy (ΔH_f) for Ru_2Mn(Sb, Sn, Te) in both structures.

The sequence in Ru_2Mn(Sb,Sn,Te) is X–Y–X–Z because the X(Ru) atom has a valence of 8, which is bigger than the Y(Mn) atom of 7. As a result, the Cu_2MnAl type structure is more stable than the Hg_2CuTi type structure. Figure III.20 shows the variation of total energies as a function of volume for Ru_2Mn (Sb, Sn, Te) with both the Cu_2MnAl-type and the Hg_2CuTi- type structures. The results of in Figure III.23 demonstrate that the Cu_2MnAl type structure is more stable than the Hg_2CuTi one.

For bulk modulus, (B GPa): Shows the stiffness of the material (greater B = stiffer).

Cu_2MnAl (203.0 GPa) > Hg_2CuTi (182.1 GPa) for Ru_2MnSb. Hg_2CuTi (165.6 GPa) > Cu_2MnAl (127.7 GPa) for Ru_2MnSn. Cu_2MnAl (187.7 GPa) > Hg_2CuTi (128.7 GPa) for Ru_2MnTe. Finding: Stiffness varies depending on the structural type; there is no uniform pattern between metals.

Based on the energy of formation (EF), we explore the phase stability of Ru_2Mn (Sb,Sn,Te). This can be used to determine whether the examined alloys can be manufactured in a laboratory. Total energies of constituent atoms of various elements involved in compound production are compared to total energies of Ru_2Mn (Sb,Sn,Te)Heusler compounds. The energy of production of Ru_2Mn (Sb,Sn,Te) materials is calculated using the following relationship:

$$\Delta E_f = E^{total}_{\mathrm{Ru_2MnZ}} - \left[2E^{bulk}_{\mathrm{Ru}} + E^{bulk}_{\mathrm{Mn}} + E^{bulk}_{\mathrm{Z}}\right] \tag{III.16}$$

Where E^{bulk}_{Ru}, E^{bulk}_{Mn}, and E^{bulk}_{Z} represent the total energy per atom for the elements Ru, Mn, and Z ($Z = \mathrm{Sb, Sn, Te}$) in their bulk form, respectively, and $E^{total}_{\mathrm{Ru_2MnZ}}$ is the equilibrium total energy for both types of crystal structures (Hg_2CuTi and Cu_2MnAl). Because the formation energy values for the Ru_2Mn (Sb,Sn,Te) compounds presented in Table III.13 are negative, indicating chemical stability, these alloys can be made experimentally. Cu_2MnAl type structure exhibit higher negative computed formation energy EF values than Hg_2CuTi type structure, implying that Cu_2MnAl type structures are more stable.

Thermodynamic stability in relation to constituent elements is shown by negative values.

Ru_2MnSb: Hg_2CuTi (-1.501187 Ry) > Cu_2MnAl (-1.621504 Ry). Hg_2CuTi (-1.444747 Ry) is marginally less stable than Ru_2MnSn: Cu_2MnAl (-1.462548 Ry). Ru_2MnTe: Hg_2CuTi (-1.395964 Ry) > Cu_2MnAl (-1.498436 Ry). Finding: Ru_2MnSn has similar stability across structures, although Cu_2MnAl is generally more stable (more negative ΔH_f) for Ru_2MnSb and Ru_2MnTe.

Ground-State Energy (E, Ry): Lower E suggests a more energetically favorable configuration.

Ru_2MnSb: Cu_2MnAl (-33412.043164 Ry) < Hg_2CuTi (-33411.922847 Ry).

Ru_2MnSn: Cu_2MnAl (−32894.803986 Ry) < Hg_2CuTi (−32802.827978 Ry).

Ru_2MnTe: Cu_2MnAl (−34038.511471 Ry) < Hg_2CuTi (−34038.408999 Ry).

Observation: Cu_2MnAl has lower E for Ru_2MnSb and Ru_2MnTe, but not for Ru_2MnSn, where Hg_2CuTi is lower. However, ΔH_f (which accounts for elemental energies) is a better stability indicator.

Table III.12: The sites occupied by atoms: A, B, C and D for both structure Hg_2CuTi and Cu_2MnAl.

Alloy	Crystallized structure	type structure	Chemical Formula	Position	Space group
Direct Heusler	L_{21}	Cu_2MnAl	X_2YZ	A (0, 0, 0) C (0.5, 0.5, 0.5) B (0.25, 0.25,0.25) D (0.75,0.75, 0.75)	225 Fm-3m
Inverse Heusler	XA	Hg_2CuTi	X_2YZ	A (0, 0, 0) B (0.25, 0.25,0.25) C(0.5, 0.5, 0.5) D(0.75,0.75, 0.75)	216 F − 43 m

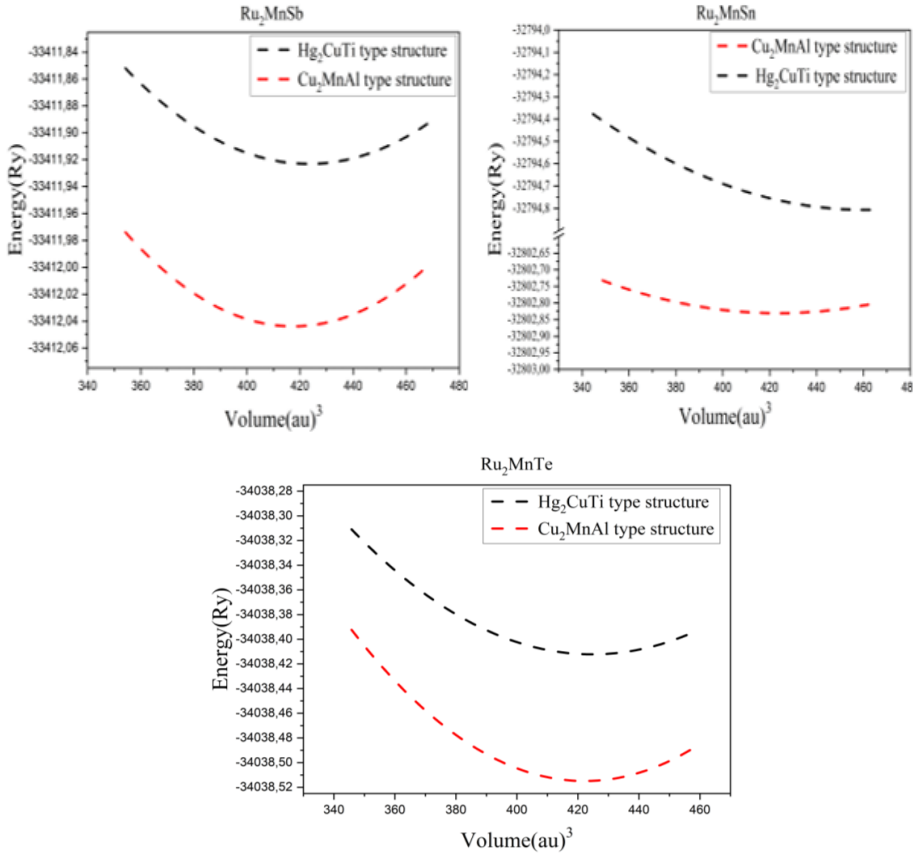


Figure III.23: Ru_2MnSb and Ru_2MnSn total energy as a function of volume for Cu_2MnAl and Hg_2CuTi type structures.

Table III.13: Calculated structural parameters of Ru_2Mn(Sb,Sn,Te) alloys for both Hg_2CuTi and Cu_2MnAl type structures; a(Å) lattice parameters, B (GPa) bulk modulus, B' pressure derivative of bulk the modulus, E minimum energy (Ry), and formation energies ΔH_f (Ry).

Alloy	Structure	a(Å)	B (GPa)	B'	E (Ry)	ΔH_f (Ry)
Ru_2MnSb	Hg_2CuTi	6.3029	182.0621	5.2532	-33411.922847	-1.501187
	Cu_2MnAl	6.2499	203.0257	4.8166	-33412.043164	-1.621504
		6.20 [46]				
Ru_2MnSn	Hg_2CuTi	6.2974	165.5978	4.6591	-32802.827978	-1.444747
		6.21 [46]				
	Cu_2MnAl	6.6395	127.6931	5.4974	-32894.803986	-1.462548
Ru_2MnTe	Hg_2CuTi	6.3100	128.7262	5.7414	-34038.408999	-1.395964
	Cu_2MnAl	6.2930	187.7294	4.6873	-34038.511471	-1.498436
Ru_2MnNb		6.19 [47]				
Ru_2MnTa		6.18 [47]				
Ru_2MnV		5.98 [47]				

Energy minima corresponding to the lattice constants in Table III.13 would be displayed in Figure III.23 (total energy vs. unit cell volume), confirming these as equilibrium structures. In accordance with the E and ΔH_f trends, the setup becomes more stable the deeper the minimum. More negative formation energies and lower ground-state energy indicate that the Cu_2MnAl structure is thermodynamically more stable for Ru_2MnSb and Ru_2MnTe. Although Cu_2MnAl has a lower B and a bigger lattice constant, which may indicate a less compact or stiffer lattice, stability for Ru_2MnSn is close between the two structures, with a tiny edge based on ΔH_f.

Ground-State Energy **(E, Ry):** Lower E suggests a more energetically favourable configuration.

Ru_2MnSb: Cu_2MnAl (-33412.043164 Ry) < Hg_2CuTi (-33411.922847 Ry)

Ru_2MnSn: Hg_2CuTi (-32802.827978 Ry) < Cu_2MnAl (-32794.803986 Ry)

Ru_2MnTe: Cu_2MnAl (-34038.511471 Ry) < Hg_2CuTi (-34038.408999 Ry)

Cu_2MnAl has lower E for Ru_2MnSb and Ru_2MnTe, but not for Ru_2MnSn, where Hg_2CuTi is lower. However, ΔH_f (which accounts for elemental energies) is a better

stability indicator.

b. Electronic properties

Any periodic crystal's electronic band structure, which is correlated with energy eigenvalues, aids in our comprehension of the Fermi levels of the substance, which establish whether a material is conducting, semiconducting, or insulating [48]. The electronic band structures and density of states DOS of $Ru_2Mn(Sb,Sn,Te)$ alloys for spin-down (↓) and spin-up (↑) states with both structures Hg_2CuTi and Cu_2MnAl are shown in Figure III.24, Figure III.25 and Figure III.26.

The valence and conduction bands of the Ru_2MnSb alloys with Hg_2CuTi type structure in Figure III.24 clearly exhibit a metallic nature as they intersect at the selected high symmetry sites. Furthermore, the corresponding total density of states of Ru_2MnSb alloys with Hg_2CuTi alloys for spin-down (↓) and spin-up (↑) components are shown in Figure III.24, which also reveals a non-symmetrical picture because of the clear polarization between these components' density of states.

The topography of the Ru_2MnSb alloy's band structure shows that there isn't an energy gap for either spin (up) or spin (down). Due to the transition metals' (Ru, Mn) composition in this alloy, there is a movement of electrons between the valence band and conduction band at the overlap level where the two bands "distribute" their electrons at the Fermi level. The Ru_2MnSb with Hg_2CuTi alloy has a metallic character, according to this result.

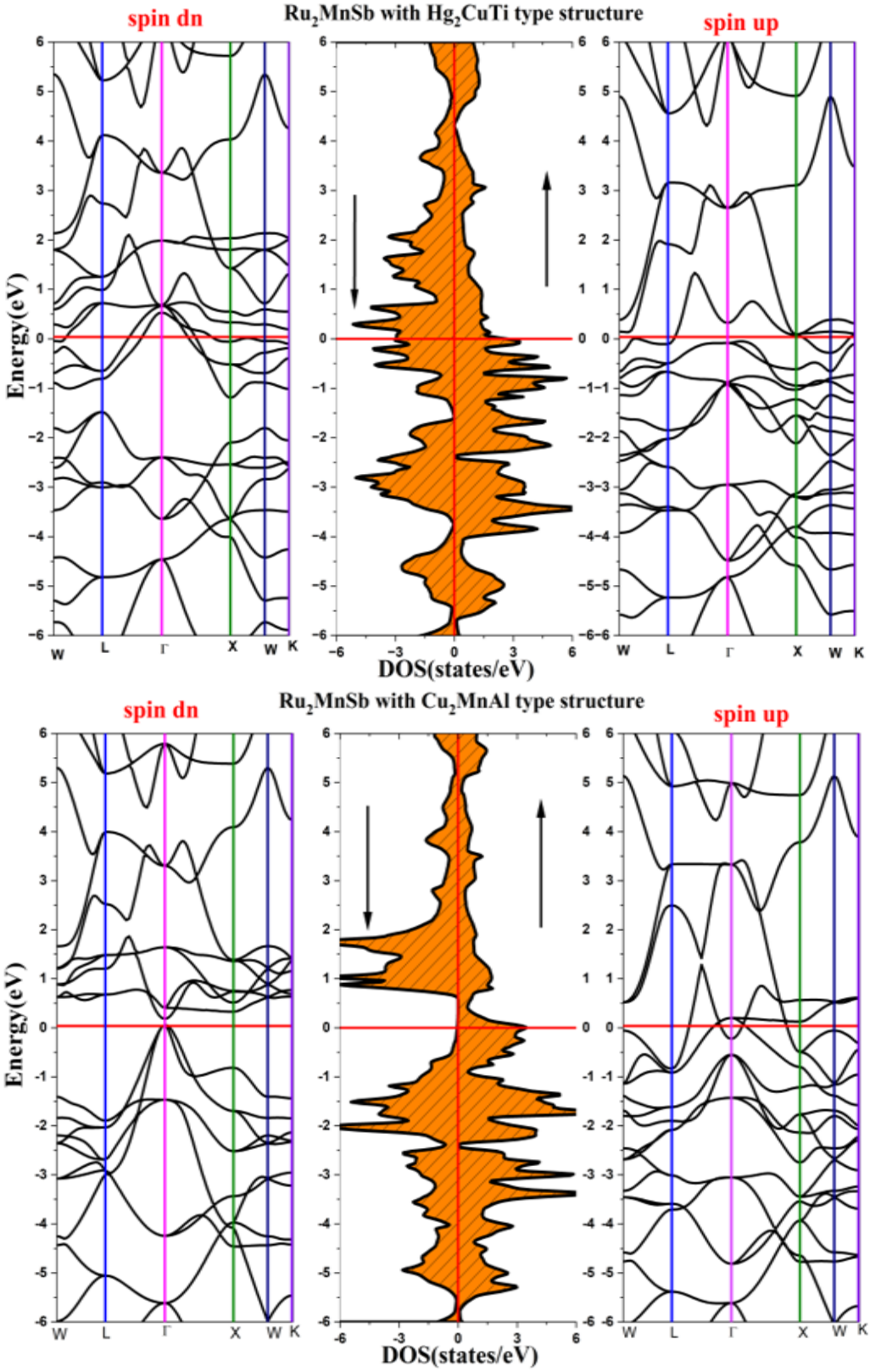


Figure III.24: Calculated spin-polarized density of states and band structure of Ru_2MnSb with both Hg_2CuTi and Cu_2MnAl types structures

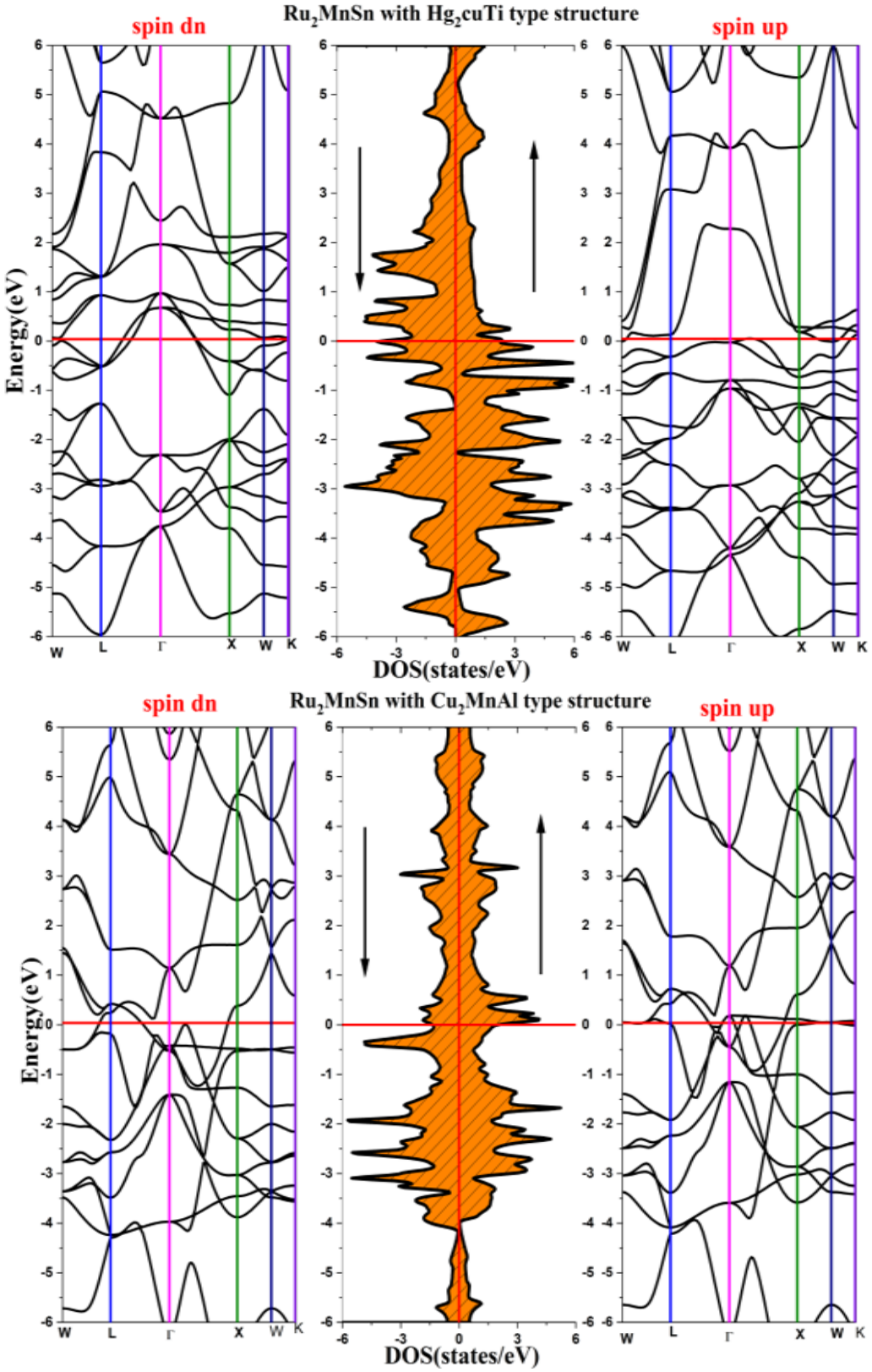


Figure III.25: Calculated spin-polarized density of Ru_2MnSn with both Hg_2CuTi and Cu_2MnAl types structures.

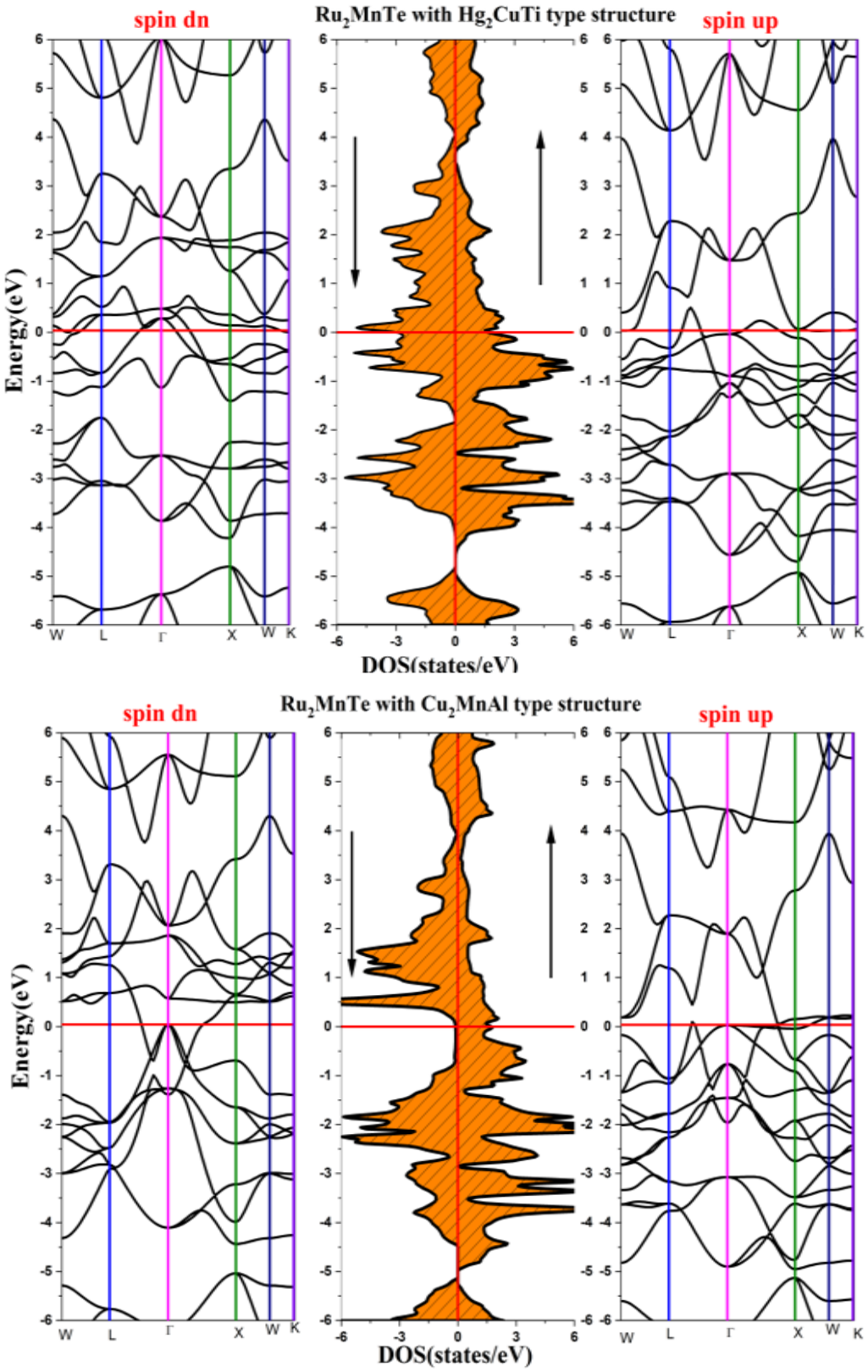


Figure III.26: Calculated spin-polarized density of states and band structure of Ru_2MnTe with both Hg_2CuTi and Cu_2MnAl types structures.

It is crucial to define the spin polarization of electrons at a material's Fermi energy, where the spin polarization at EF is provided by:

$$P = \frac{N^{\uparrow}(E_F) - N^{\downarrow}(E_F)}{N^{\uparrow}(E_F) + N^{\downarrow}(E_F)} \tag{III.17}$$

$N^{\uparrow}(E_F)$ and $N^{\downarrow}(E_F)$ are the Fermi energy's majority and minority DOS.

If one of the electron densities, $N^{\uparrow}(E_F)$ or $N^{\downarrow}(E_F)$ is equal to zero and the other is non-zero, the electrons at Ef are fully spin polarized (i.e. spin polarization = 100%) and are also referred to as half metallic.

c. Elastic properties

Since elastic constants are related to many important thermal and structural properties of solids, such as specific heat, thermal expansion, Debye temperature, mechanical deformation, binding properties, etc., determining these quantities is essential.

Cubic materials are known to have three distinct independent elastic constants, C_{11}, C_{12}, and C_{44}, as documented in literature [49, 50, 51], with $C_{11} = C_{22} = C_{33}$, $C_{12} = C_{13} = C_{23}$, and $C_{44} = C_{55} = C_{66}$. These elastic constants can be used to determine a material's longitudinal elastic behavior (C_{11}), off-diagonal behavior (C_{12}), and shear elastic characteristic (C_{44}) of a comparable material. In this work, the C_{11}, C_{12}, and C_{44} elastic constants of Ru_2Mn(Sb,Sn,Te) alloys have been determined using first-principles density functional theory (DFT).

Elastic properties of the Ru_2Mn(Sb,Sn,Te) compounds were investigated. The elastic stability criteria for cubical materials are given by the equations below:

$$C_{11} > 0,\ C_{44} > 0,\ C_{11} > |C_{12}|,\ (C_{11} + 2C_{12}) > 0 \tag{III.18}$$

Table III.14: Calculated elastic constants and moduli (in GPa) for Ru_2MnZ (Z = Sb, Sn, Te) in the Hg_2CuTi and Cu_2MnAl structures.

Compound	Structure	C_{11}	C_{12}	C_{44}	B	G_V	G_R	G_H
Ru_2MnSb	Hg_2CuTi	101.61	196.29	73.441	164.7321	25.1285	-3577.635	-1776.23
	Cu_2MnAl	328.80	136.29	109.52	200.4612	104.21	103.7997	104.007
Ru_2MnSn	Hg_2CuTi	166.90	206.55	114.10	193.3377	60.5331	-67.0338	-3.2503
	Cu_2MnAl	982.76	520.68	632.12	674.7135	471.691	373.066	422.378
Ru_2MnTe	Hg_2CuTi	94.849	167.43	45.022	143.2425	12.4957	433.695	223.095
	Cu_2MnAl	208.33	174.61	89.092	185.8530	60.1984	32.8271	46.5127

Compound	Structure	G	E	ν	C_P	G/B	A
Ru_2MnSb	Hg_2CuTi	25.12852	71.73789	0.42742	122.8513	0.15254	-1.55132
	Cu_2MnAl	104.2157	266.46971	0.27845	26.7684	0.51988	1.13783
Ru_2MnSn	Hg_2CuTi	60.53314	164.43785	0.35825	92.4492	0.31310	-5.75552
	Cu_2MnAl	471.69104	1147.63629	0.21651	-111.4382	0.69910	2.73601
Ru_2MnTe	Hg_2CuTi	12.49570	36.42784	0.45762	122.4164	0.08723	-1.24047
	Cu_2MnAl	60.19840	162.99681	0.35383	85.5224	0.32390	5.28496

The examined material is mechanically stable in the Hg_2CuTi-type structure as a result of the estimated elastic constants having positive values (see Table III.14) and satisfying the aforementioned mechanical stability conditions.

For elastic constants (GPa): C_{11} (longitudinal stiffness): Ru_2MnSn Cu_2MnAl: 982.8 GPa (extremely high). Others range from 94.8 GPa (Ru_2MnTe Hg_2CuTi) to 328.8 GPa (Ru_2MnSb Cu_2MnAl).

C_{44} (shear stiffness): Ru_2MnSn Cu_2MnAl: 632.1 GPa. So Ru_2MnSn Cu_2MnAl values are outliers, suggesting either a unique property. Shear Modulus (GH, GPa): Ru_2MnSn Cu_2MnAl: 422.4 GPa, also negative (e.g., -1776.3 for Ru_2MnSb Hg_2CuTi) or moderate (e.g., 104.0 for Ru_2MnSb Cu_2MnAl). Negative G_R values (e.g., -3577.6 for Ru_2MnSb Hg_2CuTi) indicate mechanical instability or computational issues.

Also, we determined Zener ratio (also known as the elastic anisotropy parameter,

abbreviated A), which are described as follows:

$$A = \frac{2C_{44}}{(C_{11} - C_{12})} \tag{III.19}$$

For three alloys, we found that the A value was significantly greater than 1. It is well known that materials with A values significantly different from 1 often show signs of instability in the cubic phase and have a tendency to deviate from cubic symmetry [52, 53].

The bulk modulus (B) and shear modulus (G) of an observable material are commonly used to calculate its hardness. Without a doubt, the hardness of the material affects the resistance offered at the critical point prior to a system breaking when a stress is applied [54].

Materials' ductile and brittle behavior can be inferred using the bulk modulus to shear modulus ratio (B/G), which Pugh developed [55]. Simultaneously, the brittle and ductile properties of materials are intimately associated with the critical B/G ratio value of 1.75. If the B/G is less than the critical value, the material is considered ductile; if it is larger, it is considered brittle.

The bulk, shear, and Young's moduli as well as the Poisson's ratio are among the elastic moduli that are most crucial for real-world applications and are calculated using the Voigt–Reuss–Hill [41, 42] approximation.

A measurement of resistance to volume change is the bulk modulus. Reversible shear stress deformations provide an explanation for the shear modulus [56]. The following can be ascertained by applying C_{ij} elastic constants:

$$B = \frac{1}{3}(C_{11} + 2C_{12}) \tag{III.20}$$

It is implied that the calculations are correct because the bulk modulus estimated from the ground state circumstances and elastic properties yields fairly near results.

$$G = \frac{G_V + G_R}{2} \tag{III.21}$$

With

$$G_V = \frac{(C_{11} - C_{12} + 3C_{44})}{5} \qquad \text{and} \qquad G_R = \frac{5C_{44}(C_{11} - C_{12})}{4C_{44} + 3(C_{11} - C_{12})} \tag{III.22}$$

The letters V and R stand for Voigt and Reuss bound, respectively. Representing the bulk modulus as

$$B_V = B_G = B = \frac{(C_{11} + 2C_{12})}{3} \tag{III.23}$$

We also found Young's modulus E, which defines the relationship between stress (force per unit area) and strain (proportional deformation) in a material. A material is stiffer the greater its Young's modulus value. The covalent character of the material changes with increasing value of E, which has an impact on ductility.

$$E = \frac{9BG}{3B + G} \tag{III.24}$$

One can evaluate a material's ductility or brittleness using the Poisson's ratio. When a material's Poisson's ratio is less than 0.26, it is brittle; when it is larger than 0.26, the material is ductile.

d. Magnetic properties

Table III.15: The calculated total spin magnetic moment M_{tot} (μ_B/f.u.) and atomic magnetic moments (μ_B/atom) of $Ru_2Mn(Sb,Sn,Te)$.

Alloy	M_{Ru1}	M_{Ru2}	M_{Mn}	M_Y	$M_{\text{interstitial}}$	M_{tot}
Ru_2MnSb (Hg_2CuTi)	0.31628	0.96318	3.10535	-0.00796	0.06880	4.44565
Ru_2MnSb (Cu_2MnAl)	0.20557	0.20548	3.53374	0.00733	0.05835	4.01046
						4.02 [46]
Ru_2MnSn (Hg_2CuTi)	0.29403	0.92107	3.24957	-0.02024	0.05799	4.50242
Ru_2MnSn (Cu_2MnAl)	-0.54160	-0.54163	-0.03250	0.00973	-0.01746	-1.1235
Ru_2MnTe (Hg_2CuTi)	0.21530	0.58371	3.09378	0.00258	0.06669	3.96206
Ru_2MnTe (Cu_2MnAl)	0.45643	0.45645	3.75963	0.04172	0.15659	4.87082
Ru_2MnNb						4.12 [47]
Ru_2MnTa						4.09 [47]

Based on our spin-polarized calculations, we calculated the total magnetic moment (μ_B) of $Ru_2Mn(Sb,Sn,Te)$ alloys, Table III.15 presents a comparison between the computed values of the total magnetic moment (μ_B) for $Ru_2Mn(Sb,Sn,Te)$ alloys and several other data.

Total Magnetic Moment (M_{tot}, μ_B/f.u.): Ru_2MnSb: Hg_2CuTi (4.44565) > Cu_2MnAl (4.01046, matches experimental 4.02 [46]). Ru_2MnSn: Hg_2CuTi (4.50242) vs. Cu_2MnAl (-1.12351).

Ru_2MnTe: Hg_2CuTi (3.96206) < Cu_2MnAl (4.87082). Observation: Moments vary widely; Ru_2MnSn Cu_2MnAl's negative value suggests antiferromagnetic or complex ordering.

Atomic Contributions (μ_B/atom): Mn: Dominant contributor (e.g., 3.53374 in Ru_2MnSb Cu_2MnAl). Ru: Variable, sometimes negative (e.g., -0.5416 in Ru_2MnSn Cu_2MnAl). Z (Sb, Sn, Te) and interstitial contributions: Small, typically < 0.1 μ_B.

III.4 Conclusion

In this chapter we examined the structural, electrical and magnetic properties of Heusler materials using the full potential linearized augmented plane wave approach. The structural, electrical and magnetic properties were determined using the WIEN2K software package, which is based on density functional theory (DFT). The band structure and density of states were derived using both the generalized gradient approximation (GGA) in the Perdew–Burke–Ernzerhof (PBE) scheme, with the modified Becke–Johnson potential (mBJ_{mb}), which proved effective for better electronic band reconstruction and band gap correction.

References

[1] M. Jamal, I. Ahmad, M. Bilal, S. Jalali-Asadabadi, R. Ahmad, F. Ahmad, B. Amin, and I. Murtaza. IRelast package. *Journal of Alloys and Compounds*, 735:569–579, 2018. doi:10.1016/j.jallcom.2017.10.139.

[2] A. Otero-de-la-Roza, D. Abbasi-Pérez, and V. Luaña. Gibbs2: A new version of the quasiharmonic model code. II. Models for solid-state thermodynamics, features and implementation. *Computer Physics Communications*, 182(10):2232–2248, 2011. doi:10.1016/j.cpc.2011.05.009.

[3] P. Blaha, K. Schwarz, F. Tran, R. Laskowski, G. K. H. Madsen, and L. D. Marks, "WIEN2k: An APW+lo program for calculating the properties of solids," *J. Chem. Phys.*, vol. 152, no. 7, p. 074101, 2020. doi: 10.1063/1.5143061.

[4] J. P. Perdew, K. Burke, and M. Ernzerhof, "Generalized gradient approximation made simple," *Phys. Rev. Lett.*, vol. 77, no. 18, pp. 3865–3868, 1996. doi: 10.1103/PhysRevLett.77.3865.

[5] K. Momma and F. Izumi, "VESTA 3 for three-dimensional visualization of crystal, volumetric and morphology data," *J. Appl. Crystallogr.*, vol. 44, no. 6, pp. 1272–1276, 2011. doi: 10.1107/S0021889811038970.

[6] S. Babiker, G. Gao, and K. L. Yao, "First-principle calculation of electronic structures and magnetic properties of Heusler alloys Co_2ZrPb and Zr_2MnBa," *J. Supercond. Nov. Magn.*, vol. 31, no. 3, pp. 905–913, 2018. doi: 10.1007/s10948-017-4239-6.

[7] F. Birch, "The effect of pressure upon the elastic parameters of isotropic solids, according to Murnaghan's theory of finite strain," *J. Appl. Phys.*, vol. 9, no. 4, pp. 279–288, 1938. doi: 10.1063/1.1710417.

[8] X. Wang, Z. Cheng, R. Khenata, Y. Wu, L. Wang, and G. Liu, "Lattice constant changes leading to significant changes of the spin-gapless features in inverse Heusler compound Zr_2MnGa," *J. Magn. Magn. Mater.*, vol. 444, pp. 313–318, 2017. doi: 10.1016/j.jmmm.2017.08.040.

[9] M. Khodami and F. Ahmadian, "First-principles study of magnetism and half-metallic properties for quaternary Heusler alloys CoMnTiZ (Z = P, As, Sb)," *J. Supercond. Nov. Magn.*, vol. 28, no. 10, pp. 3027–3035, 2015. doi: 10.1007/s10948-015-3126-2.

[10] M. Kundu *et al.*, "Complex magnetic properties associated with competing local and itinerant magnetism in $Pr_2Co_{0.86}Si_{2.88}$," *Sci. Rep.*, vol. 11, no. 1, p. 13245, 2021. doi: 10.1038/s41598-021-90751-0.

[11] X.-P. Wei, X. Liu, J.-Y. Zhang, Y.-L. Zhang, and X. Tao, "Investigations on full-Heusler alloys Mn_2TaAl and Mn_2WAl for spintronic and thermoelectric applications," *iScience*, vol. 27, no. 12, p. 111257, 2024. doi: 10.1016/j.isci.2024.111257.

[12] S. V. Faleev *et al.*, "Unified explanation of chemical ordering, the Slater-Pauling rule, and half-metallicity in full Heusler compounds," *Phys. Rev. B*, vol. 95, no. 4, p. 045140, 2017. doi: 10.1103/PhysRevB.95.045140.

[13] W. Kohn and L. J. Sham, "Self-consistent equations including exchange and correlation effects," *Phys. Rev.*, vol. 140, no. 4A, pp. A1133–A1138, 1965. doi: 10.1103/PhysRev.140.A1133.

[14] X.-P. Wei *et al.*, "Electronic, magnetic and transport properties of antiferromagnetic semiconductor $BaGd_2X_4$ (X = S, Se)," *Mater. Sci. Semicond. Process.*, vol. 169, p. 107856, 2024. doi: 10.1016/j.mssp.2023.107856.

[15] J. Winterlik *et al.*, "Structural, electronic, and magnetic properties of tetragonal $Mn_{3-x}Ga$," *Phys. Rev. B*, vol. 77, no. 5, p. 054406, 2008. doi: 10.1103/PhysRevB.77.054406.

[16] S. Skaftouros, K. Özdogan, E. Şaşıoğlu, and I. Galanakis, "Generalized Slater-Pauling rule for inverse Heusler compounds," *Phys. Rev. B*, vol. 87, no. 2, p. 024420, 2013. doi: 10.1103/PhysRevB.87.024420.

[17] J.-R. Liu, X.-P. Wei, W.-L. Chang, and X. Tao, "Structural stability, electronic, magnetic and thermoelectric properties of half-metallic quaternary Heusler alloys CrLaCoZ," *J. Phys. Chem. Solids*, vol. 163, p. 110600, 2022. doi: 10.1016/j.jpcs.2022.110600.

[18] X.-P. Wei, Q. Gao, P. Gao, Y.-L. Zhang, and X. Tao, "Investigations on Gilbert damping, electronic, magnetic and Curie temperature for equiatomic quaternary

Heusler alloys CrScCoZ," *J. Magn. Magn. Mater.*, vol. 512, p. 166986, 2020. doi: 10.1016/j.jmmm.2020.166986.

[19] X.-P. Wei, J. Shen, L.-L. Du, and X.-M. Tao, "Electronic and magnetic properties of two-dimensional CrX_2 under vacancy and strain effects," *Phys. B: Condens. Matter*, vol. 667, p. 415154, 2023. doi: 10.1016/j.physb.2023.415154.

[20] I. Galanakis, P. H. Dederichs, and N. Papanikolaou, "Slater-Pauling behavior and origin of the half-metallicity of full-Heusler alloys," *Phys. Rev. B*, vol. 66, no. 17, p. 174429, 2002. doi: 10.1103/PhysRevB.66.174429.

[21] J. C. Slater, "Suggestions from solid-state theory regarding molecular calculations," *J. Chem. Phys.*, vol. 43, no. 10, p. S228, 1965. doi: 10.1063/1.1701494.

[22] X. Zhang, X.-P. Wei, J. Shen, Z.-Y. Mei, L.-L. Du, and X. Tao, "Half-metallic quaternary CrYCoX (X = Si, Ge, Sn, Pb) alloys: DFT calculations and Monte Carlo simulation," *Mater. Today Commun.*, vol. 33, p. 104650, 2022. doi: 10.1016/j.mtcomm.2022.104650.

[23] X.-P. Wei, X. Zhang, J. Shen, W.-L. Chang, and X. Tao, "Gilbert damping, electronic and magnetic properties for quaternary Heusler alloys CrYCoZ: First-principles and Monte Carlo studies," *Comput. Mater. Sci.*, vol. 210, p. 111453, 2022. doi: 10.1016/j.commatsci.2022.111453.

[24] F. Dahmane *et al.*, "Structural, electronic and magnetic properties of Fe_2-based full Heusler alloys: A first-principles study," *J. Magn. Magn. Mater.*, vol. 407, pp. 167–174, 2016. doi: 10.1016/j.jmmm.2016.01.074.

[25] S. Babiker, G. Gao, and K. L. Yao, "First-principle calculation of electronic structures and magnetic properties of Heusler alloys Co_2ZrPb and Zr_2MnBa," *J. Supercond. Nov. Magn.*, vol. 31, no. 3, pp. 905–913, 2018. doi: 10.1007/s10948-017-4239-6.

[26] M. Jamal, M. Bilal, I. Ahmad, and S. Jalali-Asadabadi, "IRelast package," *J. Alloys Compd.*, vol. 735, pp. 569–579, 2018. doi: 10.1016/j.jallcom.2017.10.139.

[27] D. H. Chung and W. R. Buessem, "The Voigt-Reuss-Hill approximation and elastic moduli of polycrystalline materials," *J. Appl. Phys.*, vol. 38, no. 6, pp. 2535–2540, 1967. doi: 10.1063/1.1709944.

[28] J. Wang, S. Yip, S. R. Phillpot, and D. Wolf, "Crystal instabilities at finite strain," *Phys. Rev. Lett.*, vol. 71, no. 25, pp. 4182–4185, 1993. doi: 10.1103/PhysRevLett.71.4182.

[29] Q.-L. Fang, J.-M. Zhang, K.-W. Xu, and V. Ji, "Effect of defects on magnetic properties and spin polarization of Ti_2FeAl Heusler alloy," *J. Magn. Magn. Mater.*, vol. 351, pp. 25–28, 2014. doi: 10.1016/j.jmmm.2013.09.052.

[30] J. M. K. Al-Zyadi, G. Y. Gao, and K.-L. Yao, "Theoretical investigation of electronic structures and magnetic properties of quaternary Heusler alloy NiCoMnGa," *J. Magn. Magn. Mater.*, vol. 378, pp. 1–6, 2015. doi: 10.1016/j.jmmm.2014.11.012.

[31] S. V. Faleev *et al.*, "Unified explanation of chemical ordering, the Slater-Pauling rule, and half-metallicity in full Heusler compounds," *Phys. Rev. B*, vol. 95, no. 4, p. 045140, 2017. doi: 10.1103/PhysRevB.95.045140.

[32] A. Otero-de-la-Roza, D. Abbasi-Pérez, and V. Luaña, "Gibbs2: A new version of the quasiharmonic model code," *Comput. Phys. Commun.*, vol. 182, no. 10, pp. 2232–2248, 2011. doi: 10.1016/j.cpc.2011.05.009.

[33] C. Borgnakke, *Fundamentals of Thermodynamics*, Wiley-Blackwell, 2024.

[34] A. Moussali, M. B. Amina, B. Fassi, I. Ameri, M. Ameri, and Y. Al-Douri, "First-principles calculations to investigate structural and thermodynamic properties of Ni_2LaZ (Z = As, Sb, Bi) Heusler alloys," *Indian J. Phys.*, vol. 94, no. 11, pp. 1733–1747, 2020. doi: 10.1007/s12648-019-01627-z.

[35] S. Rouag and D. Amari, "Theoretical calculation of structural, electronic, and magnetic properties of rare-earth full Heusler alloys Pr_2CoZ (Z = Al, Ga, In)," *Phys. Solid State*, vol. 66, no. 6, pp. 176–183, 2024. doi: 10.1134/S1063783424600699.

[36] H. Bross, G. Bohn, G. Meister, W. Schubö, and H. Stöhr, "New version of the modified augmented-plane-wave method," *Phys. Rev. B*, vol. 2, no. 8, pp. 3098–3103, 1970. doi: 10.1103/PhysRevB.2.3098.

[37] H. Bross and G. M. Fehrenbach, "The spline augmented plane wave method," *Z. Phys. B: Condens. Matter*, vol. 81, no. 2, pp. 233–243, 1990. doi: 10.1007/BF01309354.

[38] R. Hill, "The elastic behaviour of a crystalline aggregate," *Proc. Phys. Soc. A*, vol. 65, no. 5, pp. 349–354, 1952. doi: 10.1088/0370-1298/65/5/307.

[39] S. Q. Wang and H. Q. Ye, "First-principles study on elastic properties and phase stability of III–V compounds," *Phys. Status Solidi B*, vol. 240, no. 1, pp. 45–54, 2003. doi: 10.1002/pssb.200301861.

[40] V. Kanchana, G. Vaitheeswaran, and A. Svane, "Calculated structural, elastic and electronic properties of $SrCl_2$," *J. Alloys Compd.*, vol. 455, no. 1–2, pp. 480–484, 2008. doi: 10.1016/j.jallcom.2007.01.163.

[41] W. Voigt, "Ueber die Beziehung zwischen den beiden Elasticitätsconstanten isotroper Körper," *Ann. Phys.*, vol. 274, no. 12, pp. 573–587, 1889. doi: 10.1002/andp.18892741206.

[42] A. Reuss, "Berechnung der Fließgrenze von Mischkristallen," *ZAMM*, vol. 9, no. 1, pp. 49–58, 1929. doi: 10.1002/zamm.19290090104.

[43] F. D. Murnaghan, "The compressibility of media under extreme pressures," *Proc. Natl. Acad. Sci.*, vol. 30, no. 9, pp. 244–247, 1944. doi: 10.1073/pnas.30.9.244.

[44] I. N. Frantsevich, *Elastic Constants and Elastic Moduli of Metals and Insulators*, Ref. Book, 1982.

[45] F. Mollaamin and M. Monajjemi, "Influence of transition metals on B_5N_{10} nanocarrier for NO sensing," *Comput. Theor. Chem.*, vol. 1237, p. 114666, 2024. doi: 10.1016/j.comptc.2024.114666.

[46] C. S. Jiang *et al.*, "First-principles investigation of martensitic transition and magnetic properties in Heusler alloys Mg_2YZ (Y = Sc, Ti, V; Z = Al, Ga, In)," *J. Magn. Magn. Mater.*, vol. 471, pp. 82–88, 2019.

[47] M. J. Alrahamneh, A. A. Mousa, and J. M. Khalifeh, "First-principles study of structural, electronic, magnetic and thermoelectric properties of Zr_2RhAl," *Physica B: Condens. Matter*, vol. 552, pp. 227–235, 2019.

[48] H. C. Kandpal, G. H. Fecher, and C. Felser, "Calculated electronic and magnetic properties of half-metallic Heusler compounds," *J. Phys. D: Appl. Phys.*, vol. 40, no. 6, p. 1507, 2007.

[49] Ş. Uğur *et al.*, "Elastic, mechanical, optical and magnetic properties of Ru_2MnX (X = Nb, Ta, V) Heusler alloys," *J. Magn. Magn. Mater.*, vol. 523, p. 167614, 2021.

[50] E. Güler and M. Güler, "High-pressure elastic properties of wurtzite aluminum nitrate," *Chinese J. Phys.*, vol. 52, no. 5, pp. 1625–1635, 2014.

[51] M. Güler and E. Güler, "Elastic and related properties of Si under hydrostatic pressure calculated using modified embedded atom method," *Mater. Res. Express*, vol. 3, no. 7, p. 075901, 2016.

[52] J. Bhattacharya, R. Dutt, and A. Chakrabarti, "Ab-initio predictions of mechanical, electronic, magnetic, and transport properties of Fe–Cr based full Heusler chalcogenide," *J. Phys. Chem. Solids*, vol. 178, p. 111307, 2023.

[53] X. Luan *et al.*, "Mechanical properties and elastic anisotropies of cubic Ni_3Al from first-principles calculations," *Crystals*, vol. 8, no. 8, p. 307, 2018.

[54] S. A. Khandy *et al.*, "Lattice dynamics, mechanical stability and electronic structure of Fe-based Heusler semiconductors," *Sci. Rep.*, vol. 9, no. 1, p. 1475, 2019.

[55] S. F. Pugh, "Relations between elastic moduli and plastic properties of polycrystalline metals," *Philos. Mag.*, vol. 45, no. 367, pp. 823–843, 1954.

[56] E. G. Özdemir and Z. Merdan, "First-principles predictions on half-metallic MnZrX (X = In, Tl, C, Si, Ge, Sn, Pb, N, P, As, Sb, O, S, Se, Te) half-Heusler compounds," *J. Magn. Magn. Mater.*, vol. 491, p. 165567, 2019.

GENERAL CONCLUSION AND FUTURE PERSPECTIVES

We have systematically explored the structural, electronic, magnetic, elastic and thermodynamic properties of a broad set of full-Heusler alloys based on Pr and transition metals, as well as the related Ir_2ScZ (Z = Ge, Ga) and Ru_2MnZ (Z = Sb, Sn, Te) systems. For the rare-earth-based Pr_2RhZ (Z = Al, Ga, In) and Pr_2CoZ (Z = Al, Ga, In) compounds, the total-energy optimisation showed that the inverse Hg_2CuTi-type structure in the ferromagnetic configuration is energetically favoured over the regular Cu_2MnAl-type phase. The negative formation energies obtained for all alloys confirm their thermodynamic stability and indicate that their experimental synthesis should be feasible.

The analysis of the elastic constants demonstrated that the ferromagnetic Hg_2CuTi-type phases of Pr_2CoZ and their Cr-doped counterparts CrPrCoZ satisfy the Born stability criteria and exhibit pronounced elastic anisotropy together with B/G ratios and Poisson's ratios characteristic of ductile behaviour. These results indicate that the investigated materials are not only mechanically stable but also capable of withstanding plastic deformation, an important requirement for practical device integration. In contrast, for the Ir_2ScZ series only the Ir_2ScGa alloy in the Cu_2MnAl-type structure was found to be mechanically stable, whereas the other structural variants display signatures of instability.

From the electronic point of view, the spin-polarized band structures and densities of states revealed that Pr_2RhZ, Pr_2CoZ and CrPrCoZ alloys are half-metallic ferromagnets: one spin channel remains metallic, while the other exhibits an indirect band gap at the Fermi level. The calculated total magnetic moments are integer values (4 μ_B for Pr_2RhZ and Pr_2CoZ, 5 μ_B for CrPrCoZ), in excellent agreement with the Slater–Pauling rule linking the magnetic moment to the total number of valence electrons. The dominant contributions to the magnetisation arise from the Pr (and Cr, when present) sublattices, whereas the p-block elements Al, Ga and In contribute only weakly. In contrast, the Ir_2ScZ alloys behave as conventional metals with compensated or nearly compensated magnetism and do not display half-metallic gaps, which makes them unsuitable as spin-filtering electrodes but potentially interesting for other metallic applications.

The thermodynamic quantities obtained within the quasi-harmonic approximation

further corroborate the stability of the Pr_2CoZ and CrPrCoZ systems over a wide temperature and pressure range. The heat capacities C_V and C_P increase with temperature and approach the Dulong–Petit limit at high temperatures, while entropy rises monotonically with temperature and decreases under pressure, reflecting the reduction of vibrational disorder. The Debye temperature decreases with increasing temperature and increases under pressure, consistent with the stiffening of the lattice at higher densities. These trends confirm that the investigated full-Heusler alloys possess robust lattice dynamics compatible with thermal cycling in realistic operating conditions.

Taken together, the present results demonstrate that Pr_2RhZ, Pr_2CoZ and their Cr-doped derivatives CrPrCoZ form a family of structurally stable, mechanically ductile and half-metallic ferromagnets with 100% spin polarisation at the Fermi level, which makes them strong candidates for spintronic and magnetoelectronic applications. The comparative study with Ir_2ScZ (Z = Ge, Ga) and Ru_2MnZ (Z = Sb, Sn, Te) alloys underlines the decisive role of chemical composition, crystal structure and electronic hybridisation in determining half-metallicity and magnetic compensation in full-Heusler compounds. These conclusions provide a solid basis for future experimental work and for further theoretical investigations, for example including spin-orbit coupling, correlation effects beyond GGA and finite-temperature magnetism, in order to refine the description of these promising materials and to guide their optimisation for specific technological devices.

APPENDIX

ISSN 1990-7931, Russian Journal of Physical Chemistry B, 2026, Vol. 20, No. 2, pp. 123–129. © Pleiades Publishing, Ltd., 2026.

STRUCTURAL OF CHEMICALS, QUANTUM CHEMISTRY, SPECTROSCOPY

First-Principles Calculations to Investigate Structural, Elastic, Electronic and Ferromagnetic Properties of Ir_2ScZ (Z = Ga, Ge) Full Heusler: a Potential Applications for Spintronic Devices

I. A. Bouadi[a], D. Amari[b], M. Mokhtari[a, c, *, **], and F. Dahmane[a]

[a] *Laboratory of modelling and simulation of the magnetic properties of hetero structure (LPMH), Faculty of Sciences and Technology, Tissemsit University, Algeria*

[b] *Material and Energies Research Laboratory, University of Tamanghasset, Tamanghasset, Algeria*

[c] *Laboratoire d'Etudes Physique des Matériaux, Université des Sciences et de Technologies USTO-MB, BP 1505 El M'Naouar, Oran, Algeria*

**e-mail: mohamed.mokhtari@yahoo.fr*

***e-mail: mokhtari.mohamed@univ-tissemsilt.dz*

Received August 31, 2025; revised October 16, 2025; accepted October 20, 2025

Abstract—In this study, we present a comprehensive first-principles investigation of the structural, electronic, magnetic, and elastic properties of the full Heusler alloys Ir_2ScGe and Ir_2ScGa. Using the full-potential linearized augmented plane-wave method within the generalized gradient approximation, we analyze the stability of these alloys in both the Cu_2MnAl and Hg_2CuTi-type structures. Our results reveal that both alloys are structurally stable in the Cu_2MnAl-type structure, with Ir_2ScGe exhibiting higher lattice parameters and lower bulk modulus compared to Ir_2ScGa, indicating a softer material (6.27 Å for Ir_2ScGa and 6.37 Å for Ir_2ScGe in the Cu_2MnAl-type structure), bulk moduli (higher for Ir_2ScGa at 210.60 GPa compared to 81.71 GPa for Ir_2ScGe). The study of the electronic properties shows metallic behavior in these materials, without any indication of half-metallicity. The magnetic calculation reveals that Ir_2ScGa in the Cu_2MnAl structure exhibits no net magnetic moment, categorizing it as a fully compensated compound. This work provides the first comprehensive analysis of the elastic constants and mechanical stability of these understudied Ir-based Heusler alloys, revealing their potential as mechanically stable, non-magnetic materials for optical applications.

Keywords: airst-principles calculations, Heusler alloy, magnetic properties, half-metallicity

DOI: 10.1134/S1990793125701490

1. INTRODUCTION

Ferromagnetic materials with half-metallic properties are important for spintronics and spin valves due to their high temperature at which the material loses its magnetism (Curie temperature) [1–3]. Spintronic is used in various solid-state devices like magnetic sensors [2, 4], memory storages [4], spin filters [5, 6], spin valves, and devices that exploit the tunnelling magnetoresistance (TMR) phenomenon [6]. Spintronic devices offer advantages such as faster data processing and lower power consumption.

The exploration of half-metallic materials began in 1983 with the NiMnSb half-Heusler alloy [7]. Since then, numerous other materials have been discovered, including full-Heusler alloys [8, 9], other half-Heusler alloys [10–12], metallic oxides [13], and some materials with a zinc blende crystal structure [14]. These materials are unique because they conduct electricity with only one electron spin (half-metallic behavior), leading to 100% spin polarization at the Fermi level. This characteristic makes them ideal for integration into spintronic and magnetoresistive devices. With continued research, half-metallic materials have the potential to revolutionize various technologies.

Iridium-based alloys are of great interest to researchers due to their potential structural stability and ability to exhibit half-metallicity properties. This interest stems from their valuable applications in spintronic devices, memory storage devices, tunneling magnetic resonance (TMR), and giant magnetoresistance (GMR). Recent investigations have examined several iridium-based binary alloys, including Ir_2CrAl, Ir_2MnSi, Ir_2VGa, Ir_2VGe, and Ir_2MnAl. Ir_2CrAl [15] and Ir_2MnSi [16] have been identified as half-metals with 100% spin polarization at the Fermi level, displaying total magnetic moments (a measure of the material's magnetism) of 3.0 μ_B and 5.0 μ_B, respectively. In contrast, Ir_2VGa and Ir_2VGe [17] were studied using three methods: local spin density approximation (LSDA), generalized gradient approximation

(GGA), and GGA + modified Becke–Johnson (mBJ). While LSDA and GGA methods did not reveal any half-metallic behavior, GGA + mBJ calculations identified such behavior with an energy gap of 0.2 eV for Ir_2VGa and 0.4 eV for Ir_2VGe.

Therefore, most Ir-based compounds exhibit high spin polarization at the Fermi level. Despite their broad potential applications, these compounds have been relatively understudied. Thus, there is considerable interest in further exploring certain iridium-based alloys to assess their half-metallicity and potential applications in spintronic.

In contrast, iridium-based binary alloys are widely utilized in data storage and spintronic devices like GMR and tunnel magnetoresistive (TMR). The choice of Ir_2–Mn alloys is attributed to their ease of fabrication in thin-film form and exceptional corrosion resistance. Experimental investigations on Ir_2MnAl and Ir_2MnGa full-Heusler alloys have established their crystal structure, saturation magnetic moment, Curie temperature. Similarly, Ir–Mn–Sn has been scrutinized for its crystallographic and magnetic properties. Additionally, other Heusler alloys like Co_2RuSi and Co_2MnSi have been studied for their structural and magnetic characteristics, revealing intriguing properties such as high-temperature electrical resistivity and exceptional spin polarization.

In the case of Ir-based materials, ab-initio calculations have been employed to predict the electronic and magnetic properties of Ir_2ScGa and Ir_2ScGe. However, a comprehensive analysis of their mechanical properties, including the calculation of elastic constants, is still lacking. In this study, we extend our investigation by calculating various elastic constants, which are crucial for understanding the materials' stiffness, ductility, and stability under stress. Additionally, the concept of fully compensated compounds is explored, where the magnetic moments of the constituent atoms align in such a way that their total magnetic moment is zero. This unique characteristic makes these alloys magnetically neutral and unsuitable for traditional spintronic applications, yet potentially valuable for other technological applications that require non-magnetic materials. Furthermore, the response of these compounds to applied pressure is considered, as the application of stress can alter both their mechanical and magnetic properties, providing further insight into their potential uses in demanding environments. Ab initio calculations using the WIEN2k code, based on density functional theory (DFT) with the full-potential linearized augmented plane-wave (FPLAPW) method and generalized gradient approximation (GGA-PBE), have been employed to predict the electronic and magnetic properties of Ir_2ScGa and Ir_2ScGe.

The present work is organized as follows: The computational methodology and crystal structure of full-Heusler compounds are described in Section 2, and the acquired results are discussed in Section 3. Section 4 offers a conclusion at the end.

2. THEORETICAL BACKGROUND, MATERIALS AND CALCULATION METHOD

The full-potential linearized augmented plane-wave (FPLAPW) approach, as implemented in WIEN2k, that utilizes the theoretical research strategy of Density Functional Theory (DFT) [18], is used in this work to compute the electronic structure and fundamental ground state features of Heusler alloys [19–21]. The Perdew–Burke–Ernzerhof parameterization of the generalized gradient approximation (GGA) is used to include exchange-correlation effects [22]. The muffin tin sphere radii were chosen as R_{MT} (Ir) = R_{MT} (Sc) = 2.2 a.u. and R_{MT} (Ga) = R_{MT} (Ge) = 2.2 a.u. The growth of the electron density and crystal potential within muffin-tin spheres has a maximum value of $l = 10$. For the plane waves in the Fourier expansion of the potential in the interstitial region, the cut-off parameter is set to $R_{MT}\,K_{max} = 8.5$. The Brillouin zone was sampled using the Monkhorst–Pack technique [23], a (12 × 12 × 12) mesh was utilized for k-space integration, yielding 72k points of the irreducible component in the Brillouin zone [24]. From the computed energy-volume points, all thermodynamic quantities can be derived using the quasi-harmonic Debye model.

The magnitude of the largest vector in charge density Fourier expansion (G_{max}) was 14 $(a.u)^{-1}$. The cut-off energy, which defines the separation of valence and core states, was chosen as –6.0 Ry. The self-consistent calculations are considered to be converged only when the total energy of the crystal is converged to less than 10^{-4} Ry. The total energy dependence on the cell volume is fitted to the Murnaghan equation of state [25] to determine the ground state properties:

$$E(V) = E_0(V) + \frac{BV}{B'(B'-1)}\left[B\left(1-\frac{V_0}{V}\right)+\left(\frac{V_0}{V}\right)^{B'}-1\right], \quad (1)$$

where E_0 is the minimum energy at $T = 0$ K, B is the bulk modulus, B' is the bulk modulus derivative and V_0 is the equilibrium volume.

3. RESULTS AND DISCUSSION

3.1. Structural Stability

The Heusler compounds have a stoichiometry composition of X_2YZ where X and Y are transition metals and Z is a main group element. The full-Heusler compounds crystallizing in the cubic structure have two types: the $AlCu_2Mn$ and $CuHg_2Ti$. The two structures consist of four interpenetrating face-centered cubic (fcc) sub-lattices and four crystal sites: A (0,0,0), B (1/4,1/4,1/4), C (1/2,1/2,1/2) and D

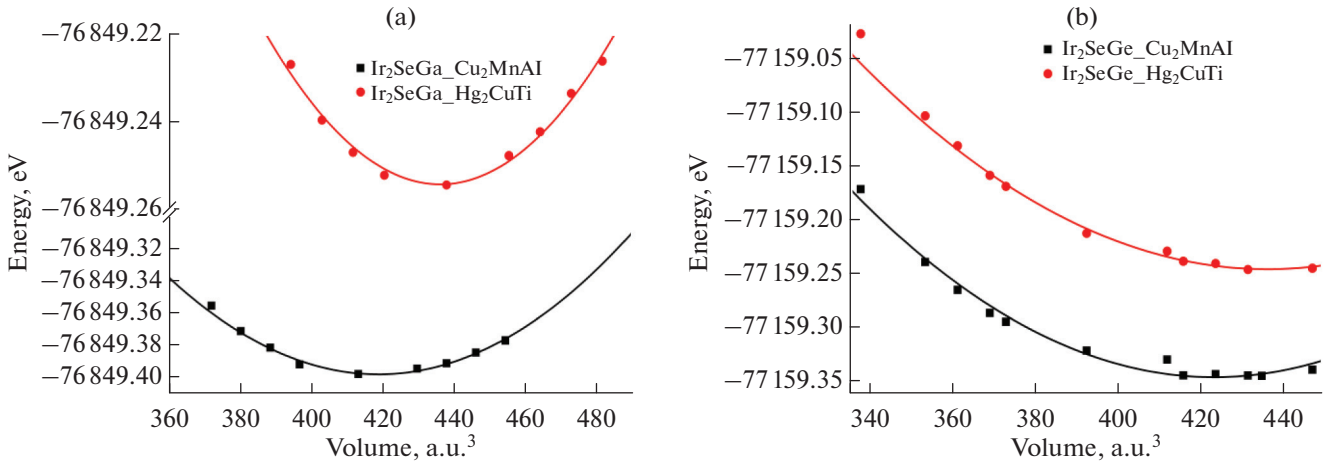


Fig. 1. Total energy as a function of unit cell volume for: (a) Ir_2ScGa for both Hg_2CuTi and Cu_2MnAl type structures, (b) Ir_2ScGe for both Hg_2CuTi and Cu_2MnAl type structures.

(3/4,3/4,3/4). In the Cu_2MnAl-type, X atoms occupy the (A, C) site, while in the Hg_2CuTi-type structure the (A, B) sites are occupied by X atoms.

Figure 1 illustrates the crystal structure of the Ir_2Sc (Ge, Ga) Heusler compound as a prototype example. Table 1 summarizes the optimal lattice constants and bulk moduli obtained for the $L2_1$ crystal structure of Ir_2ScGa and Ir_2ScGe alloys in both Cu_2MnAl and Hg_2CuTi type structure in ferromagnetic (FM) states. These values were determined by analyzing the "volume—energy curves" for each sample (Fig. 1).

Our results reveal that the Cu_2MnAl type structure has lower energy compared to the Hg_2CuTi type structure for all alloys, indicating their inherent stability in the ferromagnetic configuration. The lattice parameter steadily increases from 6.27 Å for Ir_2ScGa Heusler compound to 6.37 Å for Ir_2ScGe Heusler compound as the atomic size of the Z atom increases from Ga to Ge. This expansion is accompanied by a corresponding decrease in the bulk modulus, which measures the material's stiffness.

In this section, we explore the stability of the Ir_2ScGa and Ir_2ScGe alloys in both Cu_2MnAl and Hg_2CuTi type structure; we use the GGA-PBE method to calculate its cohesion and formation energies. This calculation can indicate the feasibility of synthesizing these compounds within a laboratory environment. Cohesion energy (E_c) reflects the binding strength between atoms in a solid state, and it's linked to the material's ground-state structural stability. To calculate the cohesion energy per formula unit of Ir_2ScGa and Ir_2ScGe alloys, we compare the total energies of individual Ir, Sc, Ga and Ge atoms with the total energy of the entire Ir_2ScGa and Ir_2ScGe alloys compounds in its equilibrium state. That is:

$$E_c = 2E_{Ir}^{iso} + E_{Ge}^{iso} + E_{Sc}^{iso} - E_{Ir_2ScGe}^{iso}, \quad (2)$$

where $E_{Ir_2ScGe}^{iso}$ is the calculated equilibrium total energy of the Ir_2ScGe compound per formula unit, and E_{Ir}^{iso}, E_{Ge}^{iso}, E_{Sc}^{iso} are the calculated total energies of isolated Ir, Ge, Sc atoms respectively.

Our calculations reveal a high cohesion energy of 11.34 and 11.62 eV for Ir_2ScGe and Ir_2ScGa alloys, signifying strong chemical bonding between its atoms. This indicates to a high degree of stability for the compound.

Formation energy provides another measure of stability, in this case, the resistance of Ir_2ScGe to decompose into its constituent elements. Formation energy is calculated by difference between the total energy of

Table 1. The variation of the lattice constant (a_0), bulk modulus (B_0), the bulk modulus' derivative, and the ground state energies of the seven quaternary Heusler alloys at both ferromagnetic and paramagnetic states

Alloys	a, Å	B, GPa	B'	E_{min}, eV	Magnetic phase
Ir_2ScGe–Hg_2CuTi type	6.4053	133.3756	6.1399	−77 159.2461	FM
Ir_2ScGe–Cu_2MnAl type	6.3711	81.7118	12.5216	−77 159.3430	FM
Ir_2ScGa–Hg_2CuTi type	6.3528	191.3582	5.5967	−76 849.2544	FM
Ir_2ScGa–Cu_2MnAl type	6.2715	210.6013	5.0614	−76 849.3976	FM

Table 2. Elastic constants for Ir_2ScGe and Ir_2ScGa full Heusler compounds

Material	C_{11}	C_{12}	C_{44}	Bulk modulus, B	Shear modulus, G	Poisson's ratio, υ	Anisotropy factor, A	B/G ratio
$Ir_2ScGa–Hg_2CuTi$	124.9013	210.6720	73.0815	182.081	26.694	0.430	−1.704	6.82
$Ir_2ScGa–Cu_2MnAl$	335.9468	181.5239	122.601	232.998	104.445	0.305	1.5879	2.23
$Ir_2ScGe–Hg_2CuTi$	72.6486	194.9840	26.4425	154.205	−8.602	0.528	−0.432	−17.93
$Ir_2ScGe–Cu_2MnAl$	22.6220	240.1652	68.2386	167.650	−2.565	0.507	−0.627	−65.35

Ir_2ScGe Heusler in its equilibrium state and the combined total energies of the individual atoms.

Mathematically, this can be expressed as

$$E_F = E^{bulk}_{Ir_2ScGe} - \left(2E^{bulk}_{Ir} + E^{bulk}_{Ge} + E^{bulk}_{Sc}\right), \quad (3)$$

where E_F represents the formation energy, and E^{bulk}_{Ir}, E^{bulk}_{Ge}, E^{bulk}_{Ga} and E^{bulk}_{Sc} represent the total energies per atom for bulk Ir, Ge, Ga and Sc respectively.

The calculated formation energy for Ir_2ScGe and Ir_2ScGa are −0.83 Ry and −0.85 Ry respectively, indicating its thermodynamic stability in the regular cubic Heusler structure.

3.2. Elastic Proprieties

The study of elastic constants provides a valuable tool for predicting the mechanical behaviour of materials due to the inherent connection between a material's mechanical and dynamical properties, ultimately determined by the internal forces. In this work, we utilized the IRelast package within the WIEN2k software to calculate the elastic constants for Ir_2ScGe and Ir_2ScGa Heusler alloys [26, 27]. In a cubic structure, the determination of elastic constants can be simplified, as only three independent parameters are needed (C_{11}, C_{12}, C_{44}). The first two components (C_{11} and C_{12} can be derived from the bulk modulus, while the second component is established through volume-conserving tetragonal strain calculations based on the total energy of both strained and unstrained structures. The third independent component is determined using a volume-conserving rhombohedral strain approach, again relying on total energy considerations [27, 28].

After calculating the elastic constants Cij, various important physical properties can be derived, such as the bulk modulus, shear modulus, Young's modulus, and Poisson's ratio, using the Hill–Voigt–Reuss approximations [26, 29, 30]. Table 2 provides the resulting values for C_{11}, C_{12}, C_{44}, B, G, E, ϑ, Anisotropy A and the B/G ratio. It is noteworthy that for Ir_2ScGa Heusler alloys in the Cu_2MnAl structure, the computed elastic constants satisfy the Born mechanical stability criteria [26], confirming their mechanical stability. However, Ir_2ScGa Heusler alloys in the Hg_2CuTi structure, as well as Ir_2ScGe Heusler alloys in both the Hg_2CuTi and Cu_2MnAl structures, are mechanically unstable.

Several mechanical parameters, including the bulk modulus (B), shear modulus (G), Young's modulus (Y), and Poisson's ratio (υ), offer insights into a material's stiffness and resistance to uniaxial stress. The calculated Young's modulus for Ir_2ScGe is higher than that of Ir_2ScGa, signifying greater elastic stiffness in Ir_2ScGe. This difference likely arises from variations in cohesive forces between the two materials. Poisson's ratio (v) serves as an indicator of solid stability, with a range of −1.0 to 0.5 for stable materials [25]. The Poisson's ratio values for Ir_2ScGa Heusler alloys in the Cu_2MnAl structure are 0.305, fall within this range, suggesting their stability under shear stress. Furthermore, according to Frantsevich et al. [31], materials with a Poisson's ratio exceeding 1/3 are typically ductile, while those below this value are brittle. Both Ir_2ScGe in both Hg_2CuTi and Cu_2MnAl structure and Ir_2ScGa in the Hg_2CuTi structure possess a Poisson's ratio greater than 1/3, indicating their ductility.

Finally, the anisotropy factor (A) serves as another indicator of mechanical stability. A negative value of (A) suggests structural instability. The positive anisotropy factors obtained Ir_2ScGa Heusler alloys in the Cu_2MnAl structure confirms their mechanical stability.

The analysis of elastic constants demonstrates the mechanical stability of Ir_2ScGa Heusler alloys in Cu_2MnAl structure. Their positive C_{ij} values satisfy the Born–Huang criteria, and their Poisson's ratio values indicate stability under shear stress. Additionally, the higher Young's modulus of Ir_2ScGe suggests greater elastic stiffness compared to Ir_2ScGa. The positive anisotropy factor (A) further supports the mechanical stability of Ir_2ScGa Heusler alloys in Cu_2MnAl structure.

3.3. Electronic and Magnetic Properties

The Density of states of Ir_2ScGa and Ir_2ScGe alloys (see Fig. 2), considering both spin-up and spin-down electrons, were calculated for the Cu_2MnAl and Hg_2CuTi crystal structures. In the Hg_2CuTi-type structure, neither Ir_2ScGe nor Ir_2ScGa exhibits any spin polarization around the Fermi level (E_f), indicating their non-magnetic character. This is because both

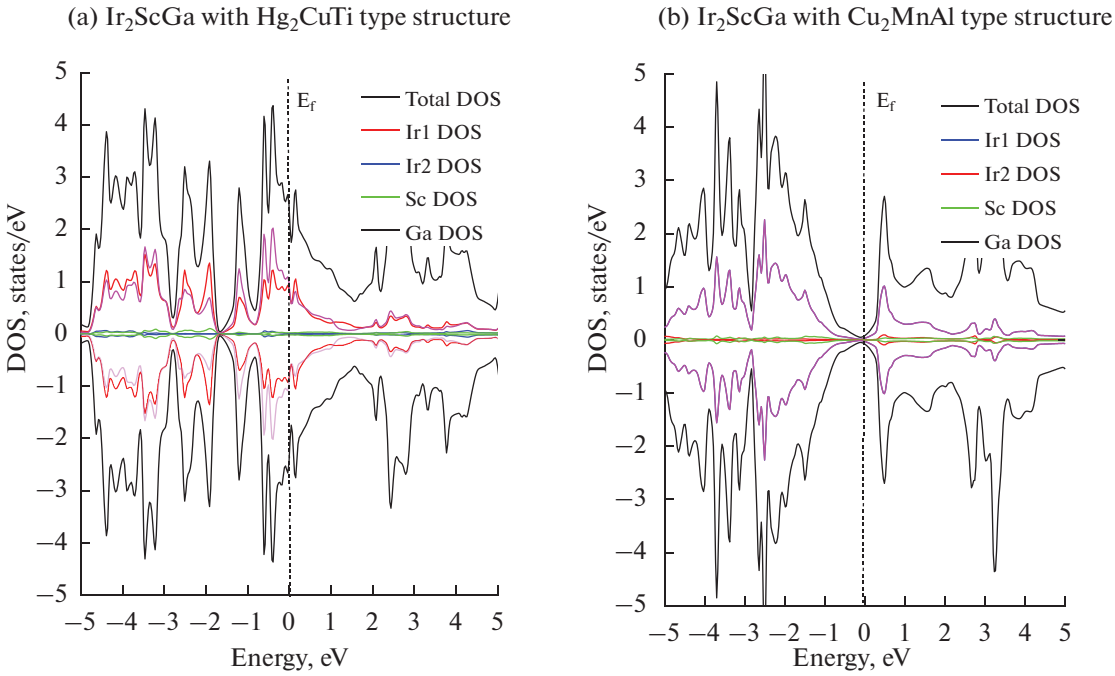


Fig. 2. Density of states (DOS) of Ir_2ScGa: (a) with Hg_2CuTi type structures, (b) with Cu_2MnAl type structures.

majority and minority spin bands intersect the Fermi level, making both spin channels conducting (metallic). The presence of these intersecting bands across both spin channels signifies that Ir_2ScGe and Ir_2ScGa in the Hg_2CuTi structure are metals with a fully-compensated total magnetic moment.

The Ir_2ScGe alloy in the Cu_2MnAl-type structure does not exhibit half-metallic behavior. Instead, it shows no significant spin polarization near the Fermi level, indicating a non-magnetic or weakly magnetic state. Figure 3 illustrates the Density of states (DOS) of Ir_2ScGe in this configuration, where both the majority and minority-spin channels are metallic, without any energy gap around the Fermi level. This characteristic classifies Ir_2ScGe (Cu_2MnAl-type) as a conventional metallic material rather than a half-metallic ferromagnet.

On the other hand, Ir_2ScGa in the Cu_2MnAl-type structure presents a fully compensated magnetic behaviour, with the total magnetic moment close to zero. This suggests that Ir_2ScGa is a fully compensated material in this structure, where the spin moments of the different atoms cancel each other out, maintaining a non-magnetic state.

Figures 2 and 3 show the total DOS for Ir_2ScGa and Ir_2ScGe, respectively. For Ir_2ScGa (Fig. 2), both Cu_2MnAl (a) and Hg_2CuTi (b) structures exhibit metallic behavior with finite DOS at E_F from both spin channels, leading to no spin polarization and fully compensated magnetism in Cu_2MnAl (logical from symmetric up/down DOS). Similarly, Ir_2ScGe (Fig. 3) shows metallic crossing at E_f in both structures, with weak asymmetry in Cu_2MnAl suggesting minor magnetism (total moment ~0.98 μ_B from Table 3), contrasting compensated cases. This DOS profile implies conduction via both spins, which is unsuitable for half-metallicity but but suitable for metallic opto-electronic applications.

In contrast to 2D materials like Sc-implanted B_5N_{10} nanocarriers, which exhibit ferromagnetic semiconductor behavior with enhanced NO sensing via DFT-calculated Density of states as reported by

Table 3. The variation of the total and partial magnetic moment calculated by GGA approximations

Alloys	μ_{Tot}	μ_{Ir}	μ_{Ir}	μ_{Sc}	μ_Z	Interstitial
Ir_2ScGe–Hg_2CuTi	0.00002	0.00001	0.00001	0.00000	–0.00000	0.00000
Ir_2ScGa–Hg_2CuTi	–0.00045	0.00000	–0.00051	0.00009	–0.00003	–0.00000
Ir_2ScGe–Cu_2MnAl	0.98312	0.45354	0.45353	0.00038	0.03968	0.03598
Ir_2ScGa–Cu_2MnAl	0.00000	0.00001	0.00001	–0.00001	–0.00000	–0.00001

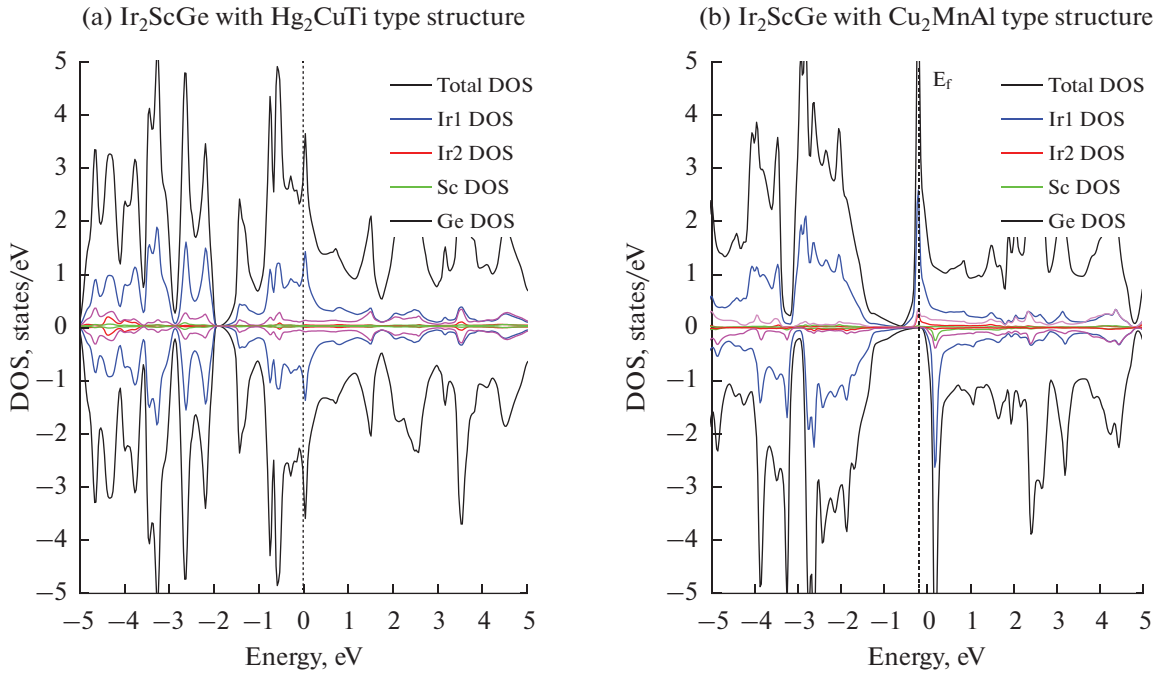


Fig. 3. Density of states (DOS) of Ir_2ScGe: (a) with Hg_2CuTi type structures, (b) with Cu_2MnAl type structures.

[32], our bulk Ir_2ScZ alloys show metallic DOS without gaps, and fully compensated magnetism in Ir_2ScGa–Cu_2MnAl. This highlights the structural dimensionality's role in tuning magnetism—2D systems often favor ferromagnetism for sensing, while our 3D Heusler suit non-magnetic applications.

Strain engineering, where controlled deformation is applied to a material, is a recognized approach for tailoring its fundamental properties. In this context, we investigated the impact of uniform strain on the band structures of Ir_2ScGa and Ir_2ScGe in both the regular and inverted cubic Heusler phases. Our initial focus was on how uniform strain affects the total and atomic magnetic moments of the two Ir atoms (Ir(A) and Ir(B)). As shown in Table 3, the total magnetic moment of both Ir_2ScGa and Ir_2ScGe in the Cu_2MnAl-type structure remains constant at 0.0 μ_B indicates preserved fully-compensated magnetism under strain. However, the individual spin moments of the two Ir atoms exhibit sensitivity to changes in the lattice constant. The magnitudes of the atomic magnetic moments for Ir at distinct crystallographic sites consistently decrease as the lattice is compressed. The magnetic moments of Sc(C) and (Ge, Ga) atoms are negligible and not shown. Notably, the characteristic of fully-compensated ferrimagnetism arises from the antiparallel alignment of the two Ir moments.

4. CONCLUSIONS

In conclusion, this ab initio study investigated the structural, magnetic, electronic, and elastic properties of the Heusler alloys Ir_2ScGa and Ir_2ScGe. In summary, both Ir_2ScGa and Ir_2ScGe stabilize in Cu_2MnAl-type with lattice parameters of 6.27 and 6.37 Å, bulk moduli of 210.60 and 81.71 GPa, and formation energies of –0.83 and –0.85 Ry, confirming thermodynamic stability. Elastic constants (e.g., C_{11} = 335.95 GPa for Ir_2ScGa-Cu_2MnAl) affirm mechanical stability. Electronic DOS shows metallic behavior (no gaps), and magnetic moments indicate fully compensated state (0 μ_B) for Ir_2ScGa-Cu_2MnAl. These results, showing high cohesive energies (~11.5 eV), suggest potential applications in stable, non-magnetic optical devices and warrant experimental validation.

Further experimental studies are needed to deepen our understanding of the mechanical and electronic properties of these materials and to explore their potential in other technological fields.

FUNDING

This work was supported by ongoing institutional funding. No additional grants to carry out or direct this particular research were obtained.

CONFLICT OF INTEREST

The authors of this work declare that they have no conflicts of interest.

REFERENCES

1. B. Balke, G. H. Fecher, and C. Felser, in *Spintronics: From Materials to Devices* (Springer, Dordrecht, 2013), pp. 15–43. https://doi.org/10.1007/978-90-481-3832-6_2
2. Y. Z. Abdullahi, T. L. Yoon, M. M. Halim, M. R. Hashim, and T. L. Lim, Surf. Sci. **667**, 112–120 (2018). https://doi.org/10.1016/j.susc.2017.10.006
3. A. Zerouali, A. Mokaddem, B. Doumi, F. Dahmane, M. Elkeurti, A. Sayede, and A. Tadjer, J. Comput. Electron. **15**, 1255–1262 (2016). https://doi.org/10.1007/s10825-016-0912-4
4. J. Atulasimha and S. Bandyopadhyay, *Nanomagnetic and Spintronic Devices for Energy-Efficient Memory and Computing* (John Wiley and Sons, Hoboken, NJ, 2016).
5. R. Ribeiro, A. Camilo Jr., and S. De Lazaro, J. Magn. Magn. Mater. **394**, 463–469 (2015). https://doi.org/10.1016/j.jmmm.2015.05.096
6. M. N. Baibich, J. M. Broto, A. Fert, et al., Phys. Rev. Lett. **61**, 2472 (1988). https://doi.org/10.1103/PhysRevLett.61.2472
7. R. A. de Groot, F. M. Mueller, P. G. van Engen, and K. H. J. Buschow, Phys. Rev. Lett. **50,** 2024 (1983). https://doi.org/10.1103/PhysRevLett.50.2024
8. A. Birsan and V. Kuncser, J. Magn. Magn. Mater. **406**, 282–288 (2016). https://doi.org/10.1016/j.jmmm.2016.01.032
9. O. Cheref, F. Dahmane, S. Benalia, D. Rached, M. Mokhtari, L. Djoudi, M. Merabet, and N. Bettahar, Comput. Condens. Matter **19**, e00369 (2019). https://doi.org/10.1016/j.cocom.2019.e00369
10. W. Huang, X. Wang, X. Chen, W. Lu, L. Damewood, and C. Y. Fong, J. Magn. Magn. Mater. **377**, 252–258 (2015). https://doi.org/10.1016/j.jmmm.2014.10.068
11. H. Mokhtari, L. Boumia, M. Mokhtari, F. Dahmane, D. Mansour, and R. Khenata, J. Supercond. Nov. Magn. **36**, 1217–1224 (2023). https://doi.org/10.1007/s10948-023-06560-1
12. M. Lazizi, M. Harmel, M. Mokhtari, F. Dahmane, R. Khenata, N. Badi, A. Bouhemadou, T. Seddik, H. Khachai, and S. Bin Omran, Inorg. Chem. Commun. **142**, 109675 (2022). https://doi.org/10.1016/j.inoche.2022.109675
13. S. M. Watts, S. Wirth, S. von Molnar, A. Barry, and J. M. D. Coey, Phys. Rev. B **61**, 9621 (2000). https://doi.org/10.1103/PhysRevB.61.9621
14. J. Li, Y. Li, X. Dai, H. Liu, and X. Yu, Phys. B: Condens. Matter. **403**, 2473–2476 (2008). https://doi.org/10.1016/j.physb.2008.01.007
15. S. Krishnaveni, M. Sundareswari, and M. Rajagopalan, IOSR J. Appl. Phys. **7**, 52–55 (2015). https://doi.org/10.9790/4861-07135255
16. E. Özdemir, E. Eser, and Z. Merdan, Chin. J. Phys. **56**, 1551–1558 (2018). https://doi.org/10.1016/j.cjph.2018.05.020
17. S. Krishnaveni, J. Phys. Conf. Ser. **1172**, 012030 (2019).
18. E. Engel, *Density Functional Theory* (Springer, Berlin, 2011).
19. P. Hohenberg and W. Kohn, Phys. Rev. **136**, B864 (1964). https://doi.org/10.1103/PhysRev.136.B864
20. W. Kohn and L. Sham, in *Conf. Proc. Ital. Phys. Soc.* (Editrice Compositori, 1996).
21. P. Blaha et al., WIEN2k: An Augmented Plane Wave + Local Orbitals Program for Calculating Crystal Properties (Vienna University of Technology, 2001).
22. J. P. Perdew, K. Burke, and M. Ernzerhof, Phys. Rev. Lett. **77**, 3865 (1996). https://doi.org/10.1103/PhysRevLett.77.3865
23. H. J. Monkhorst and J. D. Pack, Phys. Rev. B **13**, 5188–5192 (1976). https://doi.org/10.1103/PhysRevB.13.5188
24. A. Baldereschi, Phys. Rev. B **7**, 5212 (1973). https://doi.org/10.1103/PhysRevB.7.5212
25. F. D. Murnaghan, Proc. Natl. Acad. Sci. USA **30**, 244–247 (1944). https://doi.org/10.1073/pnas.30.9.244
26. R. Hill, Proc. Phys. Soc. Sect. A **65**, 349 (1952). https://doi.org/10.1088/0370-1298/65/5/307
27. S. Wang and H. Ye, Phys. Status Solidi B **240**, 45–54 (2003). https://doi.org/10.1002/pssb.200301861
28. V. Kanchana, G. Vaitheeswaran, and A. Svane, J. Alloys Compd. **455**, 480–484 (2008). https://doi.org/10.1016/j.jallcom.2007.01.163
29. W. Voigt, Ann. Phys. **274**, 573–587 (1889). https://doi.org/10.1002/andp.18892741206
30. A. Reuss, Z. Angew. Math. Mech. **9**, 49–58 (1929). https://doi.org/10.1002/zamm.19290090104
31. I. N. Frantsevich, *Elastic Constants and Elastic Moduli of Metals and Insulators: Reference Book* (Naukova Dumka, Kiev, 1982).
32. F. Mollaamin and M. Monajjemi, Comput. Theor. Chem. **1237**, 114666 (2024). https://doi.org/10.1016/j.comptc.2024.114666

Publisher's Note. Pleiades Publishing remains neutral with regard to jurisdictional claims in published maps and institutional affiliations.
AI tools may have been used in the translation or editing of this article.

SPELL: 1. Ernzerhof

Chinese Journal of Physics 100 (2026) 163–171

Contents lists available at ScienceDirect

Chinese Journal of Physics

journal homepage: www.sciencedirect.com/journal/chinese-journal-of-physics

Research Paper

First principles study of the structural, electronic and magnetic properties of full-Heusler rare earth-based alloys Pr_2RhZ (Z=Al, Ga and In)

Abdelkader Ilias Bouadi [a,b], Mahdi Abane [c], Mohamed Mokhtari [a,b], Fethallah Dahmane [a,d,*]

[a] Laboratory of Modeling and Simulation of Magnetic Properties of Hetero-structures (LPMH) Faculty of Sciences and Technology, Tissemsilt University, Tissemsilt, Algeria
[b] Laboratoire d'Etudes Physique des Matériaux, Département de physique énergétique, Université des Sciences et de Technologie, USTO-MB, BP 1505 El M'naour, Oran, Algeria
[c] Materials and Fluids Physics Laboratory, Faculty of Physics, University of Science and Technology of Oran USTO-MB Oran, BP 1505, El M'naouer, Oran, Algeria
[d] Laboratoire de Physique Quantique et de Modélisation Mathématique (LPQ3M), Département de Technologie, Université de Mascara, 29000 Mascara, Algérie

ARTICLE INFO

Keywords:
Full Heusler
DFT
WIEN2k
Rare-earth alloys
Half-metals

ABSTRACT

Using the Density functional theory (DFT) based on the full potential linearized augmented plane wave (FP-LAPW) with the GGA-PBE approximation implemented in WIEN2K code, we have investigated the structural, electronic, and magnetic properties of full-Heusler rare earth-based compounds Pr_2RhZ (where Z = Al, Ga, In) in Hg_2CuTi-type and Cu_2MnAl-type configurations. The ferromagnetic- Hg_2CuTi-type structure demonstrated superior stability compared to the Cu_2MnAl-type structure at ambient conditions for all compounds with negative formation energies confirming thermodynamic stability and synthesizability and lattice parameters between 6.846 and 7.038 Å. These alloys exhibit half-metallic behavior with 100 % spin polarization, indirect band gaps (0.235–0.345 eV), and integer magnetic moments of 4 μ_B per formula unit, obeying the Slater-Pauling rule. This work highlights their promise as candidates for spintronic devices, filling a gap in rare-earth Heusler research.

1. Introduction

Half-metal is a promising category of functional material for spintronic applications, characterised by complete spin polarisation at the Fermi energy level and distinctive properties of its two spin channels [1,2]. Due to their many uses, such as giant magnetoresistance (MR) [3,4], shape recovery [4–7], metamagnetic properties [8,9], and significant magnetocaloric effect (MCE) [10,11], magnetic shape memory alloys (MSMAs) with Heusler structure have garnered a lot of interest in recent decades. It is well known that the concentration of conduction electrons and chemical bonding have a significant impact on the magnetic characteristics of Heusler alloys. For instance, because of the arrangement of the Mn d-orbitals, Mn-based compounds exhibit relatively localised magnetism [12–14].

* Corresponding author.
E-mail address: fethallah05@gmail.com (F. Dahmane).

https://doi.org/10.1016/j.cjph.2025.11.019
Received 10 August 2025; Received in revised form 16 November 2025; Accepted 18 November 2025
Available online 19 November 2025
0577-9073/© 2025 The Physical Society of the Republic of China (Taiwan). Published by Elsevier B.V. All rights are reserved, including those for text and data mining, AI training, and similar technologies.

The total energies of the antiferromagnetic and other structures can also be compared to determine the ground-state magnetic configuration [15]. Heusler alloys are a well-known class of intermetallic compounds discovered by Fritz Heusler in 1903. They typically have a 1:1:1 (also known as half-Heusler alloys) or 2:1:1 (also known as full-Heusler alloys) composition and comprise approximately 1500 members [16]. They remain a popular area of study today [17]. In contrast, compounds based on cobalt [18–25], Mn-based alloys as Mn_2HfP and Mn_2HfSi [26], Mn_2TaAl, Mn_2WAl [27] and Ni_2MnGa [28], and other alloys as Ti_2FeGe [29] exhibit greater itinerant behaviour. The transition from the ferromagnetic phase to the antiferromagnetic phase with varying carrier concentrations is also studied for so-called full-Heusler alloys, which have a general formula unit of X2YZ, where X and Y represent transition metals, and Z is an s- or p-element, such as Al, Ga, Sn, or Sb.

The local geometry and chemical composition have a significant impact on the magnetic characteristics of Heusler alloys. The ab initio study of the electronic structure can be beneficial in understanding how magnetic characteristics depend on the atomic composition and crystal structure. The spin-polarised relativistic Korringa-Kohn-Rostoker method used by Wei et al. [30,31] in combination with Monte Carlo calculations to study the exchange interactions and Curie temperatures of Fe_2NiZ (Z = Al, Ga, In, Si, Ge, Sn, P, As, Sb). The Ni_2MnGa Heusler alloy remains the subject of extensive experimental and theoretical research [32]. The Heusler rare-earth-based compounds, known as heavy fermions, are more extensively studied for their diverse properties, which are essential for various technological fields, including thermoelectric devices and spintronics applications. There are many studies in this field, including HoPdBi and HoPtBi [33], LiSrX (X= P and As) [34], NaCaZ (Z= N, P, and As) [35], CoRuFeX (X= Si and Ge) [36], and Co_2FeGe [37].

Compared to transition-metal-based Heusler alloys (such as Co- or Mn-based), rare-earth-based alloys, especially those that contain 4f elements like Pr (praseodymium), are not as well studied. Pr provides special localised 4f electrons that can improve exchange interactions and magnetic moments, which may raise Curie temperatures and improve spin polarisation for spintronic applications [20]. Because of its partially filled 4d states, which encourage strong d-d and d-f hybridisation with Pr, which is essential for half-metallicity, Rh (rhodium) was selected as the transition metal. Such successful hybridisations in other Rh-containing Heusler alloys (e.g., references to CoRuFeX or analogous systems) serve as inspiration for this.

In this paper, we investigated the structural, electronic, and magnetic properties of the Full Heusler rare-earth-based alloys Pr_2RhZ (Z= Al, Ga, In) using first-principles calculations based on the density functional theory (DFT) [38,39]. The importance of this study lies in the fact that these alloys have never been studied before, either theoretically or experimentally. This motivated us to investigate their properties, and the results obtained enhance their importance in a wide range of technological fields, including spintronics applications. These alloys have a negative energy formation, which indicates their thermodynamic stability and the ability to synthesise them.

2. Computational details

We used the density functional theory (DFT) [38,39] based on full potential linearized augmented plane wave (FP-LAPW) [40–47] implemented in WIEN2k code [48] to achieve our investigation. Firstly, we plotted the energy as a function of volume for all compounds, considering two possible structures, Hg_2CuTi and Cu_2MnAl, in two phases: Non-magnetic (NM) and Ferromagnetic (FM). We employed the generalized gradient approximation (GGA-PBE) [49] for all properties. Then, we discussed the electronic properties and magnetic moments of our alloys, as examined by the Slater-Pauling rule [50].

The space is divided into nonoverlapping muffin tin (MT) spheres separated by an interstitial region in the FP-LAPW method. The value of the plane wave cut-off Kmax multiplied by the muffin-tin radius Rmt is Rmt × Kmax= 7 a.u. The value of partial waves inside atomic spheres is restricted to *l*max= 10. Subsequently, calculations are carried out within the initial Brillouin zone (BZ) using a plane-wave cut-off and a Monkhorst-Pack grid with 4000 points in a 15 × 15 × 15 k-mesh. For the parameter Gmax, which is defined as the

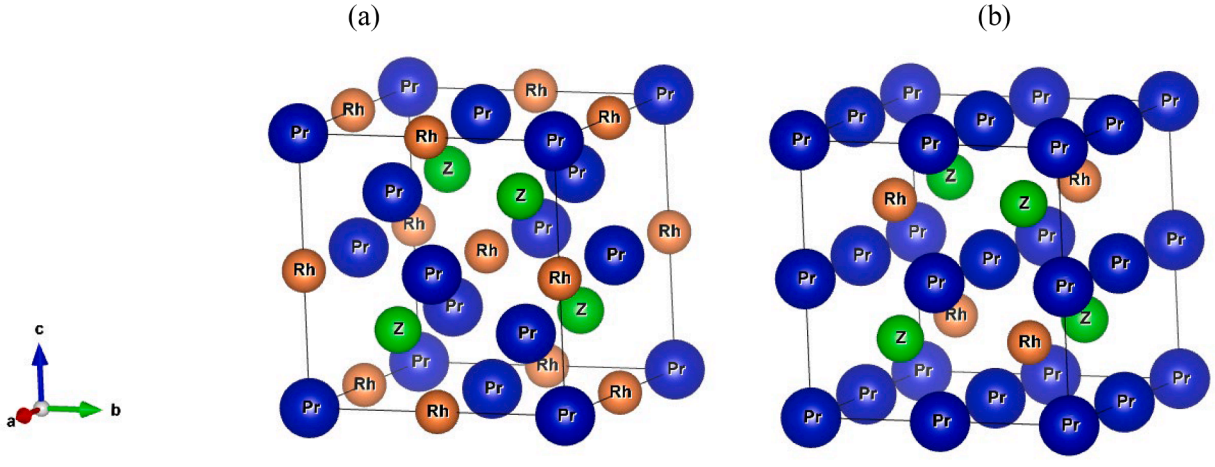


Fig. 1. Crystallographic structure of full-Heuler alloy Pr_2RhZ (Z=Al, Ga and In) in which (a) Hg_2CuTi type and (b) Cu_2MnAl type (by VESTA [51]).

magnitude of the most significant vector in the charge density Fourier expansion, a value of 14 (a.u.) $^{-1}$ was adopted. Self-consistency is established by requiring that the total energy convergence is less than 10^{-6} eV.

3. Results and discussion

3.1. Structural properties

Our compounds, which are full-Heusler-based on rare earth elements, have three types of atoms per cell: one transition metal (Rh), one post-transition metal (Al, Ga, or In), and two rare earths (Pr). They have a stoichiometry formula X2YZ. These alloys exhibit two distinct crystal structures: face-centred cubic (fcc) lattices, specifically the Cu_2MnAl and Hg_2CuTi structures (*Fig. 1*). The two structures consist of four interpenetrating face-centred cubic (fcc) sublattices with four unique crystal sites: 4a (0, 0, 0), 4b (0.25, 0.25, 0.25), 4c (0.5, 0.5, 0.5), and 4d (0.75, 0.75, 0.75).

In the Cu_2MnAl type structure, referred to as $L2_1$, the atomic arrangement inside the four sites of the unit cell adheres to the sequence X–Y–X–Z. Conversely, in the Hg_2CuTi type structure, designated as the XA structure, the sequence of atoms occupying the four sites of the unit cell is X–X–Y–Z [52].

In *Fig. 2*,we show the total energy versus the volume graphs of our alloys for both Hg_2CuTi-type and Cu_2MnAl-type in both non-magnetic and ferromagnetic phases, using the Birch-Murnaghan equation as represented in [53]:

$$E(V) = E_0 + \frac{B}{B'(B'-1)}\left[V\left(\frac{V_0}{V}\right)^{B'} - V\right] + \frac{B}{B'}(V - V_0) \quad \text{(Eq. 1)}$$

This equation incorporates the variables E for energy, V for volume, B for the equilibrium bulk modulus, V_0 for the volume of the experimental unit cell, and B' for the pressure derivative of the bulk modulus at the equilibrium volume.

The obtained results resumed in the *Table 1*.

As shown in *Fig. 2*, the Hg_2CuTi configuration in the ferromagnetic state exhibits greater energy stability compared to the alternative states of the Cu_2MnAl structure. These results are in good agreement with previous investigations, which have indicated that the

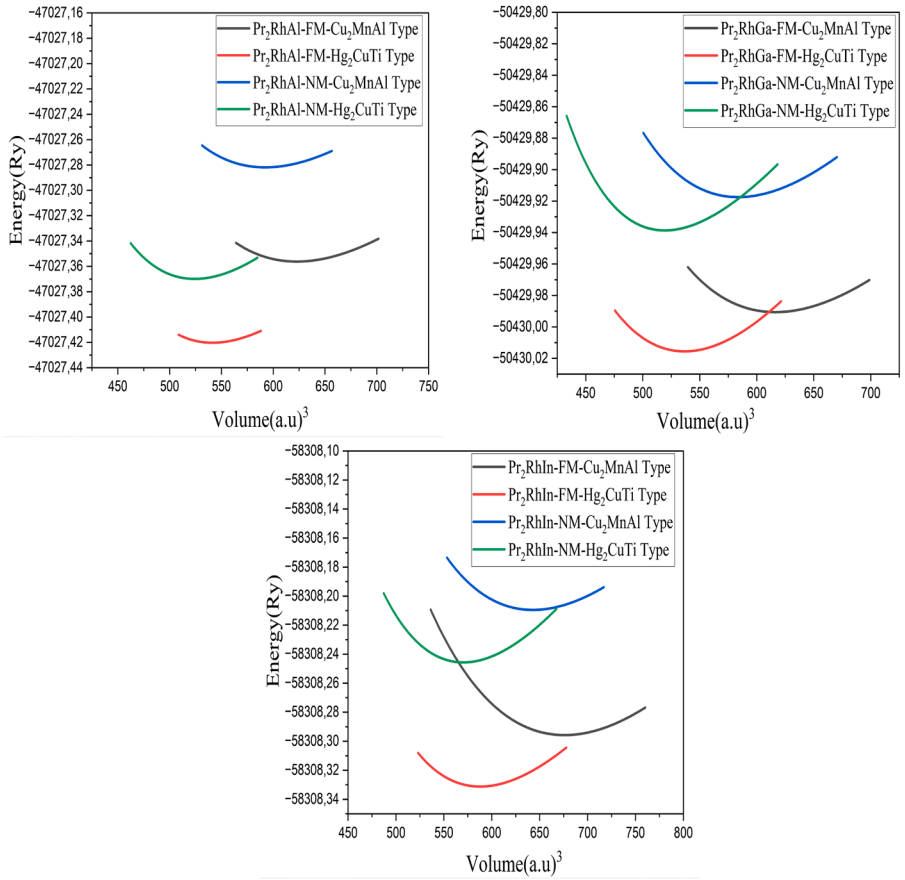


Fig. 2. Total energy versus unit cell volume for Pr_2RhZ (Z = Al, Ga and In).

Table 1
Optimized lattice constant a0 (Å), Bulk modulus B (GPa), the pressure derivative B', the total energy E_{min} (Rd), and the Formation energy ΔH (Rd) for Full Heusler compounds Pr2RhZ (Z= Al, Ga, In).

Alloy	Phases	a_0 (Å)	B (GPa)	B'	E_{min} (Rd)	ΔH (Rd)
Pr_2RhAl	Cu_2MnAl (NM)	7.0545	65.9072	4.6375	-47027.28187	–1.236609
	Cu_2MnAl (FM)	7.1736	65.5744	4.3500	-47027.35622	–1.310959
	Hg_2CuTi (NM) Hg_2CuTi (FM)	6.7733	87.5915	5.1169	-47027.36992	–1.324659
		6.8460	82.1681	5.9021	-47027.42028	–1.375019
Pr_2RhGa	Cu_2MnAl (NM)	7.0201	75.3812	4.7326	-50429.91749	–1.200406
	Cu_2MnAl (FM)	7.1492	68.5380	4.5062	-50429.99060	–1.273516
	Hg_2CuTi (NM) Hg_2CuTi (FM)	6.7517	97.7184	6.0264	-50429.93873	–1.221646
		6.8264	89.5538	4.0515	-50430.01555	–1.298466
Pr_2RhIn	Cu_2MnAl (NM)	7.2497	65.0587	4.2979	-58308.20951	–1.093645
	Cu_2MnAl (FM)	7.3721	63.3522	3.9451	-58308.29583	–1.179965
	Hg_2CuTi (NM) Hg_2CuTi (FM)	6.9663	86.7731	4.4292	-58308.24569	–1.129825
		7.0375	75.5786	4.7752	-58308.33122	–1.215355

Hg_2CuTi structure is more likely to develop when the Y element has a higher electronegativity than the X element [54].

We computed the formation energy to establish the viability of this chemical and its potential for experimental synthesis, using the following relation [55]:

$$\Delta H = E_f^{Pr_2RhZ} = E_{tot}^{Pr_2RhZ} - E_{Rh}^{builk} - E_Z^{builk} - 2E_{Pr}^{builk} \quad \text{(Eq. 2)}$$

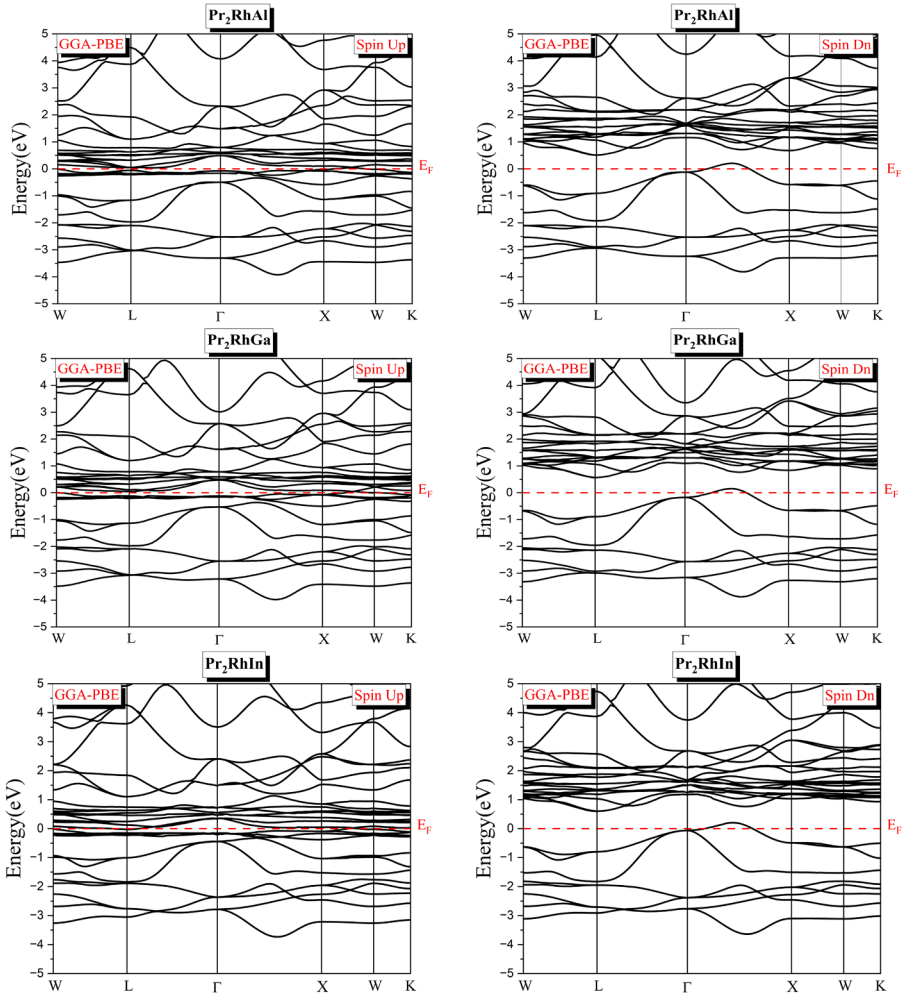


Fig. 3. Spin-polarized band structures of majority spin (Up) and minority spin (Down) of Pr2RhZ (Z= Al, Ga, In) in ferromagnetic-Hg2CuTi type structure.

where $E_f^{Pr_2CoZ}$ is the equilibrium energy of these compounds, in which $E_{tot}^{Pr_2CoZ}$ is the total energy of compounds and E_{Pr}^{builk} , E_{Rh}^{builk} and E_Z^{builk} are the chemical potential of atoms in their stable bulk for Pr, Rh, and Z(Al, Ga, In).

The estimated formation energies of the compounds Pr_2RhZ (Z= Al, Ga, In) for the Hg_2CuTi-type structure are –1.375019 Ry, –1.298466 Ry and –1.215355 Ry, respectively, indicating the thermodynamic stability of these alloys [56].

Conversely, we can remark that the Hg_2CuTi-type structure is the most stable phase by comparing the formation energy values of the Hg_2CuTi-type and Cu_2MnAl-type structures (refer to *Table 1*).

3.3. Electronic properties

The distribution of electrons in the valence and conduction bands, as well as the magnitude of the gap, fundamentally determines the solid's electronic characteristics, including its band structure, density of states, and Fermi surface. As mentioned above, we plotted the band structures and the total density of states of Pr_2RhZ (Z= Al, Ga, In) compounds for both spin directions (down and up). This investigation aims to elucidate the electronic structure of these compounds within the stable Hg2CuTi structure in a ferromagnetic configuration at the equilibrium lattice parameter, employing the GGA-PBE approximation. The band structure and DOS are illustrated in Figs. 3 and 4, respectively, with the corresponding band gap values detailed in Table 2**.**

From Fig. 3 (**a, c and e**), in which we plotted the majority spin direction (up) of our compounds Pr_2RhZ (Z = Al, Ga and In) respectively, we remark an overlap between conduction and valence band indicating the metallic behaviour of our alloys in this direction. Furthermore, the minority spin direction of our alloys is plotted in Fig. 3 (**b, d, and f**), where we observe an indirect band gap; an energy gap emerges between the higher valence band at the Γ and X points and the lower conduction band at the L point. Consequently, these compounds display the traits of indirect band gap semiconductors, possessing energy band gaps of 0.235 eV, 0.345

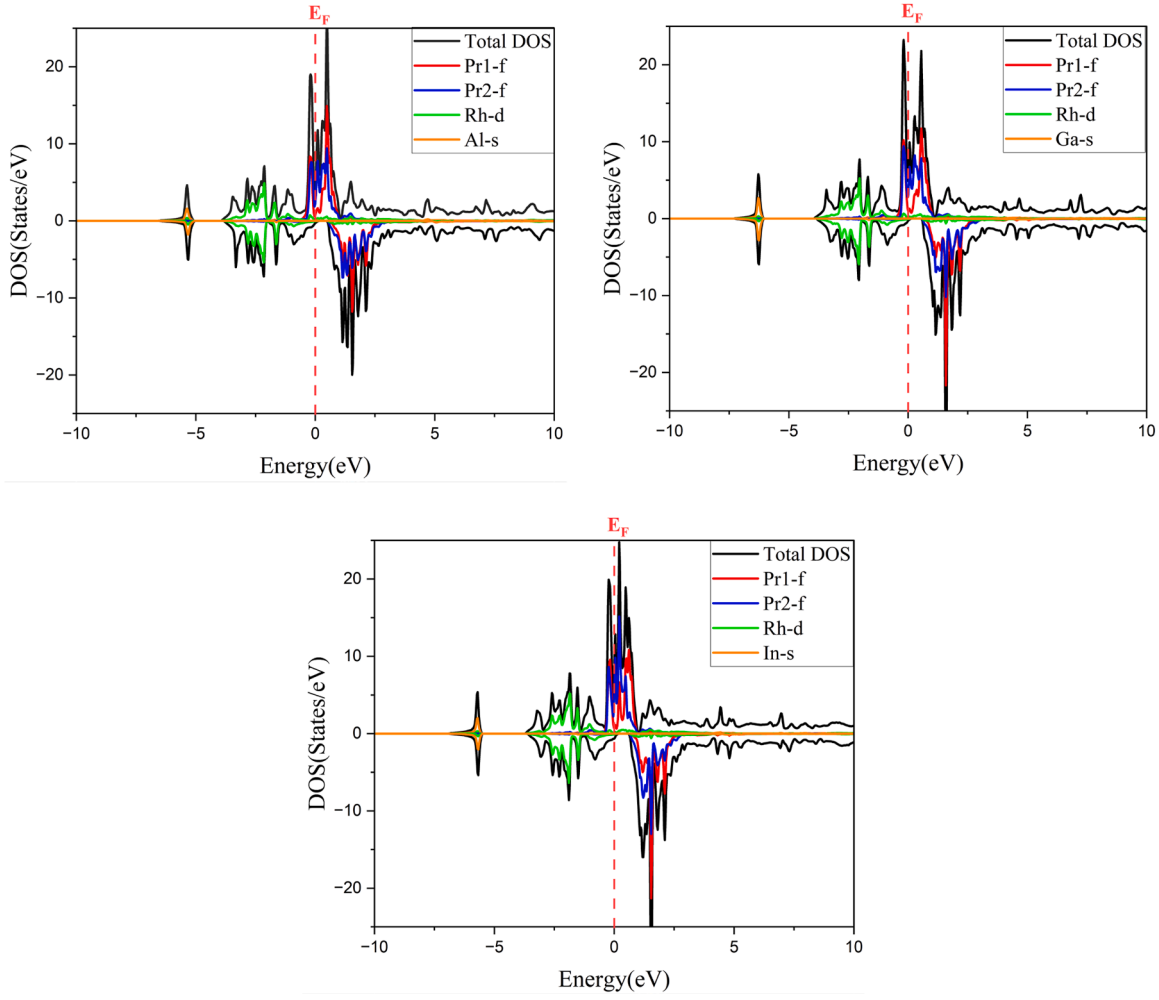


Fig. 4. Total and partial density of state with both majority and minority spin direction of Pr_2RhZ (Z= Al, Ga, In) alloys in ferromagnetic-Hg_2CuTi type structure.

Table 2
The calculated total magnetic moments (μtot), atomic and interstitial magnetic moments and the band gap energy (E_g) for the Pr_2RhZ (Z= Al, Ga, In).

Alloys	*a* (Å)	μ_{tot} (μB)	μ_{Pr1} (μB)	μ_{Pr2} (μB)	μ_{Rh} (μB)	μ_Z (μB)	μinterstitial (μB)	E_g (eV)
Pr_2RhAl	6.8460	4.05	2.04395	1.90365	-0.18607	-0.05934	0.34937	0.235
Pr_2RhGa	6.8264	4.02	2.04779	1.92582	-0.20469	-0.06759	0.32398	0.345
Pr_2RhIn	7.0375	4.06	2.08040	1.95148	-0.21877	-0.04845	0.30402	0.340

eV, and 0.34 eV for Pr_2RhAl, Pr_2RhGa, and Pr_2RhIn, respectively. Consequently, we conclude that all compounds exhibit half-metallic behaviour.

The formation of the half-metallic gap in these compounds originates from the strong hybridization between the d states of Rh and the f/d states of Pr within the $L2_1$ crystal symmetry. This hybridization splits the electronic states into bonding and anti-bonding bands. Owing to the exchange interaction, the spin-up and spin-down bands experience different energy shifts: the majority-spin channel remains metallic, whereas the minority-spin channel exhibits a gap at the Fermi level. The size and position of this gap are controlled by the degree of d–d hybridization and the crystal-field splitting of the Rh atoms, which together determine the spin polarisation at the Fermi level. Such a mechanism of gap formation has been reported for several half-metallic Heusler systems [27], and our results confirm that the same physical picture applies to Pr_2RhAl, Pr_2RhGa, and Pr_2RhIn.

Faleev et al. [57] have provided persuasive evidence for the probable hybridization of d-orbitals in transition metals, specifically in the context of the X2YZ inverse Heusler compounds. They assert that the mutual symmetry of X (1) and Y atoms induces the hybridization of their d-orbitals, resulting in five bonding d states (2eg and 3t2g) and five non-bonding d states (2eu and 3tu). The five X (1)-Y bonding d states subsequently experience hybridization with the d-orbital of X(2) atoms, leading to the creation of novel bonding and anti-bonding states [38].

It is worth noting that the electronic structure of Pr_2RhZ (Z= Al, Ga, In) alloys involves localized 4f electrons from Pr and partially filled 4d states from Rh. In the present work, the exchange–correlation potential was treated within the framework of the generalized gradient approximation (GGA). Although this approach provides accurate structural and magnetic trends for Heusler compounds, it does not explicitly include the on-site Coulomb repulsion (U) associated with localized electrons. Incorporating the GGA+U correction could further improve the description of the 4f and 4d states and slightly modify the position of the Fermi level or the width of the half-metallic gap. Nevertheless, the overall features of the electronic and magnetic behaviour reported here are consistent with previous GGA-based studies of rare-earth–transition-metal Heusler alloys.

The electronic structure and cohesive energy results can help us understand how the chemical bonds work in the Heusler alloys Pr_2RhZ (Z= Al, Ga, In). The intense mixing of the Rh d and Pr f/d states near the Fermi level shows that the material has a mixed metallic-covalent character. These enable efficient spin exchange interactions and promote ferromagnetic ordering. The relatively high cohesive energy values indicate that these compounds have strong bonds and are structurally stable. In Heusler systems, the arrangement of valence electrons determines both bonding and magnetic behaviour. Delocalized conduction electrons contribute to metallic bonding and electrical conductivity, while localized states enhance magnetic exchange interactions. An Electron Localisation Function (ELF) analysis—though not conducted here—would generally reveal intermediate ELF values (≈0.4–0.6) in the Rh–Pr regions, indicative of metallic–covalent bonding, and low ELF values (<0.2) in interstitial regions, signifying delocalized electrons. Similar correlations among ELF profiles, cohesive energy, and magnetic properties have been documented in related research [58]

The computed spin polarisation total density of states (DOS) and partial DOS of Pr_2RhZ (Z= Al, Ga, In) compounds at their equilibrium lattice parameters are presented in *Fig. 4*.

Energy levels below -5 eV, predominantly derived from the s states of post-transition metal (Al, Ga or In) atoms, are committed from *Fig. 4* owing to their near-symmetry in both majority and minority spin orientations. These states are much removed from the Fermi level and, as a result, do not influence the magnetic characteristics. The Rh-d orbitals dominated our valence band, and the f states of Pr1 and Pr2 constitute the predominant portion of the total density of states (DOS) at the Fermi level. The f electrons of Pr2 atoms and the d orbitals of Rh atoms determine the band gap around the Fermi level in all alloys. The density of states above the Fermi level is affected mainly by the Pr-f and Rh-d orbitals. We have computed the spin polarisation ratio (P) for these three compounds. The computation of spin polarisation can be accomplished using:

$$P = \frac{N\uparrow(\varepsilon_F) - N\downarrow(\varepsilon_F)}{N\uparrow(\varepsilon_F) + N\downarrow(\varepsilon_F)} \quad \text{(Eq. 3)}$$

where N ↑ (εF) and N ↓ (εF) indicate the density of states (DOS) for majority-spin and minority-spin states at the Fermi level, respectively. The three analysed compounds have a complete (100 %) spin polarisation ratio at the Fermi level.

3.4. Magnetic properties

Slater and Pauling established in two seminal publications that, for binary magnetic compounds, the addition of one valence electron causes the compound to inhabit spin-down states, resulting in a reduction of the total spin magnetic moment by 1 μB [59]. Notably, half-metallic Heusler alloys demonstrate analogous behaviour. The total spin magnetic moment in the unit cell is proportional to the total number of valence electrons [60].

Table 2 displays the computed magnetic moment for the entire Heusler alloys Pr_2RhAl, Pr_2RhGa, and Pr_2RhIn at their optimized

lattice parameters. All studied alloys exhibit integer magnetic moments of 4 μB. Half-metallic materials are distinguished by an integer total magnetic moment. Consequently, Pr_2RhAl, Pr_2RhGa, and Pr_2CoIn are classified as half-metallic ferromagnets (HMF) under the category of complete Heusler alloys.

The emergence of these integer magnetic moments in bulk Heusler alloys originates from specific microphysical mechanisms related to the electronic structure. The strong hybridisation between the Rh–Rh and Rh–Pr d orbitals gives rise to bonding and antibonding states. Due to exchange splitting, the minority-spin channel develops a semiconducting gap, whereas the majority-spin channel remains metallic. These result in complete spin polarisation at the Fermi level and give rise to an integer total magnetic moment per formula unit. Furthermore, the localised 4f electrons of Pr contribute indirectly through Ruderman–Kittel–Kasuya–Yosida (RKKY)-type exchange interactions with the Rh d states, thereby reinforcing the ferromagnetic alignment and stabilising the half-metallic state. Similar microscopic mechanisms explaining the origin of integer magnetic moments in Heusler-type compounds have been reported in the literature [61–63].

Based on the magnetic moment values for each atom in the compounds presented in Table 2, we deduce that the predominant contribution to the total magnetic moment arises from the Pr atoms. In contrast, the Al, Ga, and In atoms contribute minimally to the total magnetic moment. The electronic configurations of the atoms in our compounds are Pr: $[Xe]4f^3 6s^2$, Rh: $[Kr]4d^8 5s^1$, Al: $[Ne]3s^2 3p^1$, Ga: $[Ar]3d^{10} 4s^2 4p^1$, In: $[Kr]4d^{10} 5s^2 5p^1$.

Furthermore, the compounds Pr_2RhAl, Pr_2RhGa, and Pr_2RhIn possess the same quantity of valence electrons, totalling 22. Our findings demonstrate a linear correlation between the total spin magnetic moment and the number of valence electrons, consistent with the established Slater–Pauling connection [50], expressed by the following equation:

$$\mu_{tot} = Z_{tot} - 18 \quad \text{(Eq. 4)}$$

where Z_{tot} is the total number of valence electrons per unit cell and μ_{tot} is the total spin magnetic moment [64].

It is worth noting that the Gilbert damping constant (α), which characterises the energy dissipation and magnetisation relaxation processes, is a crucial quantity for evaluating the spintronic potential of half-metallic ferromagnets. However, its precise determination requires spin–orbit coupling and dynamic simulations, which are beyond the present static DFT framework. Future work will focus on estimating α to further clarify the spin dynamics of Pr_2RhZ alloys [65,66].

4. Conclusion

The structural, electronic and magnetic properties of the Pr_2RhZ (Z= Al, Ga, In) for both Hg_2CuTi and Cu_2MnAl type structures in nonmagnetic (NM) and ferromagnetic (FM) phases have been investigated using the FP-LAPW with the GGA-PBE approximation implemented in the WIEN2K code. The ferromagnetic- Hg_2CuT-type is more stable than Cu_2MnAl-type for Pr_2RhZ (Z= Al, Ga, In) compounds at ambient conditions. It exhibits HM nature and an indirect band gap with a magnetic moment of 4 μB, which is consistent with the Slater–Pauling rule. These properties make them candidates for spintronics applications.

CRediT authorship contribution statement

Abdelkader Ilias Bouadi: Writing – original draft. **Mahdi Abane:** Writing – review & editing. **Mohamed Mokhtari:** Validation. **Fethallah Dahmane:** Supervision.

Declaration of interest statement

We wish to confirm that there are no known conflicts of interest associated with this publication. All authors have participated sufficiently in the work to take public responsibility for its content and have agreed to the submitted version of the manuscript. All sources of funding for the research reported in this article have been acknowledged, and we confirm that no financial or personal relationships exist with other people or organizations that could inappropriately influence (bias) our work.

References

[1] X.-P. Wei, Z.-Y. Mei, X. Tao, « Surface effects for half-metallic Heusler alloy CrYCoAl », Phys. B Condens. Matter 683 (2024) 415925 https://doi.org/10.1016/j.physb.2024.415925 juin.
[2] X.-P. Wei, J.-R. Liu, X. Zhang, W.-L. Chang, X. Tao, « Stability, electronic and magnetic properties of half-metallic alloy CrLaCoAl (100) surface », Phys. B Condens. Matter 639 (2022) 414015 https://doi.org/10.1016/j.physb.2022.414015.
[3] Z.H. Liu;Z. H. Liu, H. Liu, X.X. Zhang, X.K. Zhang, JQ. Xiao, Z.Y. Zhu, X.F. Dai, G.D. Liu, J.L. Chen, G.H. Wu, « Large negative magnetoresistance in quaternary Heusler alloy Ni50Mn8Fe17Ga25 melt-spun ribbons », Appl. Phys. Lett. 86 (18) (2005) 182507 https://doi.org/10.1063/1.1925783 mai.
[4] M. Wuttig, L. Liu, K. Tsuchiya, R.D. James, « Occurrence of ferromagnetic shape memory alloys (invited) », J. Appl. Phys. 87 (9) (2000) 4707–4711, https://doi.org/10.1063/1.373135, mai.
[5] R. Kainuma, Y. Imano, W. Ito, Y. Sutou, H. Morito, S. Okamoto, O. Kitakami, K. Oikawa, A. Fujita, T. Kanomata, K. Ishida, « Magnetic-field-induced shape recovery by reverse phase transformation », Nature 439 (7079) (2006) 957–960, https://doi.org/10.1038/nature04493.
[6] J.A. Monroe, I. Karaman, B. Basaran, W. Ito, R.Y. Umetsu, R. Kainuma, K. Koyama, Y.I. Chumlyakov, « Direct measurement of large reversible magnetic-field-induced strain in Ni–Co–Mn–In metamagnetic shape memory alloys », Acta Mater. 60 (20) (2012) 6883–6891, https://doi.org/10.1016/j.actamat.2012.07.040.
[7] S.Y. Yu, Z.X. Cao, L. Ma, G.D. Liu, J.L. Chen, G.H. Wu, B. Zhang, X.X. Zhang, « Realization of magnetic field-induced reversible martensitic transformation in NiCoMnGa alloys », Appl. Phys. Lett. 91 (10) (2007) 102507 https://doi.org/10.1063/1.2783188.
[8] R. Kainuma, Y. Imano, W. Ito, H. Morito, Y. Sutou, K. Oikawa, A. Fujita, K. Ishida, S. Okamoto, O. Kitakami, T. Kanomata, « Metamagnetic shape memory effect in a Heusler-type Ni43Co7Mn39Sn11 polycrystalline alloy », Appl. Phys. Lett. 88 (19) (2006) 192513 https://doi.org/10.1063/1.2203211.

[9] J.I. Pérez-Landazábal, V. Recarte, V. Sánchez-Alarcos, C. Gómez-Polo, E. Cesari, « Magnetic properties of the martensitic phase in Ni-Mn-In-Co metamagnetic shape memory alloys », Appl. Phys. Lett. 102 (10) (2013) 101908 https://doi.org/10.1063/1.4795716.

[10] J. Du, Q. Zheng, W.J. Ren, W.J. Feng, X.G. Liu, Z.D. Zhang, « Magnetocaloric effect and magnetic-field-induced shape recovery effect at room temperature in ferromagnetic Heusler alloy Ni–Mn–Sb », J. Phys. Appl. Phys. 40 (18) (2007) 5523–5526, https://doi.org/10.1088/0022-3727/40/18/001.

[11] J. Liu, T. Gottschall, K.P. Skokov, J.D. Moore, O. Gutfleisch, « Giant magnetocaloric effect driven by structural transitions », Nat. Mater. 11 (7) (2012) 620–626, https://doi.org/10.1038/nmat3334.

[12] J. Kübler, A.R. William, C.B. Sommers, « Formation and coupling of magnetic moments in Heusler alloys », Phys. Rev. B 28 (4) (1983) 1745–1755, https://doi.org/10.1103/PhysRevB.28.1745.

[13] A. Deb, Y. Sakurai, « Electronic structure of the Cu_2 MnAl Heusler alloy », J. Phys. Condens. Matter 12 (13) (2000) 2997–3012, https://doi.org/10.1088/0953-8984/12/13/310.

[14] S.E. Kulkova, S.V. Eremeev, S.S. Kulkov, « Electronic structure and magnetic properties of Co- and Mn-based Heusler alloys and thin films », Solid State Commun. 130 (12) (2004) 793–797, https://doi.org/10.1016/j.ssc.2004.04.015.

[15] X.-P. Wei, T.-Y. Cao, X.-W Sun, Q. Gao, P. Gao, Z.-L. Gao, X.-M Tao, « Structural, electronic, and magnetic properties of quaternary Heusler CrZrCoZ compounds: a first-principles study* », Chin. Phys. B 29 (7) (2020) 077105 https://doi.org/10.1088/1674-1056/ab969b.

[16] R.A. De Groot, F.M. Mueller, P.G.V. Engen, K.H.J. Buschow, « New class of materials: half-metallic ferromagnets », Phys. Rev. Lett. 50 (25) (1983) 2024–2027, https://doi.org/10.1103/PhysRevLett.50.2024.

[17] T. Graf, C. Felser, S.S.P. Parkin, « Simple rules for the understanding of Heusler compounds », Prog. Solid State Chem. 39 (1) (2011) 1–50, https://doi.org/10.1016/j.progsolidstchem.2011.02.001.

[18] K.R.A. Ziebeck, P.J. Webster, « A neutron diffraction and magnetization study of Heusler alloys containing Co and Zr, Hf, V or Nb », J. Phys. Chem. Solids 35 (1) (1974) 1–7, https://doi.org/10.1016/0022-3697(74)90002-X.

[19] P. Mohn, P. Blaha, K. Schwarz, « Magnetism in the Huesler alloys: Co2TiSn and Co2TiAl », J. Magn. Magn. Mater. 140-144 (1995) 183–184, https://doi.org/10.1016/0304-8853(94)00941-4.

[20] M.Y. Raïâ, R. Masrour, M. Hamedoun, J. Kharbach, A. Rezzouk, A. Hourmatallah, N. Benzakour, K. Bouslykhane, « Thermodynamic, electronic, magnetic, thermoelectric, and optical properties of full Heuslers compounds Co2TiAl(Ga, In): a first principles study », Appl. Phys. A 129 (7) (2023) 493, https://doi.org/10.1007/s00339-023-06744-5.

[21] M.Y. Raïâ, R. Masrour, M. Hamedoun, J. Kharbach, A. Rezzouk, A. Hourmatallah, N. Benzakour, K. Bouslykhane, « Half-metalicity, mechanical, optical, thermodynamic, and thermoelectric properties of full Heusler alloys Co2TiZ (Z = Si; Ge; Sn) », Opt. Quantum Electron. 55 (6) (2023) 512, https://doi.org/10.1007/s11082-023-04793-x.

[22] M.Y. Raïâ, R. Masrour, M. Hamedoun, J. Kharbach, A. Rezzouk, A. Hourmatallah, N. Benzakour, K. Bouslykhane, « Diluted effect on the structural, magnetic, electronic, thermodynamic, optical and thermoelectric properties of the Heusler alloys Co2Fe1−xTixGa: GGA and GGA + U approaches », Opt. Quantum Electron. 55 (2) (2023) 140, https://doi.org/10.1007/s11082-022-04348-6.

[23] M.Y. Raïâ, R. Masrour, M. Hamedoun, J. Kharbach, A. Rezzouk, A. Hourmatallah, N. Benzakour, K. Bouslykhane, « Effect of L21 and XA ordering on structural, martensitic, electronic, magnetic, elastic, thermal and thermoelectric properties of Co2FeGe Heusler alloys », Solid State Commun. 355 (2022) 114932 https://doi.org/10.1016/j.ssc.2022.114932.

[24] M.Y. Raïâ, R. Masrour, M. Hamedoun, J. Kharbach, A. Rezzouk, A. Hourmatallah, N. Benzakour, K. Bouslykhane, « Structural, electronic, magnetic, elastic, thermoelectric, and thermal properties of Co2FeGa1−xSix Heusler alloys: first-principles calculations », J. Supercond. Nov. Magn. 36 (1) (2023) 349–365, https://doi.org/10.1007/s10948-022-06473-5.

[25] M.Y. Raïâ, R. Masrour, M. Hamedoun, J. Kharbach, A. Rezzouk, A. Hourmatallah, N. Benzakour, K. Bouslykhane, « Stability, magnetic, electronic, elastic, thermodynamic, optical, and thermoelectric properties of Co2TiSn, Co2ZrSn and Co2HfSn Heusler alloys from calculations using generalized gradient approximation techniques », J. Mater. Sci. Mater. Electron. 33 (25) (2022) 20229–20256, https://doi.org/10.1007/s10854-022-08841-2.

[26] X.-P. Wei, X. Liu, H.-K. Sun, Y.-L. Zhang, « Theoretical investigations of the mechanical, electronic, magnetic and optical properties of Heusler Mn2HfP and Mn2HfSi alloys », Mater. Today Commun. 46 (2025) 112536 https://doi.org/10.1016/j.mtcomm.2025.112536.

[27] X.-P. Wei, X. Liu, J.-Y. Zhang, Y.-L. Zhang, X. Tao, « Investigations on full-Heusler alloys Mn2TaAl and Mn2WAl for spintronic and thermoelectric applications », iScience 27 (12) (2024) 111257 https://doi.org/10.1016/j.isci.2024.111257.

[28] I.A. Elkoua, R. Masrour, « Structural, thermodynamics, optical, electronic, magnetic and thermoelectric properties of Heusler Ni2MnGa: an ab initio calculations », Opt. Quantum Electron. 54 (10) (2022) 667, https://doi.org/10.1007/s11082-022-03999-9.

[29] M.Y. Raïâ, R. Masrour, M. Hamedoun, J. Kharbach, A. Rezzouk, A. Hourmatallah, N. Benzakour, K. Bouslykhane, « Structural stability, electronic, magnetic, elastic, thermal, thermoelectric and optical properties of $L2_1$ and xa phases of Ti_2 fege heusler compound: GGA and GGA+U methods », Nanosc. Microsc. Thermophys. Eng. 27 (1) (2023) 1–24, https://doi.org/10.1080/15567265.2023.2167532.

[30] X.-P. Wei, Y.-L. Zhang, X. Sun, T. Song, P. Guo, Y. Gao, J.-L. Zhang, X.-F. Zhu, J.-B. Deng, « Exchange interactions and Curie temperatures in Fe2 NiZ compounds », J. Alloys Compd. 694 (2017) 1254–1259, https://doi.org/10.1016/j.jallcom.2016.10.105.

[31] X.-P. Wei, Y.-H. Zhou, « First-principles and Monte Carlo studies of the Fe2NiZ compounds on exchange interactions and Curie temperatures », Intermetallics 93 (2018) 283–289, https://doi.org/10.1016/j.intermet.2017.10.006.

[32] T. Eto, Y. Nakamoto, T. Kagayama, Y. Adachi, S. Kawaguchi, N. Hirao, Y. Uwatoko, M. Nagasako, T. Kanomata, « Pressure-induced structural phase transition in the ferromagnetic Heusler alloy Ni 2 MnGa », Phys. Rev. B 109 (1) (2024) 014101 https://doi.org/10.1103/PhysRevB.109.014101.

[33] M. Abane, T. Bouguetaia, S. Bahlouli, M. Elchikh, S. Hiadsi, « Investigating the structural, elastic, pressure-dependent electronic and optical properties of antiferromagnetic HoPdBi and HoPtBi alloys », Nano 20 (11) (2025) 2550039 https://doi.org/10.1142/S1793292025500390.

[34] A.;. Azouaoui, A.;. Harbi, M.;. Moutaabbid, M. Idiri, A. eddiai, N.;. Benzakour, A.;. Hourmatallah, K.;. Bouslykhane, R.;. Masrour, A. Rezzouk, « First-principle investigation of LiSrX (X=P and As) half-Heusler semiconductor compounds », Indian J. Phys. 97 (6) (2023) 1727–1737, https://doi.org/10.1007/s12648-022-02522-w.

[35] A. Azouaoui, A. Harbi, M. Moutaabbid, N. Benzakour, A. Hourmatallah, K. Bouslykhane, R. Masrour, A. Chahboun, « Influence of pressure on structural stability and physical properties of NaCaZ (Z=N, P and As) half-Heusler semiconductor materials », Int. J. Mod. Phys. B 38 (09) (2024) 2450122 https://doi.org/10.1142/S0217979224501224.

[36] L. Bainsla, M.M. Raja, A.K. Nigam, K.G. Suresh, « CoRuFeX (X = Si and Ge) Heusler alloys: high T C materials for spintronic applications », J. Alloys Compd. 651 (2015) 631–635, https://doi.org/10.1016/j.jallcom.2015.08.150.

[37] A. Ahmad, S.K. Srivastava, A.K. Das, « First-principles calculations and experimental studies on Co2FeGe Heusler alloy nanoparticles for spintronics applications », J. Alloys Compd. 878 (2021) 160341 https://doi.org/10.1016/j.jallcom.2021.160341.

[38] W. Kohn, L.J. Sham, « Self-consistent equations including exchange and correlation effects », Phys. Rev. 140 (4A) (1965) A1133–A1138, https://doi.org/10.1103/PhysRev.140.A1133.

[39] P. Hohenberg, W. Kohn, « Inhomogeneous electron gas », Phys. Rev. 136 (3B) (1964) B864–B871, https://doi.org/10.1103/PhysRev.136.B864.

[40] H. Bross, « Ein neues Verfahren zur Berechnung von Einelektronenzuständen in Kristallen », Phys. Kondens. Mater. 3 (2) (1964) 119–138, https://doi.org/10.1007/BF02422357.

[41] H. Bross, G. Bohn, G. Meister, W. Schubö, H. Stöhr, « New version of the modified augmented-plane-wave method », Phys. Rev. B 2 (8) (1970) 3098–3103, https://doi.org/10.1103/PhysRevB.2.3098.

[42] H. Bross, G.M. Fehrenbach, « The spline augmented plane wave method », Z. Für Phys. B Condens. Matter 81 (2) (1990) 233–243, https://doi.org/10.1007/BF01309354.

[43] P.M. Marcus, « Variational methods in the computation of energy bands », Int. J. Quantum Chem. 1 (S1) (2009) 567–588, https://doi.org/10.1002/qua.560010659.

[44] D.D. Koelling, G.O. Arbman, « Use of energy derivative of the radial solution in an augmented plane wave method: application to copper », J. Phys. F Met. Phys. 5 (11) (1975) 2041–2054, https://doi.org/10.1088/0305-4608/5/11/016.
[45] O.K. Andersen, « Simple approach to the band-structure problem », Solid State Commun. 13 (2) (1973) 133–136, https://doi.org/10.1016/0038-1098(73)90210-X.
[46] O.K. Andersen, « Linear methods in band theory », Phys. Rev. B 12 (8) (1975) 3060–3083, https://doi.org/10.1103/PhysRevB.12.3060.
[47] E. Wimmer, H. Krakauer, M. Weinert, A.J. Freeman, « Full-potential self-consistent linearized-augmented-plane-wave method for calculating the electronic structure of molecules and surfaces: O2 molecule », Phys. Rev. B 24 (2) (1981) 864–875, https://doi.org/10.1103/PhysRevB.24.864.
[48] P. Blaha, K. Schwarz, F. Tran, R. Laskowski, G.K.H. Madsen, L.D. Marks, « WIEN2k: an APW+lo program for calculating the properties of solids », J. Chem. Phys. 152 (7) (2020) 074101 https://doi.org/10.1063/1.5143061.
[49] J.P. Perdew, K. Burke, M. Ernzerhof, « Generalized gradient approximation made simple », Phys. Rev. Lett. 77 (18) (1996) 3865–3868, https://doi.org/10.1103/PhysRevLett.77.3865.
[50] I. Galanakis, P.H. Dederichs, N. Papanikolaou, « Slater-Pauling behavior and origin of the half-metallicity of the full-Heusler alloys », Phys. Rev. B 66 (17) (2002) 174429 https://doi.org/10.1103/PhysRevB.66.174429.
[51] K. Momma, F. Izumi, « *VESTA 3* for three-dimensional visualization of crystal, volumetric and morphology data », J. Appl. Crystallogr. 44 (6) (2011) 1272–1276, https://doi.org/10.1107/S0021889811038970.
[52] S. Babiker, G. Gao, K.L. Yao, « First-principle calculation of electronic structures and magnetic properties of Heusler alloys Co2ZrPb and Zr2MnBa », J. Supercond. Nov. Magn. 31 (3) (2018) 905–913, https://doi.org/10.1007/s10948-017-4239-6.
[53] F. Birch, « The effect of pressure upon the elastic parameters of isotropic solids, according to Murnaghan's theory of finite strain », J. Appl. Phys. 9 (4) (1938) 279–288, https://doi.org/10.1063/1.1710417.
[54] X. Wang, Z. Cheng, R. Khenata, Y. Wu, L. Wang, G. Liu, « Lattice constant changes leading to significant changes of the spin-gapless features and physical nature in a inverse Heusler compound Zr2MnGa », J. Magn. Magn. Mater. 444 (2017) 313–318, https://doi.org/10.1016/j.jmmm.2017.08.040.
[55] M. Khodami, F. Ahmadian, « First-principles study of magnetism and half-metallic properties for the quaternary Heusler alloys CoMnTiZ (Z = P, As, and Sb) », J. Supercond. Nov. Magn. 28 (10) (2015) 3027–3035, https://doi.org/10.1007/s10948-015-3126-2.
[56] M. Kundu, S. Pakhira, R. Choudhary, D. Paudyal, N. Lakshminarasimhan, M. Avdeev, S. Cottrell, D. Adroja, R. Ranganathan, C. Mazumdar, « Complex magnetic properties associated with competing local and itinerant magnetism in Pr_2 $Co_{0.86}Si_{2.88}$ », Sci. Rep. 11 (1) (2021) 13245 https://doi.org/10.1038/s41598-021-90751-0.
[57] S.V. Faleev, Y. Ferrante, J. Jeong, M.G. Samant, B. Jones, S.S.P. Parkin, « Unified explanation of chemical ordering, the Slater-Pauling rule, and half-metallicity in full Heusler compounds », Phys. Rev. B 95 (4) (2017) 045140 https://doi.org/10.1103/PhysRevB.95.045140.
[58] X.-P. Wei, L.-L. Du, J. Shen, Z.-Q. Sun, Z.-M. Zhang, W.-L. Chang, X. Tao, « Electronic, magnetic and transport properties of anti-ferromagnetic semiconductor BaGd2X4(X S, Se) », Mater. Sci. Semicond. Process 169 (2024) 107856 https://doi.org/10.1016/j.mssp.2023.107856.
[59] J. Winterlik, B. Balke, GH. Fecher, C. Felser, MC.M. Alves, F. Bernardi, J. Morais, « Structural, electronic, and magnetic properties of tetragonal Mn 3 − x Ga : experiments and first-principles calculations », Phys. Rev. B 77 (5) (2008) 054406 https://doi.org/10.1103/PhysRevB.77.054406.
[60] S. Skaftouros, K. Özdoğan, E. Şaşıoğlu, I. Galanakis, « Generalized slater-pauling rule for the inverse Heusler compounds », Phys. Rev. B 87 (2) (2013) 024420 https://doi.org/10.1103/PhysRevB.87.024420.
[61] J.-R. Liu, X.-P. Wei, W.-L. Chang, X. Tao, « Structural stability, electronic, magnetic and thermoelectric properties for half-metallic quaternary Heusler alloys CrLaCoZ », J. Phys. Chem. Solids 163 (2022) 110600 https://doi.org/10.1016/j.jpcs.2022.110600.
[62] X.-P. Wei, Q. Gao, P. Gao, Y.-L. Zhang, X. Tao, « Investigations on Gilbert damping, electronic, magnetic and Curie temperature for equiatomic quaternary Heusler alloys CrScCoZ », J. Magn. Magn. Mater. 512 (2020) 166986 https://doi.org/10.1016/j.jmmm.2020.166986.
[63] X.-P. Wei, J. Shen, L.-L. Du, X.-M. Tao, « Electronic and magnetic properties of two-dimensional CrX2 under vacancy and strain effects », Phys. B Condens. Matter 667 (2023) 415154 https://doi.org/10.1016/j.physb.2023.415154.
[64] J.C. Slater, « Suggestions from solid-state theory regarding molecular calculations », J. Chem. Phys. 43 (10) (1965) S228, https://doi.org/10.1063/1.1701494.-S228.
[65] X. Zhang, X.-P. Wei, J. Shen, Z.-Y. Mei, L.-L. Du, X. Tao, « Half-metallic quaternary CrYCo X (X = Si, Ge, Sn, Pb) alloys: DFT calculations and Monte Carlo simulation », Mater. Today Commun. 33 (2022) 104650 https://doi.org/10.1016/j.mtcomm.2022.104650.
[66] X.-P. Wei, X. Zhang, J. Shen, W.-L. Chang, X. Tao, « Gilbert damping, electronic and magnetic properties for quaternary Heusler alloys CrYCoZ: first-principles and Monte Carlo studies », Comput. Mater. Sci. 210 (2022) 111453 https://doi.org/10.1016/j.commatsci.2022.111453.

Journal of Superconductivity and Novel Magnetism (2026) 39:84
https://doi.org/10.1007/s10948-026-07182-z

RESEARCH

Investigating the Structural, Elastic, Electronic, Magnetic and Thermodynamic Properties of Full-Heusler Alloys Pr_2CoZ (Z = Al, Ga and In)

Abdelkader Ilias Bouadi[1,2] · Mahdi Abane[3] · Mohamed Hammadi[4] · Aissam Hidoussi[5] · Mohamed Mokhtari[1,2] · Fethallah Dahmane[1,6]

Received: 6 August 2025 / Accepted: 20 April 2026
© The Author(s), under exclusive licence to Springer Science+Business Media, LLC, part of Springer Nature 2026

Abstract

The structural, electronic, and magnetic characteristics of full-Heusler compounds Pr_2CoZ (where Z=Al, Ga, In) in Hg_2CuTi-type and Cu_2MnAl-type configurations were examined utilizing the first principle based on the FP-LAPW with Generalized gradient approximation (GGA) implemented in WIEN2k software. The Hg_2CuTi-type structure demonstrated superior stability compared to the Cu_2MnAl-type structure at ambient conditions for all compounds. The Hg_2CuTi-type structure demonstrated superior stability compared to the Cu_2MnAl-type at ambient conditions for all compounds, with optimized lattice parameters of 6.85 Å (Pr_2CoAl), 6.82 Å (Pr_2CoGa), and 7.02 Å (Pr_2CoIn). These compounds display the characters of indirect band gap semiconductors, possessing energy band gaps of 0.359, 0.483, and 0.492 eV for Pr_2CoAl, Pr_2CoGa, and Pr_2CoIn, respectively. Our alloys exhibited half-metallic (HM) characteristics with an indirect band gap and a total magnetic moment of 4 μB, by the Slater-Pauling (SP) rule. The thermodynamic characteristics were assessed at temperatures ranging from 0 to 1000 K and pressures from 0 to 20 GPa utilizing the quasi-harmonic Debye model. The analysis of the elastic characteristics validated the mechanical stability of the three alloys inside the examined structure, demonstrating a strong correlation between the derived bulk modulus from the structural properties and that obtained from the elastic values. Additionally, other elastic characteristics, including modulus B, shear modulus G, Young's modulus E, Poisson's ratio (ν), Pugh's ratio (κ), and the Zener anisotropy parameter (A), indicate that the Pr_2CoZ (Z=Al, Ga, and In) alloys exhibit high anisotropy, and ductile behaviour.

Keywords Full Heusler · DFT · WIEN2k · Rare-earth alloys · Half-metals

✉ Fethallah Dahmane
fethallah05@gmail.com

[1] Laboratory of Modeling and Simulation of Magnetic Properties of Hetero-structures (LPMH), Faculty of Sciences and Technology, Tissemsilt University, Tissemsilt, Algeria

[2] Laboratory for Materials Physics Studies, Department of Energy Physics, University of Science and Technology, USTO-MB, PO Box 1505, El M'naour, Oran, Algeria

[3] Materials and Fluids Physics Laboratory, Faculty of Physics, University of Science and Technology of Oran USTO-MB Oran, El M'naouer, BP 1505, Oran, Algeria

[4] Laboratory for the Development and Physico-Mechanical and Metallurgical Characterization of Materials (ECP3M), Abdelhamid Ibn Badis University, Kharouba, Mostaganem 27000, Algeria

[5] Department of Science and Technology, Institute of Science, University Center of Barika Amdoukal Road, Barika 05001, Algeria

[6] Laboratory of Quantum Physics and Mathematical Modeling (LPQ3M), Department of Technology, University of Mascara, Mascara 29000, Algeria

Published online: 28 April 2026

1 Introduction

Advanced materials, particularly rare-earth-based Heusler alloys, are pivotal in driving innovations in spintronic, offering high spin polarization and multifunctionality for applications in magnetic tunnel junctions and non-volatile memory [1–5].

Modern spintronic research has two main goals to develop next-generation computing technologies after major breakthroughs that change the game, and to improve existing industrial applications like magnetic memory cells and read heads at the same time. The main goals are to improve the efficiency of spin filtering and to create new high-spin-polarization materials that will improve the performance of devices. Giant magnetoresistive (GMR) multilayered structures used to be the most common in this field, but now magnetic tunnel junctions (MTJs) are more efficient. These are called MTJs or tunnelling magnetoresistance (TMR) [6–8].Device sutilizingspin-dependent electron tunneling through thin insulatingbarriers, suchas MgO, exhibit significantly greater resistance variation than giant magnetoresistance (GMR). This shift in perspective has resulted in significant enhancements in storage density per unit area, facilitating advancements in ultra-high-capacity storage media and non-volatile memory, such as MRAM [9, 10].

Ferromagnetic oxides exhibiting half-metallicity and half-metallic ferromagnetic metals, particularly Heusler alloys, are two highly promising categories of alloys for the fabrication of high spin-polarization electrodes [11]. Heusler and half-Heusler (HH) alloys have garnered significant theoretical and experimental attention due to their extensive array of advantageous and pertinent features. This encompasses intrinsic half-metallic ferromagnetism, shape memory effects, and substantial magnetocaloric effects, all of which possess significant potential for advanced applications.

Heusler alloys have been effectively utilized as electrodes in magnetic tunnel junctions (MTJs) due to their distinctive spin polarization, which enhances device performance. In 1903, Fritz Heusler observed that the Cu_2MnAl alloy exhibited ferromagnetism despite the absence of ferromagnetic components. This is the origin of this family of materials. This significant finding demonstrated that novel magnetic states can emerge when non-magnetic atoms are organized in a specific configuration. This fundamental concept persists in motivating contemporary research on Heusler systems [12].

In recent decades, Heusler alloys have become favored options for multifunctional materials owing to their several advantageous features, including the magnetocaloric effect [13], enormous magneto-resistance [14], half-metallicity [15], and Hall effect [16]. Moreover, several Heusler compounds exhibit exceptional thermoelectric characteristics [17].

In the last decade, substantial scientific studies have concentrated on half-metal materials (HMM) [18], which hold promise for applications in spintronic devices, enormous magneto-resistance spin valves, and spin injection into semiconductors. According to first-principle calculations, it is anticipated that several materials will demonstrate this unique behavior [19].

There have been theoretical and experimental studies on several half-metallic magnets in the past few years. These include perovskites like $CaCoO_3$ and $SrCoO_3$ [20], Heusler compounds with structures of L_{21} and C_{1b} like Ti_2YAl (Y=Co, Fe, Mn) [21] Co_2CrZ (Z=Al, Ga, In) [22]. RXVZ (R=Yb, Lu; X=Fe, Co, Ni; Z=Al, Si) [23], $Mn_2Co_{1-x}V_xZ$ (Z=Ga, Al) [24], Co2CrGe [25] Sc2CoZ (Z=Si, Ge, Sn) [26], Co2MnX (X=Si, Ge, Al, Ga) [27], X_2YAl (X=Co, Fe and Y=Cr, Sc) [28], Si-doped Co2MnGe [29] Ru2TGa (T=Cr, Mn, and Co) [30], Ir2MnAl [31].

New Heusler compounds have appeared which contain in their composition rare-earth elements [32], we can cite as examples ErPdSb [33], Cu_2GdIn, Fe_2CeAg, Pd_2DySn, Pd_2HoSn [34, 35], LiScNiGe [36] Zr2CoZ (Z=Al, Ga, In, Si, Ge, Sn, Pb, Sb) [37].

The aim of the present work is to perform a comprehensive first-principles investigation of the full-Heusler Pr_2CoZ (Z=Al, Ga, In) compounds in both Hg_2CuTi and Cu_2MnAl structures, with particular emphasis on (i) confirming the energetic preference for the inverse Heusler (Hg_2CuTi) structure, (ii) detailed elastic and mechanical properties, (iii) thermodynamic properties under high temperature and pressure using the quasi-harmonic Debye model, and (iv) estimation of the Curie temperature. To the best of our knowledge, no study of the elastic, phonon, or thermodynamic properties of these alloys has been reported to date.

This paper is organised as follows: part 2 provides a brief description of the computational approach that was employed in this work, while Sect. 3 contains the findings and discussions of our investigation. Section 4 concludes with a synopsis of the works.

2 Computational Details

The FP-LAPW method utilised in the WIEN2k package (version 21.1) is employed to obtain results [38, 39], while the Perdew–Burke–Ernzerhof parameterisation of the generalised gradient approximation (PBE-GGA) is applied to investigate the exchange-correlation potential [40], and the Kohn–Sham equations are solved self-consistently.

This approach involves partitioning space into two regions: non-overlapping muffin tin spheres centred at

atomic sites, where a spherical harmonic expansion is employed, and the interstitial zone, which utilises a plane wave basis set selected outside the sphere [41]. The angular momentum reaches its maximum value of $l_{max} = 10$, a mesh of $10 \times 10 \times 10$ K-points was used, while the density is Fourier expanded to $G_{max} = 14$ (a.u)$^{-1}$. All fundamental functions have been expanded inside the muffin-tin spheres to $R_{MT} \times K_{MAX} = 9$ (where R_{MT} is the muffin-tin radius and K_{MAX} is the maximal modulus of the reciprocal lattice vectors) Energy cutoff between core and valence states: −6.0 Ry, while the energy criterion employed in the self-consistent computations is below 10^{-6} Ry and charge convergence of 0.0001 e. The muffin-tin radii (R_{MT}) for each atom are: R_{MT} (Pr)=2.5 a.u., R_{MT} (Co)=2.3 a.u., R_{MT} (Z)=2.2 a.u. The generalised gradient approximation is employed for computations of band structure and density of states. The mechanical properties are also computed using the IRelast code provided by the WIEN2k package [42] of Heusler alloys Pr_2CoZ (Z=Al, Ga and In) in Hg_2CuTi-Type structure. The determination of thermodynamic properties relied on a quasi-harmonic Debye model, implemented through the Gibbs2 code [43].

3 Results and Discussion

3.1 Structural Properties

Heusler alloys consist of transition metal elements X and Y, along with main group element Z [44]. Their composition adheres to stoichiometry, characterised by the formula X_2YZ. These alloys exhibit two distinct crystal structures: face-centered cubic (fcc) lattices, specifically the Cu_2MnAl and Hg_2CuTi structures (Fig. 1). The two structures consist of four interpenetrating face-centered cubic (fcc) sublattices with four unique crystal sites: A(0, 0, 0), B(0.25, 0.25, 0.25), C(0.5, 0.5, 0.5), and D(0.75, 0.75, 0.75).

In the Cu_2MnAl type structure, referred to as $L2_1$, the atomic arrangement inside the four sites of the unit cell adheres to the sequence X–Y–X–Z. Conversely, in the Hg_2CuTi type structure, designated as the XA structure, the sequence of atoms occupying the four sites of the unit cell is X–X–Y–Z [45].

The empirical Birch–Murnaghan equation of states delineates the relationship between total energies and volumes per formula unit for both Hg_2CuTi-type and Cu_2MnAl-type, as represented in [46]:

$$E(V) = E_0 + \frac{9V_0B_0}{16}\left[\left\{\left(\frac{V_0}{V}\right)^{\frac{2}{3}} - 1\right\}^3\right]B_0' + \left\{\left(\frac{V_0}{V}\right)^{\frac{2}{3}} - 1\right\}^2\left\{6 - 4\left(\frac{V_0}{V}\right)^{\frac{2}{3}}\right\} \quad (1)$$

Table 1 shows the optimised lattice constants and bulk modulus, obtained from the minimum of the energy-volume curves seen in Fig. 2, including all ferromagnetic and non-magnetic phases for both Hg_2CuTi and Cu_2MnAl-type structures.

The equation employed in this study incorporates the variables E for energy, V for volume, B for the equilibrium bulk modulus, V_0 for the volume of the experimental unit cell, and B' for the pressure derivative of the bulk modulus at the equilibrium volume.

The findings demonstrate that the Hg_2CuTi configuration in the ferromagnetic state has greater energy stability compared to the alternative states of the Cu_2MnAl structure. Previous investigations have indicated that the Hg_2CuTi structure is more likely to develop when the Y element possesses more electronegativity than the X element [48]. Consequently, our further computations will be predicated on the ferromagnetic (FM) condition of the Hg_2CuTi -type structure.

We examine the formation energy to establish the viability of this chemical and its potential for experimental

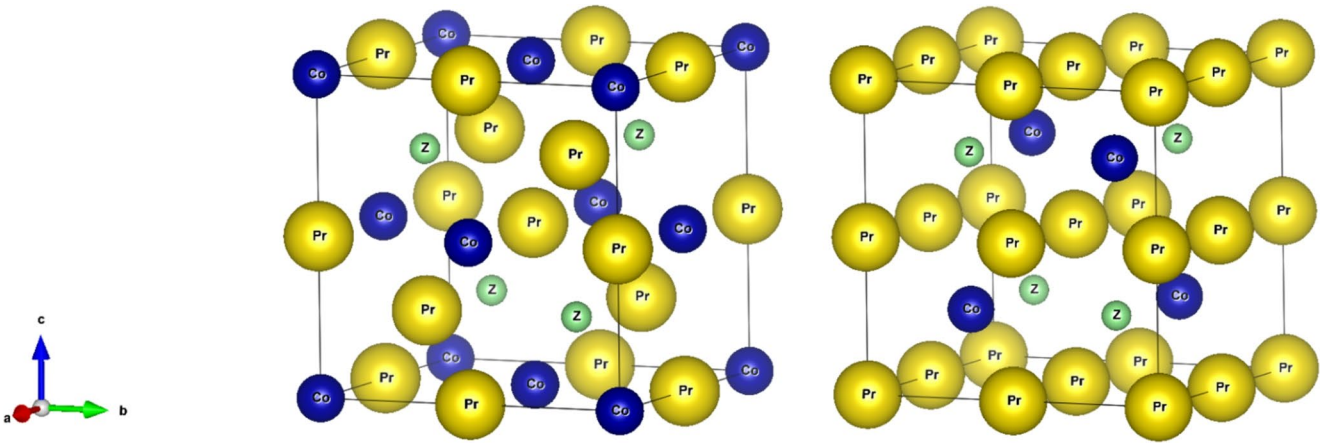


Fig. 1 Crystallographic structure of full-Heuler alloy Pr_2CoZ (Z=Al, Ga and In) in which (**a**) Hg_2CuTi type and (**b**) Cu_2MnAl type

Table 1 Optimized lattice constant a_0 (Å), Bulk modulus B_0(GPa), the pressure derivative B_0', the total energy Emin (eV), and the Formation energy ΔH (Ryd) for Full Heusler compounds Pr_2CoZ (Z=Al, Ga, In)

Alloy	Phases	a_0 (Å)	B_0(GPa)	B_0'	E_{min} (eV)	ΔH (Ryd)
Pr_2CoAl	Cu_2MnAl(NM)	6.9426	68.4729	3.6102	−40243.64009	−1.232703
	Cu_2MnAl(FM)	7.1111 7.1137 [47]	52.5918	4.2491	−40243.70746	−1.286372
	Cu_2MnAl(AFM)	7.1294	49.6159	5.2811	−40243.69635	−1.269491
	Hg_2CuTi(NM) Hg_2CuTi (FM)	6.6416	88.1645	4.1350	−40243.69562	−1.270491
	Hg_2CuTi (AFM)	6.7422	74.4919	4.6438	−40243.76273	−1.322845
		6.7930	69.2096	4.8924	−40243.72873	−1.304328
Pr_2CoGa	Cu_2MnAl(NM)	6.9207	69.2837	3.9519	−43646.28321	−1.173918
	Cu_2MnAl(FM)	7.0910 7.0729[47]	44.8762	5.4881	−43646.33556	−1.246940
	Cu_2MnAl(AFM)	7.0829	61.7320	4.8798	−43646.33234	−1.240953
	Hg_2CuTi(NM) Hg_2CuTi (FM)	6.6223	84.5964	5.7954	−43646.28764	−1.203819
	Hg_2CuTi (AFM)	6.7184	81.2231	4.1335	−43646.36170	−1.273954
		6.7640	73.6881	4.9131	−43646.32450	−1.239753
Pr_2CoIn	Cu_2MnAl(NM)	7.1719	52.3517	5.7862	−51524.54414	−1.052953
	Cu_2MnAl(FM)	7.3445 7.3518[47]	51.6078	4.1110	−51524.63701	−1.148534
	Cu_2MnAl(AFM)	7.3515	40.5122	5.6966	−51524.62934	−1.133629
	Hg_2CuTi(NM) Hg_2CuTi (FM)	6.8599	82.4667	4.5535	−51524.57210	−1.082489
	Hg_2CuTi (AFM)	6.9696	69.0836	4.4314	−51524.65776	−1.171425
		7.0233	59.1493	5.5422	−51524.62849	−1.130629

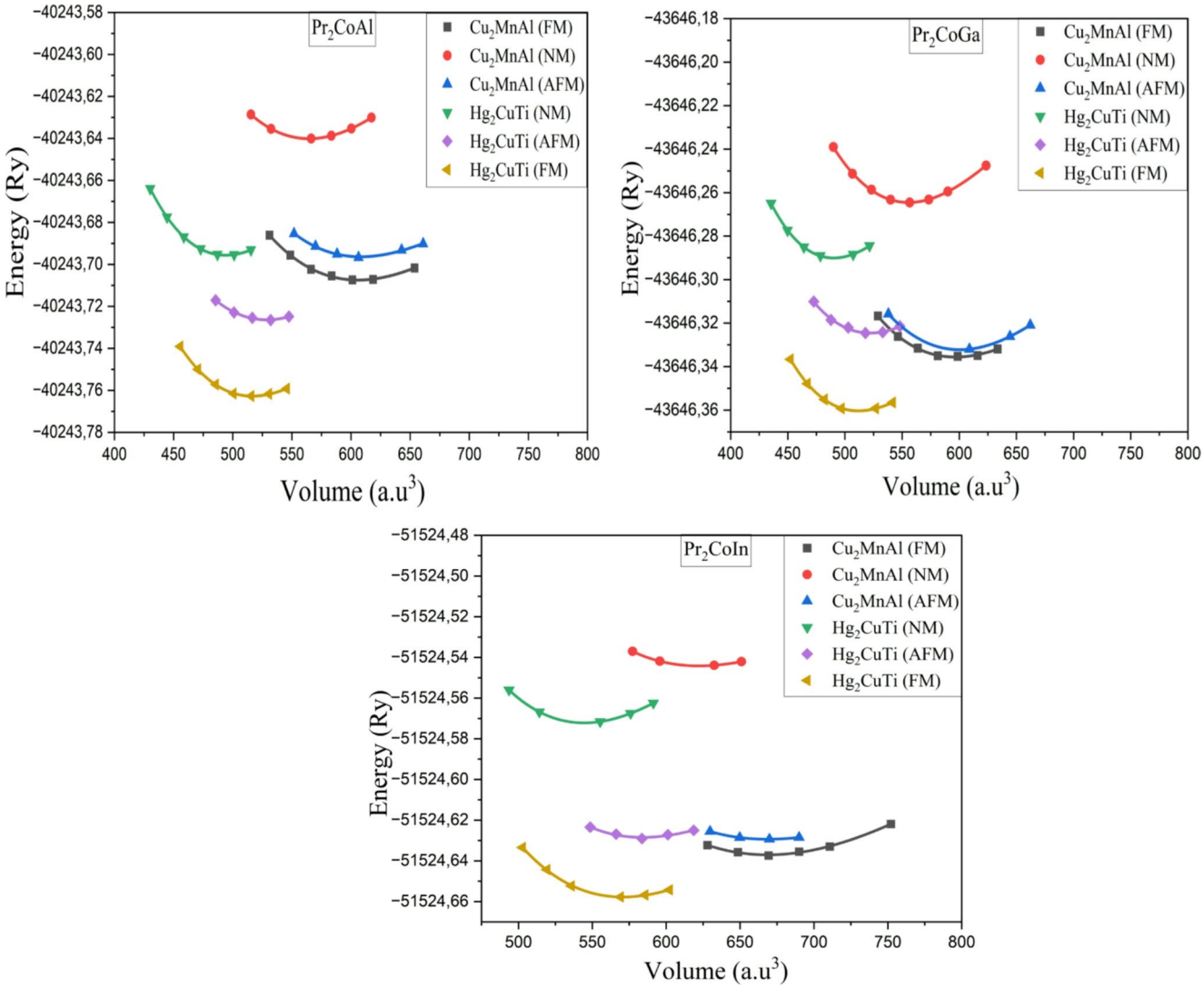


Fig. 2 Total energy versus unit cell volume for Pr_2CoZ (Z=Al, Ga and In)

synthesis; the formation energy is expressed by the following relation [49]:

$$\triangle H = E_f^{Pr_2CoZ} = E_{tot}^{Pr_2CoZ} - E_{Co}^{build} - E_Z^{build} - 2E_{Pr}^{build} \quad (2)$$

Where $E_f^{\mathrm{Pr_2CoZ}}$ is the equilibrium energy of these compounds, in which $E_{\mathrm{tot}}^{Pr_2\mathrm{CoZ}}$ is the total energy of compounds and $E_{\mathrm{Pr}}^{\mathrm{builk}}$, $E_{\mathrm{Co}}^{\mathrm{builk}}$ and $E_{\mathrm{Z}}^{\mathrm{builk}}$ are the chemical potential of atoms in their stable bulk for Pr, Co, and Z(Al, Ga, In).

The estimated formation energies of the compounds Pr_2CoZ (Z=Al, Ga, In) for the Hg_2CuTi-type structure are −1.322845, −1.273954, and −1.171425 Ryd, respectively, indicating the stability of these alloys [50].

Conversely, we can as certain that the Hg2CuTi-type structure is the most stable phase by comparing the formation energy values of the Hg_2CuTi-type and Cu_2MnAl-type structures (refer to Table 1).

3.2 Elastic Properties

We calculated the elastic properties of our Heusler ferromagnetic Pr_2CoZ (Z=Al, Ga and In) in Hg_2CuTi-Type structure by the IRelast package [42]. Table 2 represents our results using the Voigt–Reuss–Hill approximations [51, 52]. As one can observe, C_{11}, C_{12}, and C_{44} values satisfy the condition $(C_{11}-C_{12})>0$, $(C_{11}+2C_{12})>0$, $C_{11}>0$, and C44>0 [53]. All three materials meet these criteria, indicating they are mechanically stable. K represents the material's resistance to uniform (hydrostatic) compression. It's the reciprocal of compressibility: higher K means the material is harder to squeeze. Pr2CoAl: 73.944 GPa, Pr2CoGa: 77.938 GPa, Pr2CoIn: 65.425 GPa, These values are moderate for intermetallic. The trend suggests Pr2CoGa is the most volumetrically rigid, possibly due to optimal electronic bonding. Shear Modulus (G) decreases from Al to In, implying easier shear deformation in heavier analogs. This could relate to applications where shear strength is key. Poisson's Ratio (ν) Values between 0.25 and 0.35 are typical for metals, indicating central-force bonding (ionic/covalent materials have lower ν~0.1–0.2; rubbers~0.5). Higher ν suggests more ductility. All three are in the ductile range, with Pr2CoIn being the most "rubbery." Zener Anisotropy (A), A=1 means isotropic (same in all directions). A>1 indicates anisotropy, with shear easier in certain planes. Pr2CoAl is most anisotropic (properties vary more by direction), while Pr2CoIn is closer to isotropic.The values of anisotropy in Pr2CoAl, Pr2CoGa, and Pr2CoIn are 2.25, 2.00, and 1.57, respectively; Pugh's ratios are 0.56, 0.51, and 0.50 (see Table 2). Thus, indicating a high elastic anisotropy and confirming that full-Heusler compounds are ductile and not elastically isotropic.

Then we drew the influence of Young's modulus (E), Linear compressibility (β) and Bulk modulus (K) in Fig. 3. The analyses of 3D representations show a marked deviation from the spherical shape characteristic of homogeneous materials in both the Young's modulus (E) and shear modulus (G) plots. The minimum values of Young's modulus appear along the crystal axes (100), (010), and (001), while the maximum values are identified along the (111) direction for all compounds. Conversely, the shear modulus (G) reaches its highest values along the axes (100), (010), and (001), but decreases to its lowest values along the (111) direction. These directional variations highlight the irregular nature of the crystalline materials, with stiffness and resistance to bond angle deformation increasing significantly along the (111) direction. Meanwhile, the linear compressibility (β) plots show significant compressive strength in all directions, for all full Heusler compounds Pr2CoAl, Pr2CoGa, and Pr2CoIn.

Standard relations were used to determine the thermal parameters from the elastic moduli. The optimized lattice constant was used to get the density and the shear and bulk moduli were used to determine the transverse, longitudinal, and average sound velocities. Lastly, the average sound velocity within the Debye approximation was used to estimate the Debye temperature.(See Table 3).

Density (ρ) $\rho = \frac{M}{N_A.V}$ M=molar mass of the formula unit, N_A = Avogadro's number, V=a^3=volume of the unit cell.

Transverse velocity (νt): $v_t = \sqrt{\frac{G}{\rho}}$ where G=shear modulus.

Longitudinal velocity (νl): $v_l = \sqrt{\frac{(3B+4G)}{3\rho}}$ where B=bulk modulus.

Mean velocity v_m $v_m = \left[\frac{1}{3}\left(\frac{3}{v_t^3} + \frac{1}{v_l^3}\right)\right]^{\frac{1}{3}}$, Debye temperature $\theta_D = \frac{h}{K_B}\left[\frac{3nN_A\rho}{4\pi M}\right]^{\frac{1}{3}} v_m$.

where h denotes Planck constant, N_A denotes Avogadro number, k_B represents Boltzmann constant, ρ denotes

Table 2 Elastic constants (Cij), bulk modulus (K), Shear modulus (G), Young modulus (E), Poisson's coefficient (ν). The zener anisotropy (A) Pugh's Ratio (κ)

	C_{11}	C_{12}	C_{44}	K	G	E	ν	A κ
Pr_2CoAl	105.986	57.924	53.975	73.944	41.997	105.935	0.261	2.25 0.56
Pr_2CoGa	111.118	61.348	49.820	77.938	39.846	102.133	0.282	2.00 0.51
Pr_2CoIn	97.897	49.189	38.249	65.425	32.69	84.070	0.286	1.57 0.50

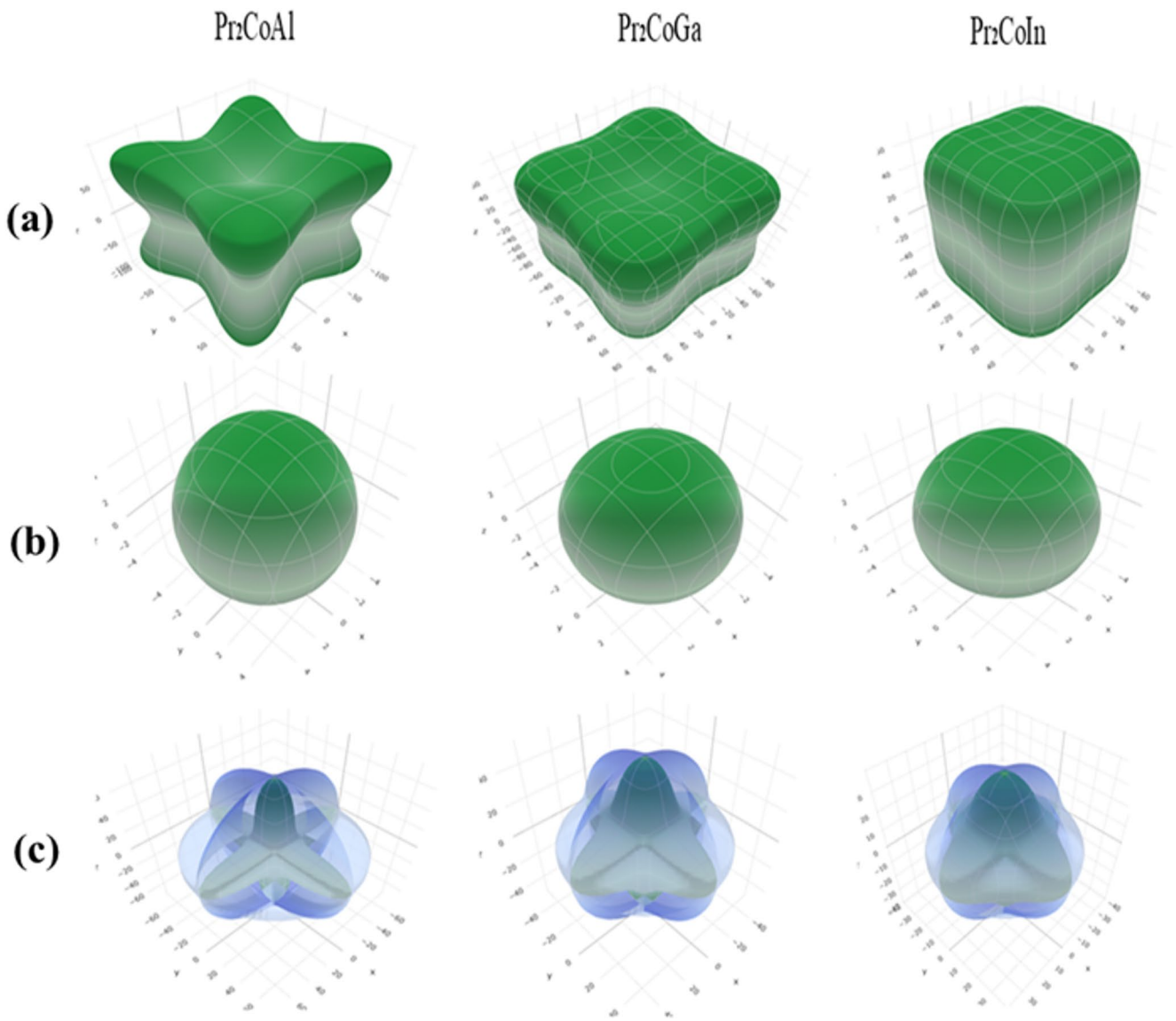


Fig. 3 3D representations of the influence of (**a**) Young's modulus (E, in GPa), (**b**) Bulk modulus (k, in GPa) and (**c**) Compressibility (β, in GPa-1) on the crystal direction for Pr_2CoAl, Pr_2CoGa and Pr_2CoIn

Table 3 The Thermal parameters density ρ in g/cm3, Transverse velocity **ν**t, Longitudinal velocity **ν**l, Mean velocity **ν**m in m/s), and Debye temperature (*Θ*D (K)) for the Pr2CoZ(Z=Al, Ga and In) alloys

	Density (ρ) g/cm³	Transverse velocity(vt) m/s)	Longitudinal velocity(vl) (m/s)	Mean velocity vm (m/s)	Debye temperature θ_D
Pr2CoAl	7.12	3200	5500	3550	420
Pr2CoGa	8.45	2950	5200	3300	390
Pr2CoIn	9.03	2800	5000	3150	370

density, n represents the number of electrons in the unit cell, v_m is average sound velocity and M is molar mass.

3.3 Electronic Properties

We analyse the band structures and the total density of states of Pr_2CoZ (Z=Al, Ga, In) compounds for both spins' direction (down and up). This investigation aims to elucidate the electronic structure of these compounds within the stable Hg_2CuTi structure in a ferromagnetic configuration at the equilibrium lattice parameter, employing the GGA approximation. The findings are illustrated in Fig. 4.

Band structures act as a depiction of the allowable electronic energy levels in solid materials, and they are utilised

to deepen our comprehension of their electronic properties. The band structure facilitates a swift evaluation of whether a material exhibits metallic, semi-metallic, or insulating characteristics. For materials possessing a band gap, it also elucidates whether the gaps are direct or indirect, in addition to their magnitude.

Furthermore, the curvature of the bands serves as an indicator of the mobility of the carriers residing within those bands. Upon examination of the band structure for all compounds analysed, as illustrated in Fig. 4, it is evident that in the spin-polarized state (specifically spin down), an energy gap emerges between the higher of the valence band at the Γ point and the lower of the conduction band at the X point. Consequently, these compounds display the traits of indirect band gap semiconductors, possessing energy band gaps of 0.359, 0.483, and 0.492 eV for Pr_2CoAl, Pr_2CoGa, and Pr_2CoIn, respectively. Moreover, it is clear that in the spin-up direction, the bands demonstrate overlap, signifying the metallic character of these compounds. Consequently, we arrive at the conclusion that all compounds exhibit half-metallic behaviour. Three distinct origins of band gaps are typically identified: the charge transfer band gap, the.

d–d band gap, and the covalent band gap. The covalent band gap has been found to be present in the Half Heusler compounds. The *d–d* band gap is responsible for the half-metallicity observed in Full Heusler compounds [54, 55].

Faleev et al. [56] have provided persuasive evidence for the probable hybridisation of *d*-orbitals in transition metals concerning the X_2YZ inverse Heusler compounds.

They assert that the mutual symmetry of X(1) and Y atoms induces the hybridisation of their *d*-orbitals, resulting in five bonding d states ($2_{e.g.}$ and $3t_{2g}$) and five non-bonding *d* states (2_{eu} and 3_{tu}). The five X(1)-Y bonding *d* states subsequently experience hybridisation with the *d*-orbital of X(2) atoms leads to the creation of novel bonding and anti-bonding states [40].

The computed spin polarisation total density of states (DOS) and partial DOS of Pr_2CoZ (Z=Al, Ga, In) compounds at their equilibrium lattice parameters are presented in Fig. 5.

Energy levels below −5 eV, predominantly derived from the s states of transition metal (TM=Co, Pr) atoms, are comitted from Fig. 5 owing to their near-symmetry in both majority and minority spin orientations. These states are much removed from the Fermi level and, as a result, do not influence the magnetic characteristics. The d states of Pr constitute the predominant portion of the total density of states (DOS) at the Fermi level. The d electrons of Pr atoms determine the band gap around the Fermi level in all alloys. The density of states above the Fermi level is mostly affected by the Pr and Co atoms, and we have computed the spin polarisation ratio (P) for these three compounds. The computation of spin polarisation can be accomplished using by.

$$P = \frac{N\uparrow(\varepsilon_F) - N\downarrow(\varepsilon_F)}{N\uparrow(\varepsilon_F) + N\downarrow(\varepsilon_F)} \tag{3}$$

Were N ↑ (εF) and N ↓ (εF) indicate the density of states (DOS) for majority-spin and minority-spin states at the Fermi level, respectively. The three analysed compounds have a complete (100%) spin polarisation ratio at the Fermi level.

3.4 Magnetic Properties

A fundamental idea in condensed matter physics, the Slater–Pauling rule links the magnetic moment of transition metal alloys to the number of valence electrons in those alloys. It offers a straightforward yet effective method for forecasting magnetization patterns in alloys, particularly Heusler compounds and 3D transition metals [57]. Slater and Pauling established in two seminal publications that, for binary magnetic compounds, the addition of one valence electron causes the compound to inhabit spin-down states, resulting in a reduction of the total spin magnetic moment by **1** μB [58]. Notably, half-metallic Heusler alloys demonstrate analogous behaviour. The total spin magnetic moment in the unit cell is proportional to the total number of valence electrons [59, 60]. Table 4 displays the computed magnetic moment for the entire Heusler alloys Pr_2CoAl, Pr_2CoGa, and Pr_2CoIn at their optimised lattice parameters. All studied alloys exhibit integer magnetic moments of 4 μB. Half-metallic materials are distinguished by an integer total magnetic moment. Consequently, Pr_2CoAl, Pr_2CoGa, and Pr_2CoIn are classified as half-metallic ferromagnets (HMF) under the category of complete Heusler alloys.

Based on the magnetic moment values for each atom in the compounds presented in Table 4, we deduce that the predominant contribution to the total magnetic moment arises from the Pr atoms. In contrast, the Al, Ga, and In atoms contribute minimally to the total magnetic moment.

The electronic configurations of the atoms in our compounds are Pr: $[Xe]4f^3 6s^2$, Co: $[Ar]4s^2 3d^7$, Al: $[Ne]3s^2 3p^1$, Ga: $[Ar]3d^{10} 4s^2 4p^1$, In: $[Kr]4d^{10} 5s^2 5p^1$.

Furthermore, the compounds Pr_2CoAl, Pr_2CoGa, and Pr_2CoIn possess the same quantity of valence electrons, totalling 22. Our findings demonstrate a linear correlation between the total spin magnetic moment and the number of valence electrons, consistent with the established Slater–Pauling connection [61, 62], expressed by the following equation:

$$\mu_{tot} = Z_{tot} - 18 \tag{4}$$

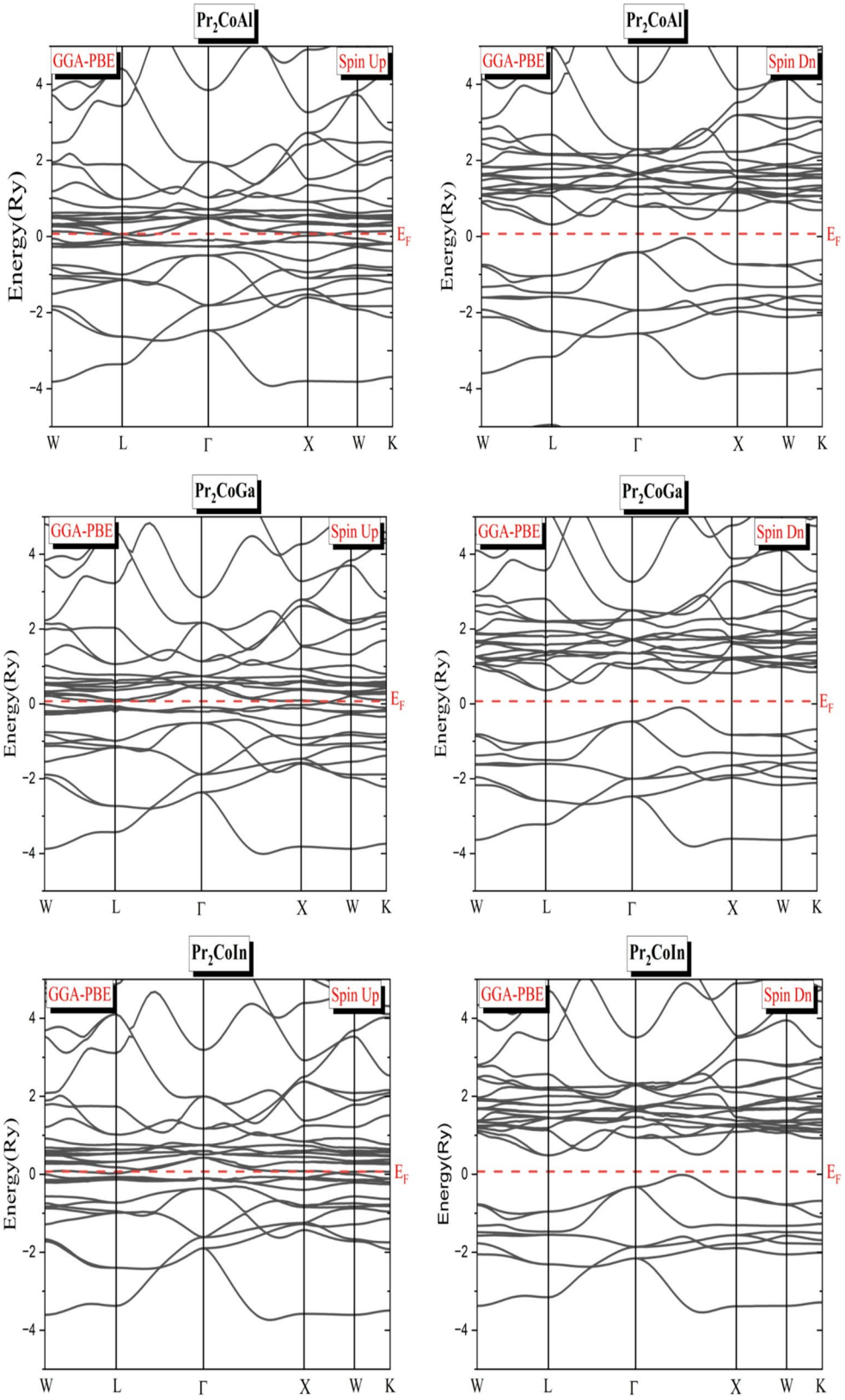


Fig. 4 Spin-polarized band structures of majority spin (Up) and minority spin (Down) of Pr_2CoZ (Z = Al, Ga, In) in Hg_2CuTi type structure

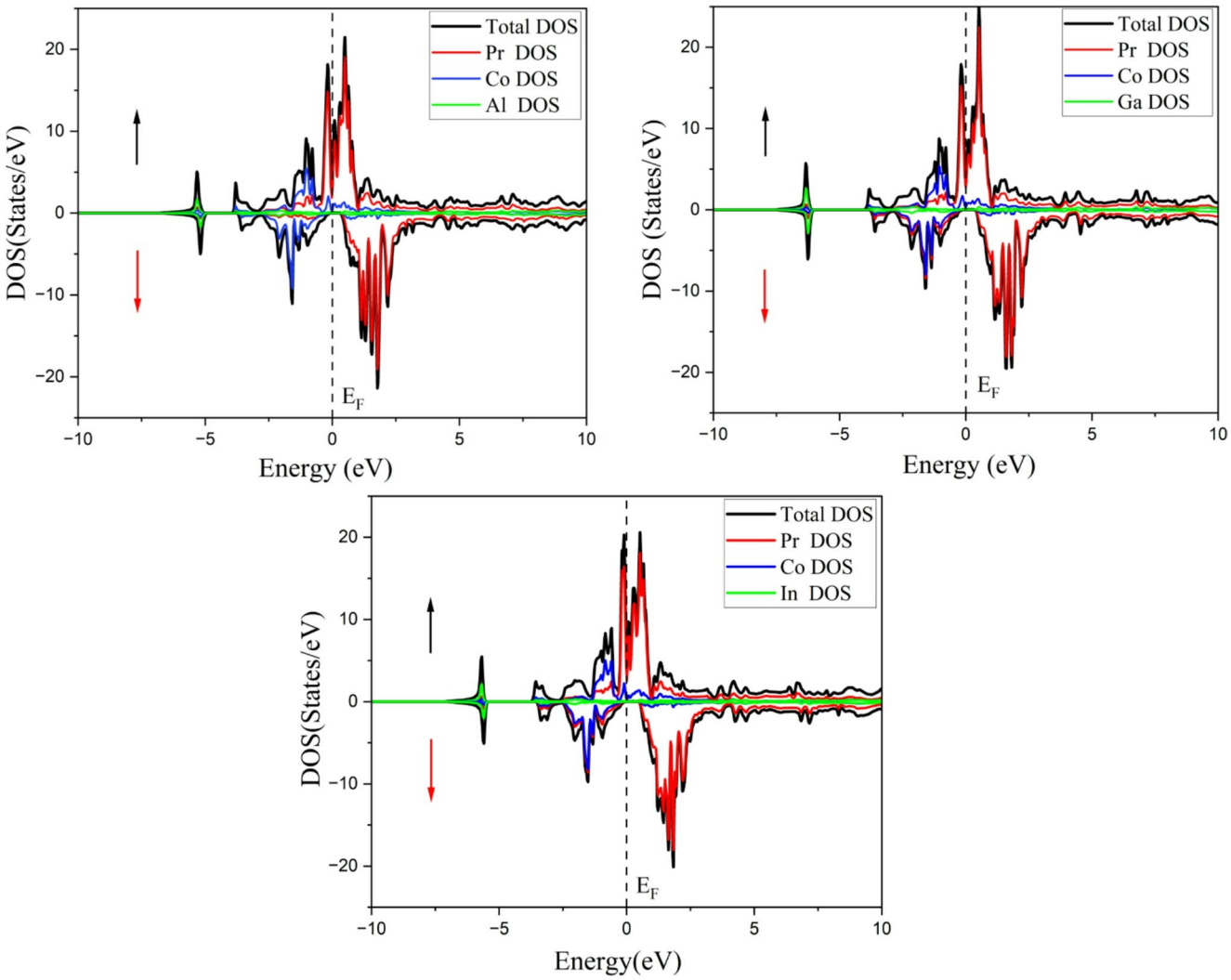


Fig. 5 Total density of state of Pr_2CoZ (Z=Al, Ga, In) alloys in Hg_2CuTi type structure

Table 4 The calculated total magnetic moments (Mt) and atomic magnetic moments for the Pr2CoZ (Z=Al, Ga, In)

Alloys	a (Å)	μtot	μPr1	μPr2	μCo	μ_Z	μinterstitial	E_g (eV)	Tc
Pr_2CoAl	6.7422	4.00 3.99 [47]	2.14972	2.06037	−0.77074	−0.02783	0.58868	0.359	747
Pr_2CoGa	6.7184	4.00 3.99 [47]	2.15491	2.09430	−0.78300	−0.03955	0.57506	0.483	747
Pr_2CoIn	6.9696	4.00 3.99 [47]	2.21622	2.15584	−1.01045	−0.03128	0.66852	0.492	747

where Z tot the total number of valence electrons per unit cell and μtot is the total spin magnetic moment [63].

The Curie temperature (Tc), which is a crucial quantity in the spintronic domains from which the magnetic phase transition may be precisely established, is one of the ways that has been used to evaluate it. It is calculated using the relation (Method 1) described by Wurmehl & al. The expression that shows the linear relationship between Curie temperature (Tc) and total magnetic moments is [64–66].

$$Tc = 23 + 181 \times Mtot \tag{5}$$

where Mtot stands for the global magnetic moments of the Heusler system. The calculated total magnetic moments (Mt), atomic magnetic moments for the Pr2CoZ (Z=Al, Ga, In), and Curie temperature (Tc) are presented in Table 3.

3.5 Thermodynamic Properties

The thermodynamic properties of our Heusler ferromagnetic alloys (Pr_2CoZ (Z=Al, Ga and In) in Hg_2CuTi-Type structure were calculated using the Gibbs 2 package, a new version of the quasiharmonic model for solid-state thermodynamics [43, 67]. The temperature range was chosen between 0 and 1000 K. In addition, the pressure value varies from 0 to 20 GPa to evaluate the energy or the number of phonons needed to raise the temperature of the materials. Figure 6 shows the calculated connections between heat capacities (C_V and C_P) and temperatures at various pressures for all materials: (a) Pr_2CoAl, (b) Pr_2CoGa, and (c) Pr_2CoIn.

Within the range of 0 to 300 K, both C_V and C_P increase rapidly until they reached the Dulong-Petit Limit (100 J/mol·K) then they increase linearly in the rest of the range. We have also seen that for C_v and C_P, their values at ambient pressure are higher than under pressure (up to 20 GPa). This behavior indicates that atomic interactions are dominant at low temperatures in these compounds.

The Fig. 7 shows the entropy (S) as a function of temperature (T) under two different pressures (0 GPa and 20 GPa) for three Heusler ferromagnetic alloys Pr_2CoZ (Z=Al, Ga and In) in Hg_2CuTi-Type structure. We observe that the entropy increases monotonically with temperature due to increased thermal disorder. This is consistent with the basic thermodynamic relationship [68]. However, at constant temperatures, the entropy decreases with increasing pressure. This is due to the decrease in atomic disorder under pressure. This indicates that higher pressure reduces entropy, likely due to the inhibition of vibrational motion in the crystal lattice [69].

The Fig. 8 illustrates how the Debye temperature Θ (K) changes with temperature (T) at two pressure values (0 GPa,

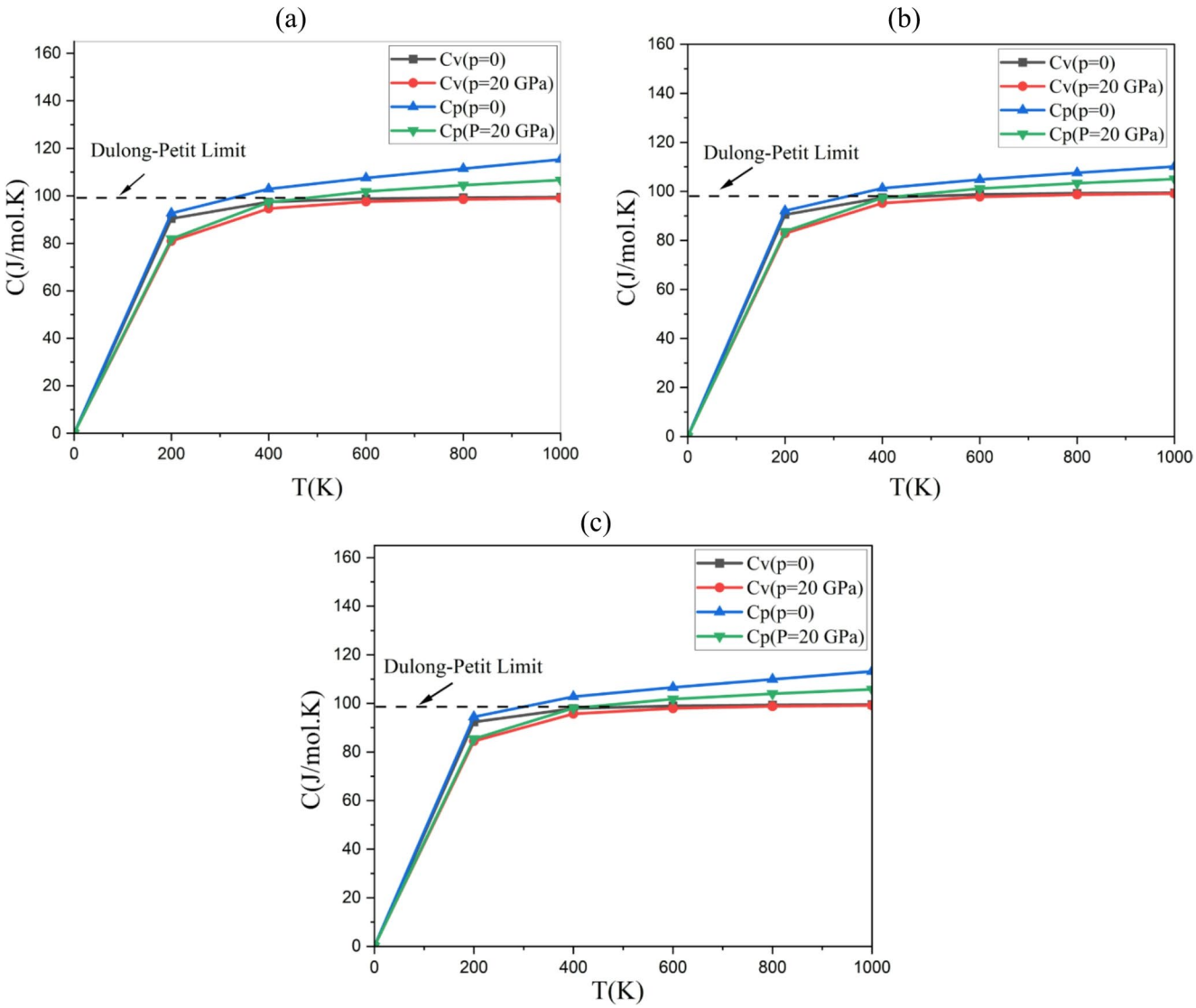


Fig. 6 Heat capacity as function of temperature in different pressure for Pr_2CoZ in witch (**a**) Pr_2CoAl, (**b**) Pr_2CoGa and (**c**) Pr_2CoIn

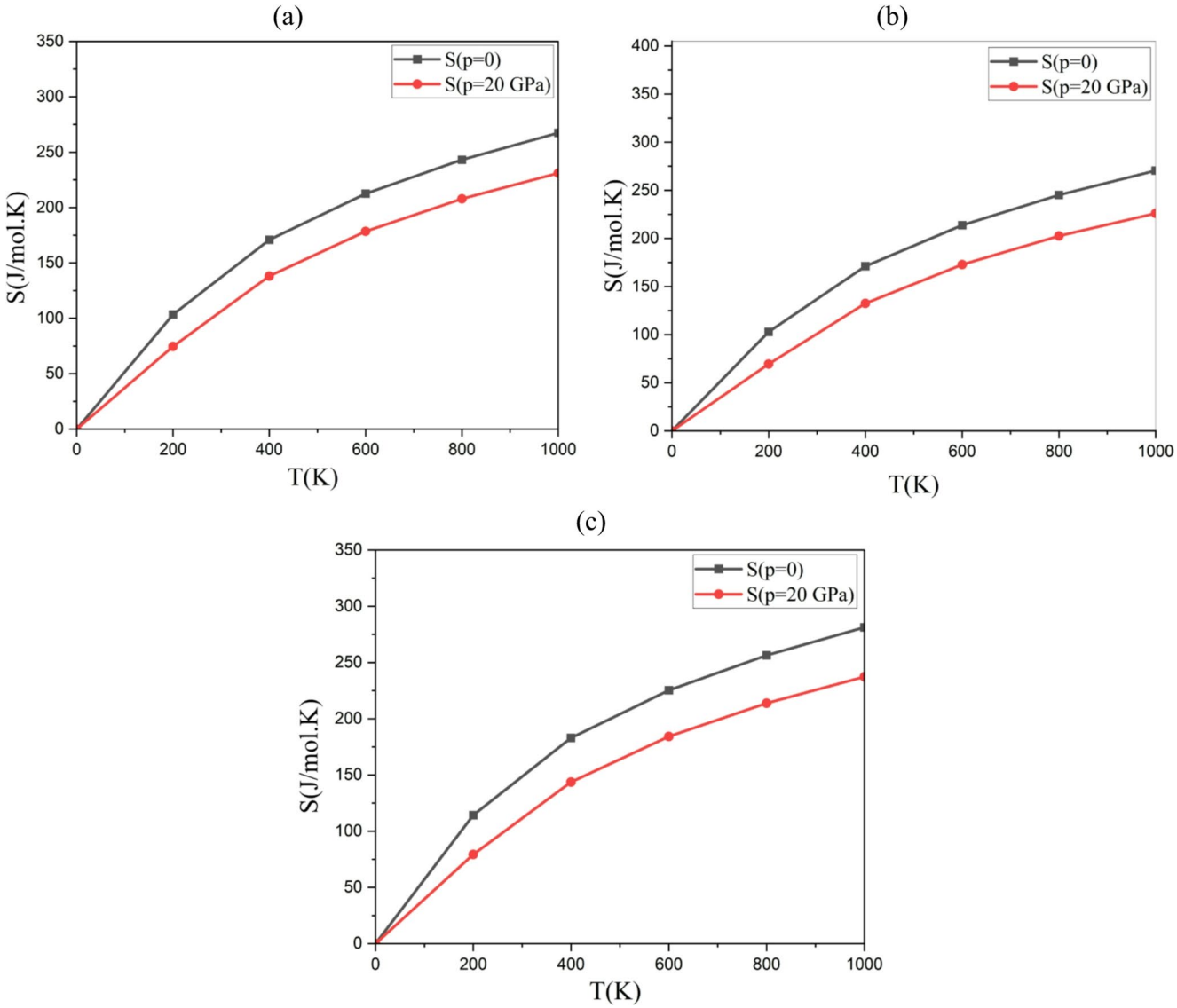


Fig. 7 Entropy as function of temperature in different pressures for Pr_2CoZ in which (**a**) Pr_2CoAl, (**b**) Pr_2CoGa and (**c**) Pr_2CoIn

20 GPa). This basic parameter provides important information on the specific heat and melting temperature. We note that the Debye temperature decreases with increasing temperature in all Heusler ferromagnetic Pr_2CoZ (Z=Al, Ga and In) in Hg_2CuTi-Type structure, whether at 0 or 20 GPa. As the temperature increases in these materials, the intensity of atomic vibrations increases, causing the atoms to vibrate around their positions at relatively regular frequencies [70]. This leads to a weakening of the dynamic rigidity of the material, meaning that the atoms move more freely, thus decreasing the Debye temperature. Meanwhile, the Debye temperature increases with increasing pressure at a constant temperature.

When we apply high pressure to a solid, the atoms in the crystal lattice become closer together. This closeness leads to increased interatomic forces because the atoms are now at shorter distances. As a result, the rigidity of the crystal lattice increases, and it becomes more difficult to make the atoms vibrate, which increases the vibrational frequencies of the phonons, thus increasing the Debye temperature.

3.6 Phonon Properties

Phonon dispersion curves for full Heusler alloys Pr_2CoZ (Z=Al, Ga and In) without andwith pressure are plotted in Figure. 9. Results of phonon dispersion curves are displayed in the first Brillouin zone. Since the structure of both Heusler alloys under study is fcc, which contains four atoms in a primitive cell. Therefore, we observed 12 vibrational modes of phonon at any chosen q-point, out of which three are acoustic modes, while the remaining nine are optical. However, it can be seen in the Figure. 9, that some transverse and

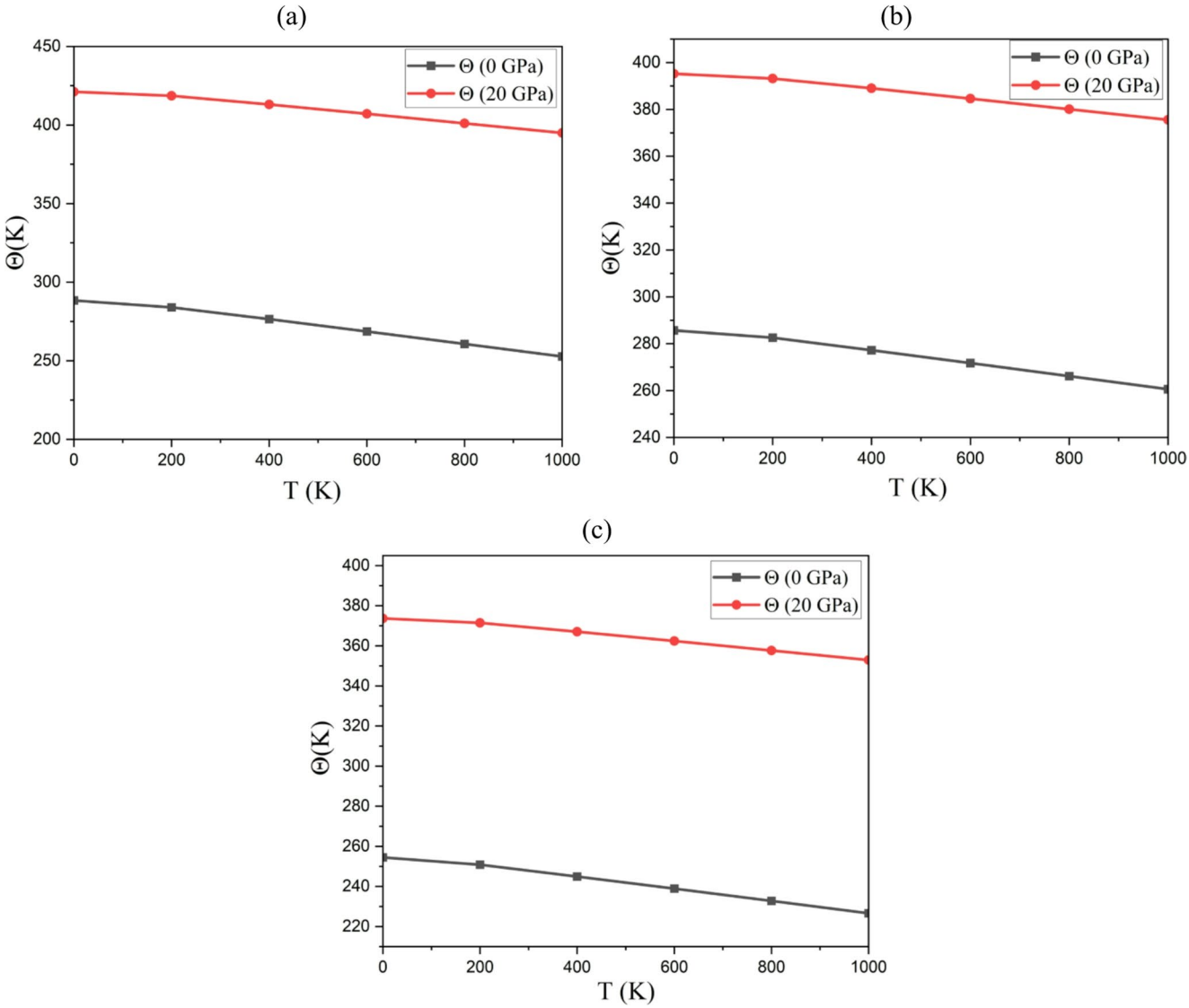


Fig. 8 Debye temperature as function of temperature in different pressure for Pr_2CoZ witch (**a**) Pr_2CoAl, (**b**) Pr_2CoGa and (**c**) Pr_2CoIn

acoustic branches are degenerate along specific high symmetry points.

For our three compounds, the phonon dispersion shows an imaginary phonon in some ranges, indicating instability at 0 GPa; after applying pressure, we observed the disappearance of the negative phonon at 5 GPa for Pr_2CoGa and at 10 GPa for both Pr2CoAl and Pr2CoIn, indicating that our alloys are dynamically stable under pressure.

4 Conclusion

The structural, electronic and magnetic properties of the Pr_2CoZ (Z=Al, Ga, In) for both Hg_2CuTi and Cu_2MnAl type structures have been investigated using the FP-LAPW in the GGA approximation method employed in the WIEN2K code. The Hg_2CuTi-type is more stable than that of Cu_2MnAl-type for Pr_2CoZ (Z=Al, Ga, In) compounds at ambient conditions. It exhibits HM nature and an indirect band gap with a magnetic moment of 4 μB, which is consistent with the Slater–Pauling rule.

The half-metallic nature (100% spin polarization) and total magnetic moment make Pr_2CoZ (Z=Al, Ga, In) ideal for spin-injection electrodes in MTJs.

The quasi-harmonic Debye model is successfully applied to examine the thermodynamic behaviors of its Heusler at different temperatures and pressures. By calculating the elastic properties, it was possible to confirm that full-Heusler Pr_2CoZ (Z=Al, Ga, In) Hg_2CuT-type structures are elastically stable in the phase under study and are ductile and not elastically isotropic, where the anisotropy values are 2.25, 2.00, and 1.57, respectively. These alloys are promising

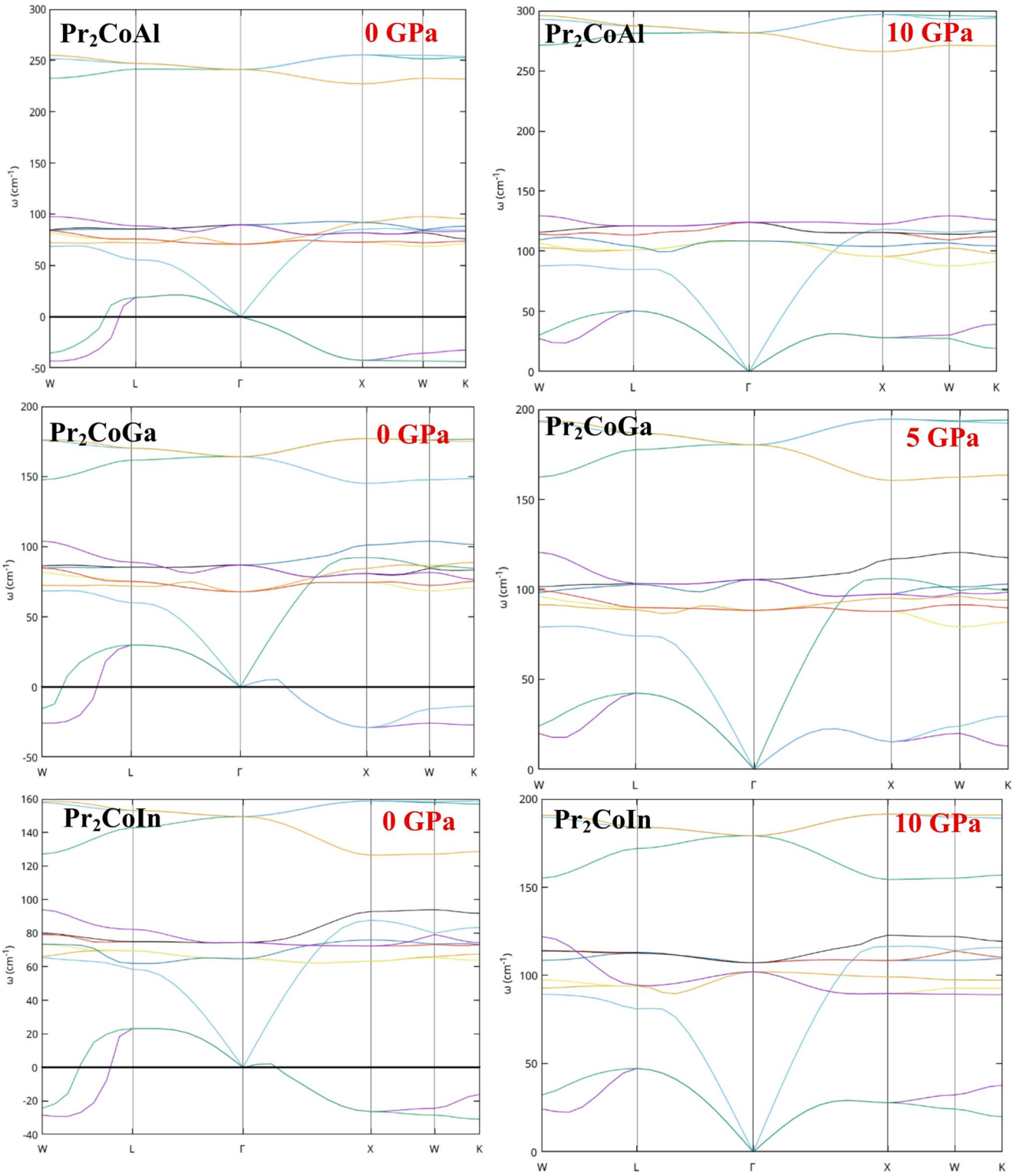


Fig. 9 Calculated phonon dispersion curves for Pr_2CoZ (Z = Al, Ga and In) without and with pressure

for spintronic devices due to their half-metallicity, spin polarization, robust mechanical thermal stability. The ductile behavior (Pugh's ratio > 1.75) and mechanical stability indicate robustness for flexible magnetic random-access memory (MRAM) or giant magnetoresistance. Thermodynamic analysis shows Debye temperatures (~300–400 K) and heat capacities approaching Dulong-Petit limits, suggesting potential in magnetocaloric refrigeration.

Author contributions A I BOUADI, M ABANE, M HAMMADI.prepared figures and Tables Aissam Hidoussi. Methodology, SoftwareM MOKHTARI, F DAHMANE wrote the main manuscript text.

Data Availability No datasets were generated or analysed during the current study.

Declarations

Competing interests The authors declare no competing interests.

References

1. Hong, T., et al.: Discovery of new topological insulators and semimetals using deep generative models. npj Quantum Mater. **10**(1), 12 (2025)
2. Dong, W., et al.: Wire-based friction stir welding enables equal-strength joining of aluminum alloys even with assembling gaps. J. Manuf. Process. **151**, 426–433 (2025)
3. Yu, H., et al.: The design of oxidation resistant Ni superalloys for additive manufacturing. Additive Manuf. **97**, 104616 (2025)
4. Zhao, Y.-C., et al.: A Xanthium sibiricum biomimetic Fe-based medium-entropy alloy with significant antibacterial and mechanical behaviors. Rare Met. **44**(7), 4913–4935 (2025)
5. Li, D., et al.: Theoretical studies on the structural, electronic, and optical properties of Cu2CdGeSe4. Phys. B: Condens. Matter. **406**(17), 3299–3302 (2011)
6. Zhou, Z., Zhang, K., Leng, Q.: Tunneling magnetoresistance (TMR) materials and devices for magnetic sensors, pp. 51–92. Materials, Devices and Applications, Spintronics (2022)
7. Dahmane, F., et al.: First principles study of the electronic structures and magnetic properties of transition metal-doped cubic indium nitride. Mater. Sci. Semiconduct. Process. **21**, 66–73 (2014)
8. Dahmane, F., et al.: Structural, Electronic and Magnetic Properties of Zinc-Blende Ga1 – xTMxN (TM = Cr, Mn, Fe, V). J. Supercond. Novel Magn. **26**(12), 3339–3348 (2013)
9. Chadov, S., et al.: Efficient spin injector scheme based on Heusler materials. Phys. Rev. Lett. **107**(4), 047202 (2011)
10. Zerouali, A., et al.: First-principle calculations of electronic and ferromagnetic properties of $$\hbox {Al}_{1-x}\hbox {V}_{x}\hbox {Sb}$$. J. Comput. Electron. **15**(4), 1255–1262 (2016)
11. De Groot, R.A., et al.: New class of materials: half-metallic ferromagnets. Physical review letters **50**(25), 2024 (1983)
12. Heusler, F., Starck, W., Haupt, E.: Magnetisch-chemische studien. Verh Dtsch. Phys. Ges. **5**, 219–232 (1903)
13. Tishin, A.M., Spichkin, Y.I.: The magnetocaloric effect and its applications. CRC Press (2016)
14. Wu, K., et al.: Giant magnetoresistance biosensors in biomedical applications. ACS Appl. Mater. Interfaces. **14**(8), 9945–9969 (2022)
15. Amari, D., et al.: Structural, elastic, electronic, magnetic, and half-metallic properties of a novel rare earth-based quaternary Heusler Alloys LaXTiSi (X = Co, Rh, Ir). Emergent Mater. **6**(1), 299–306 (2023)
16. Chatterjee, S., et al.: Half-metallic ferromagnetism and intrinsic anomalous Hall effect in the topological Heusler compound Co 2 MnGe. Phys. Rev. B. **108**(20), 205108 (2023)
17. Singh, J., et al.: LiNbCoX (X = Al, Ga) quaternary Heusler compounds for high-temperature thermoelectric properties: a computational approach. Bull. Mater. Sci. **46**(2), 103 (2023)
18. Zhai, M.-X., Liang, X., Li, D.-X.: Bipolar magnetic semiconductors and half-metals in transition metals doped SnSe2 zigzag nanoribbons. Results Phys. **39**, 105733 (2022)
19. Çanlı, M., Ilhan, E., Arıkan, N.: First-principles calculations to investigate the structural, electronic, elastic, vibrational and thermodynamic properties of the full-Heusler alloys X2ScGa (X = Ir and Rh). Mater. Today Commun. **26**, 101855 (2021)
20. Sun, C., Alonso, J.A., Bian, J.: Recent advances in perovskite-type oxides for energy conversion and storage applications. Adv. Energy Mater. **11**(2), 2000459 (2021)
21. Zhang, X., et al.: Theoretical and experimental study of the phase formation for Ti2YAl and Ti2Y′ Ga (Y = Co, Fe; Y′= Cr, Fe). Intermetallics. **73**, 26–30 (2016)
22. Boumia, L.: Physical Properties of Heusler Alloys. In: Contemporary Advancements in Materials Technology, pp. 155–175. Apple Academic Press (2025)
23. Huang, H.-L., Tung, J.-C., Jeng, H.-T.: A first-principles study of rare earth quaternary Heusler compounds: RXVZ (R = Yb, Lu; X = Fe, Co, Ni; Z = Al, Si). Phys. Chem. Chem. Phys. **23**(3), 2264–2274 (2021)
24. Abuova, F., et al.: Structural, Electronic and Magnetic Properties of Mn2Co1-xVxZ (Z = Ga, Al) Heusler Alloys: An Insight from DFT Study. Magnetochemistry. **7**(12), 159 (2021)
25. Rai, D.P., et al.: Electronic and magnetic properties of a full-Heusler alloy Co2CrGe: a first-principles study. J. Theoretical Appl. Phys. **7**(1), 3 (2013)
26. Birsan, A.: Electronic structure and magnetism of new scandium-based full Heusler compounds: Sc2CoZ (Z = Si, Ge, Sn). J. Alloys Compd. **598**, 230–235 (2014)
27. Candan, A., et al.: Electronic structure and vibrational properties in cobalt-based full-Heusler compounds: A first principle study of Co2MnX (X = Si, Ge, Al, Ga). J. Alloys Compd. **560**, 215–222 (2013)
28. Arıkan, N., et al.: Electronic and phonon properties of the full-Heusler alloys X2YAl (X = Co, Fe and Y = Cr, Sc): a density functional theory study. J. Mater. Sci. **49**(12), 4180–4190 (2014)
29. Özduran, M., et al.: Structural, elastic, electronic, and magnetic properties of Si-doped Co2MnGe full-Heusler type compounds. J. Alloys Compd. **845**, 155499 (2020)
30. Candan, A.: Magnetic, Electronic, Mechanic, Anisotropic Elastic and Vibrational Properties of Antiferromagnetic Ru2TGa (T = Cr, Mn, and Co) Heusler Alloys. J. Electron. Mater. **48**(12), 7608–7622 (2019)
31. Candan, A.: A study on magnetic, electronic, elastic and vibrational properties of Ir2MnAl Heusler alloy for spintronic applications. Mater. Res. Express. **6**(9), 096571 (2019)
32. Mehta, S., Saini, S.M.: Transport and optical study of mechanically stable novel RNiSb (R = Tb, Dy, Tm) half-Heusler compounds for thermoelectric and optoelectronic applications. Phys. Scr. **100**(1), 015955 (2024)
33. Satyam, J.K., Saini, S.M.: Electronic structure and optical properties of Rare-Earth based ErPdSb half Heusler Compound: A GGA + U study. Mater. Today: Proc. **44**, p3040–3044 (2021)
34. Bouchenafa, H., et al.: Exploring the electronic structure, mechanical stability, thermodynamic and magnetic properties of rare-earth full-Heusler alloys Pd2Gd x La1 – x In (x = 1, 0.75, 0.5, 0.25, and 0): a DFT approach. Eur. Phys. J. B. **97**(8), p117 (2024)
35. Donaberger, R., Stager, C.: Magnetic structures of the rare earth heusler alloys Pd2DySn and Pd2HoSn. J. Less Common. Met. **127**, 93–98 (1987)
36. Bahhar, S., et al.: Impact of pressure on quaternary Heusler alloy LiScNiGe for optoelectronic application. Mater. Sci. Semiconduct. Process. **193**, 109497 (2025)
37. Wang, X.T., et al.: Electronic structures and magnetism in the Li2AgSb-type Heusler alloys, Zr2CoZ (Z = Al, Ga, In, Si, Ge,

Sn, Pb, Sb): A first-principles study. J. Magn. Magn. Mater. **394**, 50–59 (2015)
38. Petersen, M., et al.: Improving the efficiency of FP-LAPW calculations. Comput. Phys. Commun. **126**(3), 294–309 (2000)
39. Blaha, P., et al.: Full-potential, linearized augmented plane wave programs for crystalline systems. Comput. Phys. Commun. **59**(2), 399–415 (1990)
40. Kohn, W., Sham, L.J.: Self-consistent equations including exchange and correlation effects. Phys. Rev. **140**(4A), A1133 (1965)
41. Amari, D., et al.: A comparative study between Hg2CuTi and Cu2MnAl type structures for Zr2CoZ (Z=Al, Ga, In) Heusler alloys. Chin. J. Phys. **60**, 450–461 (2019)
42. Jamal, M., et al.: IRelast package. J. Alloys Compd. **735**, 569–579 (2018)
43. Otero-de-la-Roza, A., Luaña, V.: Gibbs2: A new version of the quasi-harmonic model code. I. Robust treatment of the static data. Comput. Phys. Commun. **182**(8), 1708–1720 (2011)
44. Dahmane, F., et al.: Structural, electronic and magnetic properties of Fe2-based full Heusler alloys: A first principle study. J. Magn. Magn. Mater. **407**, 167–174 (2016)
45. Babiker, S., Gao, G., Yao, K.L.: First-principle calculation of electronic structures and magnetic properties of Heusler alloys Co2ZrPb and Zr2MnBa. J. Supercond. Novel Magn. **31**(3), 905–913 (2018)
46. Birch, F.: The effect of pressure upon the elastic parameters of isotropic solids, according to Murnaghan's theory of finite strain. J. Appl. Phys. **9**(4), 279–288 (1938)
47. Rouag, S., Amari, D.: Theoretical Calculation of the Structural, Electronic, and Magnetic Properties of a New Rare-Earth Based Full Heusler Alloys Pr2CoZ (Z=Al, Ga, In). Phys. Solid State. **66**(6), 176–183 (2024)
48. Wang, X., et al.: Lattice constant changes leading to significant changes of the spin-gapless features and physical nature in a inverse heusler compound Zr2MnGa. J. Magn. Magn. Mater. **444**, 313–318 (2017)
49. Khodami, M., Ahmadian, F.: First-principles study of magnetism and half-metallic properties for the quaternary Heusler alloys CoMnTiZ (Z=P, As, and Sb). J. Supercond. Novel Magn. **28**(10), 3027–3035 (2015)
50. Kundu, M., et al.: Complex magnetic properties associated with competing local and itinerant magnetism in Pr 2 Co 0.86 Si 2.88. Sci. Rep. **11**(1), 13245 (2021)
51. Chung, D., Buessem, W.: The voigt-reuss-hill approximation and elastic moduli of polycrystalline MgO, CaF2, β-ZnS, ZnSe, and CdTe. J. Appl. Phys. **38**(6), 2535–2540 (1967)
52. Ghebouli, M.A., et al.: Structural, elastic and optoelectronic properties of Sr-based perovskite-type oxides SrXO3 (M=Th, Zr) via first-principles calculations. Chin. J. Phys. **56**(4), 1515–1524 (2018)
53. Wang, J., et al.: Crystal instabilities at finite strain. Phys. Rev. Lett. **71**(25), 4182 (1993)
54. Fang, Q.-L., et al.: The effect of defects on the magnetic properties and spin polarization of Ti2FeAl Heusler alloy. J. Magn. Magn. Mater. **351**, 25–28 (2014)
55. Al-zyadi, J.M.K., Gao, G., Yao, K.-L.: Theoretical investigation of the electronic structures and magnetic properties of the bulk and surface (001) of the quaternary Heusler alloy NiCoMnGa. J. Magn. Magn. Mater. **378**, 1–6 (2015)
56. Faleev, S.V., et al.: Unified explanation of chemical ordering, the Slater-Pauling rule, and half-metallicity in full Heusler compounds. Phys. Rev. B. **95**(4), 045140 (2017)
57. Jain, V.K., et al.: Induced spin polarization in Fe2VAl by substitution of Co at Fe site. Comput. Mater. Sci. **108**, 56–61 (2015)
58. Winterlik, J., et al.: Structural, electronic, and magnetic properties of tetragonal Mn 3−x Ga: Experiments and first-principles calculations. Phys. Rev. B—Condensed Matter Mater. Phys. **77**(5), 054406 (2008)
59. Skaftouros, S., et al.: Generalized Slater-Pauling rule for the inverse Heusler compounds. Phys. Rev. B—Condensed Matter Mater. Phys. **87**(2), 024420 (2013)
60. Skaftouros, S., et al.: Generalized Slater-Pauling rule for the inverse Heusler compounds. Phys. Rev. B. **87**(2), 024420 (2013)
61. Galanakis, I., Dederichs, P., Papanikolaou, N.: Slater-Pauling behavior and origin of the half-metallicity of the full-Heusler alloys. Phys. Rev. B. **66**(17), 174429 (2002)
62. Galanakis, I., Mavropoulos, P., Dederichs, P.H.: Electronic structure and Slater–Pauling behaviour in half-metallic Heusler alloys calculated from first principles. J. Phys. D. **39**(5), 765 (2006)
63. Slater, J.: Suggestions from solid-state theory regarding molecular calculations. J. Chem. Phys. **43**(10), S228–S228 (1965)
64. Raïâ, M.Y., et al.: Comparative study of magnetic stability, electronic, optical, thermoelectric and thermal properties of Co2FeSn and Fe2CoSn full Heusler alloys from first principles approch. Computational Condensed Matter **38**, e00861 (2024)
65. Enamullah, Lee, S.-C.: High-efficient and defect tolerant Co2MnSb ternary Heusler alloy for spintronic application. J. Alloys Compd. **765**, 1055–1060 (2018)
66. Sanga, L., et al.: A DFT investigation of the basic properties for Cr2XAl (X=V, Nb, Ta) full Heusler alloys. Phys. B: Condens. Matter. **717**, 417847 (2025)
67. Otero-De-La-Roza, A., Abbasi-Pérez, D., Luaña, V.: Gibbs2: A new version of the quasiharmonic model code. II. Models for solid-state thermodynamics, features and implementation. Comput. Phys. Commun. **182**(10), 2232–2248 (2011)
68. Borgnakke, C.: Fundamentals of thermodynamics. Wiley (2025)
69. Benaddi, F., Bentouaf, A., Rached, A.A.: Structural, electronic and thermoelectric properties of the RENi2 (RE=Dy, Er, Ho) rare Earth intermetallic compounds: a density-functional-theory investigation. Eur. Phys. J. B. **98**(7), 139 (2025)
70. Moussali, A., et al.: First-principles calculations to investigate structural and thermodynamic properties of Ni2LaZ (Z=As, Sb and Bi) Heusler alloys. Indian J. Phys. **94**(11), 1733–1747 (2020)

Publisher's Note Springer Nature remains neutral with regard to jurisdictional claims in published maps and institutional affiliations.

Springer Nature or its licensor (e.g. a society or other partner) holds exclusive rights to this article under a publishing agreement with the author(s) or other rightsholder(s); author self-archiving of the accepted manuscript version of this article is solely governed by the terms of such publishing agreement and applicable law.